NANOSTRUCTURED SENSORS AND INTEGRATED SYSTEMS FOR ADVANCED BIOSENSING

YUQING SHI

PhD

The Hong Kong Polytechnic University

2026

The Hong Kong Polytechnic University

Department of Applied Biology and Chemical Technology

Nanostructured Sensors and Integrated Systems for Advanced Biosensing

Yuqing Shi

A thesis submitted in partial fulfilment of the requirements for the degree of Doctor of Philosophy

August 2025

CERTIFICATE OF ORIGINALITY

I hereby declare that this thesis is my work and that, to the best of my knowledge and belief, it reproduces no material previously published or written, nor material that has been accepted for the award of any other degree or diploma, except where due acknowledgement has been made in the text.

_____(Signed)

Yuqing Shi (Name of Student)

ABSTRACT

In the critical domains of public health surveillance and personalized medical interventions, the capability of high-performance sensors to achieve real-time monitoring and precise intervention has become a fundamental requirement. However, current technologies face three major challenges: insufficient sensitivity in complex matrices, limited long-term operational stability, and a lack of intelligent responsiveness. To overcome these barriers, this dissertation advances sensing design and integrated system engineering centered on the core theme of enhancing sensing performance through nanomaterials. A structured three-tiered research framework is established, beginning with ultrasensitive detection of trace analytes in complex environments, advancing to stable wearable monitoring under dynamic conditions, and culminating in intelligent closed loop intervention system for pathological regulation.

To achieve an ultralow detection limit in electrochemical biosensing, a printable electrochemical biosensor was developed with an ultralow detection limit and high operational stability. The sensor features a dendritic gold nanostructure modified with a PBASE-functionalized interface, tailored for efficient antigen recognition. By leveraging the increased surface area and localized electric field amplification afforded by the fractal electrode morphology, the sensor enables ultralow detection limit of SARS-CoV-2 and H_3N_2 antigens in wastewater, reaching a detection limit of 0.025 fg/mL. Without requiring complex sample preprocessing, the device exhibits excellent selectivity and operational robustness, thereby enabling real-time viral surveillance in wastewater-based epidemiology (WBE).

Beyond achieving ultralow detection limits, long-term stability and washability are essential for real-world deployment. To address the need for stable and continuous monitoring of sweat biomarkers, a wearable textile-based sodium ion sensor was developed by incorporating β-Bi_2O_3 nanoflakes with fast ion diffusion. These nanostructures substantially enhance the adhesion strength and structural stability of the ion-selective membrane, resulting in excellent washability and mechanical durability.

The sensor maintained over 90% of its initial performance after 20 washing cycles. Integrated with a Bluetooth Low Energy module, the system enables real-time visualization of sodium levels in sweat, offering a practical and reliable platform for personal health monitoring under dynamic conditions. These results establish a durable sensing front end suitable for integration into a closed loop therapeutic architecture.

Building on this sensing front end, we realize a comprehensive closed-loop system coupling continuous monitoring with precise intervention. The architecture integrates a high-performance flexible pH sensor and a PMA hydrogel battery array that ensures reliable power below 0°C. To achieve autonomous regulations, an active therapeutic unit was developed by combining a nanostructured palladium black electrode with a pH-sensitive PAM/CS hydrogel. In a cold liver model, sensor-detected acidosis triggers chitosan protonation, leading to rapid hydrogel swelling and NAC release while the palladium interface manages proton flux. This synergistic cycle demonstrates a practical platform that coordinates detection, decision, and delivery to effectively mitigate oxidative stress and enhance organ viability.

This dissertation systematically explores how nanomaterials enhance sensing performance at the device and system levels. First, dendritic gold nanostructures are employed to amplify sensitivity through localized surface effects. Then, β-Bi_2O_3 nanoflakes are introduced to improve the structural stability and washability of wearable sensors. Finally, functional hydrogels are integrated to enable a closed-loop therapeutic response, completing a full-chain intelligent sensing-intervention system. The three types of sensing systems developed in this work demonstrate substantial application potential in early public health warning through wastewater surveillance, personalized health management via sweat biomarkers, and clinical resource optimization by improving organ viability. Collectively, these strategies not only address fundamental bottlenecks in current sensing technologies but also offer a scalable paradigm that advances the frontiers of intelligent, adaptive sensing systems.

LIST OF PUBLICATIONS

Published papers:

1. **Yuqing Shi**, Kemeng Zhou, Xiaohao Ma, Liting Huang, Xinmeng Hu, Pengwei Wang, Yaokang Zhang, Fan Chen, Mingli Huang, Jianzhen Wu, Xin He, Qiyao Huang, Zijian Zheng*, Yuanjing Lin*, Washable textile biosensors enabled by nanostructured oxides with fast ion diffusion, Device, 2, 100503 (2024)

2. Yuqing Shi[#], Yan-Kin Lau[#], Ruochen Ding, Yuqi Wang, Yutian Xiao, Weijia Wen, Kwong Hoi Tsui*, Yuanjing Lin*, Nanostructured Biosensors with Ultra-Low Detection Limit and High Selectivity for Real-Time and Continuous Sewage Monitoring, ACS sensors, 10(10), 7378-7387 (2025)

3. **Yuqing Shi,** Ziyu Zhang, Qiyao Huang*, Yuanjing Lin*, Zijian Zheng, Wearable sweat biosensors on textiles for health monitoring, Journal of Semiconductors, 44(2), 021601 (2023)

Paper in Preparation:

1. **Yuqing Shi**[#], Yuting Fu[#], Xiong Yu, Yuao Guo, Yanjun Liu, Dan Luo*, Yuanjing Lin*, Adaptive and Highly Efficient Thermoregulation based on Multi-dimensional Janus Membrane

ACKNOWLEDGEMENTS

Foremost, I wish to express my deepest gratitude and profoundest appreciation to my esteemed supervisors, Professor Zijian Zheng and Professor Yuanjing Lin. I am immensely grateful for the invaluable opportunity they granted me to pursue my Ph.D. studies within their exceptional research groups. Professor Zheng's visionary leadership and Professor Lin's rigorous scientific approach have not only set the highest standards for my research but have also profoundly shaped my academic thinking. Their patient mentorship, unwavering encouragement, and insightful guidance have been the cornerstone of my progress and the most treasured gifts throughout my doctoral journey.

My heartfelt thanks extend to all members of Professor Zheng's and Professor Lin's research groups. Your collective dedication fostered an outstanding laboratory environment brimming with dynamism and a spirit of collaboration, which provided me with constant warmth and support. I am particularly indebted to Professor Qiyao Huang, Dr. Fan Chen, Dr. Pengwei Wang, Dr. Miya Ng, Dr. Xian Song, Dr. Jiehua Cai, Dr. Leni Zhong, Dr. Qiuna Zhuang, Dr. Jingjing Fu, Dr. Yufei Zhang, Dr. Yanpeng Guo, Mr. Xiaohao Ma, Ms. Liting Huang, Ms. Kemeng Zhou, Ms. Xinyi Zhang, Mr. Le Chen, Mr. Junjie Su, Mr. Xiaolong Zeng, Mr. Ruiheng Peng, Mr. Jiaheng Liang, and Mr. Ruochen Ding. Thank you for your selfless assistance, dedicated training, insightful discussions, and constructive suggestions throughout my research endeavors. I also sincerely appreciate the contributions of all the technicians and collaborators actively involved in this project. My sincere appreciation also goes to the technical and support staff at the School of Fashion and Textiles, the Department of Applied Biology and Chemical Technology, and the School of Microelectronics for their indispensable help with sample characterization and analysis. The generous financial support from the Southern University of Science and Technology and The Hong Kong Polytechnic University is gratefully acknowledged.

Finally, and above all, I reserve my deepest love and boundless gratitude for my parents, my brother, and Mr. Peiran Wang. You have been my unwavering anchor and safe

harbor. Your unconditional love, constant understanding, steadfast support, and endless encouragement have been my enduring source of strength, sustaining me unfailingly throughout this remarkable journey. Your selfless devotion has been my strongest foundation, illuminating my path forward.

TABLE OF CONTENTS

NANOSTRUCTURED SENSORS AND INTEGRATED SYSTEMS FOR ADVANCED BIOSENSING **1**

CERTIFICATE OF ORIGINALITY 1

ABSTRACT ..... **II**

ACKNOWLEDGEMENTS ..... **V**

TABLE OF CONTENTS ..... **VII**

LIST OF FIGURES **11**

LIST OF TABLES **21**

CHAPTER 1 INTRODUCTION **23**

1.1 Background and Challenges 23

1.2 Research Objectives 25

1.3 Research Originality 27

1.4 Outline of the Thesis 29

CHAPTER 2 LITERATURE REVIEW **32**

2.1 Ultralow Detection Limit in Complex Matrices with Dendritic Gold 32

2.1.1 Ultralow detection challenge and evaluation metrics 32

2.1.2 Dendritic Gold Nanostructures for Sensitive Electrochemical Sensing ... 34

2.1.3 Device oriented WBE application for viral antigen sensing 38

2.1.4 Summary 47

2.2 Washability and long-term stability with β-Bi_2O_3 reinforced wearable sensors 48

2.2.1 Fundamental Mechanisms for Biosensing and Stability 50

2.2.2 Materials and Structural Designs for Skin-Conformal and Washable Biosensors 60

2.2.3 Material Strategies for Mechanical Robustness and Durability 64

2.2.4 Integration Challenges and Solutions for Washable and Flexible Biosensor Systems 66

2.2.5 Summary and Outlook 68

2.3 Closed-Loop Intelligent Sensing and Intervention Systems for Biomedical Preservation Applications 70

2.3.1 Limitations of Conventional Strategies in Biomedical Preservation and Intervention Systems 73

2.3.2 Acid-Responsive Pathological Microenvironments and the Need for On-Demand Closed-Loop Intervention 76

2.3.3 Stimuli-Responsive Hydrogels for Sensing and Therapeutic Release 79

2.3.4 Recent Advances in Integrated Low-Temperature Sensing Platforms for Closed-Loop Biomedical Applications 81

CHAPTER 3 METHODOLOGY 84

3.1 Materials 84

3.2 Fabrication of integrated biosensing and biomedical applications 85

3.2.1 Fabrication of virus biosensor 85

3.2.2 Fabrication of electrode patterns on textile 86

3.2.3 Fabrication of ion-selective sensor 87

3.3 Characterization 88

CHAPTER 4 DENDRITIC GOLD-ENABLED ELECTROCHEMICAL BIOSENSOR FOR ULTRA-SENSITIVE AND REAL-TIME VIRUS DETECTION IN WASTEWATER 90

4.1 Introduction 90

4.2 Experiment 93

4.2.1 Design Requirements for Virus Biosensors 93

4.2.2 Development of the Virus Biosensor 95

4.2.3 Characterization 98

4.3 Results and Discussion 100

4.3.1 Dendritic Gold Nanostructures for Electrochemical Signal Amplification 100

4.3.2 Characterization of the Virus Biosensor 104

4.3.3 Sensing Performance and LOD 109

4.3.4 System Integration and On-Site Validation in Sewage Samples 113

4.3.5 Conclusion 118

CHAPTER 5 WASHABLE TEXTILE BIOSENSORS ENABLED BY NANOSTRUCTURED OXIDES WITH FAST ION DIFFUSION 120

5.1 Introduction: 121

5.2 Experiment 123

5.2.1 Fabrication Process of Textile Electrode 123

5.2.2 Fabrication of Ion-Selective Textile Sensors 123

5.2.3 Functionalization of Sensors with Oxide Nanomaterials 125

5.2.4 Characterization 126

5.3 Results and Discussion 128

5.3.1 Structural Characteristics and Fast Ion Conducting Mechanism of β-Bi_2O_3 Nanoflakes 128

5.3.2 Comparative Studies on Material Structures and Validation of the Unique Role of β-Bi_2O_3 136

5.3.3 Construction and Fundamental Performance Evaluation of Wearable Na^+ Sensor 139

5.3.4 Enhancement of Sensor Washability by Fast Ion-Conducting β-Bi_2O_3 Nanoflakes 143

5.3.5 Design of Wearable Textile Structure and Evaluation of Wearing Comfort 150

5.3.6 BLE Wireless Module and Human-Machine Interaction System 153

5.4 Conclusion 157

CHAPTER 6 DESIGN AND INTEGRATION OF AN INTELLIGENT RESPONSIVE SYSTEM FOR ORGAN TRANSPORTATION UNDER COLD CONDITIONS 159

6.1 Introduction 159

6.2 Experiment 161

6.2.1 Preparation of the pH-Responsive Hydrogel 161

6.2.2 Preparation of the Palladium Electrode for Active pH Regulation 162

6.2.3 Fabrication of PMA Hydrogel-Based Batteries 163

6.3 Results and Discussion 164

6.3.1 System Architecture and Operating Mechanism 164

6.3.2 Flexible pH Sensor Module 167

6.3.3 Characterization of the Active Responsive Therapeutic Unit 174

6.3.4 PMA Hydrogel Battery 191

6.4 Conclusion and Outlook 194

6.4.1 Conclusion 194

6.4.2 Future Perspectives 195

7.1 Conclusions 197

7.2 Suggestions for Future Research 199

REFERENCES 201

LIST OF FIGURES

Figure 2.1 SEM images of dAu with high specific surface area[8]. 35

Figure 2.2 Schematic of mechanism underlying anti-biofouling of nano structured Au electrodes[15]..... 36

Figure 2.3 A schematic representation illustrating the deposition of electrochemical dendritic gold nanostructures on graphite rod electrodes, followed by the immobilization of glucose oxidase and glucose determination using the developed biosensor[18]. 37

Figure 2.4 Cyclic voltammograms of EPLE and AuDNs/EPLE[48]..... 37

Figure 2.5 Schematic illustration of the general WBE process[29]..... 39

Figure 2.6 Sanger sequencing data were obtained and aligned with the SARS-CoV-2 spike (S) gene to confirm the presence and identity of viral genetic material[9]..... 40

Figure 2.7 Workflow for molecular testing SARS CoV-2[49]..... 42

Figure 2.8 A schematic illustrating the competition between RNase and reverse transcriptase (RT) in a one-pot RT-LAMP reaction, where no purification is required and the pretreatment is performed in a single step[50]. 44

Figure 2.9 SHERLOCK enables single-molecule nucleic acid detection through the following steps: (a) The SHERLOCK workflow involves dsDNA and RT-RPA amplification. (b) ssRNA targets (highlighted in blue) are detected through the collateral activity of Cas13a. (c) SHERLOCK (Cas13a + RPA) demonstrates ~2 aM sensitivity for ssRNA, outperforming Cas13a alone (mean ± SEM, n = 4). (d) Additionally, SHERLOCK is capable of detecting single-molecule DNA (mean ± SEM, n = 4)[54]. 46

Figure 2.10 The evolution of biosensors for wearable devices[55]. 49

Figure 2.11 Wearable sweat sensors for multiplexed detection of key health-related biomarkers[61]..... 50

Figure 2.12 (a) Sweat gland secretion and sodium ion fluctuation during exercise. (a) Schematic illustration of a sweat gland and representative analytes present in sweat. (b) Variation of sodium ion concentration during physical activity, where an abnormal increase indicates dehydration[55,70]. 52

Figure 2.13 Wearable wristwatch for sweat electrolyte monitoring. (a,b) Three-

channel sensor array design. (c) Optical image showing the sensor. (d) Exploded view of the watch assembly. (e) System diagram for data transmission and processing. (f, g) Internal photos of the watch during use. (h) Real-time K^+, Na^+, and Ca^{2+} monitoring during exercise (red line), six-month stability test (gray line), ICP-MS validation (circles), and display module (inset)[80]. 54

Figure 2.14 Wearable devices for glucose monitoring are designed to enhance diabetes management and meet the critical demands in clinical care[82]..... 55

Figure 2.15 A schematic diagram illustrating the components of a wearable sweat biosensor and the personalized medical diagnosis process[85]. 56

Figure 2.16 Schematic of wireless sensing system with a antenna[88]. 57

Figure 2.17 Response mechanism of ISE for detection of biomarkers in sweat[92]. 58

Figure 2.18 The advantages of wearable biosensors based on textile or fibers[98]. 61

Figure 2.19 Schematic showing the bonding between conductive materials and fibers[107]. 62

Figure 2.20 Diagram of sweat pore-inspired nanofiber fabric design and its directional sweat transport/detection function[110]..... 63

Figure 2.21 The mechanical durability text of a textile-based pressure sensor[114]. 64

Figure 2.22 Diagram illustrating the sequential steps involved in the polymer-assisted metal deposition fabrication process[121]..... 67

Figure 2.23 Diagrammatic illustration of the roles of permeable cryoprotective agents and nonpermeable cryoprotective agents in subzero preservation[122]. 71

Figure 2.24 Key challenges in organ transplantation[128]..... 72

Figure 2.25 Preparation, design, and applications of pH-responsive hydrogels[133]. 73

Figure 2.26 HTK-N and its site of actions on preserved organs[141]..... 75

Figure 2.27 Overview of IRI affecting organs following procurement[149]. 77

Figure 2.28 Molecular events of ischemia and reperfusion[151]. 78

Figure 2.29 Schematic: H_2S release from hypothermia-sensitive micelle protects

against A/R cardiomyocyte injury[159]. 80

Figure 2.30 Schematic and digital picture showing flexible pH biosensor for early detection of gastric leakage[131]. 82

Figure 2.31 Schematic of low temperature working hydrogel supercapacitors[162]. 83

Figure 4.1 The molecular structure of PBASE. 96

Figure 4.2 Design and Construction of the Electrochemical Virus Biosensor. (a) The fabrication process for the working electrode of the virus biosensor. (b) Digital image and structural diagram of the complete biosensor, comprising the working and counter electrodes for the detection of SARS-CoV-2 and H_3N_2..... 97

Figure 4.3 Schematic illustration of the operational procedure of the virus biosensor for the detection of SARS-CoV-2 and H_3N_2. 98

Figure 4.4 SEM characterization dAu..... 101

Figure 4.5 Electrochemical performance of bare Ag and dendritic Au-modified Ag electrodes. (a) CV curves of bare Ag electrode and dendritic gold-modified Ag (dAu@Ag) electrode. (b) EIS Nyquist plots of bare Ag and dAu@Ag electrodes. 102

Figure 4.6 Surface wettability characterization of bare and dendritic gold-modified Ag electrodes. Contact angle (CA) measurements of: (a) blank Ag electrode, (b) blank Ag electrode after antibody immobilization, (c) dAu@Ag electrode, and (d) dAu@Ag electrode after antibody immobilization. 103

Figure 4.7 Raman spectra of Au, PBASE fabricated on the dendritic Au layer (Au/PBASE) and antibody immobilized on PBASE (dAu/PBASE/antibody). 105

Figure 4.8 Structural characterization of dAu electrode and subsequent functionalization steps. (a-c) SEM images demonstrating the morphological evolution from bare dAu structures, through PBASE coating, to antibody immobilization. (d-f) AFM images and corresponding surface roughness profiles of dAu, dAu/PBASE, and dAu/PBASE/antibody, indicating that the root-mean-square (RMS) of roughness gradually decreases with the completion of the biosensor. 106

Figure 4.9 Characterization of Au/PBASE/antibody biosensor. (a) CV curves of biosensor with different structures. (b) EIS curves of Au, Au/PBASE and

Au/PBASE/antibody. (c) CV curves recorded at biosensor with N antibody in 50 fg/mL N antigen solution at scan rates ranging from 0.06 to 0.30 Vs^{-1} (0.03 Vs^{-1} interval). (d) Plot showing variation of I_{pa} and I_{pc} peak currents with respect to the square root of scan rate values. 108

Figure 4.10 Schematic illustration of the biosensor design for detecting (a) SARS-CoV-2 protein and (b) H3N2 protein in synthetic analyte solutions. 109

Figure 4.11 Schematic representations of (a) the SARS-CoV-2 virus particle and (b) the H3N2 virus particle, depicting their structural components along with the genomic material enclosed within the viral envelope. 110

Figure 4.12 Real-time electrochemical response and performance evaluation of the virus biosensor. (a, b) Real-time current responses of the biosensor toward increasing concentrations of SARS-CoV-2 and H_3N_2 antigen proteins in PBS. (c, d) Comparative sensing performance of biosensors with and without dendritic Au modification. (e, f) Calibration curves showing the LOD of 0.025 fg/mL for both viral targets. 111

Figure 4.13 Repeatability of the dAu/PBASE/antibody biosensor. (n=3) 111

Figure 4.14 Selectivity of biosensor with (a) N antibody and (b) H_3N_2 antibody. 112

Figure 4.15 Mechanical and Long-Term Stability of virus biosensor. Real-time response of (a) SARS-CoV-2 and (b) H_3N_2 biosensor under 15 degrees bending. (c) Signal draft of virus biosensor. (d) Long-term stability. 113

Figure 4.16 Virus biosensing system. (a) Photograph and (b) A system-level block diagram illustrating the integrated architecture of the biosensing platform. 114

Figure 4.17 Circuit integration of the portable biosensing system. (a, b) Photograph and schematic diagram of the flexible circuit board used in the sensing patch. (c) Block diagram of the high-impedance electrochemical sensing and transmission circuit. 115

Figure 4.18 Comparison of detection workflows for virus in sewage. (a) Diagram illustrating the qRT-PCR and biosensor-based workflows. (b) Custom-developed mobile app interface for real-time signal display. 116

Figure 4.19 Real-time performance of the biosensor in sewage detection. (a) Real-time electrochemical responses of the biosensor to sewage samples with

varying Ct values. (b) Correlation between biosensor output current and Ct values from qRT-PCR. 117

Figure 4.20 Performance comparison of various SARS-CoV-2 wastewater detection methods, highlighting detection limit and response time advantages of this work. 117

Figure 5.1 SEM images reveal the surface morphology of β-Bi_2O_3 nanoflakes, exhibiting a flake-like structure with an average diameter of approximately 4.14 μm. 130

Figure 5.2 Crystallographic and surface chemical characterization of β-Bi_2O_3 deposited on Au@PET substrate. (a) XRD spectrum of the β-Bi_2O_3 deposited on Au@PET. (b)Bi 4f XPS spectra of Bi_2O_3, with discernible peaks at 159.30 and 164.62 eV corresponding to Bi^{3+} within the Bi_2O_3 component. 131

Figure 5.3 TEM characterization of structure and chemistry of β-Bi_2O_3. (a) The TEM image of β-Bi_2O_3 and selective area for focus ion beam (FIB) TEM preparation. (b-e) FIB-TEM image and Energy-dispersive X-ray spectroscopy (EDS) element mappings of O, Pt and Bi taken from a β-Bi_2O_3 nanoflake. (f) High-resolution TEM image showing the atomic structure and the existence of the β-Bi_2O_3 phase. 132

Figure 5.4 TEM characterization of structure and chemistry of Bi_2O_3. (a-d) TEM image and EDS element mappings of O Bi taken from Bi_2O_3. (e) High-resolution TEM image showing the atomic structure and the coexistence of metal-Bi and α-Bi_2O_3 phase. 133

Figure 5.5 Comparison of ion transport-related molecular structures in bismuth oxide polymorphs. (a) Molecular structure of β-Bi_2O_3, highlighting its tetragonal unit cell with open ion diffusion channels. (b) Molecular structure of α-Bi_2O_3, illustrating its monoclinic crystal framework with limited ion mobility. 134

Figure 5.6 Electrochemical performance comparison of ion-selective sensors with and without β-Bi_2O_3 modification. (a) EIS of membrane with and without β-Bi_2O_3. (b) Comparison of Na^+ sensor output voltage at different concentrations, demonstrating enhanced signal amplitude with β-Bi_2O_3 nanoflakes. 135

Figure 5.7 Optimization and schematic representation of the protective layer applied to the ISM. (a) A schematic illustrates various metal oxide protective layers with distinct morphologies and device configurations. (b) SEM images

display the surface morphologies of different protective materials deposited on the ISM. 137

Figure 5.8 Systematic study on the oxides layers. (a) The schematic of the sensor with different structures. The (b) performance, (c) drift and (d) adhesion strength of this group of sensors. 138

Figure 5.9 Systematic study on the Bi_2O_3 layers. (a) Quantitative evaluation of the adhesion strength. (b) Performance assessment of Na^+ biosensors incorporating Bi_2O_3 with varying morphologies and spatial configurations. 139

Figure 5.10 Structural construction and morphological features of the textile-based ion sensor platform. (a) Schematic illustration of the fabrication process. (b-f) SEM images of each functional layer: (b) pristine PET textile substrate; (c) Cu-deposited textile (Cu@PET); (d) dendritic gold nanostructures electrodeposited on Cu; (e) high-resolution view of the dendritic Au architecture; (f) spin-coated PEDOT:PSS conductive layer; and (g) top view of the ISM layer. 140

Figure 5.11 Performance and sensing mechanism of the textile-based ion-selective sensor: (a) Photo of the sensor with integrated working and reference electrodes; (b) Washability test under running water; (c) Schematic of sensing mechanism based on β-Bi_2O_3 nanoflake-functionalized ISM. (d) Reproducibility of sensor performance across different samples functionalized with β-Bi_2O_3 nanoflakes. (e) Signal drift analysis of the sensor with dendritic gold electrode when immersed in 160 mM NaCl solution. (f) Repeatability of open-circuit potential (OCP) responses from the Na^+-selective sensor over multiple measurements. 141

Figure 5.12 Stability and selectivity assessment of the textile-based Na^+ ion sensor. (a) Long-term storage stability of the sensor over 20 days. Error bars indicate the relative standard deviation (RSD) of the evaluated sensitivity from three independent samples. (b) Mechanical stability under repeated bending cycles (50-200 cycles), demonstrating negligible variation in response. (c) Selectivity analysis of the Na^+ ion-selective sensor in the presence of common interfering ions. 142

Figure 5.13 Washing protocol and morphological comparison of ion sensors with and without β-Bi_2O_3 nanoflakes. (a) Sequential images demonstrating sensor contamination and cleaning: i) Pristine sensor surface; ii) Application of artificial stains; iii) Sensor with stains adhered to the surface; iv) Rinsing

under water; v) Sensor restored to a clean state. (b) Photograph of the standardized washing simulation setup using magnetic stirring at 1800 rpm. (c-d) SEM images of the sensor surfaces after 300 seconds of washing: (c) Sensor functionalized with β-Bi_2O_3 nanoflakes, maintaining structural integrity; (d) Control sensor without β-Bi_2O_3, showing severe delamination and exposure of the underlying PEDOT:PSS layer. 144

Figure 5.14 Washing durability and performance retention of β-Bi_2O_3 nanoflake-functionalized sensors. (a) Comparison of Na^+ sensor responses with and without β-Bi_2O_3 nanoflakes after washing. (b) Sensitivity retention over successive washing cycles. (c) Baseline drift during the first 20 cycles. (d) Stepwise sensing performance after every five washing cycles. (e) Retained sensitivity and (f) correlation coefficient over 50 cycles. 145

Figure 5.15 Washability enhanced by β-Bi_2O_3 nanoflakes on (a) K^+ and (b) pH sensors. Additional tests were conducted in various cleaning solutions such as laundry detergent and soapy water to simulate harsh chemical exposure. The β-Bi_2O_3-modified sensors not only preserved function but also showed improved resistance to these chemical environments (Figure 5.16). 146

Figure 5.16 Versatile washability enhancement of β-Bi_2O_3 nanoflake-functionalized biosensors. (a-b) Improved washability of K^+ and pH sensors functionalized with β-Bi_2O_3 nanoflakes, evaluated before and after five washing cycles. (c-d) Washing durability of β-Bi_2O_3-based biosensors under exposure to laundry detergent and soapy water, assessed before and after five cycles. 147

Figure 5.17 Validation of washability enhancement by β-Bi_2O_3 nanoflakes under standardized laundry conditions. (a-b) Photographs of biosensors before and after washing based on AATCC Standard LP1-2021 (Home Laundering Protocol). (c-d) Optical microscopy images of biosensors without (c) and with (d) β-Bi_2O_3 nanoflakes after standard washing. (e-f) Comparison of OCP response (e) and sensitivity (f) of biosensors functionalized with β-Bi_2O_3 before and after washing. 148

Figure 5.18 Comparison of contact angles. The contact angle of bare ISM (a) at the beginning and (b) after 1 min. The contact angle of ISM with β-Bi_2O_3 nanoflakes (c)at the beginning and (d) is after 1 min. 149

Figure 5.19 Integration and deployment of the wearable sensing wristband. (a) Photograph of the assembled wristband system, showcasing the integrated textile-based ion-selective sensor, detachable circuit module, and micro-

battery unit. (b) Stepwise illustration of the wristband assembly and wearing process: (i) Display of key components, including the battery, textile band with embedded sensor, and flexible circuit; (ii) Connection and assembly of all functional modules; (iii) Insertion of the assembled system into the wristband pocket; (iv) Final wearing of the complete device on the wrist. 150

Figure 5.20 Evaluation of breathability and moisture permeability of the wearable sensor system. (a) Quantitative measurement of moisture permeability for different sensor-integrated textiles using the ASTM E96 standard method. (b) Visual comparison of residual water content in bottles sealed with various samples, highlighting differences in moisture barrier properties. (c) Demonstration of water vapor permeability for the wristband integrated with the washable ion-selective sensor, indicating its ability to maintain skin breathability during wear. 151

Figure 5.21 Photographs of skin irritation tests conducted by wearing a commercial smartwatch, a flexible circuit, and the fabricated textile wristband on the forearm. 152

Figure 5.22 Real-time wireless sensing framework and interface design. (a) Schematic illustration of the system workflow for continuous and wireless monitoring of Na^+ levels in sweat. (b) Screenshot of the custom-developed APP designed for real-time visualization and remote tracking of Na^+ concentration. 154

Figure 5.23 (a) Photograph and (b) schematic of the removal circuit. 155

Figure 5.24 Validation of on-body sweat Na^+ monitoring during exercise. (a) Real-time monitoring of sweat Na^+ concentrations during cycling at 8 km/h using the wearable wristband, with results validated by ICP analysis. (b) Comparative analysis of sweat Na^+ concentrations measured by the wristband and corresponding ICP values at cycling speeds of 5, 8, and 10 km/h, recorded at 5-minute intervals. 156

Figure 6.1 Schematic of the all-in-one hydrogel patch for hypothermic organ transport, including circuit and Bluetooth part, battery part and pH-response drug hydrogel part. 165

Figure 6.2 Functional circuit block diagram. 166

Figure 6.3 Schematic showing the structure of flexible pH sensor. Role of Hydrogel Protective Layer in Enhancing Structural. (a) Schematic showing the structure of flexible pH sensor. (b) Comparison of sensitivity of pH

sensor with and without a hydrogel protective layer at various baking temperatures. 168

Figure 6.4 Fundamental performance evaluation of the flexible pH sensor. (a) Potentiometric response of the sensor to standard buffer solutions ranging from pH 4 to 8 at 25 ℃. (b) Selectivity assessment of the sensor under the interference of 50 mM Na^+, 100 mM K^+, and 5 mM glucose at pH 8 and pH 7. (c) Comparison of potentiometric response before and after ultraviolet (UV) irradiation. 170

Figure 6.5 Evaluation of the Stability Performance of the Flexible pH Sensor. (a) Reproducibility of the pH sensor across three independently fabricated samples. (b) Long-term stability of the pH sensor over five consecutive days. (c) Mechanical stability of the pH sensor under 500 bending cycles. 171

Figure 6.6 Sensitivity of the flexible pH sensor under different temperatures (25 ℃, 4 ℃, 0 ℃, and -2 ℃) 172

Figure 6.7 Potential response of the pH sensor continuously monitored over 13 hours under cold storage conditions. 173

Figure 6.8 High resolution N 1s XPS spectra of PAM/CS hydrogels with varying mass ratios. 175

Figure 6.9 Optimization of PAM/CS hydrogel formulations based on swelling ratio differences between pH 7.5 and pH 6.8. 177

Figure 6.10 EIS spectra of NAC-loaded hydrogels in PBS at pH 6.0, 7.4, and 8.0 over 36 hours. 178

Figure 6.11 Experimental setup for studying the influence of hydrogel state (dry vs. wet) on drug adsorption. 179

Figure 6.12 UV-Vis spectra of NAC standard solution and NAC-loaded hydrogels. (a) The UV-Vis spectrum of the standard NAC solution used for calibration. (b) UV-Vis spectrum of the NAC-loaded dry hydrogel. (c) UV-Vis spectrum of the NAC-loaded wet hydroge 181

Figure 6.13 pH-dependent drug release behavior of NAC-loaded PAM-CS hydrogel. The hydrogel was immersed in PBS at different pH values, including (a) pH=7.5, (b) pH=7.0, (c) pH=6.8, and (d) pH=6.5 over a 15-hour period. 182

Figure 6.14 HPLC analysis of NAC drug release from hydrogel under different conditions. (a) Linear calibration curve of NAC concentration based on the

absorbance at 412 nm in the standard NAC solution, R^2=0.999. (b) Drug release profile of NAC from the hydrogel under pH=6.5. 183

Figure 6.15 Cyclic voltammetry profiles for the electrodeposition of nanostructured palladium black on the gold-plated silver substrate for active pH regulation 185

Figure 6.16 Hydrogen storage performance and morphology of palladium electrodes across varying electrolyte concentrations. (a-b) Galvanostatic charging and discharging curves at 10 microamperes. (c) Comparison of charge-discharge duration..... 187

Figure 6.17 Hydrogen storage performance and morphology of palladium electrodes across varying scanning speed and cycles. (a-b) Galvanostatic charging and discharging curves at 10 microamperes. (c) Comparison of charge-discharge duration..... 189

Figure 6.18 SEM image showing the morphology of pallium black surface. ... 189

Figure 6.19 EDS elemental mapping and quantification of the optimized palladium electrode. 190

Figure 6.20 Cycling performance of the stretchable dual-plated Zn-I_2 battery.. 192

Figure 6.21 Electrochemical performance of the dual-plated Zn-I_2 battery under bending conditions..... 193

Figure 6.22 Electrochemical performance of the dual-plated Zn-I_2 battery under stretching conditions..... 193

Figure 6.23 GCD curves of parallel and series-connected Zn-I_2 battery packs. 194

LIST OF TABLES

Table 2.1 The challenges of current WBE technologies. 47

Table 6.1 Composition and formulation details of PAM-CS hydrogels with varying Am and CS content. 176

Table 6.2 Drug loading rate of hydrogel under dry and wet state 180

LIST OF ABBREVIATIONS

Polyester	PET
Carbon nanotubes	CNTs
polyaniline	PANI
poly(3,4-ethylenedioxythiophene):poly(styrene sulfonate)	PEDOT: PSS
Copper	Cu
Gold	Au
Dendritic Gold	dAu
Contact angle	CA
1-Pyrenebutyric acid N-hydroxysuccinimide ester	PBASE
Polymer-assisted metal deposition	PAMD
Ion-selective electrode	ISE
Ion-selective membrane	ISM
Microcontroller units	MCU
Analog digital converter	ADC

CHAPTER 1 INTRODUCTION

With the growing need for advanced sensing capabilities in fields such as health management and environmental safety, there is an increasing emphasis on achieving superior sensor performance, including ultra-low limits of detection, robust operational stability, and seamless system integration. Nanomaterials have attracted significant research interest due to their unique physicochemical properties, which offer promising pathways to enhance sensitivity, durability, and intelligence in sensing systems. This chapter begins by discussing the performance-driven requirements and key technical challenges in areas such as trace-level virus detection, continuous biomarker monitoring, and real-time quality assessment during organ preservation. The core objectives and scientific innovations of this study are subsequently outlined, followed by a summary of the thesis structure.

1.1 Background and Challenges

In critical fields such as public health, personalized medicine, and organ preservation, sensing systems are increasingly relied upon to provide early warning, real-time monitoring, and dynamic intervention. As the global demand for efficient, portable, and intelligent diagnostic technologies continues to rise, the development of high-performance sensors with exceptional sensitivity, stability, rapid response, and system-level integration has become a central focus in sensor science. However, current mainstream sensing technologies face significant limitations, particularly in complex environments such as wastewater, sweat, and hypothermic preservation solutions, where issues related to stability, accuracy, and practicality remain unresolved.

One major challenge lies in achieving ultra-sensitive detection at low target concentrations. For example, in wastewater-based epidemiology (WBE), traditional methods such as quantitative real-time polymerase chain reaction (qRT-PCR) offer high sensitivity but suffer from complex preprocessing, long detection times, and high operational costs. These limitations make them unsuitable for dynamic, on-site applications. Moreover, the extremely low abundance of viral biomarkers and the

presence of various interfering substances in wastewater severely compromise the reliability and practicality of conventional detection approaches.

Another critical challenge concerns the development of sensing systems that are mechanically stable, wearable, and capable of long-term operation. Flexible and textile-based substrates are essential for wearable platforms but often exhibit insufficient conductivity, weak interfacial adhesion, and significant signal drift under real-life conditions such as sweating, washing, or mechanical deformation. Existing sensor designs often fail to balance mechanical flexibility and electrochemical stability, thereby limiting their practical deployment in continuous and dynamic body environments.

Furthermore, most current sensing systems are limited to passive data acquisition and lack the capability for active response or closed-loop feedback. In high-risk biomedical scenarios such as cold organ preservation, environmental parameters including pH and temperature fluctuate rapidly. Although some sensors can monitor these changes, they typically do not possess the functionality to autonomously trigger protective measures, such as controlled drug release or microenvironmental regulation. This functional disconnect between sensing and intervention significantly reduces therapeutic effectiveness. Therefore, the realization of intelligent, closed-loop systems capable of real-time monitoring and adaptive intervention remains a critical unmet need.

The root cause underlying these challenges is largely associated with the limited functionality and poor structural design of conventional materials. In this context, nanomaterials have emerged as promising candidates due to their unique surface properties, high specific surface area, and superior electronic and ionic transport characteristics. Rational engineering of nanomaterial structures, compositions, and interfaces offers a powerful strategy to enhance sensor sensitivity, improve mechanical and electrochemical stability, and enable multifunctional system integration. These advancements pave the way for a new generation of sensors that transition from isolated

performance optimization to holistic system-level enhancement and adaptive intervention capabilities.

This dissertation aims to address the aforementioned challenges by systematically exploring the role of nanomaterials in enhancing the performance of next-generation sensing systems. A progressive research framework is established, moving from materials to devices and ultimately to system integration. Specifically, three representative studies are presented. The first focuses on the development of an electrochemical biosensor based on dendritic gold and molecular interface engineering for ultra-sensitive virus detection in wastewater. The second investigates the construction of a washable and ion-conductive textile-based ion sensor enabled by β-Bi_2O_3 nanoflakes, targeting long-term reliability in wearable applications. The third integrates a pH-responsive drug-releasing hydrogel, a flexible pH sensor, and a hydrogel-based power supply into a unified system for real-time monitoring and on-demand antioxidant release during cold organ preservation. Together, these studies not only advance the performance limits of sensors in harsh environments but also propose novel strategies for real-world applications in environmental monitoring, health management, and precision biomedical intervention.

1.2 Research Objectives

This dissertation aims to systematically investigate the pivotal role of nanomaterials in enhancing the performance of advanced sensing systems. A progressive research framework is established, encompassing material-level innovation, device-level optimization, and system-level integration. In response to critical limitations in sensitivity, environmental stability, wearability, and intervention capability of conventional sensors, three representative research objectives are formulated as follows:

Objective 1: To develop an electrochemical biosensor based on dendritic gold nanostructures for ultra-sensitive.

In the context of wastewater-based epidemiology, conventional nucleic acid detection techniques such as qRT-PCR suffer from long processing times, complex workflows, and limited field adaptability, making them unsuitable for rapid surveillance and on-site applications. This study proposes a nanostructure-driven strategy that employs dendritic gold with high surface area and localized electric field enhancement, combined with a PBASE-modified molecular interface, to enable high-density antibody immobilization and selective target recognition. The objective is to establish a cost-effective electrochemical biosensor capable of detecting SARS-CoV-2 and H3N2 viral proteins in wastewater at concentrations as low as 0.025 fg/mL, while maintaining operational stability in complex matrices and enabling rapid response.

Objective 2: To construct a washable, durable, and flexible textile-based ion sensing system for stable and continuous sweat analysis.

Wearable sweat sensors often exhibit performance degradation due to signal drift caused by mechanical deformation, environmental fluctuations, or washing procedures, which limits their practical deployment. In this study, β- Bi_2O_3 nanoflakes with high ionic conductivity and strong interfacial adhesion are introduced to improve the mechanical and electrochemical stability of ion-selective membranes on flexible substrates. Building upon this material platform, a textile-based sensor array is developed and integrated with a Bluetooth Low Energy (BLE) module to enable real-time monitoring of sodium ions in sweat. The objective is to overcome current barriers related to washability, durability, and wireless data transmission in wearable systems, thereby promoting their application in personalized health management.

Objective 3: To design a pH-responsive drug-releasing hydrogel system for close-loop intelligent intervention during cold organ preservation.

During hypothermic organ storage and transportation, ischemic stress, acidosis, and oxidative damage can significantly impair organ viability. Conventional preservation fluids lack the ability to sense pathological changes or provide timely intervention. This

study presents a smart hydrogel system that responds to pH changes in the microenvironment by releasing N-acetylcysteine (NAC), an antioxidant therapeutic agent, under mildly acidic conditions. The hydrogel is further integrated with a flexible pH sensor and a hydrogel-based micro battery capable of operating at low temperatures. This configuration forms a closed-loop platform that combines monitoring, energy supply, and on-demand drug release. The objective is to enable real-time tracking of organ status and adaptive therapeutic intervention, thereby improving the safety and effectiveness of organ preservation.

Through these three research stages, this work aims to demonstrate the multifaceted role of nanomaterials in improving sensing performance, enhancing system stability, and enabling intelligent response capabilities, ultimately contributing to the development of next-generation sensor systems for environmental monitoring, wearable healthcare, and biomedical intervention.

1.3 Research Originality

This dissertation presents a comprehensive exploration of nanomaterial-based strategies for enhancing sensing performance and enabling intelligent intervention. The originality of this work lies in the multiscale innovations achieved across three levels: material design, device interface optimization, and system integration. The main contributions are summarized as follows:

(1) A dendritic gold nanostructure was integrated with a PBASE-modified interface to construct an ultrasensitive electrochemical biosensor for virus detection in wastewater, achieving an exceptionally low detection limit and stable performance in complex environments.

To address the limitations of traditional nucleic acid testing methods, such as qRT-PCR, which are time-consuming, costly, and unsuitable for rapid on-site monitoring, this study developed a biosensor based on dendritic gold with a high surface area and enhanced local electric field. The introduction of a PBASE-modified interface

facilitated dense antibody immobilization and efficient target recognition. The resulting biosensor demonstrated a detection limit down to 0.025 fg/mL for SARS-CoV-2 and H3N2 proteins in real wastewater, while maintaining high selectivity and robust signal output, offering a low-cost and rapid solution for wastewater-based epidemiology.

(2) A new mechanism was proposed to enhance the washability of wearable textile ion sensors through the introduction of β- Bi_2O_3 nanoflakes with fast ionic conductivity, and a wireless sweat sodium monitoring system was successfully developed.

Conventional wearable sensors often suffer from signal degradation due to mechanical deformation, environmental exposure, and washing processes. This study revealed that β- Bi_2O_3 nanoflakes not only provide high ionic conductivity but also improve the interfacial adhesion and structural stability of ion-selective membranes without introducing significant impedance. A multilayer architecture composed of Cu@PET, PEDOT:PSS, an ion-selective membrane, and β- Bi_2O_3 was constructed to ensure long-term performance under washing, bending, and extended usage. A Bluetooth Low Energy (BLE) module was also integrated to enable real-time, wireless monitoring of sodium levels in sweat, demonstrating the practical potential of this system for wearable healthcare applications.

(3) A novel closed-loop intervention system was developed by integrating a pH-responsive drug-releasing hydrogel, a flexible pH sensor, and a high-voltage hydrogel-based battery, enabling real-time monitoring and adaptive antioxidant delivery during organ preservation.

To mitigate acidosis and oxidative stress during hypothermic organ preservation, a smart hydrogel system capable of releasing N-acetylcysteine (NAC) in mildly acidic conditions was designed using pH-sensitive dynamic covalent bonds. In addition, a series-connected hydrogel micro battery based on polyacrylamide was fabricated, achieving an output voltage exceeding 3.7 V, which effectively overcomes the low-voltage limitation of traditional hydrogel batteries and provides sufficient power for

circuit operation. By integrating the hydrogel with a flexible pH sensor, the system enables stable monitoring, energy supply, and on-demand drug release under low-temperature conditions. This closed-loop platform offers a novel strategy for real-time organ status assessment and responsive therapeutic intervention.

In summary, this dissertation contributes original advancements in the structural engineering of sensing materials, functional interface design, and cross-domain system integration. These innovations provide a foundational framework and technical pathway for next-generation intelligent sensor systems applicable to environmental monitoring, wearable healthcare, and biomedical engineering.

1.4 Outline of the Thesis

This dissertation focuses on the development of nanomaterial-based strategies for advanced sensing and adaptive intervention. The research is organized into eight chapters, each addressing a specific aspect of the study in a logically progressive manner.

Chapter 1 provides an introduction, outlining the research background, key challenges, objectives, and the main innovations of this work. It also presents an overview of the thesis structure.

Chapter 2 reviews the relevant literature and theoretical foundations. It summarizes recent advances in the application of nanomaterials for biosensing, with emphasis on the enhancement of sensitivity, selectivity, and stability. The chapter also discusses progress in flexible and wearable sensors, challenges in system integration, and emerging biomedical applications involving responsive interventions. This provides the rationale and scientific context for the current research.

Chapter 3 describes the materials, fabrication methods, and characterization techniques used throughout the study. This includes the synthesis of nanomaterials, the construction of sensor electrodes, the design of responsive hydrogels, and the protocols

for electrochemical, mechanical, and bioresponsive testing, which together form the experimental foundation of the thesis.

Chapter 4 presents the development of an ultra-sensitive electrochemical biosensor for viral detection in wastewater based on dendritic gold nanostructures. A high-surface-area dendritic gold electrode was functionalized with a PBASE-modified interface to improve antibody immobilization and signal transduction. The resulting sensor achieved an exceptionally low detection limit for SARS-CoV-2 and H3N2 proteins and demonstrated high accuracy, selectivity, and stability in real sewage samples. This work supports practical deployment of biosensors for wastewater-based epidemiology.

Chapter 5 introduces a washable and wearable textile sensor system based on β- Bi_2O_3 nanoflakes for sodium detection in sweat. The use of β-Bi_2O_3 with high ionic conductivity enhances interfacial adhesion and structural robustness of the ion-selective membrane, significantly improving durability against washing and mechanical stress. A multilayer sensor architecture was fabricated and integrated with a Bluetooth Low Energy (BLE) module, enabling continuous wireless monitoring of sodium concentration under wearable conditions.

Chapter 6 presents a closed-loop system for organ preservation, integrating a pH-responsive drug-releasing hydrogel, a flexible pH sensor, and a high-voltage hydrogel micro battery. The hydrogel system, designed to release N-acetylcysteine (NAC) under mildly acidic conditions, is based on dynamic covalent chemistry. A series-connected PAM-based hydrogel battery array was fabricated to achieve an output voltage exceeding 3.7 V, addressing the common limitation of low voltage in conventional hydrogel batteries. This chapter demonstrates the construction of a functional platform capable of monitoring, powering, and therapeutically intervening in organ preservation under hypothermic conditions.

Chapter 7 summarizes the main findings and scientific contributions of the dissertation. It also outlines future research directions, including the development of multimodal

sensing systems, autonomous energy supply, and broader applications in biomedical engineering.

CHAPTER 2 LITERATURE REVIEW

2.1 Ultralow Detection Limit in Complex Matrices with Dendritic Gold

This section outlines a device-level route to achieving an ultralow detection limit (LOD) in complex matrices, centered on dendritic gold electrodes. We first define LOD and the associated figures of merit, including selectivity, antifouling performance, signal-to-noise ratio (SNR), and operational robustness. We then describe the fabrication of dendritic gold electrodes and the relationship between their fractal morphology and performance, clarifying how geometric parameters and local-field enhancement work to reduce LOD, together with essential interface functionalization considerations. A case study on wastewater viral antigen detection is used to validate the strategy, followed by a concise summary of reusable device design guidelines.

2.1.1 Ultralow detection challenge and evaluation metrics

In electrochemical biosensing, the ultralow detection limit (LOD) is a primary performance figure that defines the lowest analyte level that can be reliably distinguished from the baseline under specified measurement conditions and stated statistical confidence. LOD is not an intrinsic constant of a material or a sensor. It depends on the measurement system, the readout modality, and the decision criterion. A rigorous discussion of LOD therefore returns to the device level, where interfacial recognition, signal transduction, and noise control must operate in concert.

The determinants of LOD can be organized into three coupled domains: capture, transduction, and noise. Capture concerns the affinity and kinetics of the receptor-target interaction, as well as immobilization strategies and molecular orientation that support efficient charge or ion transfer at the interface. Transduction concerns how electrode morphology and geometry set the effective surface area and the local field, and how interfacial charge transfer resistance and double layer behavior shape the amplitude and dynamics of the measurable signal. Noise and non specific processes include thermal and low frequency noise, environmental perturbations, solution conductivity and

impedance coupling, non-specific adsorption, and baseline drift. Together these factors define the separation between the minimal discriminable signal and background fluctuations and therefore determine the practical LOD.

On this basis, the evaluation in this work adopts a device-oriented framework. Minimum detectable capability is reported as LOD with an explicit confidence statement, together with the dynamic range and sensitivity in the low concentration linear regime. Selectivity and specificity are quantified through cross reactivity ratios or selectivity coefficients using representative interferents and structural analogues. Antifouling capacity and matrix tolerance are assessed through spike and recovery tests, signal retention during continuous measurement, and baseline stability. Readout robustness is characterized by signal to noise ratio (SNR), relative standard deviation (RSD), and both intraday and interday repeatability, and can be supported by changes in charge transfer resistance (R_{ct}) and double layer capacitance (C_{dl}) as mechanistic evidence. Response time and throughput are recorded to indicate the time required to reach a stable decision at low concentration. Regeneration and reusability are established through multi cycle measurements that track performance decay.

To ensure comparability across electrodes, batches, and measurement days, all metrics are obtained under a consistent measurement window and data processing protocol, with sufficient replicates near the LOD region to reduce sampling error. Lowering LOD is a systems problem that requires concurrent progress along three paths: increasing the measurable signal produced by a unit change in concentration, suppressing nonspecific processes at the interface, and reducing readout noise and drift. Section 2.1.2 examines how dendritic gold morphology and geometry link quantitatively to performance. Section 2.1.3 integrates geometric amplification with essential interface functionalization to balance sensitivity, selectivity, and robustness without reliance on complex sample processing.

2.1.2 Dendritic Gold Nanostructures for Sensitive Electrochemical Sensing

Dendritic gold (dAu) electrodes, as a revolutionary material for electrochemical sensing interfaces, exhibit structural advantages that traditional planar electrodes cannot match. Their fractal topology, constructed from self-similar multilevel branches (extending from micro-scale trunks to nanometer-scale tips), forms a three-dimensional network that enhances performance dramatically. This architecture increases the real surface area by more than 30-fold compared to planar gold (roughness factor reaching 35.4), and, through unique tip effects and porosity modulation, offers exceptional sensitivity, selectivity, and stability in virus biosensing applications. This section systematically describes the structural-functional design of dAu electrodes, sensing enhancement mechanisms, and their potential for practical application.

(1) Structural Features and Signal Amplification Mechanism

Enhanced electroactive surface area enabled by fractal architecture. The fractal structure of dendritic gold electrodes features a self-similar, multi-branched morphology that greatly increases the specific surface area compared to traditional gold thin-film electrodes (Figure 2.6)[1-4]. This intricate three-dimensional structure features numerous branches and tips, greatly increasing the contact area between the electrode and electrolyte[5]. The enlarged electroactive area increases the number of available binding sites and the interfacial current response at a given analyte level, which directly benefits the low end sensitivity[6]. Furthermore, the enlarged surface area promotes the efficient electrochemical reactions, allowing for high sensitivity and response speed in complex samples, which is important near the detection limit[6,7].

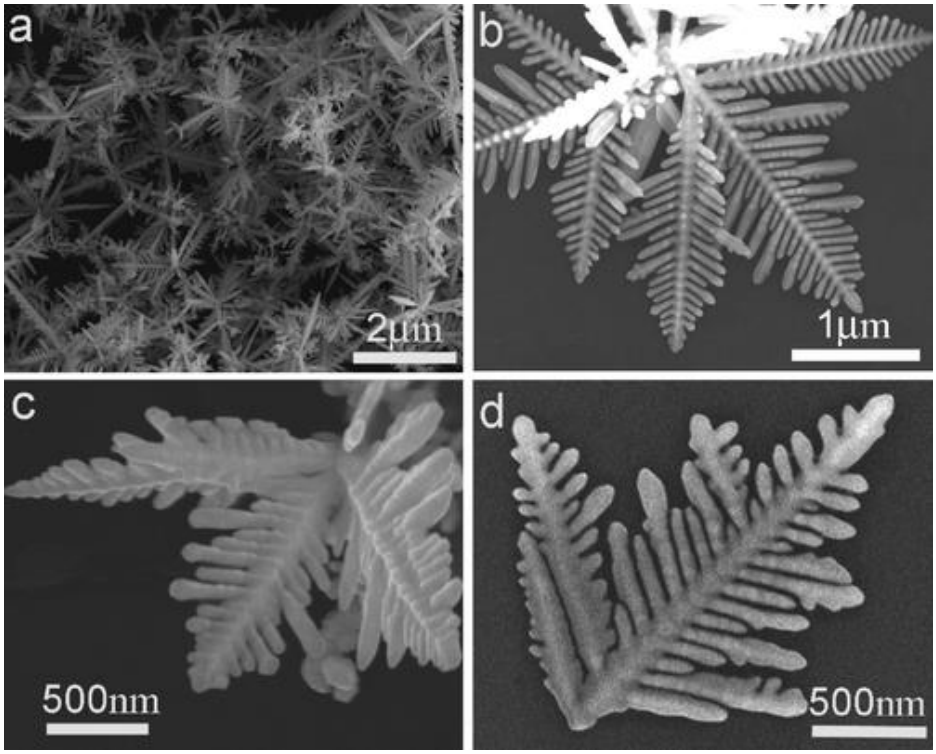

Figure 2.1 SEM images of dAu with high specific surface area[8].

Localized Electric Field Intensification Induced by High-Curvature Features: The microstructure of dendritic gold electrodes, particularly the high curvature sites at the tips, exhibits a significant tip effect when an electrical potential is applied [9]. This phenomenon results in a localized amplification of the electric field, with the electric field strength being significantly greater at the tips compared to the flat regions of the electrode[10]. This localized field enhancement accelerates charge accumulation at the interface, promoting faster electron transfer from the electrolyte to the electrode surface[11]. The tip effect notably lowers the interfacial reaction barriers and amplifies the signal, which is crucial for detecting subtle biological recognition events, such as the binding of trace viral proteins[12].

Porous Microstructure Contributing to Anti-Fouling and Wastewater Matrix Tolerance: The multi-level branching and micron-sized pore structures of dendritic gold electrodes make them highly resistant to biofouling and interference from suspended solids in wastewater (Figure 2.7) [13,14]. In wastewater-based epidemiology (WBE), samples often contain large amounts of suspended solids (TSS), organic matter, and other particulate

matter, which can block electrode surfaces or cause signal interference. The high porosity of dendritic gold electrodes helps alleviate these issues by preventing particle accumulation on the electrode surface, thereby maintaining its effectiveness and stability. Consequently, dendritic gold electrodes exhibit superior interference resistance and long-term stability in complex environmental samples, such as sewage.

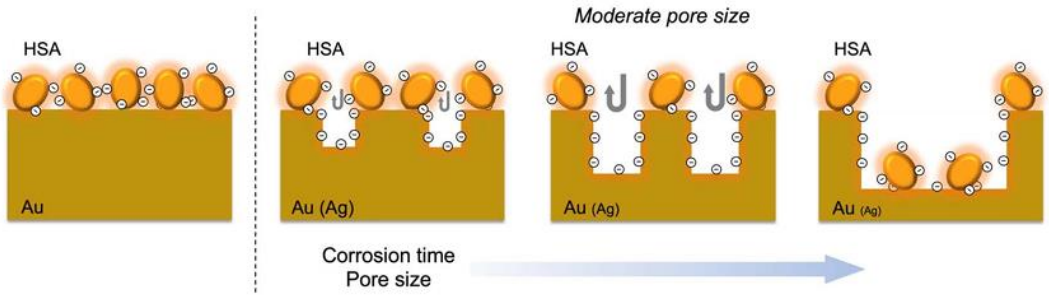

Figure 2.2 Schematic of mechanism underlying anti-biofouling of nano structured Au electrodes[15].

(2) Unique Advantages in Biosensing

Ultra-high Antibody Loading Density: The large specific surface area and numerous active sites of dendritic gold electrodes enable the high-density immobilization of biomolecular recognition elements, such as antibodies. This feature enables dendritic gold electrodes to carry a large number of antibodies, which significantly enhances the molecular recognition efficiency of the sensor [16,17]. In virus detection applications, a higher antibody loading density ensures stronger molecular recognition ability, enabling dendritic gold electrodes to efficiently detect low concentrations of viral proteins, such as the SARS-CoV-2 N protein or H3N2 HA protein, with enhanced sensitivity and accuracy (Figure 2.8).

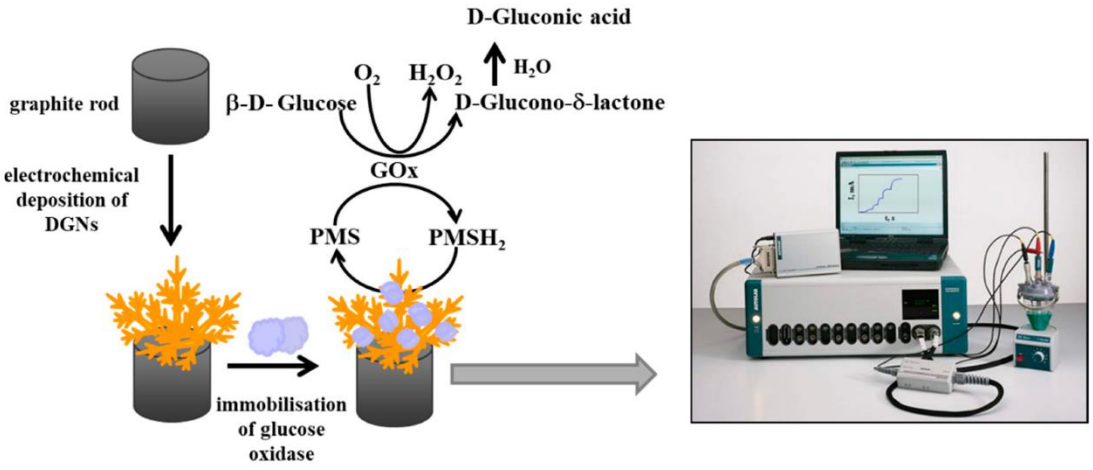

Figure 2.3 A schematic representation illustrating the deposition of electrochemical dendritic gold nanostructures on graphite rod electrodes, followed by the immobilization of glucose oxidase and glucose determination using the developed biosensor[18].

Accelerated Mass Transport Kinetics: The branched structure of dendritic gold electrodes not only provides more reactive sites but also enhances the mass transfer rate of electrons and ions between the electrode and the electrolyte (Figure 2.9) [19,20]. The dendritic architecture improves the electron transport rate by providing a continuous conductive path, which facilitates rapid electrochemical reactions[21]. The enhanced mass transport kinetics are crucial for achieving fast virus capture and signal transduction, particularly in applications involving complex biological samples where rapid detection is required[22].

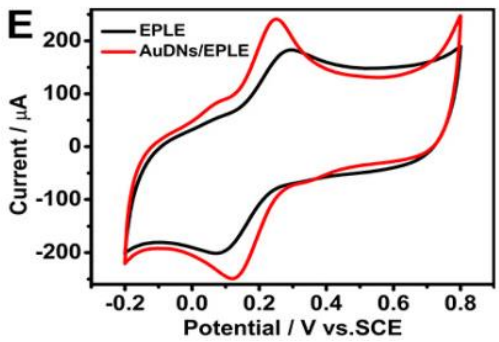

Figure 2.4 Cyclic voltammograms of EPLE and AuDNs/EPLE[48].

Intrinsic Chemical Stability of Gold Substrates Ensures Long-Term Electrochemical Signal Reliability: Gold, as a highly chemically stable metal, provides excellent resistance to corrosion and degradation, maintaining the structural integrity and functional stability of the electrode in harsh conditions[23]. The gold substrate in dendritic gold electrodes prevents oxidation or material degradation, ensuring consistent performance over long periods of use[24]. This stability is essential for maintaining reliable signal output and avoiding signal drift due to electrode aging or material degradation. Furthermore, the biocompatibility of gold allows for long-term stable interactions with biomolecules (such as antibodies or viral antigens), ensuring the sensor's effective and consistent performance over extended periods of use[25].

2.1.3 Device oriented WBE application for viral antigen sensing

Building on Section 2.1.1 and Section 2.1.2, this section frames wastewater-based epidemiology as an application context that defines device level requirements for ultralow detection and sensitive electrochemical sensing.

The Rise and Importance of WBE in Public Health

Wastewater-based epidemiology (WBE) represents a novel approach in public health surveillance, designed to assess community health status and detect disease outbreaks through the analysis of biomarkers present in municipal wastewater[26]. This approach is grounded in the premise that viral pathogens, pharmaceuticals, and metabolic by-products are excreted through human urine, feces, and other body fluids, eventually entering the urban sewage system[27,28]. Wastewater thus serves as an aggregated sample that reflects the health status of an entire community in a non-invasive and anonymized manner (Figure 2.1) [29,30].

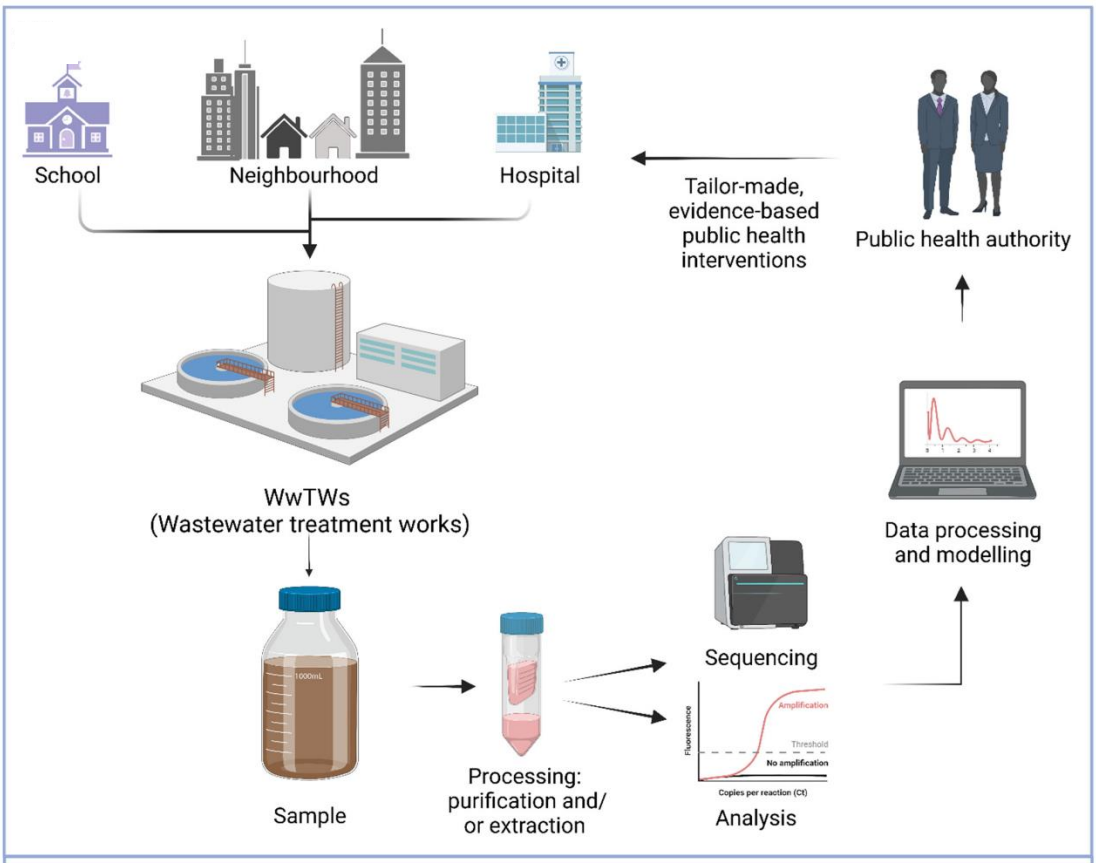

Figure 2.5 Schematic illustration of the general WBE process[29].

WBE was initially developed for tracking illicit drug consumption, such as estimating community level use of cocaine and opioids through the analysis of urinary metabolites in sewage[31,32], and its scope expanded with advances in molecular biology and detection technologies. It has proven especially valuable during the COVID-19 pandemic, when traditional clinical testing capacity was limited or delayed.

Studies have demonstrated that SARS-CoV-2 RNA can remain detectable in fecal matter for prolonged durations, including in individuals who exhibit no symptoms or only mild symptoms (Figure 2.2)[33,34]. Consequently, sewage monitoring emerged as a powerful complementary tool for tracking virus prevalence, often providing early warnings before official case reports. For instance, in March 2020, the Dutch RIVM institute detected SARS-CoV-2 RNA in sewage from cities with no confirmed cases, 6-10 days ahead of clinical reports [35]. Similarly, a study by MIT demonstrated a strong

correlation between viral titers in Boston sewage and subsequent case counts, underscoring the potential of WBE as a proactive surveillance tool[36].

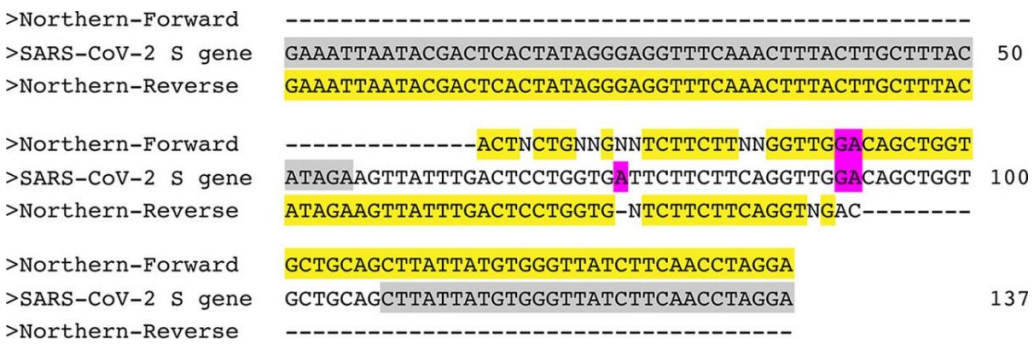

Figure 2.6 Sanger sequencing data were obtained and aligned with the SARS-CoV-2 spike (S) gene to confirm the presence and identity of viral genetic material[9].

Compared to traditional diagnostic methods, WBE offers several advantages: [28,37-39]

- Non-invasive and anonymous monitoring: It does not rely on individual participation or consent, avoiding ethical and compliance issues.
- Cost-effectiveness and wide coverage: A single sewage sample can represent a large population segment, enabling scalable surveillance even in low-resource settings.
- Real-time and early warning capability: WBE can detect infection signals several days before clinical diagnoses, providing critical lead time for intervention.
- Population-level insights: It enables macro-scale trend analysis, including tracking the effectiveness of public health policies.

In addition to SARS-CoV-2, WBE has been increasingly utilized to track a widening range of infectious pathogens, including norovirus, adenovirus, monkeypox virus (mpox), and hepatitis A virus, among others[40-42]. Several countries have now institutionalized WBE as part of their national health infrastructure. Since 2022, the United States Centers for Disease Control and Prevention (CDC) has implemented the National Wastewater Surveillance System (NWSS), which encompasses data collection

from more than 1,300 wastewater treatment facilities. Similar networks have been established in the EU, Australia, and Japan, reflecting a global shift from experimental use to policy adoption[43]. These developments set quantitative expectations for sensor performance at the device level, especially at ultralow analyte abundance and under variable matrix conditions.

Despite its promise, WBE faces several key technical challenges:

1) Extremely low analyte concentrations: Viral RNA in wastewater is typically present at extremely low concentrations, necessitating detection sensitivity in the sub-femtogram per milliliter (fg/mL) range.

2) Complex sample matrices: Sewage contains inhibitors, proteases, and suspended solids that interfere with molecular recognition and signal extraction.

3) Cumbersome sample preprocessing: Conventional approaches like qRT-PCR require multiple steps, including virus concentration, RNA extraction, and thermal lysis.

4) Limited availability of portable detection systems: The majority of current technologies are confined to laboratory settings, making them unsuitable for real-time, in-field monitoring applications.

These limitations have catalyzed efforts to develop portable, pre-treatment-free, and ultra-sensitive sensing platforms. Recent advances in electrochemical sensors, nanostructured interfaces, and microfluidic integration have accelerated progress in this field. Furthermore, incorporating wireless communication modules and real-time data transmission has facilitated the development of intelligent WBE systems that support mobile accessibility, remote diagnostics, and cloud-based analytical processing.

Limitations of Current Virus Detection Technologies in Wastewater Surveillance

In wastewater-based epidemiology (WBE), viruses are generally present at very low concentrations (fg/mL to pg/mL) within a complex and fluctuating matrix, presenting substantial challenges for detection technologies regarding sensitivity, selectivity, response time, and suitability for on-site use. Currently, the mainstream viral detection strategies can be categorized into three primary types: molecular biology-based assays, immunological protein assays, and emerging portable sensing platforms. While these methods have shown promise in clinical and public health applications, their direct deployment in wastewater samples remains hindered by several technical bottlenecks.

(1) Molecular Detection Techniques

The most widely used method is quantitative reverse transcription PCR (qRT-PCR), which enables semi-quantitative analysis of viral RNA through reverse transcription and fluorescence-based amplification. qRT-PCR is highly sensitive (limit of detection, LOD: 10-100 copies/mL) and target-specific, and has been endorsed as the standard method for SARS-CoV-2 surveillance in wastewater by organizations like the WHO and CDC [35,44-48].

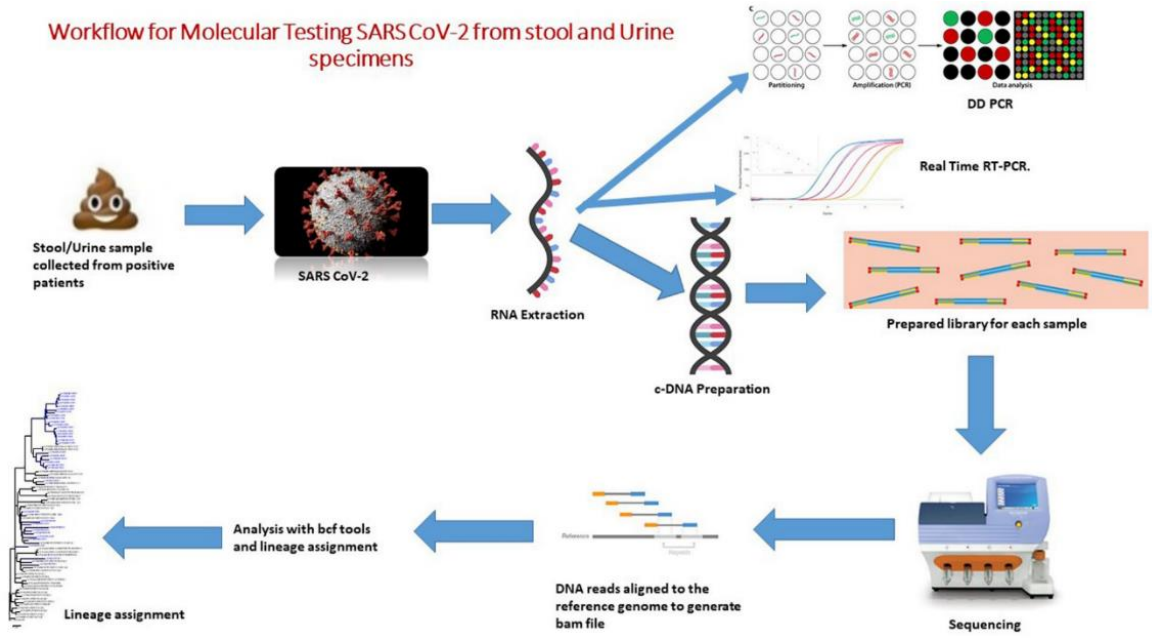

Figure 2.7 Workflow for molecular testing SARS CoV-2[49].

However, several limitations hinder its use in WBE scenarios:

- Cumbersome pretreatment: Viral enrichment methods, including polyethylene glycol (PEG) precipitation and membrane filtration, are time-consuming and often result in low recovery rates, typically under 40%.
- High equipment dependency: Thermal cyclers and RNA extraction platforms are required, limiting on-site applicability.
- Vulnerability to inhibitors: Enzymatic reactions are often suppressed by organic matter or heavy metals in wastewater, reducing accuracy.
- Lack of real-time feedback: Batch processing delays results, making timely public health response challenging.

Additionally, digital PCR (dPCR) improves detection precision and quantification range by partitioning the reaction mixture, making it suitable for absolute quantification of trace viral RNA. However, its high cost and complex operation currently preclude widespread field deployment.

(2) Isothermal Amplification Techniques

Isothermal amplification techniques, such as RT-LAMP and RPA, have attracted attention for their ability to amplify nucleic acids at a constant temperature without the need for thermal cycling, making them potentially more suitable for field applications.[31,50,51]. RT-LAMP has demonstrated LODs as low as 25-100 copies/reaction, with reaction times under 30 minutes.

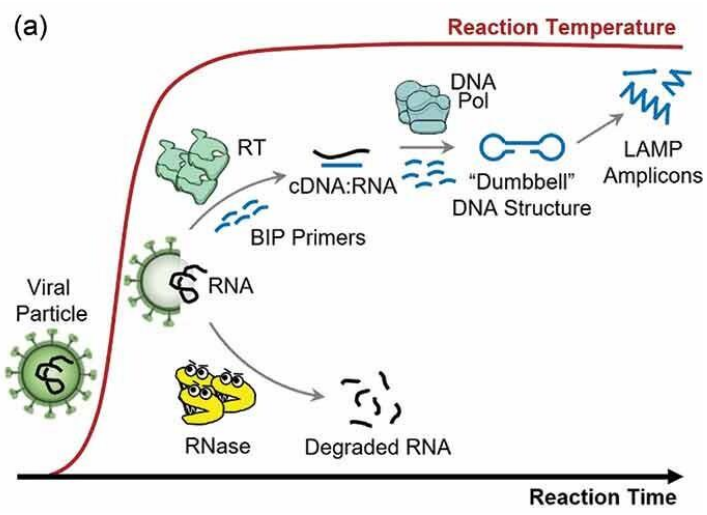

Figure 2.8 A schematic illustrating the competition between RNase and reverse transcriptase (RT) in a one-pot RT-LAMP reaction, where no purification is required and the pretreatment is performed in a single step[50].

However, several drawbacks limit their use in WBE:

- Primer sensitivity: Complex primer design increases the risk of nonspecific amplification.
- Background interference: Signal interpretation becomes difficult in unfiltered wastewater samples due to high noise.
- Unresolved pretreatment bottlenecks: Virus concentration and RNA extraction are still prerequisites.

While isothermal amplification shows promise for portability, it remains dependent on complementary sample processing steps for effective WBE application.

(3) Protein-Based Immunoassays

Protein detection commonly employs enzyme-linked immunosorbent assays (ELISA) and lateral flow immunoassays (LFIA), which focus on structural viral proteins,

including the nucleocapsid and spike proteins[52]. ELISA offers good throughput and standardized protocols, while LFIA provides rapid, visual results suitable for field use.

However, their application to wastewater samples is significantly constrained:

- Insufficient sensitivity: Traditional ELISA generally has LODs in the 1-10 ng/mL range, inadequate for detecting fg-pg/mL targets in WBE.
- Matrix interference: Complex components in wastewater can lead to nonspecific adsorption or antibody deactivation.
- Manual operation: Multiple steps and reliance on manual reading hinder high-frequency monitoring.

Recent advances in electrochemical immunosensors, which immobilize antibodies on conductive electrodes and use voltammetric or impedance methods for signal readout, offer advantages such as fast response, miniaturization, and wearable integration. These sensors are viewed as a promising direction for protein-level viral monitoring in environmental settings.

(4) Emerging Molecular Diagnostic Technologies

The CRISPR-Cas system has become a highly effective molecular diagnostic tool, with platforms such as SHERLOCK (Cas13a) and DETECTR (Cas12a) enabling target RNA or DNA detection through collateral cleavage and fluorescent signal generation (Figure 2.5)[53]. These systems can reach attomolar-level sensitivity and have been adapted for SARS-CoV-2 detection.

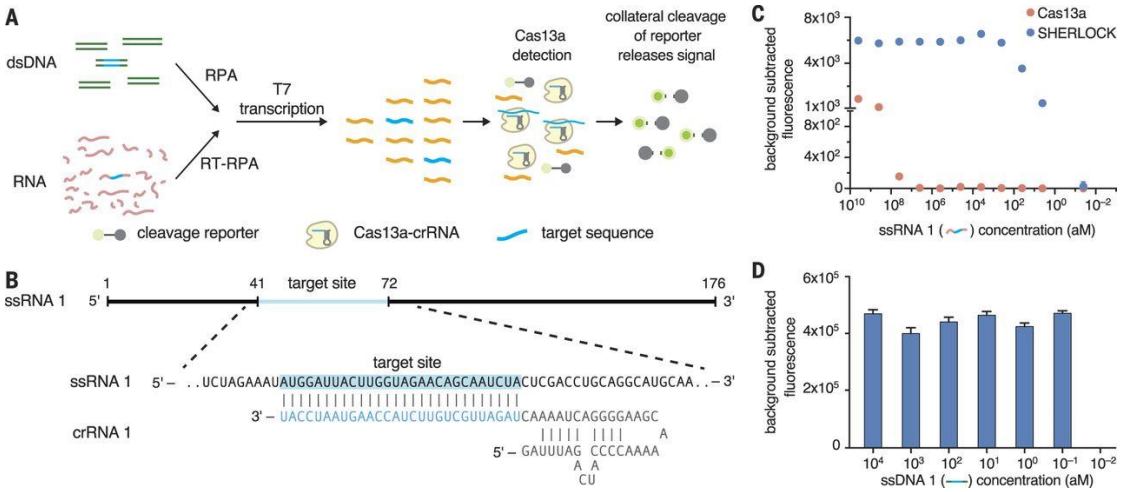

Figure 2.9 SHERLOCK enables single-molecule nucleic acid detection through the following steps: (a) The SHERLOCK workflow involves dsDNA and RT-RPA amplification. (b) ssRNA targets (highlighted in blue) are detected through the collateral activity of Cas13a. (c) SHERLOCK (Cas13a + RPA) demonstrates ~2 aM sensitivity for ssRNA, outperforming Cas13a alone (mean ± SEM, n = 4). (d) Additionally, SHERLOCK is capable of detecting single-molecule DNA (mean ± SEM, n = 4)[54].

Some implementations combine CRISPR with isothermal amplification to further enhance detection of low viral concentrations. However, current CRISPR-based assays face several obstacles:

- Instability of biological reagents, requiring stringent storage and transportation conditions.
- Inapplicability to raw wastewater, due to their inability to tolerate unfiltered complex matrices.
- High cost and standardization challenges, limiting scalability and accessibility.

(5) Common Bottlenecks and Technological Needs

The current landscape of virus detection technologies faces several shared challenges when applied to WBE.

Challenge	Description
Insufficient sensitivity	Difficulty detecting targets in fg/mL range without sample concentration
Long detection time	Total processing and analysis time often exceeds 2 hours
Poor portability	Large instruments hinder deployment in non-laboratory settings
Low anti-interference	Signal extraction is impacted by inhibitors and particulates in wastewater
Lack of wireless integration	Most systems cannot transmit data to cloud or mobile platforms

Table 2.1 The challenges of current WBE technologies.

These gaps define device-oriented targets for ultralow detection sensors, including high sensitivity at the fg/mL level without complex preprocessing, tolerance to complex matrices, shorter time to result, and compatibility with on site operation. In subsequent sections the dendritic gold based electrochemical approach is positioned against these targets as an application in WBE.

2.1.4 Summary

This section establishes a device oriented route to achieving an ultralow detection limit in complex matrices with dendritic gold electrodes. Section 2.1.1 defines the evaluation metrics at the device level, including sensitivity near the low concentration regime, selectivity, antifouling performance, signal to noise ratio, repeatability, response time, and on site compatibility under minimal preprocessing. Section 2.1.2 links controllable dendritic morphology to these metrics through quantitative relations. Increased

electrochemically active surface area raises the number of accessible binding sites and the interfacial current at trace analyte levels. High curvature tips concentrate the local field, reduce charge transfer resistance, and increase double layer capacitance, which strengthens transduction efficiency. The porous branched network supports percolated conduction and shortened diffusion lengths, improving mass transport, while the open architecture mitigates fouling and baseline drift during extended measurements.

Taken together, these morphology driven effects act on the three determinants of detection at low abundance. Capture capacity improves through area and spacing control of recognition elements. Transduction strengthens through local field enhancement and favorable interfacial kinetics. Readout robustness increases through antifouling structure and stable electrochemical parameters. Section 2.1.3 presents wastewater-based epidemiology as a representative application that specifies quantitative targets for these device metrics, while the central focus of the chapter remains the sensor level strategy for ultralow detection enabled by dendritic gold. This device-oriented framework provides a reproducible basis for design, comparison, and reporting, and it prepares the transition to subsequent chapters on stability, washability, and closed loop integration.

2.2 Washability and long-term stability with β-Bi_2O_3 reinforced wearable sensors

With the rapid development of personalized healthcare, smart wearables, and remote medical diagnostics, flexible biosensors have emerged as a promising solution for enabling non-invasive, continuous, and real time monitoring of physiological parameters (Figure 2.10). Unlike traditional sampling methods such as blood or urine analysis, sweat offers a readily accessible and non-invasive body fluid that contains a wealth of electrolytes and metabolites. These biomarkers provide real time insights into an individual's hydration status, electrolyte balance, and overall metabolic activity, making sweat an attractive medium for next generation wearable diagnostic platforms.

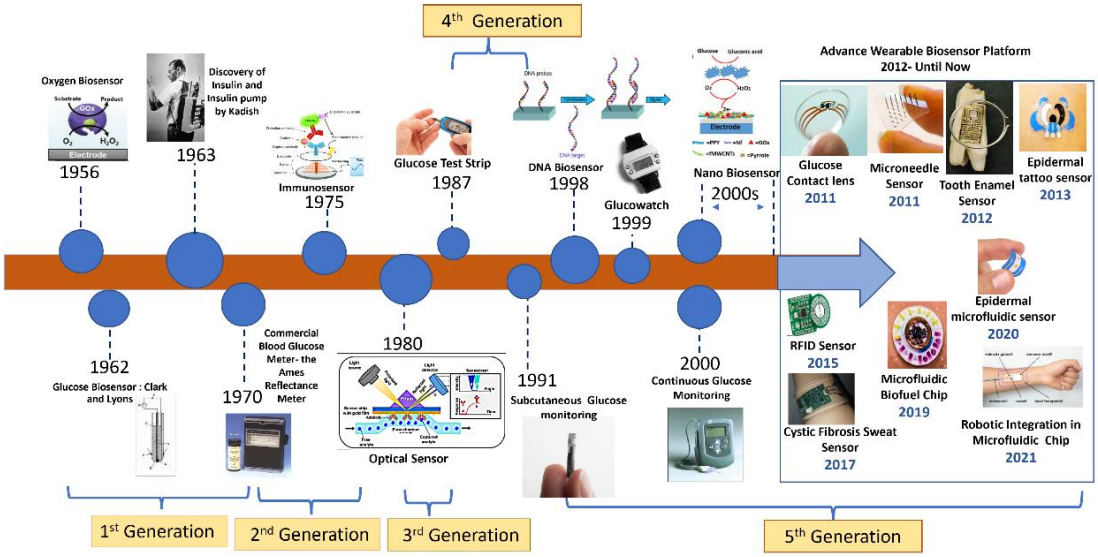

Figure 2.10 The evolution of biosensors for wearable devices[55].

The use of sweat sensors in real-world dynamic environments such as extended skin contact, repetitive mechanical stress, and exposure to complex electrolytic conditions places significant demands on the materials and structural design of these devices. Sensors need to not only exhibit mechanical flexibility and skin conformity for long-term wearability, but also maintain signal stability, chemical integrity, and functional performance under repeated washing and environmental exposure. Furthermore, as system integration progresses, seamlessly combining sensing interfaces, electrode arrays, and communication modules on a soft, stretchable substrate has become a major obstacle in the development of fully functional wearable systems.

This section provides an in-depth review of the most recent material approaches used in the development of wearable sweat biosensors, with a particular focus on comfort-driven substrate design, durability enhancement mechanisms, and functional integration technologies, including recent advances in micro/nanopatterning and textile-compatible fabrication techniques. Representative studies are discussed to highlight the current bottlenecks and future directions in material innovation, aiming to provide a foundation for building robust, reusable, and fully integrated wearable biosensing platforms.

2.2.1 Fundamental Mechanisms for Biosensing and Stability

(1) Advantages of Sweat as a Biological Information Carrier

Human biofluids, including blood, urine, sweat, and saliva, are valuable sources of physiological and metabolic data, offering essential information for real-time health monitoring and early disease detection[56,57]. Tracking biomarkers in these fluids, such as electrolytes, metabolites, and hormones, allows for real-time assessment of an individual's nutritional health, immune response, endocrine function, and disease progression[58-60]. The rapid advancement of wearable electronics and flexible sensors has made biofluid-based sensing a key technology for non-invasive, continuous, and real-time health monitoring. (Figure 2.11).

Figure 2.11 Wearable sweat sensors for multiplexed detection of key health-related biomarkers[61].

Among various biological samples, sweat has gained increasing attention in wearable health monitoring research due to its non-invasive, continuous, and real-time collection advantages [56]. Unlike traditional biological samples such as blood or urine, sweat can be naturally secreted by the glands onto the skin surface, eliminating the need for punctures or complex sampling devices [62]. This greatly enhances the acceptability and comfort of sensors for users [63]. Furthermore, sweat is produced stably under conditions such as exercise, heat stress, or electrical stimulation, providing a controlled sampling basis that is conducive to the dynamic tracking of physiological status changes, thereby meeting the needs of continuous monitoring and remote healthcare system s[64].

From a compositional standpoint, sweat contains a range of important electrolytes (e.g., Na^+, K^+, Cl^-, H^+, NH_4^+) and metabolites (such as lactate, glucose, and cortisol), which can reflect an individual's electrolyte balance, metabolic activity, and endocrine levels (Figure 2.12a) [55,65-67]. For example, changes in Na^+ and K^+ concentrations are directly related to hydration status, electrolyte intake, and renal function regulation; an increase in lactate content may indicate muscle metabolic abnormalities or exercise overload; cortisol, a typical stress hormone, is an important indicator for assessing neuroendocrine status and emotional fluctuations[67-69]. Building on this, sweat sensors have found widespread application in diverse health monitoring contexts, including electrolyte monitoring and dehydration detection during physical activity, personalized nutrition management, identification of fatigue or heat stress risks, and supporting the diagnosis and treatment follow-up of conditions like cystic fibrosis (Figure 2.12b) [70-72]. These applications not only provide real-time individual health feedback but also offer more detailed data support for precision medicine.

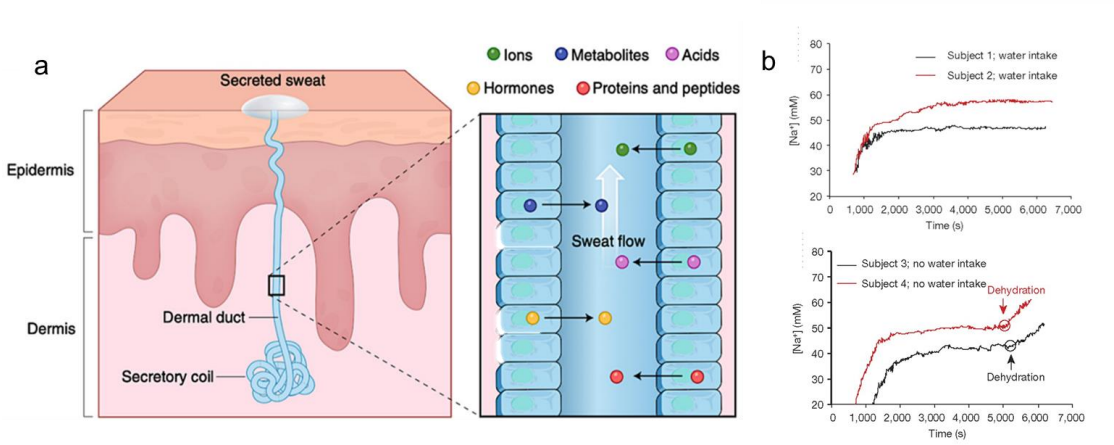

Figure 2.12 (a) Sweat gland secretion and sodium ion fluctuation during exercise. (a) Schematic illustration of a sweat gland and representative analytes present in sweat. (b) Variation of sodium ion concentration during physical activity, where an abnormal increase indicates dehydration[55,70].

Furthermore, with advancements in wearable devices, artificial intelligence, and remote healthcare systems, sweat sensors are progressively evolving towards greater integration, intelligence, and connectivity[73,74]. Through the integration of low-power circuitry, Bluetooth or NFC wireless modules, and algorithm-based data processing units, sweat sensing platforms enable real-time analysis and remote data transmission, facilitating the development of a closed-loop system for mobile health management[75,76]. In this trend, sweat sensors not only serve as information collection terminals but also become key nodes linking the human body, environment, and cloud platforms in the digital healthcare ecosystem, with increasing clinical translation and commercialization potential.

(2) Application Scenarios of Sweat Sensors

Sweat sensors represent an emerging class of wearable analytical technologies that are increasingly applied in areas ranging from daily health management to clinical diagnostics, highlighting their significant practical value and broad developmental potential.

In the realm of sports and fitness monitoring, dynamic changes in sweat electrolytes (e.g., Na^+, K^+, Cl^-) can reflect real-time fluctuations in the body's hydration and electrolyte balance [77]. For instance, a continuous rise in sodium concentration is indicative of dehydration, while abnormal potassium levels may suggest muscle fatigue or electrolyte imbalance (Figure 2.13)[78-80]. Unlike traditional assessments based on subjective perception or intermittent sampling, integrated sweat sensors offer continuous and real-time data acquisition during exercise, enabling early warnings for dehydration and optimized fluid and electrolyte replenishment strategies to avoid complications such as exercise-induced hyponatremia[81].

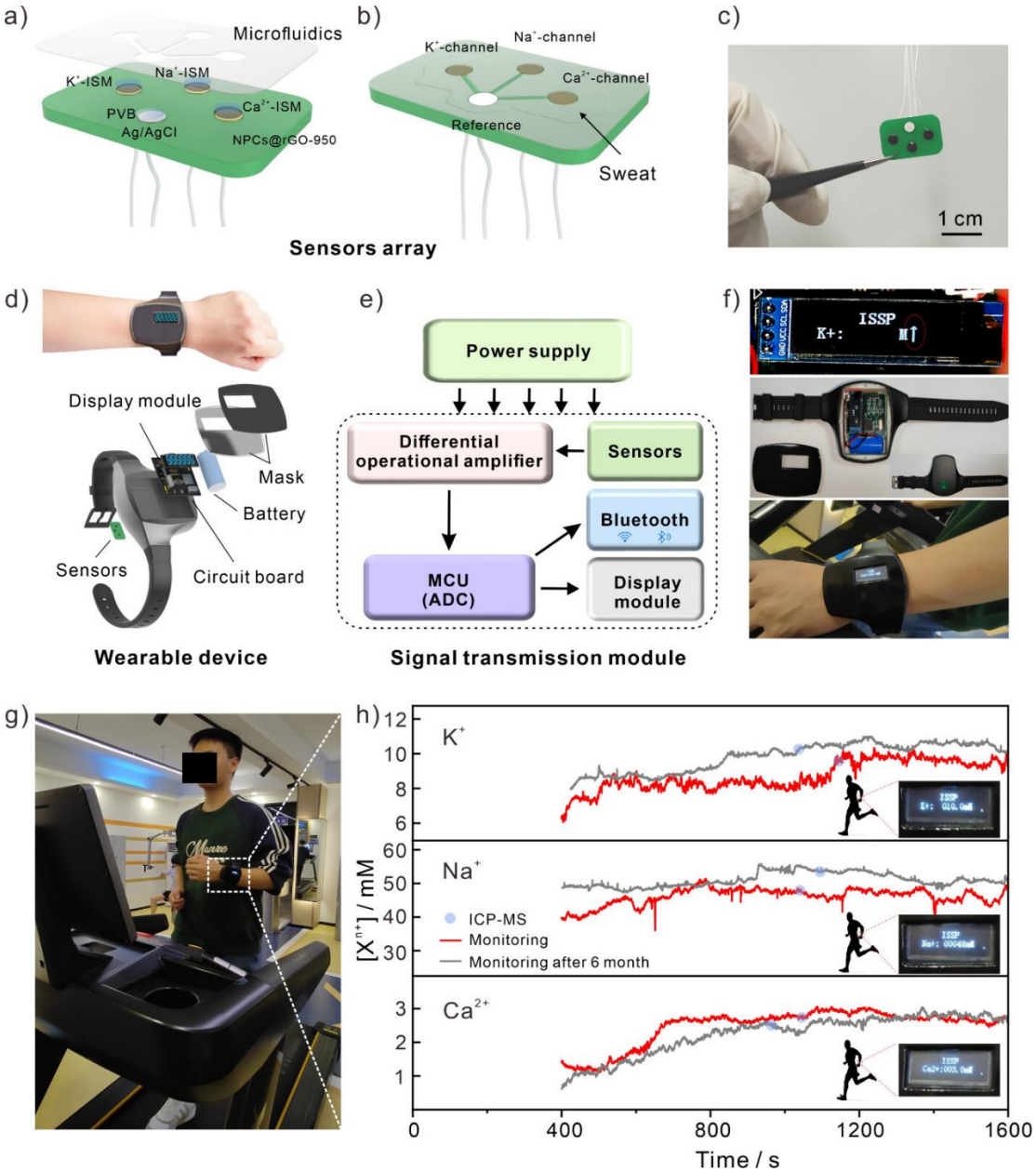

Figure 2.13 Wearable wristwatch for sweat electrolyte monitoring. (a,b) Three-channel sensor array design. (c) Optical image showing the sensor. (d) Exploded view of the watch assembly. (e) System diagram for data transmission and processing. (f, g) Internal photos of the watch during use. (h) Real-time K^+, Na^+, and Ca^{2+} monitoring during exercise (red line), six-month stability test (gray line), ICP-MS validation (circles), and display module (inset)[80].

For personalized nutrition management, sweat sensors are capable of tracking key metabolites including glucose, lactate, and amino acids, thus providing biochemical feedback on individual metabolic status and energy expenditure. For example, elevated lactate levels can serve as indicators of anaerobic threshold during physical exertion, while sweat glucose trends offer non-invasive insight into postprandial glucose fluctuations, supporting dietary planning for individuals with diabetes (Figure 2.14). This real-time, physiological feedback enables intelligent adjustments to diet and exercise regimens tailored to an individual's health goals and physiological responses.

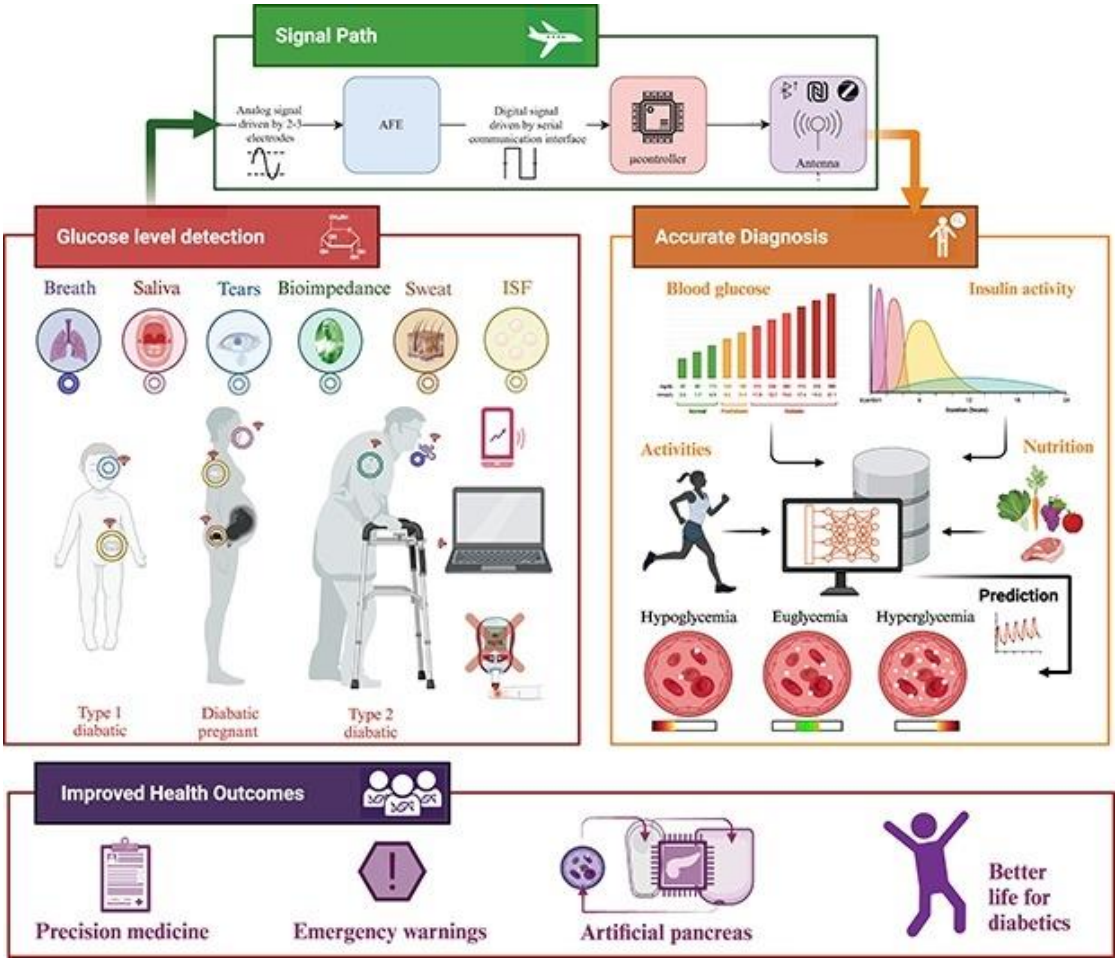

Figure 2.14 Wearable devices for glucose monitoring are designed to enhance diabetes management and meet the critical demands in clinical care[82].

In disease diagnostics and chronic health monitoring, sweat analysis is increasingly recognized as a complementary tool to traditional biofluid assays. For instance, cystic fibrosis (CF), which is a genetic disorder involving impaired ion transport, leads to significantly elevated concentrations of Na^+ and Cl^- in sweat[83]. This characteristic has been recognized by the FDA as a gold-standard diagnostic criterion. Beyond CF, sweat-borne biomarkers such as lactate, ammonia, and cortisol also provide physiological insights relevant to metabolic syndromes, autonomic dysfunction, and chronic fatigue syndrome, supporting early diagnosis and individualized therapy monitoring (Figure 2.15)[84,85].

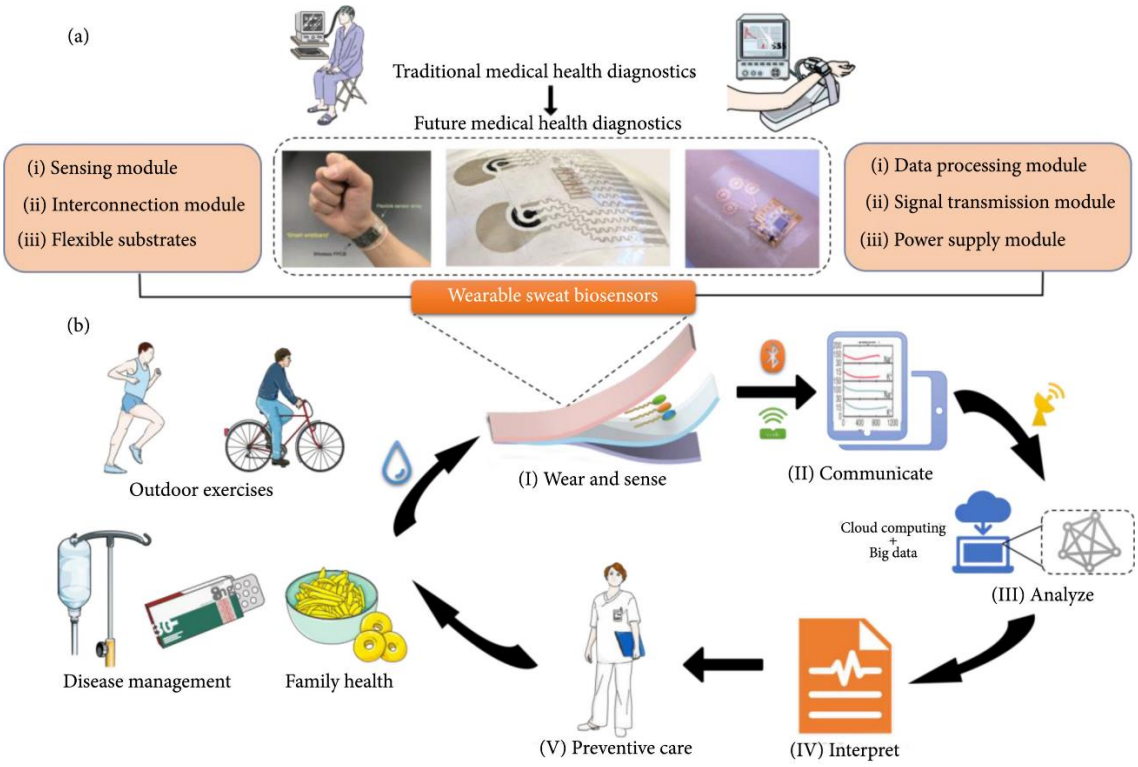

Figure 2.15 A schematic diagram illustrating the components of a wearable sweat biosensor and the personalized medical diagnosis process[85].

With rapid advances in flexible electronics, microfabrication, and wireless communication technologies, sweat sensors are evolving toward fully integrated and intelligent platforms. The development of stretchable substrates and skin-conformal sensing components enhances user comfort and measurement accuracy. Meanwhile, the incorporation of low-power wireless modules such as Bluetooth Low Energy (BLE) and Near Field Communication (NFC) enables real-time transmission and remote sharing of physiological data (Figure 2.16) [86-88]. As such, sweat sensors are poised to become critical nodes within the broader mobile health (mHealth) ecosystem, seamlessly interfacing with smartwatches, mobile apps, and cloud-based platforms to support home-based health monitoring, elderly care, and remote clinical follow-up[89,90].

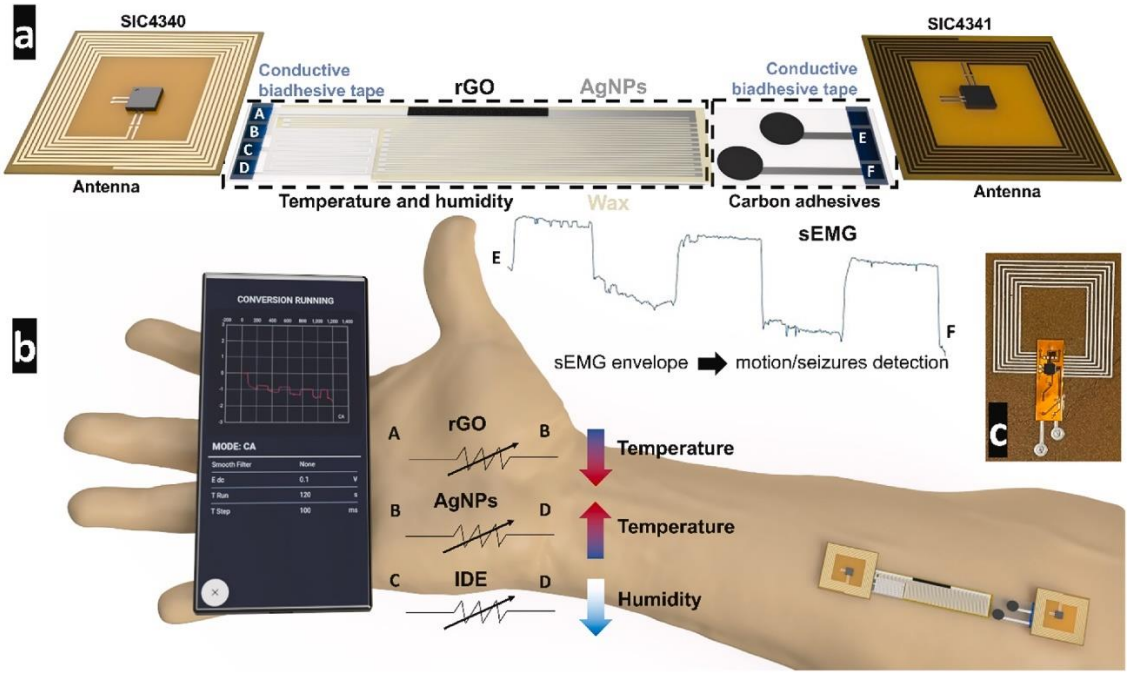

Figure 2.16 Schematic of wireless sensing system with a antenna[88].

In summary, sweat sensors are no longer confined to laboratory-based physiological investigations, but are rapidly maturing into practical, intelligent, and wearable health monitoring solutions. Their applications span sports medicine, precision nutrition, disease screening, and digital healthcare, offering immense potential for future integration into next-generation health management systems.

(3) Working Principles of Ion-Selective Electrodes

Ion-selective electrodes (ISEs) represent a fundamental class of electrochemical sensors capable of selectively detecting target ions, and they play a critical role in sweat analysis. Their main advantage is the ability to monitor ionic concentrations with high sensitivity, continuously, and non-invasively, making them well-suited for integration into wearable sweat sensing systems[91].

A conventional ISE is structured around three principal functional elements: a conducting substrate, an interposed solid-contact layer, and the ion-selective membrane (ISM) (Figure 2.17).

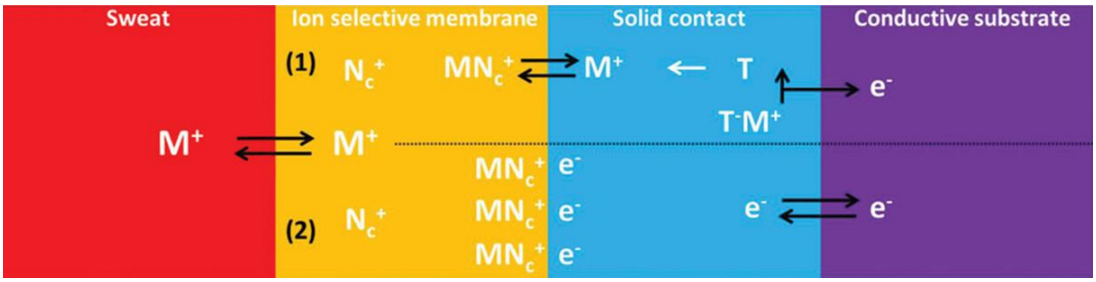

Figure 2.17 Response mechanism of ISE for detection of biomarkers in sweat[92].

- The conductive substrate serves as the electron collector and is usually fabricated from metals such as silver or gold, or from flexible conductive materials like PEDOT:PSS or carbon-based films. For wearable applications, this layer need to possess good mechanical flexibility and strong adhesion to maintain stable output under motion or deformation.

- Situated between the conductive substrate and ISM, the solid-contact layer functions as a transducer, effectively converting ionic interactions at the membrane interface into measurable electrical signals. PEDOT:PSS is widely employed as the solid-contact material because its superior electronic conductivity and robust interfacial stability reduce interface impedance and maintain reliable sensor performance.

- The ISM is the core functional component of the ISE. It contains ionophores that selectively recognize and bind to specific target ions such as Na^+, K^+, or H^+. The membrane typically consists of a hydrophobic polymer matrix (such as PVC), a plasticizer to modulate membrane flexibility and ion mobility, and the ionophore for selective sensing.

The ISE operates based on the Nernst equation, which describes a logarithmic relationship between the membrane potential and the activity of the target ion:

$$\varphi = \varphi_0 + \frac{RT}{zF} lna \quad (1)$$

In the initial step, the ISM's ionophore (Nc) exhibits high specificity for the target monovalent cation (M^+), coordinating with it to yield the MNc^+ complex. Subsequently, the MNc^+ complex migrates to the membrane-solid-contact interface, where electron transfer into the conductive substrate generates a corresponding potential difference. Under idealized circumstances, a monovalent ion exhibits a theoretical Nernstian sensitivity of approximately 59.16 mV for each tenfold variation in its concentration. For example, a change in Na^+ concentration from 10 mM to 100 mM would ideally produce a potential shift of around 60 mV. This potentiometric detection technique operates without consuming reagents, thereby supporting low-power operation and rapid response, and the concentration of target ions can be determined from the measured potential using the Nernst equation[93,94].

Key performance metrics for ISEs include:

- Sensitivity: The change in potential per tenfold concentration variation, measured in mV/dec. A value close to the theoretical limit indicates high sensor performance.

- Potential drift: The rate of signal change over time (mV/h), reflecting long-term stability. Ideally, this value should be below 5 mV/h.

- Selectivity coefficient: Selectivity quantifies a sensor's capacity to differentiate the target ion from competing ions within a complex matrix, with lower selectivity coefficient values indicating superior discrimination performance.

- Response time: Response time is defined as the interval needed for the sensor's output to reach 90 % of its equilibrium value, with optimal devices achieving this within 10 seconds.

- Reproducibility and reversibility: Essential for repeated usage and reliability.

- Mechanical flexibility and washability: Critical for wearable applications, ensuring consistent function under stretching, bending, or washing conditions.

Given the low ion concentrations and sluggish flow characteristics of sweat, ISEs need to be engineered with superior surface wettability, high-fidelity ion recognition, and robust antifouling properties to prevent interference from proteins, lipids, and other biomolecular constituents. Moreover, modern sweat sensors require integration with low-power electronics, wireless communication modules, and data processing circuits to enable intelligent functionality and seamless operation within wearable health monitoring platforms.

2.2.2 Materials and Structural Designs for Skin-Conformal and Washable Biosensors

A critical consideration in designing wearable sweat sensors is ensuring the comfort of the skin-sensor interface, as this directly affects user adherence and the device's sustained performance over extended periods. To achieve non-irritating, conformal, and durable skin contact, researchers have increasingly shifted from rigid substrates to flexible, breathable, and biocompatible materials, often combined with structural engineering strategies to enhance wearing experience. Through careful substrate material selection, precise microstructural engineering, and the integration of multilayer architectures, wearable sensors can achieve synergistic improvements in ergonomic comfort and skin compatibility.

Common flexible substrates include polyethylene terephthalate (PET), polyurethane (PU), polydimethylsiloxane (PDMS), hydrogels, and textile fabrics. Each of these materials offers distinct advantages in terms of mechanical flexibility, biocompatibility, and surface wettability[95]. PET is cost-effective and mechanically robust but exhibits poor water vapor transmission, which may lead to sweat accumulation and skin irritation. PDMS offers good skin conformity and elasticity but has limited moisture permeability[96]. PU and hydrogels show improved softness and hydrophilicity, making them more comfortable for short-term wear or low-intensity activities[97].

Among these options, textile substrates are considered one of the most promising candidates due to their inherent fibrous structure and balanced mechanical-breathability profile (Figure 2.18)[98,99]. Compared to dense films such as PET or PDMS, textiles possess naturally interwoven fiber networks and micron-scale porosity[100]. These features enable excellent water vapor transmission rates and gas exchange capabilities, significantly enhancing breathability and comfort during prolonged use[101]. In addition, textiles exhibit high flexibility and stretchability, allowing them to conform to complex skin contours and reducing the risk of localized pressure or delamination[102].

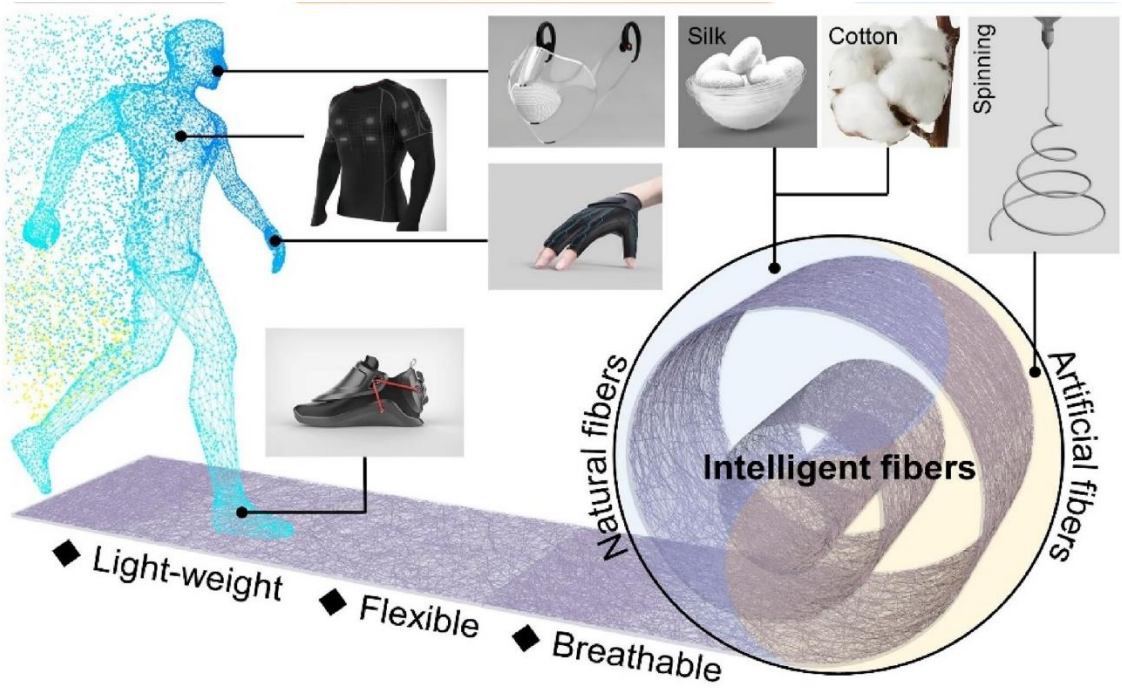

Figure 2.18 The advantages of wearable biosensors based on textile or fibers[98].

Importantly, the surface texture of fabrics provides abundant anchoring sites for functional materials such as conductive layers and sensing membranes (Figure 2.19). Techniques such as electrospinning, spray coating, and thermal lamination can be employed to directly integrate sensing components onto textile surfaces, forming stable and durable multi-functional layers [103,104]. Moreover, the wide variety of available textiles, such as natural cotton, nylon, and synthetic fibers, provides diverse options in

terms of biocompatibility, mechanical properties, and surface wettability [105,106]. This versatility facilitates customization for different wearable applications.

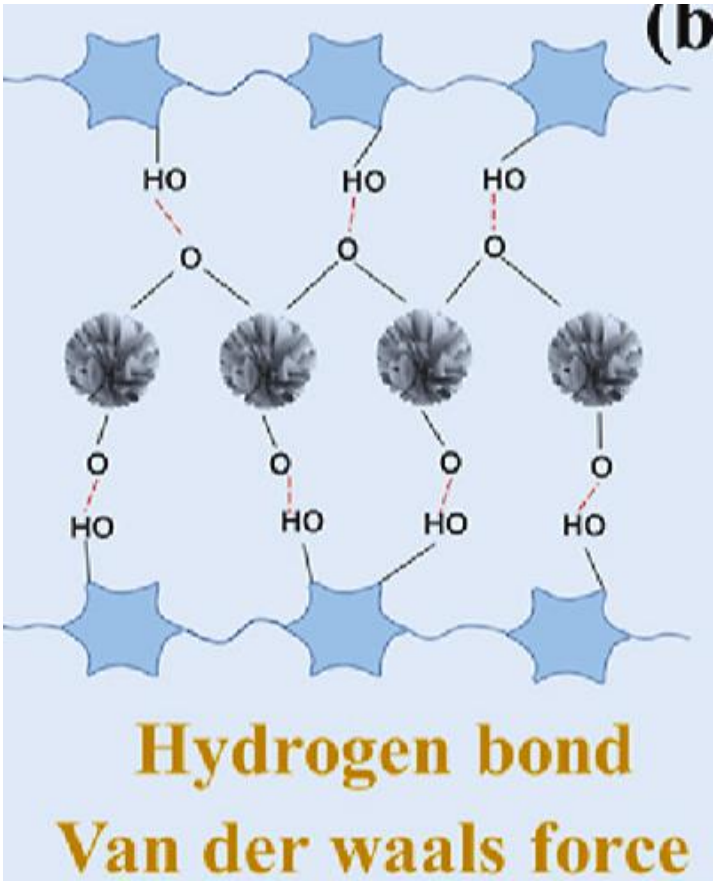

Figure 2.19 Schematic showing the bonding between conductive materials and fibers[107].

From a structural perspective, various microengineering strategies have been proposed to further enhance comfort [108]. Mesh structures allow for tunable porosity and mechanical support, while electrospun nanofiber membranes provide large surface areas and excellent conformability for high-fidelity skin contact [109]. The intrinsic three-dimensional structure of woven fabrics helps relieve local pressure points and improves the overall mechanical integrity during dynamic movement. Furthermore, open-pore architectures facilitate sweat diffusion and evaporation, helping regulate local humidity and thermal comfort during extended wear (Figure 2.20).

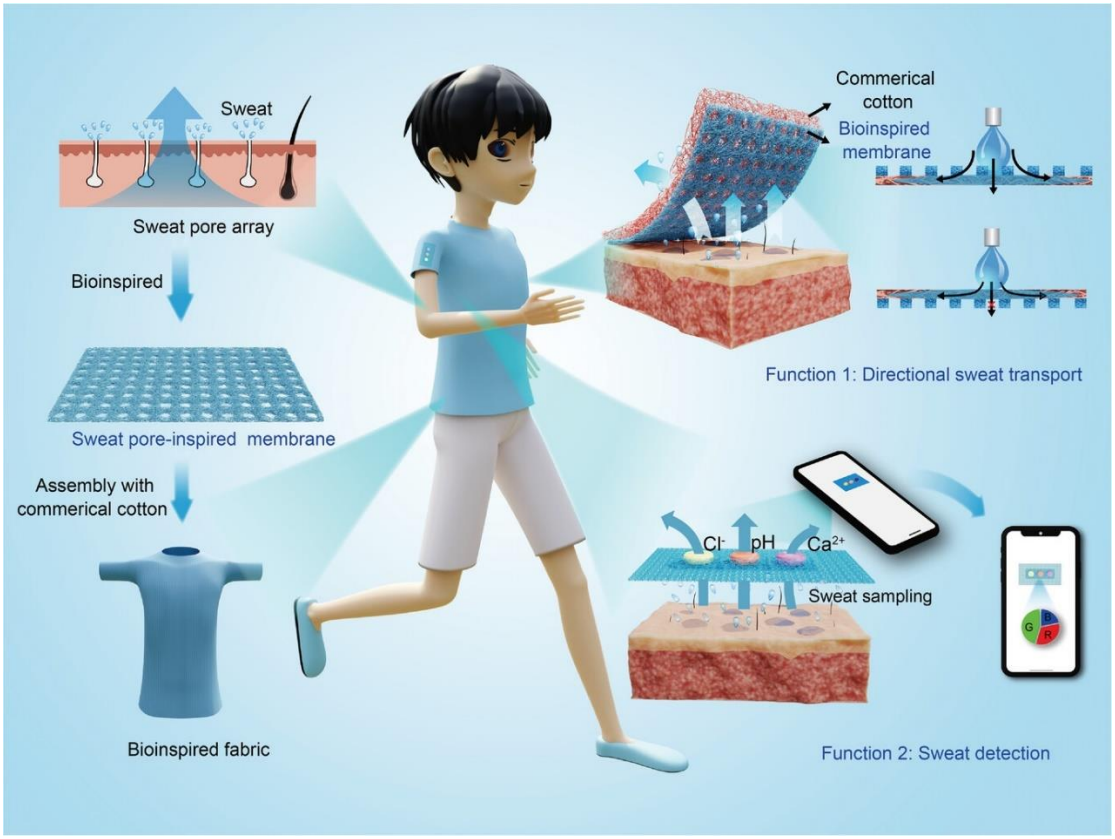

Figure 2.20 Diagram of sweat pore-inspired nanofiber fabric design and its directional sweat transport/detection function[110].

In practical devices, multilayered configurations are commonly adopted to simultaneously optimize comfort and sensing performance. These typically include a soft supporting base layer, a functional middle layer with integrated electronics, and a protective top layer with hydrophilic or breathable properties. Key parameters such as interfacial adhesion, thermal expansion compatibility, and gradient mechanical modulus are essential for achieving both functionality and wearability in next-generation wearable sensors.

2.2.3 Material Strategies for Mechanical Robustness and Durability

In practical applications, wearable sweat sensors are required to maintain stable performance under continuous skin contact and various external stresses, including repeated bending, washing, friction, stretching, and exposure to sweat (Figure 2.21). Therefore, durability and reusability are regarded as critical metrics for assessing the readiness of wearable devices for real-world use [111]. To evaluate the robustness of these sensors, several standard protocols have been proposed [112]. These include the retention of electrochemical performance after standardized washing cycles, sensitivity variation during mechanical fatigue tests, and long-term signal drift characterization. A drift rate below 5 mV per hour, for example, is often considered acceptable for stable operation [113].

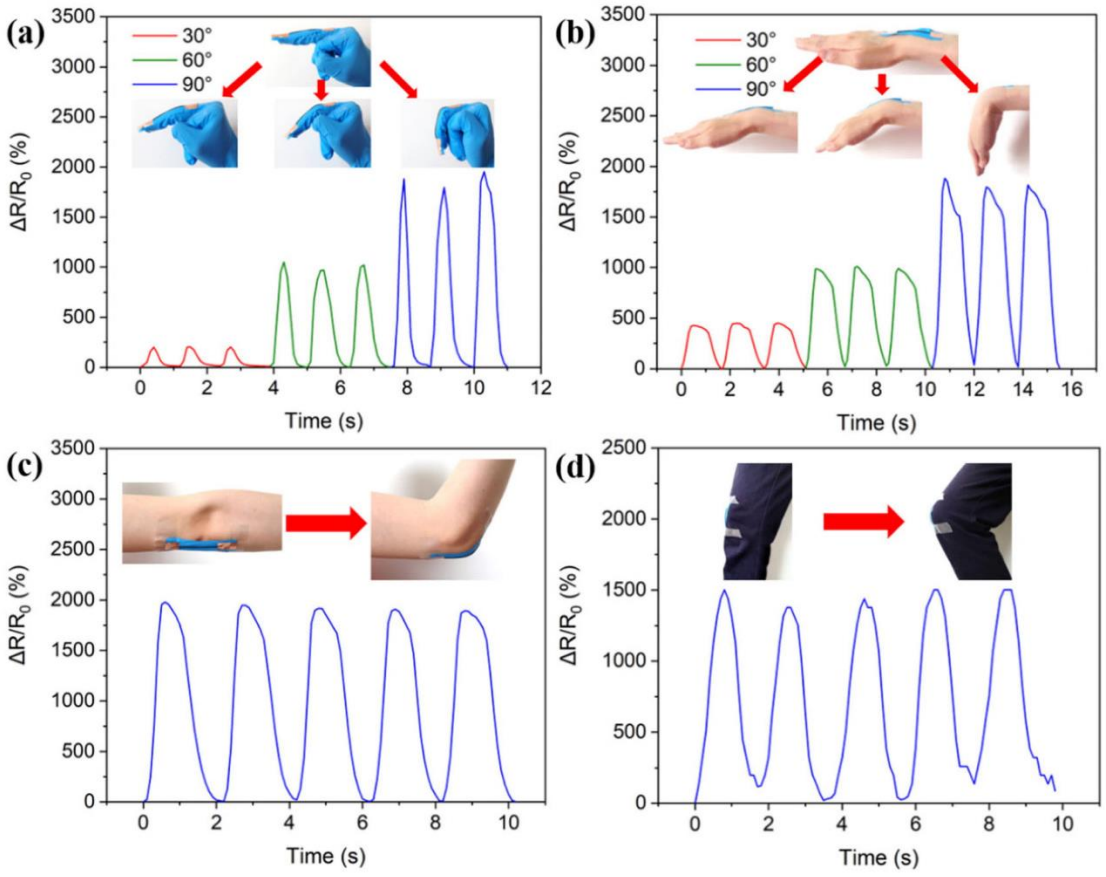

Figure 2.21 The mechanical durability text of a textile-based pressure sensor[114].

Interfacial stability between sensor layers is one of the most decisive factors affecting device durability. In this context, diverse material innovations and engineering strategies have been devised to reinforce the skin-sensor interface and mitigate device performance degradation over time[113]. Fast ionic conductors such as β-Bi_2O_3 and Li_3PO_4 combine superior ionic transport characteristics with robust structural integrity, thereby reinforcing the interface between the ISM and electrode while ensuring consistent ion flux[115]. Hydrophobic protective layers serve as moisture barriers that prevent sweat penetration, which can otherwise lead to swelling or delamination [90]. In addition, self-healing coatings that incorporate dynamic cross-linking networks can autonomously recover from microcracks, effectively prolonging device lifespan.

To further enhance the adhesion at the membrane-electrode interface, several interface engineering techniques have been explored. Electropolymerization enables in situ growth of functional layers directly onto the conductive substrate, forming seamless and robust interfacial regions[116]. Layer-by-layer self-assembly capitalizes on electrostatic forces or hydrogen bonding to construct successive molecular layers, yielding cohesive multilayer architectures with enhanced integrity[117]. Chemical crosslinking treatments create covalent bonds across different layers, significantly increasing structural integrity and resistance to delamination during washing or bending.

Recent studies have demonstrated various reusable flexible electrode designs with outstanding mechanical and electrochemical robustness. For instance, embedding metallic nanowires into elastic matrices has yielded devices that retain functionality after more than 1,000 bending cycles. Surface modification of conductive textiles with MXene, PEDOT:PSS, or graphene-based materials has also shown marked improvement in conductivity retention and washing endurance. Comparative evaluations suggest that multi-functional material systems that simultaneously address mechanical durability, interfacial adhesion, and electrochemical stability are central to advancing the long-term reusability of wearable sensors.

2.2.4 Integration Challenges and Solutions for Washable and Flexible Biosensor Systems

Reliable operation of flexible wearable biosensors depends on the coordinated assembly of multiple functional layers, including the sensing interface, electrode components, interconnect structures, and signal processing modules. However, due to inherent differences in electrical, mechanical, and surface properties among these materials, it remains technically challenging to construct low-impedance, stable, and durable integrated systems. This is particularly true when using non-planar flexible substrates such as textiles and elastomers, where conventional microfabrication approaches often fail to achieve strong adhesion, pattern fidelity, or mechanical resilience.

Multiple fabrication strategies have emerged recently to overcome these obstacles, among which are screen-printing processes, inkjet-based deposition, electrochemical layering methods, laser ablation techniques, and microcontact printing. Each technique offers unique advantages: screen printing is suitable for scalable, rapid fabrication; inkjet printing provides material efficiency and digital control; electrochemical deposition enables site-specific growth of functional layers; and microcontact printing offers high resolution for complex structures. Nevertheless, achieving high-resolution and strongly adhered metal patterns on rough and porous textile substrates remains a significant bottleneck.

Within this framework, polymer-assisted metal deposition (PAMD) has been identified as an especially promising approach. Originally developed for the fabrication of interconnects in microelectronics, PAMD has recently been adapted for use in flexible electronics and textile-based systems[118]. This technique involves three essential steps: first, introducing a functional polymer layer onto the substrate that contains reactive groups such as amines or carboxyls; second, initiating the selective deposition of metal (e.g., silver, copper, or gold) through chemical reduction or autocatalytic processes; and finally, forming a conductive metal pattern with high adhesion and structural integrity (Figure 2.22)[119-121].

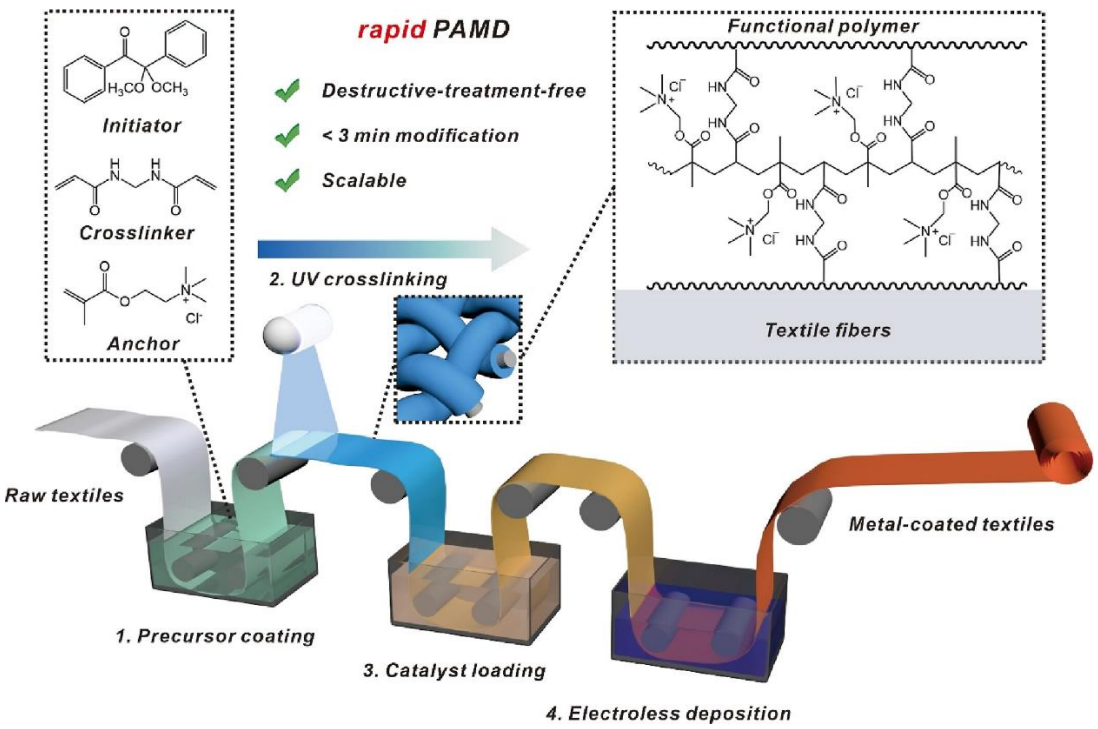

Figure 2.22 Diagram illustrating the sequential steps involved in the polymer-assisted metal deposition fabrication process[121].

PAMD offers several key advantages:

- Strong interfacial adhesion: A polymer interfacial layer markedly improves the adhesion between the metal coating and the textile substrate, enabling robust integration on substrates with considerable surface roughness.

- High pattern resolution and substrate compatibility: By combining PAMD with soft lithographic or transfer printing techniques, micron-scale metal patterns can be fabricated with high accuracy across various textile weaves and fiber geometries.

- Environmentally friendly and low-temperature processing: PAMD can be performed under ambient or mild conditions without requiring high-temperature sintering or harsh chemical treatments, making it ideal for thermally sensitive substrates such as fabrics.

- Excellent compatibility with downstream functionalization: The deposited metal surfaces are chemically active, allowing for easy integration of ISMs, enzyme layers, or biofunctional coatings.

Within wearable sweat sensor development, polymer-assisted metal deposition enables the direct formation of highly conductive metal patterns on both natural and synthetic textile substrates such as cotton, polyester and nylon. These patterns can serve as electrodes or interconnects, providing robust electrical performance even under repeated washing, stretching, or mechanical abrasion. Compared to traditional methods like vacuum deposition or metal coating, PAMD is simpler, more cost-effective, and better suited for scalable manufacturing on flexible substrates.

Furthermore, to ensure seamless connection between the electrodes and functional modules such as chips or Bluetooth units, various soft interconnection strategies have been adopted. These include anisotropic conductive films (ACF), conductive silver paste, flexible printed circuit boards (FPCBs), and stretchable conductive links. These approaches effectively reduce contact resistance, enhance mechanical flexibility, and improve the integration density of the overall system.

Overall, the deployment of material integration strategies is pivotal for engineering durable wearable sweat sensors. The introduction of PAMD technology expands the toolkit available for constructing highly conductive, mechanically durable, and wash-resistant flexible systems, laying the groundwork for next-generation wearable health platforms.

2.2.5 Summary and Outlook

Interdisciplinary advancements in materials science, flexible electronics, and biomedical engineering have been the principal drivers of progress in wearable sweat sensor technology. This section reviewed the key materials-related strategies underlying the development of high-performance sweat sensing systems, focusing on four critical dimensions: biochemical relevance and working principles of ion-selective sensors,

comfort-oriented material and structural design, durability and reusability strategies, and system-level integration approaches.

Initially, researchers identified sweat as a noninvasive biofluid rich in various analytes, including electrolytes, metabolic byproducts, and stress-related biomarkers. ISEs, based on solid-contact architectures and Nernstian response principles, have become a core technology enabling real-time, continuous ion monitoring with high sensitivity and selectivity.

Second, to ensure user comfort during prolonged skin contact, the choice and design of substrate materials play a pivotal role. Textile-based substrates, with their intrinsic softness, breathability, and conformability, offer unique advantages over conventional polymer films. Further, porous, nanofiber, or woven structures can enhance water vapor transport and minimize skin irritation, contributing to long-term wearability.

Third, durability and reuse remain major challenges, particularly under repeated mechanical stress, washing cycles, and chemical exposure. Material innovations—such as the introduction of ion-conducting interfacial layers, hydrophobic coatings, and self-healing polymers—have proven effective in enhancing signal stability and mechanical integrity. Strategies to reinforce membrane-electrode adhesion, including electropolymerization, layer-by-layer assembly, and chemical crosslinking, further support sensor longevity.

Fourth, we emphasized recent progress in flexible device integration. Among various patterning technologies, Polymer-Assisted Metal Deposition (PAMD) stands out for its ability to directly fabricate highly conductive, robust metal patterns on rough textile substrates under mild, scalable conditions. Combined with reliable interconnect strategies, these advances have significantly improved the feasibility of building fully integrated, skin-compatible, and wireless-enabled sensing platforms.

Looking forward, the field of wearable sweat sensors will continue to evolve toward greater system-level sophistication. Prospective investigations should aim for the concurrent refinement of detection efficacy, ergonomic comfort, and ecological sustainability. This includes developing multifunctional materials capable of real-time biofeedback, self-powered operation, and adaptive responses to dynamic physiological states. Additionally, initiatives need focus on transitioning laboratory prototypes into scalable manufacturing by employing printable electronics, roll-to-roll fabrication techniques, and packaging that meets regulatory requirements. Collectively, these innovations will accelerate the translation of wearable sweat biosensors from proof-of-concept studies into practical healthcare tools for personalized diagnostics, continuous monitoring, and digital medicine.

2.3 Closed-Loop Intelligent Sensing and Intervention Systems for Biomedical Preservation Applications

With the growing demand for organ transplantation, ensuring the structural and functional integrity of harvested organs during cold storage and transportation has become a major challenge in both clinical and biomedical engineering domains[122-124]. While numerous strategies have been proposed to improve preservation efficiency, most conventional methods rely on passive approaches that lack the ability to respond to evolving pathological microenvironments in real time[125,126]. The inability to provide adaptive, on-demand intervention during transport limits the effectiveness of these strategies, making it difficult to prevent damage caused by factors such as temperature fluctuations, hypoxia, and acidosis.

Currently, static cold storage (SCS) remains the prevailing clinical method. By suppressing metabolic activity through hypothermia, SCS can delay tissue degradation. However, it is insufficient to counteract the adverse effects associated with prolonged transport, such as temperature fluctuations, hypoxia, and acidosis. These factors

significantly contribute to cold ischemic injury and ischemia-reperfusion injury (IRI), which may result in suboptimal graft function or, in severe cases, graft failure. This highlights the need for intelligent, closed-loop systems that can actively monitor and adjust conditions in real-time to mitigate these risks.

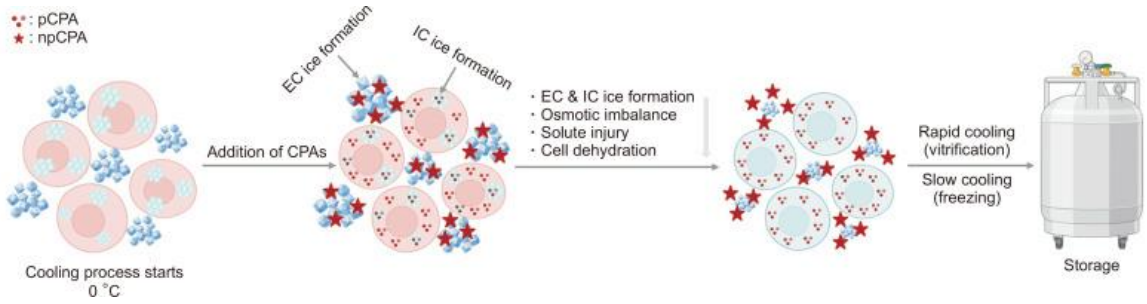

Figure 2.23 Diagrammatic illustration of the roles of permeable cryoprotective agents and nonpermeable cryoprotective agents in subzero preservation[122].

Traditional preservation solutions, such as the University of Wisconsin (UW) solution and histidine-tryptophan-ketoglutarate (HTK) solution, provide passive protection by maintaining osmotic balance and delivering essential nutrients[127,128]. Nevertheless, their inability to actively respond to dynamic environmental changes, such as shifts in pH or elevated reactive oxygen species (ROS), limits their efficacy[129]. In the absence of intelligent regulation or therapeutic feedback, critical windows for timely intervention are often missed[130]. The incorporation of real-time biosensing and therapeutic feedback mechanisms in these solutions could enhance their ability to respond dynamically, improving organ viability during transport.

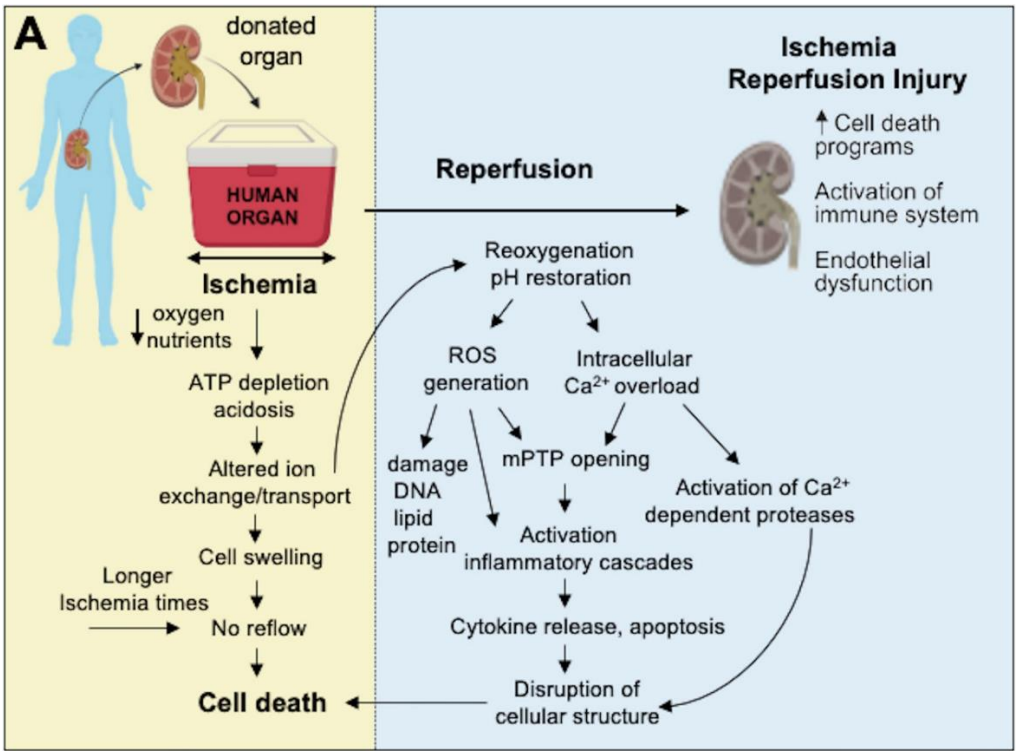

Figure 2.24 Key challenges in organ transplantation[128].

These limitations underscore the urgent need for advanced preservation platforms that integrate real-time sensing with responsive therapeutic delivery[131]. Recent advances in stimuli-responsive hydrogel systems, especially those that respond to pH fluctuations, offer promising pathways toward this goal[132]. Such hydrogels, when integrated into closed-loop systems, enable the on-demand release of antioxidants or pH-buffering agents in response to acidification, thus helping mitigate oxidative stress and metabolic imbalance during hypothermic storage.

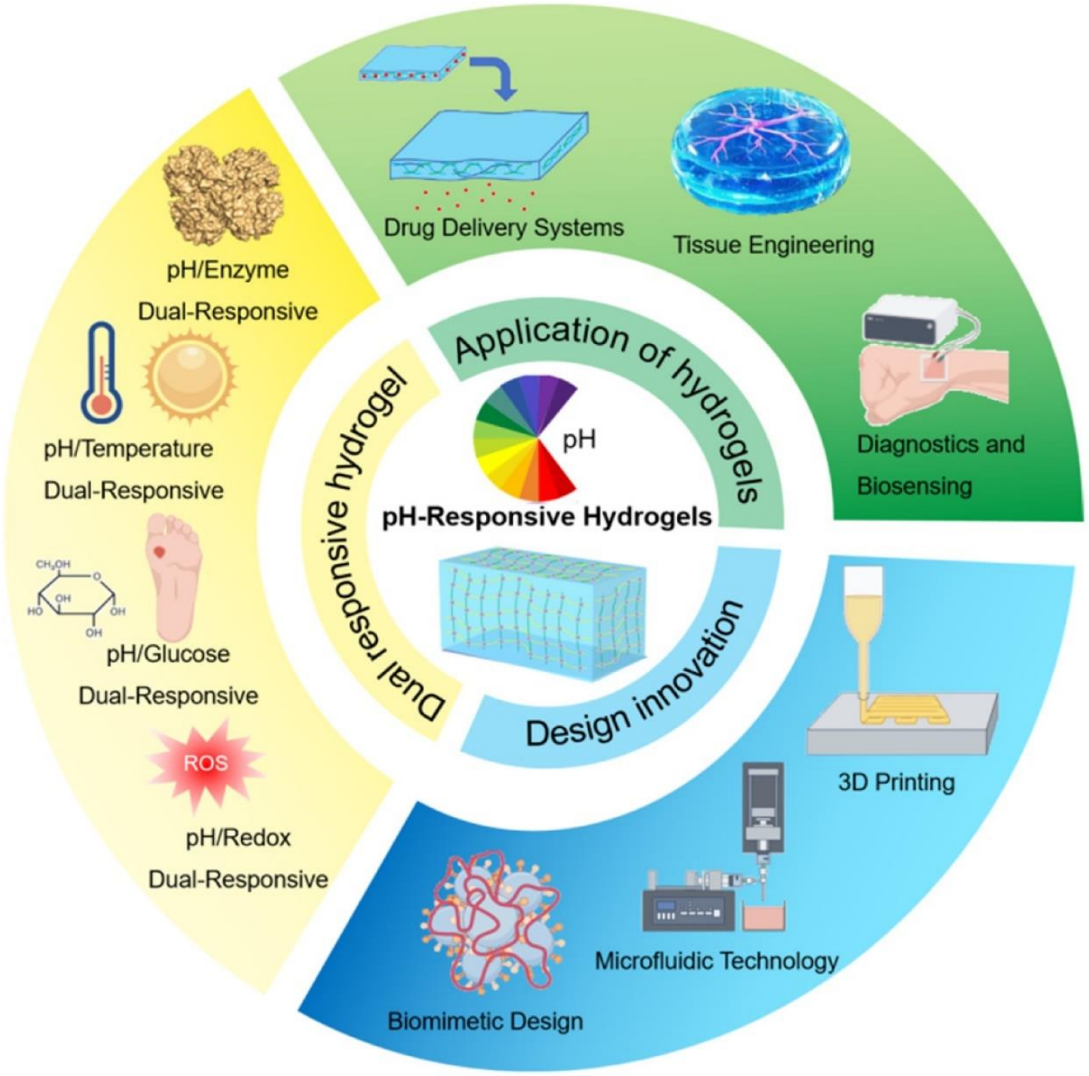

Figure 2.25 Preparation, design, and applications of pH-responsive hydrogels[133].

In this section, we critically examine the mechanisms of cold-induced organ injury and evaluate the limitations of traditional preservation strategies. Building on these challenges, we explore the role of integrated, closed-loop systems involving pH-responsive hydrogels and real-time biosensing, as next-generation solutions for adaptive intervention during organ transport.

2.3.1 Limitations of Conventional Strategies in Biomedical Preservation and Intervention Systems

Organ hypothermic preservation is a critical component of clinical organ transplantation, aiming to maintain the viability and function of harvested organs during transport and pre-transplant storage[133]. The core strategy involves reducing metabolic activity through low-temperature conditions, typically around 4 ℃, which significantly lowers enzymatic reaction rates, oxygen consumption, and adenosine triphosphate (ATP) depletion. This approach extends the viable time window for organ transplantation and is commonly referred to as hypothermic storage.

The most widely used method in current practice is static cold storage (SCS), in which organs are immersed in a specialized preservation solution and maintained at a constant low temperature[134]. While SCS is cost-effective and easy to implement, it fails to provide continuous nutrient supply and waste removal, resulting in energy depletion and hypoxic injury during prolonged storage[135]. Conversely, machine perfusion (MP) has gained attention as a viable alternative, particularly well-suited for maintaining the viability of highly metabolic organs such as the liver and kidney[136]. MP maintains a controlled perfusion of oxygenated preservation solution, simulates physiological flow and pressure conditions, and thereby better mitigates cold ischemia-induced damage[137].

Current clinical protocols predominantly rely on SCS and standardized preservation fluids such as the UW solution and HTK solution (Figure 2.26). These fluids are preformulated with antioxidants, buffering ions, metabolic substrates, and membrane stabilizers, which are perfused into the organ prior to storage[138]. The UW solution, in particular, serves as the benchmark for hepatic and pancreatic grafts, as it contains lactobionate, hydroxyethyl starch, adenosine, and glutathione to regulate osmotic pressure, provide energy substrates, and reduce oxidative stress[139,140].

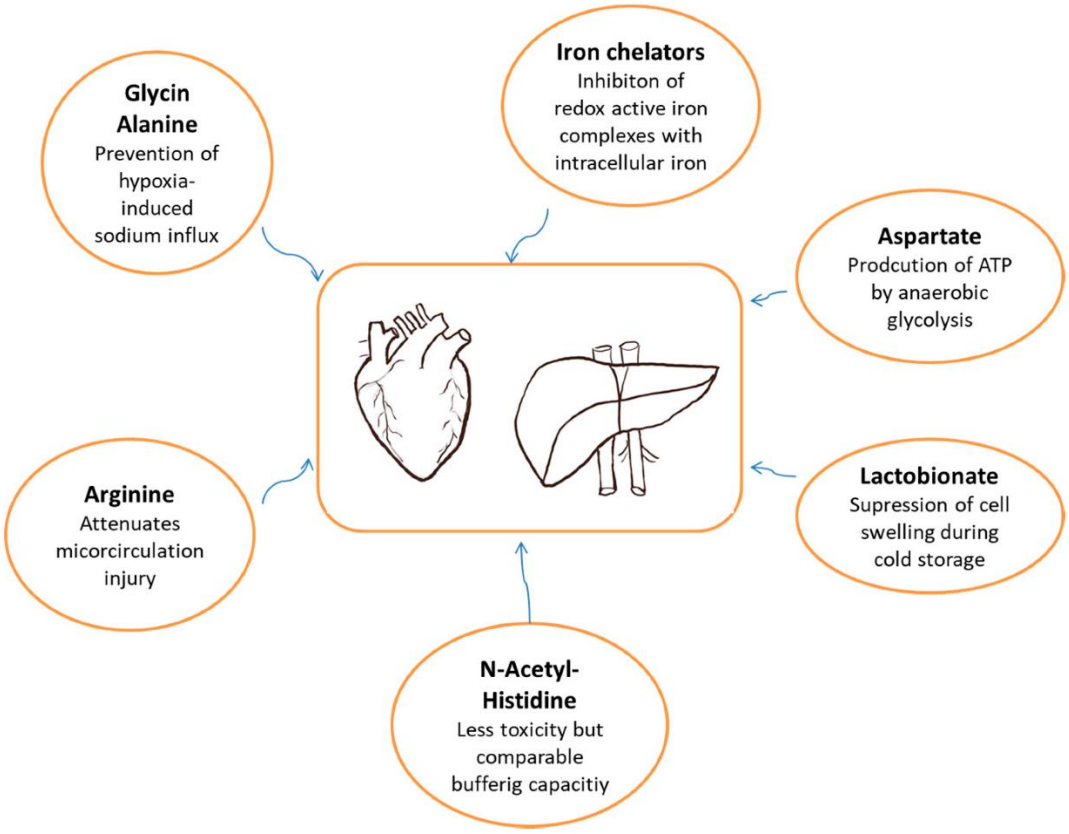

Figure 2.26 HTK-N and its site of actions on preserved organs[141].

However, these preservation methods are inherently passive and lack real-time adaptability. Once perfused, the protective agents are gradually depleted during storage, particularly under long-distance transport or suboptimal temperature control, leaving the organ vulnerable to physiological stress[142]. The drug delivery mechanism is typically based on a diffusion-dominated model, in which therapeutic agents such as antioxidants, calcium channel blockers, or anti-apoptotic compounds are released at a fixed rate, independent of the organ's real-time status.

This static release behavior can lead to premature depletion of therapeutic agents during early storage or delayed availability when intervention is most needed, ultimately compromising graft protection[143-145]. More critically, conventional preservation platforms are incapable of sensing or responding to microenvironmental changes such as pH fluctuation, ROS accumulation, or hypothermia-induced stress[146].

As preservation needs vary significantly depending on the organ type, donor condition, and transport duration, the inability to personalize or dynamically adapt protection strategies represents a major limitation. Hypothermic storage is also frequently challenged by cold ischemic injury and subsequent ischemia-reperfusion injury (IRI), where oxygen reintroduction upon reperfusion triggers ROS burst, calcium overload, and inflammation-mediated apoptosis or necrosis.

Overcoming these limitations demands the creation of next-generation organ preservation systems that integrate embedded sensing and adaptive therapeutic modules, enabling responsive intervention matched to the organ's evolving physiological state. This lays the foundation for the development of intelligent preservation systems discussed in subsequent sections.

2.3.2 Acid-Responsive Pathological Microenvironments and the Need for On-Demand Closed-Loop Intervention

Organ transportation and preservation constitute critical stages in the transplantation process, during which structural and functional deterioration can occur rapidly[147]. Once an organ is removed from the donor, it immediately enters a state of cold ischemia[148]. Although hypothermia reduces basal metabolic activity, it does not completely halt intracellular biochemical processes. Cold ischemic injury primarily manifests through three interrelated mechanisms (Figure 2.27). First, the absence of oxygen supply causes mitochondrial respiratory arrest, leading to severe depletion of ATP and the collapse of ion homeostasis. Second, anaerobic glycolysis compensates for the energy loss but produces lactic acid, resulting in intracellular acidosis that disrupts organelle function. Third, under low temperatures, calcium pumps are impaired, resulting in intracellular calcium overload, which activates proteases and phospholipases that contribute to membrane damage and cytoskeletal degradation.

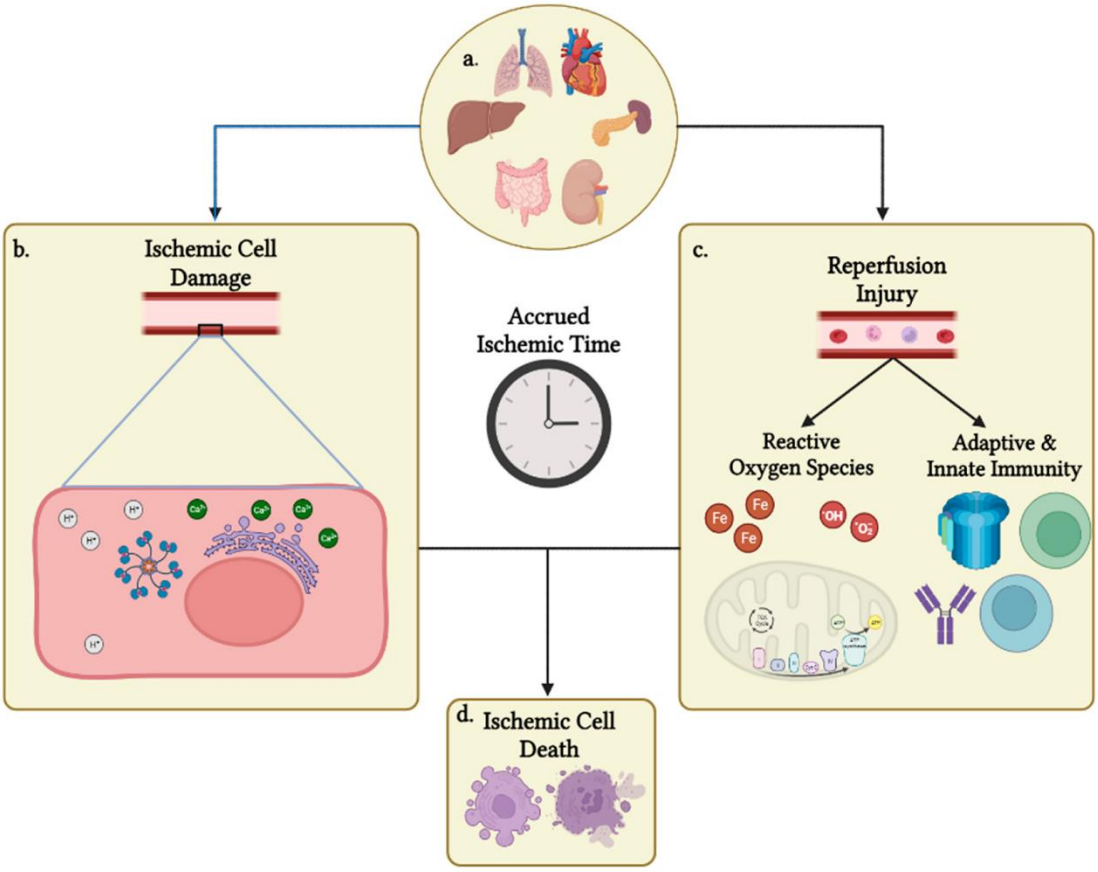

Figure 2.27 Overview of IRI affecting organs following procurement[149].

Furthermore, temperature fluctuations during transportation, due to inadequate insulation or imperfect cooling systems, can exacerbate ischemia-reperfusion injury (IRI) [150]. IRI occurs when oxygen-rich blood is reperfused into ischemic tissue, leading to a burst generation of reactive oxygen species (ROS), such as superoxide anions (O_2^-), hydrogen peroxide (H_2O_2), and hydroxyl radicals (•OH) (Figure 2.28). These ROS trigger oxidative stress, damage DNA and proteins, and initiate lipid peroxidation, ultimately causing cellular dysfunction, apoptosis, and inflammatory cascades.

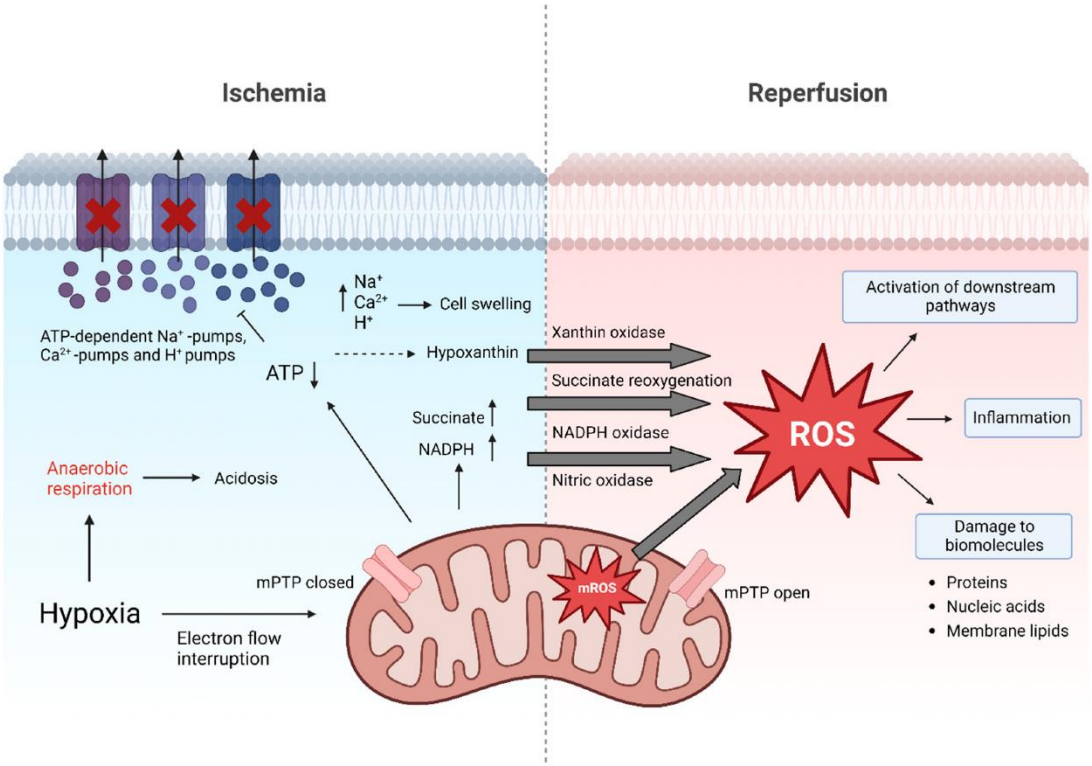

Figure 2.28 Molecular events of ischemia and reperfusion[151].

Among these interrelated stressors, pH imbalance plays a pivotal and underappreciated role. pH imbalance plays a central role throughout this process. During ischemia, lactic acid accumulation lowers intracellular pH, impairing mitochondrial function [152]. Upon reperfusion, the extracellular pH often increases abruptly, creating a transmembrane proton gradient that disrupts membrane potential and ion transport [125]. Moreover, variations in pH influence the function of intrinsic antioxidant enzymes such as superoxide dismutase and catalase, thereby impairing the ability of the tissue to neutralize reactive oxygen species when protection is most critical.

The severity and nature of these injuries vary across different organs. For example, in the liver, with its high metabolic demands, ischemia-reperfusion leads to marked elevations in transaminases and widespread hepatocyte necrosis[153]. In the kidney, oxidative damage to proximal tubules impairs filtration and elevates serum creatinine levels[154]. The heart is particularly susceptible to calcium overload and membrane depolarization, which can induce arrhythmias and contractile dysfunction. Despite their

organ-specific manifestations, these injuries consistently involve dynamic acid-base fluctuations and ROS surges, which are not adequately addressed by conventional preservation methods.

These observations underscore the urgent need for preservation platforms that incorporate real-time pH monitoring and environment-responsive therapeutic release. Such systems could enable timely intervention against acidification-induced damage, improve redox balance, and preserve organ viability during cold ischemia and transport.

2.3.3 Stimuli-Responsive Hydrogels for Sensing and Therapeutic Release

To address the limitations of conventional organ preservation strategies, particularly the lack of dynamic regulation and personalized intervention, stimuli-responsive drug delivery systems have emerged as a promising solution [155-157]. These smart materials are capable of sensing changes in the physiological microenvironment, such as pH, temperature, ROS, and enzyme activity, and triggering the controlled release of therapeutic agents accordingly. This dynamic behavior enables precise, timely, and efficient organ protection throughout the preservation and transportation process.

During cold storage and transport, organs often experience fluctuations in pH, oxidative stress, and inflammatory responses. Stimuli-responsive systems are designed to respond selectively to these internal cues and initiate drug release only when needed [158]. This on-demand mechanism minimizes premature drug depletion and reduces waste, while improving therapeutic efficacy during critical time windows.

Among various materials, pH-responsive hydrogels have garnered particular interest due to their high biocompatibility, tunable swelling behavior, and ease of integration with biomedical devices. These hydrogels can detect local acidosis caused by ischemia-induced lactic acid accumulation and release antioxidants such as glutathione (GSH) or N-acetylcysteine (NAC) to scavenge ROS and prevent apoptosis. Compared to conventional pre-loaded systems dominated by passive diffusion, such responsive platforms offer enhanced adaptability and therapeutic precision.

Several representative strategies have demonstrated significant potential in preclinical studies. Thermo-sensitive micelles, for example, can release anti-apoptotic agents upon mild temperature elevation, offering protection against cold chain failure. Oxygen-sensitive microspheres are capable of releasing protective molecules under hypoxic conditions to maintain mitochondrial stability and reduce ischemic damage. These advancements lay the groundwork for constructing responsive preservation systems tailored to the biochemical dynamics of organ stress.

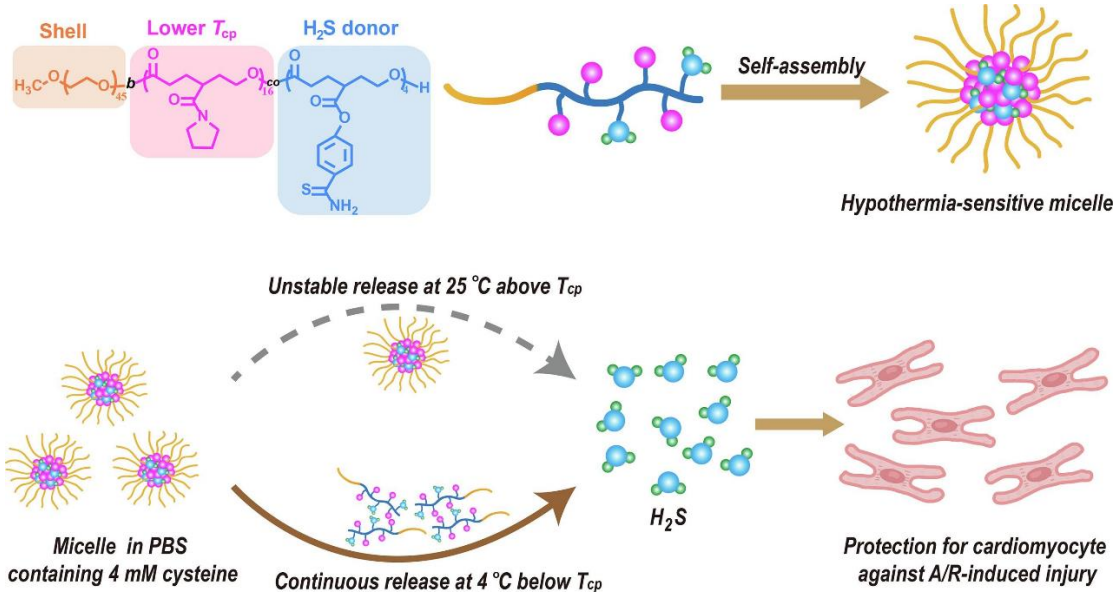

Figure 2.29 Schematic: H_2S release from hypothermia-sensitive micelle protects against A/R cardiomyocyte injury[159].

While these systems operate under different triggers, the integration of pH-responsive hydrogel matrices offers a particularly promising route toward constructing closed-loop preservation platforms tailored to biochemical fluctuations during transport.

In summary, stimuli-responsive drug delivery systems integrate sensing, feedback, and intervention into a closed-loop mechanism, offering promising advantages for organ preservation. With future integration of flexible sensors, wireless communication, and modular patch designs, these systems are expected to evolve into intelligent, all-in-one platforms capable of real-time protection and intervention during organ storage and

transplantation. Looking forward, their combination with flexible sensors, wireless communication modules, and wearable patch designs may enable intelligent, all-in-one platforms for real-time intervention and organ protection during cold storage and transplantation.

2.3.4 Recent Advances in Integrated Low-Temperature Sensing Platforms for Closed-Loop Biomedical Applications

With a growing understanding of dynamic microenvironmental changes during organ cold preservation, increasing research efforts have focused on the development of integrated sensing platforms that remain operational under hypothermic conditions. These platforms are capable of continuously monitoring key physiological parameters, including pH, temperature, and reactive oxygen species, while simultaneously coordinating with feedback-controlled therapeutic modules. Such systems enable closed-loop interventions and offer more precise protection during organ transportation and storage.

Recent advances have been achieved in several key areas. Flexible pH sensors have emerged as essential tools for monitoring acidosis induced by ischemic conditions. Electrochemical interfaces constructed from conductive polymers, metal oxides, or nanocomposites have demonstrated excellent stability and sensitivity under low-temperature conditions, such as 4 degrees Celsius. These sensors provide real-time information on subtle pH fluctuations, thereby enabling early identification of organ stress during preservation.

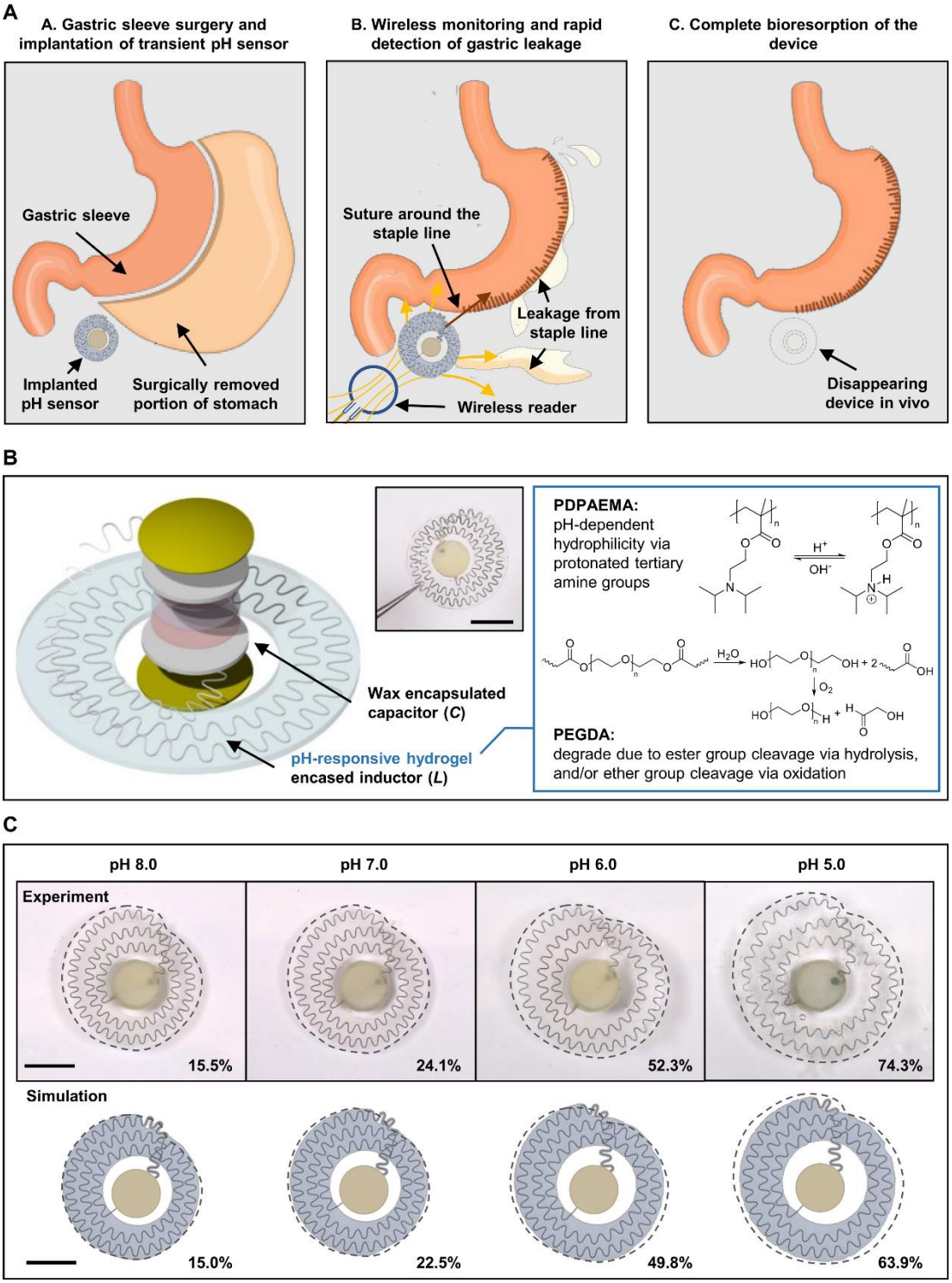

Figure 2.30 Schematic and digital picture showing flexible pH biosensor for early detection of gastric leakage[131].

In parallel, considerable progress has been made in the design of low-temperature-compatible micro power sources, particularly hydrogel-based flexible batteries. These

systems offer stable energy output to support sensing, control, and drug delivery modules, addressing the common limitations of conventional batteries at low temperatures, including electrolyte freezing and voltage instability (Figure 2.31)[160-162].

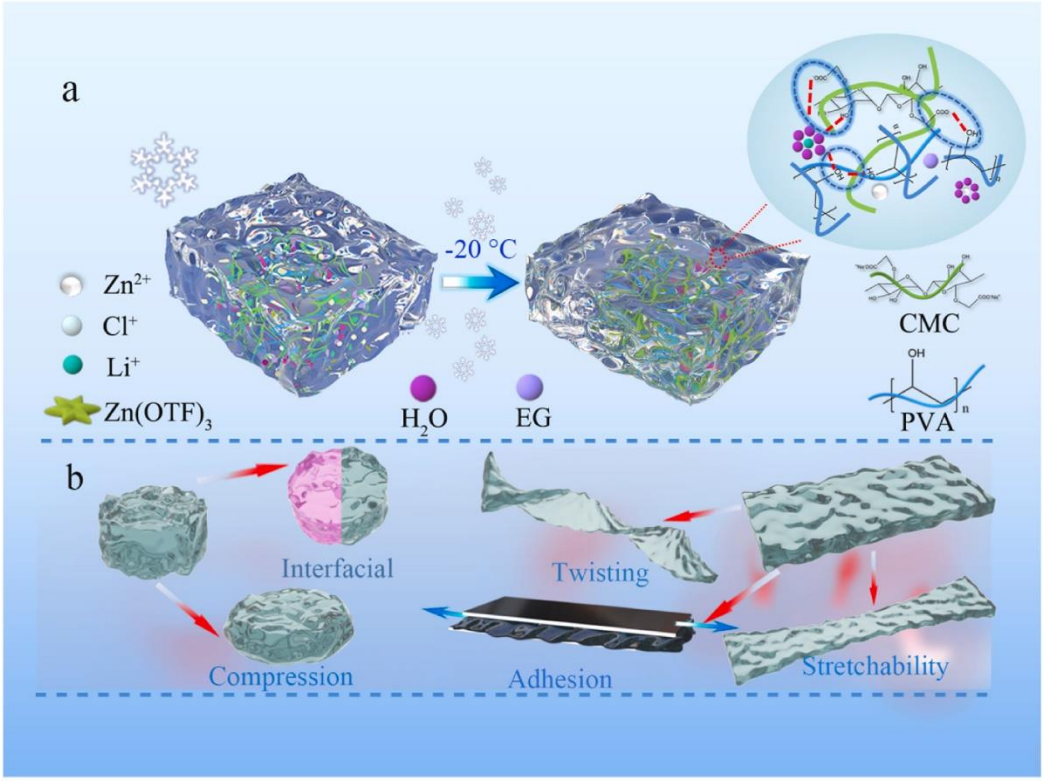

Figure 2.31 Schematic of low temperature working hydrogel supercapacitors[162].

Efforts have also been directed toward the integration of wireless communication units and skin-conformal flexible encapsulation strategies. These developments facilitate real-time data transmission, enhance system adaptability, and allow scalable integration. For instance, by embedding sensors, power sources, and drug reservoirs into a single soft patch, continuous on-organ monitoring and intervention can be achieved, significantly improving practical feasibility for clinical applications [163].

In summary, the development of integrated low-temperature sensing platforms has established a foundational framework for intelligent preservation systems that combine sensing, feedback, and therapeutic response. With further integration of responsive materials, microcontrollers, and remote monitoring interfaces, these platforms are expected to enable smart, closed-loop organ preservation in the future.

CHAPTER 3 METHODOLOGY

This chapter provides a comprehensive description of the materials, fabrication procedures, sensor construction protocols, characterization techniques, and experimental methods employed throughout this research. Tailored experimental strategies and analytical workflows were developed for each of the three core studies, including the fabrication of electrochemical biosensors for pathogen detection, the development of washable textile-based sweat sensing systems, and the construction and evaluation of an integrated pH-responsive hydrogel platform. The methodology presented in this chapter establishes a rigorous scientific and technical foundation for the experimental results discussed in subsequent chapters, ensuring the reliability and reproducibility of the research.

3.1 Materials

All chemicals were used as received unless otherwise specified. Key reagents included Conductive silver ink (seli-2-12021) from Shengli Technology. Hydrochloric acid (HCl), chloroauric acid ($HAuCl_4$), 16-Hexanediol diacrylate technical grade (80 %), Glycine (ReagentPlus®, >99 %) and Anti-SARS-CoV-2 nucleocapsid NC1 Antibody (clone 6G3-G6) were purchased from Sigma-Aldrich. SARS-CoV-2 Spike Protein N Chimeric Recombinant Human Monoclonal Antibody (H6) was purchased from Invitrogen (MA535940). 1-Pyrenebutyric acid N-hydroxysuccinimide ester (PBASE) (95%) were purchased from SantaCruz (sc-213409). Phosphate-buffered saline (PBS) was purchased from Gibco. SARS/SARS-COV-2 CORONAVIRUS NU were purchased from Invitrogen. Nodium hydroxide (NaOH), manganese acetate ($MnAC_2$) , acetic acid, 3-(Trimethoxysilyl) propyl methacrylate (KH570), ethyl alcohol, Copper sulfate pentahydrate ($CuSO_4 \cdot 5H_2O$), ammonium acetate (NH_4Ac), dimethyl sulfoxide (DMSO), acetate buffer solution (ABS) potassium peroxodisulfate ($K_2S_2O_8$), ammonium tetrachloropalladate(II), methacrylatoethyl trimethyl ammonium chloride (METAC), Magnesium sulfate ($MgSO_4$) 2,2-bimethoxy-2-phenylacetophenone (DMPA), N,N'-methylenebisacrylamide (NMBA), potassium sodium tartrate, copper

sulfate pentahydrate, formaldehyde solution and chloroauric acid ($HAuCl_4$) were purchased from Sigma-Aldrich. Hydrochloric acid (HCl), Bis(2-ethylehexyl) sebacate (DOS), sodium tetrakis [3,5-bis(trifluoromethyl)phenyl], borate (Na-TFPB), high-molecular-weight polyvinyl chloride (PVC), valinomycin (potassium ionophore), (NH4)2PdCl4, cyclohexanone and tetrahydrofuran (THF) were purchased from J&K Scientific. PEDOT: PSS (PH1000), potassium ferricyanide (III), chloroauric acid, silver paste, polyvinyl butyral resin BUTVAR B-98 (PVB), sodium chloride (NaCl), iron (III) chloride ($FeCl_3$) and potassium chloride (KCl) were purchased from Aladdin Biochemical Technology. All other chemicals were commercially available and used without further purification. All solutions were prepared using deionized water (16 M Ω·cm) produced from a Millipore water purification system.

3.2 Fabrication of integrated biosensing and biomedical applications

3.2.1 Fabrication of virus biosensor

Fabrication of electrodes. Silver ink was printed onto PET or PI substrates to define the electrode pattern, then dried at 60 °C for 30 minutes. Gold nanostructures were subsequently grown on these screen-printed silver electrodes using a CHI 760E potentiostat in an electrolytic bath containing 50 mM chloroauric acid and 50 mM hydrochloric acid. A pulsed potential waveform ranging from 0 V to 0.8 V with a 50 percent duty cycle at 50 Hz was applied for sixty cycles to deposit the gold onto the printed silver.

Immobilization of SARS-CoV-2 N antibodies. Anti-SARS-CoV-2 nucleocapsid antibodies were covalently attached to the electrode surface via PBASE linkers. Substrates were initially incubated in 2 mM PBASE dissolved in methanol for one hour at ambient temperature, rinsed twice with methanol and four times with deionized water, then immersed in 250 ng/mL antibody solution in phosphate-buffered saline and stored at 4 °C overnight to achieve optimal binding. Following antibody attachment, electrodes were washed with PBS and deionized water before being treated with

20 mg/mL glycine in deionized water at 4 °C for one hour to block residual binding sites, then rinsed again with deionized water. The finalized dendritic gold-PBASE-antibody immunosensors were kept at 4 °C until use. For the counter electrode, 10 µL of counter solution was deposited onto an Ag/AgCl electrode and allowed to air dry overnight.

Immobilization of H_3N_2 antibodies. H_3N_2 antibodies were covalently attached to the electrode surface via PBASE linkers. Substrates were initially incubated in 2 mM PBASE dissolved in methanol for one hour at ambient temperature, rinsed twice with methanol and four times with deionized water, then immersed in 250 ng/mL antibody solution in phosphate-buffered saline and stored at 4 °C overnight to achieve optimal binding. Following antibody attachment, electrodes were washed with PBS and deionized water before being treated with 20 mg/mL glycine in deionized water at 4 °C for one hour to block residual binding sites, then rinsed again with deionized water. The finalized dendritic gold-PBASE-antibody immunosensors were kept at 4 °C until use. For the counter electrode, 10 µL of counter solution was deposited onto an Ag/AgCl electrode and allowed to air dry overnight.

3.2.2 Fabrication of electrode patterns on textile

Fabrication of Cu-PET cloth: The textile substrates underwent initial purification through sequential 15-minute ultrasonication steps in acetone, isopropanol, and deionized water. A one-minute immersion in an ethanol solution containing 2.0 g L^{-1} DMPA, 16.0 g L^{-1} NMBA, and 30.0 mL L^{-1} METAC was followed by ultraviolet irradiation (UVA, 80.0 mW cm^{-2}) for one minute and a thorough rinse with water. The samples were then treated with a 3.2 g L^{-1} ammonium tetrachloropalladate solution for one minute and rinsed again. Electroless copper plating was subsequently performed by immersing the activated textiles for two hours in a bath comprising equal volumes of Solution A, which contained 52 g L^{-1} $CuSO_4 \cdot 5H_2O$, 48 g L^{-1} NaOH, and 117 g L^{-1} potassium sodium tartrate tetrahydrate, and Solution B, consisting of 9.5 mL L^{-1}

formaldehyde (37%) aqueous dilution. This process yielded uniformly copper-coated conductive textiles.

Metallic electrodes patterning: The fabrication process commenced with the deposition of a uniform photoresist layer (NR9-1500p, Futurrex, USA) onto the metallic textile via immersion coating. This was followed by thermal curing at 120 °C for 5 minutes to achieve consolidation of the photoresist. The substrate was subsequently exposed to bilateral UV irradiation for 1 minute through matched photomasks, and then post-exposure baked at 120 °C for 3 minutes to complete the cross-linking process. Unexposed regions were dissolved in RD6 developer, after which the unprotected metal areas were etched using a 1 M ferric chloride solution. Any residual photoresist covering the patterned features was removed with acetone. Finally, the samples were rinsed sequentially with ethanol and deionized water, and air-dried under ambient conditions prior to subsequent processing.

3.2.3 Fabrication of ion-selective sensor

Fabrication of textile-based Na^+ sensors: The textile-based sodium ion sensors were fabricated through sequential functionalization of copper electrodes. Initially, nanodendritic gold (dAu) was electrodeposited using a solution of 50 mM $HAuCl_4$ and 50 mM HCl under a periodic waveform of −2 V, 50 Hz frequency, and 50% duty cycle applied over 9000 cycles. A 3 μL volume of PEDOT:PSS (PH1000) was then drop-casted onto the working electrode to serve as an ion-to-electron transduction interface. The ion-selective membrane was prepared by dissolving a mixture composed of 1 wt% sodium ionophore X, 0.55 wt% Na-TFPB, 33 wt% PVC, and 65.45 wt% DOS (totaling 100 mg) in 660 μL tetrahydrofuran; 6 μL of this cocktail was applied onto the PEDOT:PSS/dAu surface. For the reference electrode, a solution containing 79.1 mg PVB and 50 mg NaCl in 1 mL methanol was cast in a 10 μL aliquot onto a Ag/AgCl substrate and dried overnight.

3.3 Characterization

The morphological and topographical features of the samples were evaluated using scanning electron microscopy (SEM; Hitachi TM3000 and ZEISS Gemini 300), transmission electron microscopy (TEM; Thermo Scientific Talos F200X G2), atomic force microscopy (AFM; Oxford Instruments CYPHER S), and polarized optical microscopy (Nikon). Crystalline structure and composition were examined by X-ray diffraction (XRD; Rigaku SmartLab) and Raman spectroscopy (Horiba LabRAM HR Evolution, equipped with an 800 mm monochromator, confocal optics, and a CCD detector). Surface chemical states were analyzed via X-ray photoelectron spectroscopy (XPS; ULVAC-PHI VersaProbe III). Fluorescence imaging was performed on a confocal laser scanning microscope (Leica TCS SP8).

Electrochemical characterizations, such as cyclic voltammetry (CV) and electrochemical impedance spectroscopy (EIS) across a frequency range of 100 Hz to 0.01 Hz, were performed using CHI 760E and Ivium Soft 4 potentiostats.

Biomarker concentrations in collected sweat samples were quantitatively confirmed using inductively coupled plasma mass spectrometry (ICP-MS; Thermo Scientific Q Exactive). Moisture permeability was assessed via the gravimetric cup method in compliance with the ASTM E96/E96M-13 standard. Testing was carried out over a 20-day period under controlled conditions of 22 °C and 63% relative humidity. Mechanical characterization was performed with a universal testing system (Instron 5599), while electrical behavior under strain was monitored using a Keithley 2400 SourceMeter integrated with a programmable linear actuator. All on-body sweat monitoring procedures adhered to institutional ethical guidelines (SUSTech Institutional Review Board, Approval No. 20200037; Ethics Guidelines for Research Involving Human Subjects or Human Tissue).

On-body sweat analysis was conducted with healthy volunteers aged 24-26 years. Real-time monitoring was achieved using a wearable wristband connected wirelessly to a

smartphone application via Bluetooth. Participants first completed a 20-minute warm-up cycling session while wearing the sensor, followed by an additional 20 minutes of stationary cycling. Throughout the exercise, the application initiated data acquisition and displayed decoded sweat analysis results in real time on the smartphone interface. Simultaneously, sweat samples were collected at 5-minute intervals for subsequent off-body validation using inductively coupled plasma mass spectrometry (ICP-MS).

Statistical Analysis. All experimental measurements were performed at least in triplicate ($n \geq 3$), and the results are presented as mean ± standard deviation (SD) or standard error of the mean (SEM) as indicated.

CHAPTER 4 DENDRITIC GOLD-ENABLED ELECTROCHEMICAL BIOSENSOR FOR ULTRA-SENSITIVE AND REAL-TIME VIRUS DETECTION IN WASTEWATER

WBE has become a critical strategy for tracking viral outbreaks at the community level. However, conventional WBE methods, primarily based on RT-PCR, are hindered by complex protocols, high costs, and delayed reporting, limiting their utility for real-time public health response. To overcome these challenges, we have developed a fully integrated, highly sensitive electrochemical biosensor capable of detecting SARS-CoV-2 and H3N2 viruses in wastewater. To overcome these challenges, we have developed an all-in-one, highly sensitive electrochemical biosensor capable of detecting SARS-CoV-2 and H3N2 in wastewater. This platform employs three-dimensional dendritic gold nanostructures in conjunction with PBASE linkers to establish an extensive interfacial surface that facilitates dense antibody attachment and improves the efficiency of signal generation. The biosensor demonstrates a detection limit down to 0.025 fg mL^{-1}, representing an enhancement by a factor of ten to one hundred compared with traditional techniques. The biosensor exhibits high specificity in complex sewage environments and retains consistent signal output during mechanical deformation and prolonged operation. Moreover, it has been incorporated into a compact wireless system that transmits data in real time to mobile devices, facilitating field-based viral surveillance and rapid decision making. This work represents a significant advancement in environmental biosensing, offering a rapid, low-cost, and scalable solution for virus detection in real-world settings. By combining nanostructured electrode engineering with wireless system integration, this platform provides a powerful tool for continuous sewage analysis and early-warning surveillance during epidemics.

4.1 Introduction

Wastewater-Based Epidemiology (WBE) has emerged as a cutting-edge tool for public health surveillance, becoming increasingly recognized as one of the most effective strategies for addressing public health emergencies globally[164]. By analyzing viral

concentrations in wastewater, WBE delivers essential insights for continuous surveillance and forecasting of community health dynamics. In the nascent phase of an outbreak, wastewater-based epidemiology supports the swift identification of viral and pathogenic agents in sewage, thereby enabling early recognition of emerging epidemic hazards and underpinning prompt public health interventions[29]. For example, continuous tracking of the abundance of SARS-CoV-2 variants in wastewater can reveal hidden transmission chains, while dynamic monitoring of H_3N_2 influenza viruses can predict the intensity of seasonal flu outbreaks[26,33]. This dynamic monitoring supports the prediction of epidemic trends, transmission rates, and their impact on public health across different regions[165]. This monitoring paradigm, based on pooled population samples, significantly mitigates the coverage gaps and time delays associated with individual detection methods. As a result, WBE has become an essential tool for monitoring public health safety, providing timely warnings, and facilitating the response to epidemic outbreaks.

However, existing viral monitoring techniques, especially traditional qRT-PCR methods, while offering significant advantages in sensitivity and specificity, still face numerous limitations that affect the efficiency and widespread application of WBE. Despite its high specificity due to nucleic acid amplification, qRT-PCR, which has traditionally served as the benchmark method for viral detection, encounters three major systemic bottlenecks in WBE practice. Firstly, the detection process involves several time-consuming steps, including virus concentration, RNA extraction, reverse transcription, PCR amplification, and fluorescence quantification, which typically take more than 4 hours. During periods of rapid epidemic growth (such as when the basic reproduction number $R_0 > 3$), the daily increase in infection cases can expand by a factor of ten, causing delays that directly lead to the closing of critical intervention windows[166-168]. Secondly, this technology requires specialized equipment such as -80℃ cold chain transport, centrifuges, and nucleic acid purification systems, with the World Health Organization reporting that only 35% of healthcare facilities worldwide have molecular detection capabilities. This infrastructure gap severely limits the equitable deployment of WBE in resource-limited areas[169-172]. Lastly, the batch sampling approach (typically weekly) fails to capture the diurnal

fluctuations in viral loads within wastewater (which can vary by 2-3 orders of magnitude), with these fluctuations being significantly influenced by excretion patterns and hydraulic loading[173-175]. Discrete sampling often misses peak viral shedding events, potentially leading to underestimation of epidemic intensity or failure of early warning signals.

These limitations have prompted public health researchers and technology developers to seek more efficient, faster, and cost-effective viral monitoring technologies to meet real-world needs. In recent years, biosensor technology, especially electrochemical biosensors, has emerged as a promising solution and a research hotspot in the field of WBE[176-180]. Electrochemical sensors combine biological recognition elements with electronic detection systems to enable direct virus analysis in wastewater, providing benefits such as rapid response, continuous monitoring, cost efficiency, and user-friendly operation[181-183]. Compared to traditional qRT-PCR methods, electrochemical sensors can complete detection in a shorter time, making them more suitable for on-site applications and offering greater flexibility and scalability[184,185].

In particular, dendritic gold (dAu) electrodes have shown great potential as key materials for electrochemical biosensors. Dendritic gold electrodes, characterized by exceptionally large surface areas, outstanding electrical conductivity, and robust resistance to interfering species, have demonstrated remarkable effectiveness in detecting viruses within wastewater samples[186-188]. These dAu electrodes present an expanded array of active interfacial regions, which promotes dense antibody attachment and efficient viral binding, thereby enhancing both detection sensitivity and selectivity. The innovative design of these nano materials effectively enhances the performance of electrochemical sensors, enabling real-time, highly sensitive, and low-cost virus detection in wastewater and providing a new technical path for public health monitoring[115,189-193].

Therefore, the development of an integrated, convenient, and real-time electrochemical virus detection platform, particularly for wastewater-based epidemiology, would significantly enhance the efficiency and accuracy of public health responses. Electrochemical biosensors based on dAu electrodes, combined with modern wireless

communication technologies, can enable real-time virus concentration detection and data transmission from wastewater. This would allow public health departments to obtain virus monitoring data more quickly, facilitating timely decision-making, slowing virus transmission, and improving societal capacity to respond to public health emergencies.

4.2 Experiment

4.2.1 Design Requirements for Virus Biosensors

In the context of wastewater-based epidemiology (WBE), virus biosensors need meet a series of technical requirements to efficiently and accurately monitor pathogens in complex wastewater environments. To address the needs of public health safety, the design of these sensors need ensure they possess the following key characteristics:

Ultra-high Sensitivity and LOD. Virus concentrations in wastewater are often extremely low, especially during the early or late stages of an epidemic when virus levels may be in the fg/mL range. For instance, during large-scale outbreaks, SARS-CoV-2 concentrations in sewage could be as low as 0.1 fg/mL or even lower, which is far below the threshold of conventional detection methods. Therefore, biosensors need be designed to detect extremely low concentrations, with an LOD typically set below 0.1 fg/mL. This sensitivity ensures the early detection of viruses, providing an effective early warning mechanism and enabling timely interventions before the virus spreads further.

High Selectivity and Interference Resistance. Wastewater is a complex matrix that contains a variety of substances that can interfere with the detection of viruses, such as inorganic ions (e.g., Mg^{2+}, Na^{+}), organic compounds (e.g., surfactants), suspended solids (TSS), and other chemicals that may non-specifically bind to the sensor. The sensor need deliver exceptional selectivity to discriminate the intended viral antigens, such as the SARS-CoV-2 nucleocapsid protein or the H_3N_2 nucleoprotein, from the diverse background components in wastewater. Achieving this level of precision requires employing high-affinity antibodies or alternative molecular recognition

elements that bind exclusively to the target antigens. In addition, meticulous optimization of surface modification procedures is essential to suppress nonspecific adsorption and further refine the sensor's discriminatory performance.

Structural Flexibility and Engineering Compatibility. The sensor need be robust enough to withstand the mechanical challenges associated with wastewater treatment systems, where it may experience fluid disturbances, temperature fluctuations, and other environmental changes. Therefore, the sensor design needs to incorporate flexibility, allowing it to operate stably in such dynamic environments. This requires the use of flexible materials, such as polyethylene terephthalate (PET) films, which offer good mechanical properties, water resistance, and UV stability, ensuring long-term performance. Additionally, the design should facilitate easy integration with existing infrastructure, making the sensor suitable for large-scale deployment and compatibility with other monitoring systems.

Rapid Response and Real-Time Monitoring. Traditional RT-PCR methods, though highly sensitive, are time-consuming and require several steps, hindering the rapid detection of viruses. During public health emergencies, rapid detection of viral agents is essential for effective outbreak containment and control. Biosensors need be capable of providing results within minutes, enabling the real-time monitoring of viral concentrations in wastewater. This rapid response capability makes electrochemical biosensors more suitable for on-site applications, offering faster results and greater flexibility compared to traditional methods.

Wireless Communication and Data Visualization. To support large-scale deployment and remote monitoring, the sensor system need have wireless communication capabilities. Integration of low power Bluetooth or Near Field Communication modules enables the sensor to deliver data in real time to mobile devices or cloud-based platforms. This wireless functionality allows public health authorities to monitor viral concentrations remotely and receive timely data for

decision-making. Additionally, the data visualization feature enables clearer interpretation of results, providing early detection and response capabilities.

Scalability and Cost-effectiveness. Cost-effectiveness is a crucial factor for large-scale deployment of biosensors. Compared to traditional qRT-PCR methods, electrochemical biosensors are relatively low-cost, and their materials and components are easier to source. Ensuring that sensor architecture supports scalable mass production without compromising its analytical performance is essential. Furthermore, the sensor should be flexible enough to accommodate different biological recognition elements, enabling the detection of various viruses or pathogens, thereby broadening its applicability across numerous domains.

Durability and Long-Term Stability. The stability of the sensor is essential for its effective operation in real-world wastewater environments, where it may be exposed to harsh conditions such as pH extremes, oxidizing agents, and biofouling. The sensor need to be designed to maintain its performance over extended periods, ensuring reliable operation without degradation. High-stability materials and effective encapsulation technologies need to be used to protect the sensor components from environmental damage, ensuring that the sensor continues to function optimally during long-term use.

4.2.2 Development of the Virus Biosensor

This work reports the creation of a pliable electrochemical biosensor employing dendritic gold nanostructures for the continuous, ultra-sensitive identification of SARS-CoV-2 and H_3N_2 viral particles in wastewater. The sensor was fabricated via a scalable and printable process, combining high-surface-area gold nanostructured electrodes with antibody-functionalized interfaces. This design enables high selectivity, low detection limits, and wireless data visualization. The development process consists of two main components: fabrication and functionalization of the biosensor device, and integration with the virus detection platform.

(1) Sensor Fabrication and Interface Functionalization

The biosensor was fabricated on a flexible polyethylene terephthalate or polyimide substrate by printing conductive patterns with silver ink, followed by thermal curing at 60 °C for half an hour. Gold nanostructures were then grown on the silver electrodes via electrochemical deposition using a CHI 760E workstation in an electrolyte of 50 mM chloroauric acid and 50 mM hydrochloric acid. A series of sixty pulsed potentials between 0 and 0.8 V at 50 Hz with a 50 percent duty cycle produced dendritic gold architectures with a high surface area. These structures enhanced electron transfer efficiency, improved resistance to fouling, and provided numerous sites for antibody attachment.

Surface modification employed 1-pyrenebutyric acid N-hydroxysuccinimide ester as the linking agent (Figure 4.1) [194,195]. Dendritic gold-coated electrodes were submerged in a 2 mM solution of this ester in methanol at ambient temperature for one hour, then rinsed extensively with methanol and deionized water. For SARS-CoV-2 detection, the substrates were immersed overnight at 4 °C in phosphate-buffered saline containing 250 ng/mL of nucleocapsid protein antibodies, allowing covalent attachment via the linker[196]. Subsequent washes with phosphate-buffered saline and deionized water were followed by a one-hour incubation at 4 °C in a 20 mg/mL glycine solution to quench unreacted linker sites and minimize nonspecific adsorption. The completed immunosensors were stored at 4 °C until deployment.

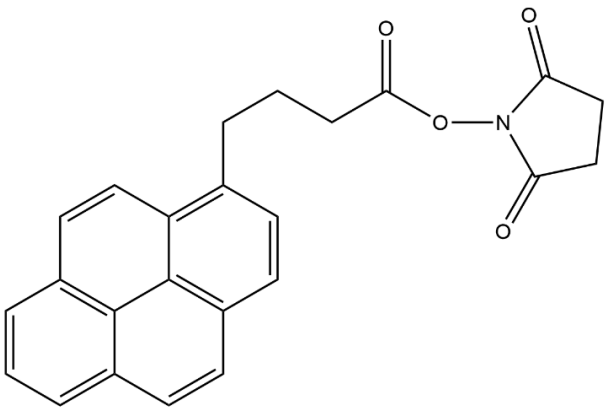

Figure 4.1 The molecular structure of PBASE.

For H_3N_2 biosensors, the same protocol was followed, replacing the SARS-CoV-2 antibodies with 250 ng/mL of H_3N_2-specific antibodies. All sensors used Ag/AgCl as the counter electrode. To establish a stable two-electrode configuration, 10 µL of the counter solution was applied onto the Ag/AgCl electrode and permitted to air dry at room temperature overnight. The final integrated dAu/PBASE/antibody/Ag/AgCl biosensor structure is illustrated in Figure 4.2.

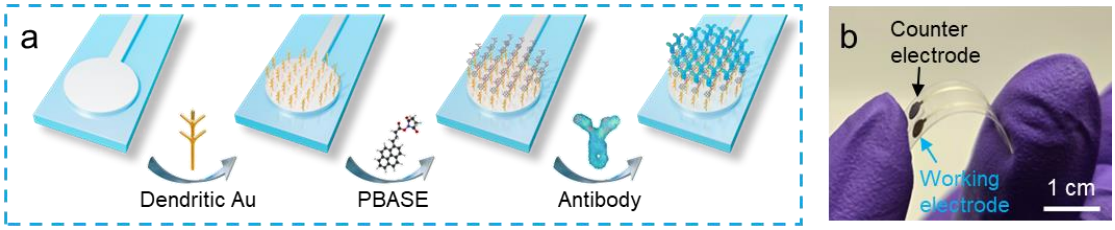

Figure 4.2 Design and Construction of the Electrochemical Virus Biosensor. (a) The fabrication process for the working electrode of the virus biosensor. (b) Digital image and structural diagram of the complete biosensor, comprising the working and counter electrodes for the detection of SARS-CoV-2 and H_3N_2.

(2) Virus Detection Method and System Integration

To facilitate prompt and continuous monitoring of viral concentrations in wastewater, the fabricated biosensor was incorporated into a compact wearable analytical system. As shown in Figure 4.3, the system comprises a virus sensing module, signal acquisition and processing circuits, a low-power Bluetooth communication module, and a user interface through a smartphone application. The mobile application allows real-time visualization of virus detection results and supports switching between SARS-CoV-2 and H_3N_2 detection modes.

Wastewater specimens were obtained from municipal treatment facilities to assess the sensor's performance within complex real-world matrices. In contrast to conventional RT-PCR techniques, the proposed platform eliminates the need for sample pretreatment by enabling the direct detection of viral antigens and transducing the recognition

process into an electrical signal. By combining the high-sensitivity sensing interface with a compact and user-friendly design, this platform offers a low-cost and field-deployable solution for wastewater-based epidemiological surveillance.

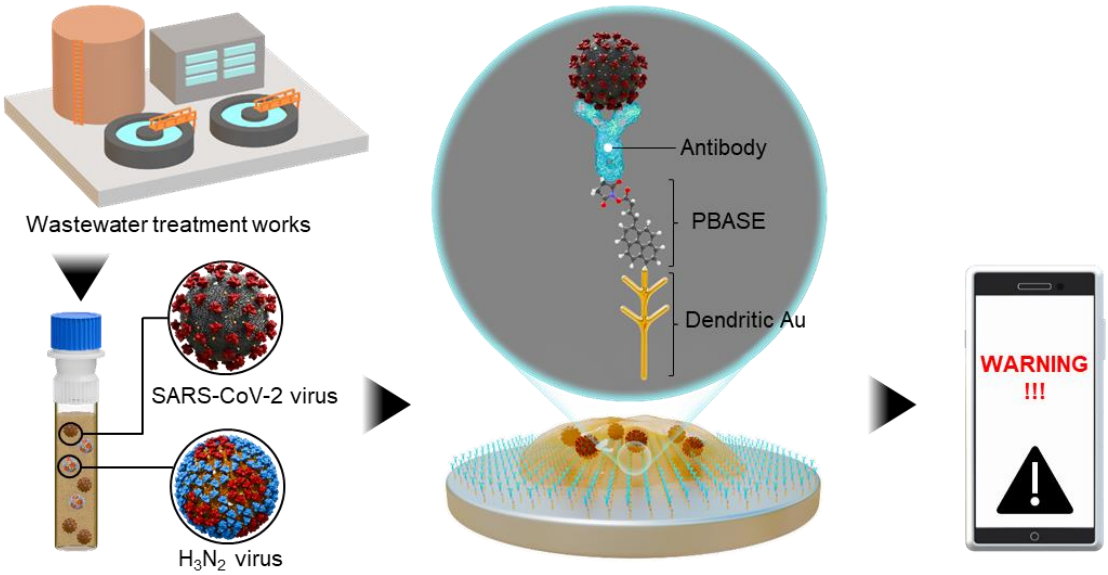

Figure 4.3 Schematic illustration of the operational procedure of the virus biosensor for the detection of SARS-CoV-2 and H_3N_2.

4.2.3 Characterization

To comprehensively evaluate the structural and functional performance of the flexible electrochemical biosensor for virus detection, a series of physical, chemical, and electrochemical characterizations were conducted, covering both synthetic analytes and real sewage samples.

The morphology and surface properties of the sensing materials were first analyzed using multiple advanced techniques. SEM was employed to examine the dAu nanostructures electrochemically deposited on the silver electrodes, revealing their branched architecture and uniform distribution. XRD confirmed the crystalline phases of the metallic components, while Raman spectroscopy was used to identify the characteristic vibrational modes of surface-modified molecules, providing evidence of

successful chemical functionalization. Surface roughness and nanoscale topography were further examined by AFM, and spatial distribution of the interface components was visualized using confocal laser scanning microscopy.

Electrochemical performance was evaluated using a CHI 760E electrochemical workstation. CV was performed to assess the redox activity of the electrode surface before and after biomolecular immobilization. EIS was conducted in the frequency range of 100 Hz to 0.01 Hz, with equivalent circuit modeling applied to extract charge transfer resistance (Rct) and assess interface conductivity changes during sensor fabrication.

The analytical performance of the sensor was systematically assessed using synthetic analytes. Standard solutions of SARS-CoV-2 N protein and H_3N_2 protein were prepared by serial dilution in PBS, ranging from 0.1 fg/mL to 100,000 fg/mL. A volume of 50 μL of each concentration was applied to the sensor, and corresponding current signals were recorded to determine the limit of detection (LOD), linear response range, and signal stability under mechanical bending. The results demonstrated that the dAu/PBASE/antibody-modified electrodes retained high sensitivity even at extremely low concentrations, indicating excellent potential for trace-level virus detection.

To validate the sensor's applicability in real-world conditions, municipal sewage samples collected during the COVID-19 pandemic were tested. Selected samples were thermally inactivated at 65 ℃ for 10 minutes and analyzed using a qRT-PCR protocol to obtain reference Ct values[197-199]. Untreated sewage was directly applied to the flexible biosensor without any preprocessing. The device successfully detected viral signals in the complex matrix of raw sewage, highlighting its robustness, reliability, and practicality for on-site wastewater-based epidemiological monitoring.

4.3 Results and Discussion

4.3.1 Dendritic Gold Nanostructures for Electrochemical Signal Amplification

The interfacial microstructure of electrode materials is a key factor influencing the sensitivity, selectivity, and long-term stability of high-performance electrochemical biosensors. This consideration becomes especially crucial in demanding scenarios, such as the detection of ultralow-concentration analytes (e.g., viral proteins at the femtogram per milliliter level) or sensor deployment in complex environments like raw wastewater. Conventional planar electrodes often suffer from limitations in terms of reactive surface area, signal-to-noise ratio, and molecular recognition efficiency. Therefore, advancing electrode materials that possess a high surface area, superior electron transfer capabilities, and controllable nanostructures is vital for achieving significant improvements in sensor performance.

Dendritic gold nanostructures represent a class of hierarchically self-assembled metallic materials with distinct multi-level branched morphologies, consisting of trunks, primary branches, and secondary offshoots forming a three-dimensional fractal network. This architecture imparts dAu with several critical advantages for biosensing applications:

(1) Ultrahigh Specific Surface Area and Binding Site Density

Compared with traditional flat gold films, the branched architecture of dAu significantly increases the effective surface area per unit footprint, enabling a higher loading capacity of biomolecules such as antibodies. This high-density functionalization improves recognition efficiency and amplifies signal output. In the context of this study, dAu provides ample surface space for the antibody's immobilization of SARS-CoV-2 and H_3N_2 in a highly oriented manner.

(2) Enhanced Electron/Ion Exchange and Signal Amplification

The multibranched architecture of dAu establishes a continuous conductive network, promoting efficient electron transfer across the electrode-electrolyte interface. The

high-curvature tip sites inherent to the dendritic geometry give rise to local electric field enhancement, also known as the tip effect, under applied potentials. This phenomenon promotes charge accumulation and electron injection at the interface, reduces the kinetic barriers of electrochemical reactions, and effectively amplifies weak recognition signals arising from trace antigen-antibody interactions.

(3) Structurally Stable and Reproducible Electrodes

Gold offers excellent chemical inertness and biocompatibility, maintaining the integrity of the electrode-electrolyte interface and functional layers under electrochemical operating conditions. The dendritic morphology can be precisely controlled via electrochemical deposition by tuning parameters such as deposition potential, cycle number, and precursor concentration. This controllability ensures batch-to-batch consistency and facilitates scale-up for practical applications.

To validate the structural and electrochemical merits of dAu, we performed comprehensive characterization and analysis. SEM images (Figure 4.4) show that the dendritic structures uniformly grow on silver electrode substrates under optimized deposition conditions, exhibiting well-defined branched architectures with sharp tips and high self-similarity-hallmarks of effective fractal growth. This morphology increases interfacial roughness and enhances the reactivity of the biosensing interface.

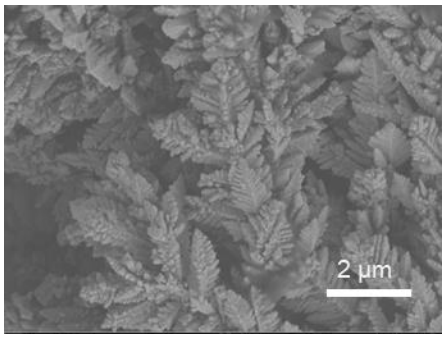

Figure 4.4 SEM characterization dAu.

In terms of electrochemical performance, CV measurements reveal a significantly larger enclosed area and higher peak currents for dAu-modified electrodes compared to

unmodified silver electrodes (Figure 4.5a), indicating a higher electroactive surface area and enhanced electron transport capability[200]. Furthermore, EIS results highlight the superior interfacial conductivity of the dAu-modified electrodes. As illustrated in the Nyquist plots (Figure 4.5b), the dAu-modified electrodes exhibit markedly reduced impedance relative to bare silver electrodes, confirming a substantial decrease in charge transfer resistance (R_{ct}). This improvement arises from the continuous conductive network formed by the dendritic nanostructure, which enhances the exchange rate at the interface and reduces reaction energy barriers. More importantly, the lower R_{ct} not only facilitates signal amplification for weak recognition events but also improves antifouling capacity and response speed in complex sample environments. It is worth emphasizing that the dAu nanostructures employed in this study not only improved the current response of the virus biosensor but also significantly suppressed background noise, resulting in more stable and reliable amperometric signal outputs

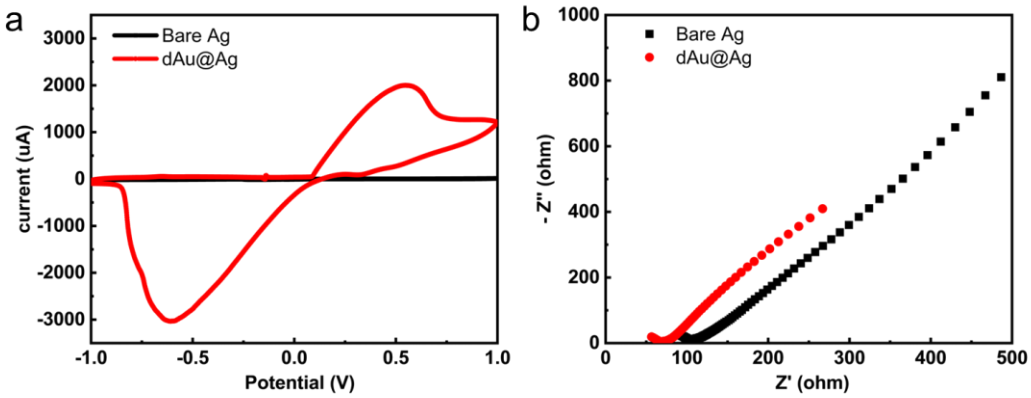

Figure 4.5 Electrochemical performance of bare Ag and dendritic Au-modified Ag electrodes. (a) CV curves of bare Ag electrode and dendritic gold-modified Ag (dAu@Ag) electrode. (b) EIS Nyquist plots of bare Ag and dAu@Ag electrodes.

Furthermore, the tip-enhanced field effect of dAu contributed to increased target protein capture efficiency. To further investigate the impact of dAu nanostructures on surface wettability and protein immobilization efficiency, static water contact angle measurements were performed on four types of electrodes: bare Ag, antibody-

functionalized Ag, dAu@Ag, and antibody-functionalized dAu@Ag (Figure 4.6). The contact angles were measured to be 136.9°, 95.9°, 98.4°, and 68.5°, respectively. This progressive reduction in contact angle reflects a marked enhancement in surface hydrophilicity following dAu modification and subsequent antibody immobilization.

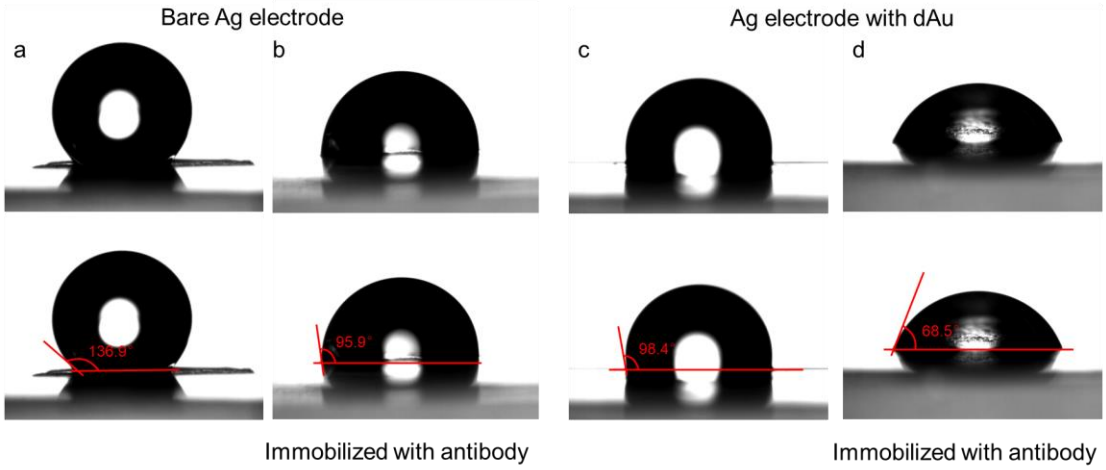

Figure 4.6 Surface wettability characterization of bare and dendritic gold-modified Ag electrodes. Contact angle (CA) measurements of: (a) blank Ag electrode, (b) blank Ag electrode after antibody immobilization, (c) dAu@Ag electrode, and (d) dAu@Ag electrode after antibody immobilization.

From a physicochemical standpoint, the observed trend arises from the combined influence of two synergistic effects. First, the hierarchical nanostructure of dAu increases surface roughness and effective surface area, which according to the Wenzel model leads to improved wetting of hydrophilic layers such as antibodies. Second, the dense coverage of polar functional groups (e.g., amino, carboxyl) introduced during antibody modification further enhances the surface's affinity for aqueous media, facilitating efficient protein-analyte interactions. Notably, the antibody-functionalized dAu electrode exhibited the lowest contact angle (68.5°), suggesting an optimal interface for target antigen binding in aqueous biological environments such as wastewater. Enhanced surface wettability facilitates uniform analyte diffusion and accelerates antigen-antibody interactions, while also supporting improved signal

stability and reproducibility within the biosensor system. Collectively, these findings underscore the multifaceted advantages of dAu in constructing an electrochemically active, biofunctional, and wettable interface for high-performance biosensing applications.

In summary, dAu nanostructures integrate morphological advantages (high surface area, tip effect), electrochemical benefits (low impedance, high conductivity), and material stability (chemical inertness, biocompatibility). In this work, dAu was effectively employed as the primary signal amplification material in the fabrication of high-performance viral biosensors, providing a robust material and interfacial platform for the ultrasensitive detection of SARS-CoV-2 and H_3N_2.

4.3.2 Characterization of the Virus Biosensor

To validate the surface functionalization and electrochemical performance of the developed virus biosensor, a comprehensive suite of structural, spectroscopic, and electrochemical characterization techniques was employed.

Raman spectroscopy was first used to monitor changes in the surface composition of dAu electrodes during functionalization with PBASE and subsequent antibody immobilization. Figure 4.7 presents the Raman spectra of three samples: dAu only, dAu/PBASE, and dAu/PBASE/antibody. Three prominent peaks are observed at 1350 cm^{-1}, 1589 cm^{-1}, and 2712 cm^{-1}, corresponding to the ring-breathing modes and C-H vibrations of the PET substrate[201-204]. Upon PBASE modification, the intensities of the 1350 and 1589 cm^{-1} peaks increase significantly due to the benzene-rich structure of PBASE, indicating successful adsorption of PBASE onto the gold surface and enhanced Raman scattering[202,205]. After antibody immobilization, both peaks decrease in intensity, suggesting that the protein layer alters the molecular environment at the interface and attenuates the Raman signal—an indirect confirmation of successful antibody conjugation.

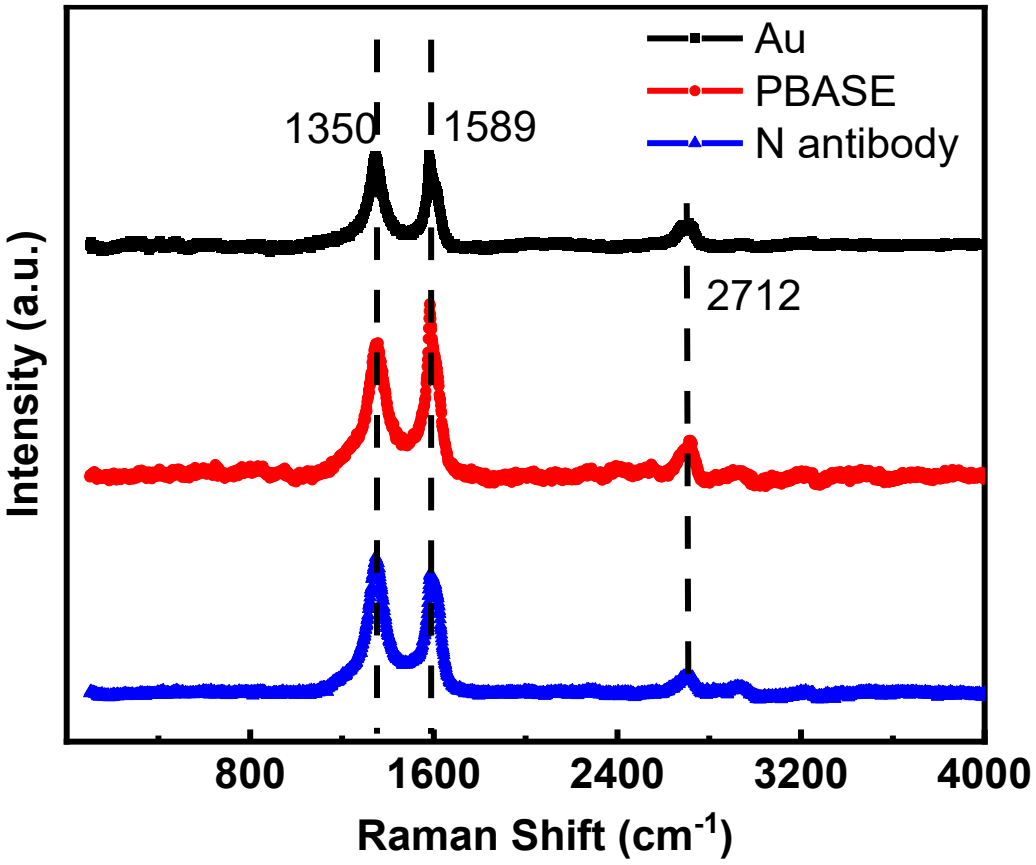

Figure 4.7 Raman spectra of Au, PBASE fabricated on the dendritic Au layer (Au/PBASE) and antibody immobilized on PBASE (dAu/PBASE/antibody).

Morphological evolution of the dAu surface was tracked using SEM and AFM (Figure 4.8). SEM images revealed a transition from rough dendritic structures to smoother and more uniform surfaces after functionalization with PBASE and antibodies. AFM further confirmed these observations, showing a decrease in root-mean-square (RMS) surface roughness upon each functionalization step. The 3D AFM topography data demonstrated that antibody immobilization filled surface voids and reduced scanning depth from 16 nm (dAu/PBASE) to 12 nm (dAu/PBASE/antibody), suggesting denser molecular packing and effective surface coverage.

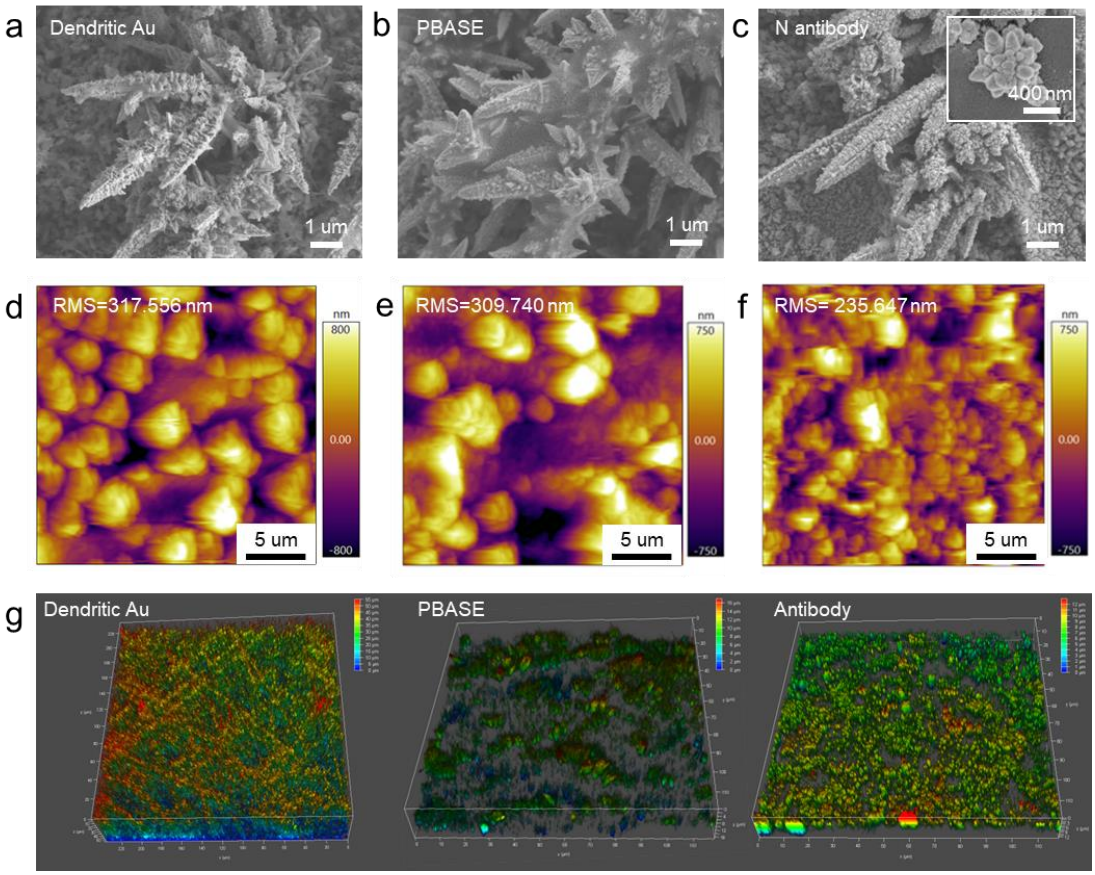

Figure 4.8 Structural characterization of dAu electrode and subsequent functionalization steps. (a-c) SEM images demonstrating the morphological evolution from bare dAu structures, through PBASE coating, to antibody immobilization. (d-f) AFM images and corresponding surface roughness profiles of dAu, dAu/PBASE, and dAu/PBASE/antibody, indicating that the root-mean-square (RMS) of roughness gradually decreases with the completion of the biosensor.

These findings substantiate that the dAu electrode was successfully functionalized via PBASE-mediated covalent binding, ensuring stable and uniform immobilization of viral antibodies. The bonding mechanism involves the strong π-π stacking interactions between the pyrene moieties of PBASE and the dendritic gold surface, which provides a high-capacity molecular anchor. Subsequently, the N-hydroxysuccinimide (NHS) ester groups of PBASE form covalent amide bonds with the primary amines of the antibodies. This dual-mode bonding ensures a robust molecular foundation for high-

density antibody immobilization by leveraging the extensive surface area provided by the dAu nanostructure. This engineered interface provides the biochemical foundation for sensitive and selective electrochemical virus detection.

The antigen-antibody binding occurs through strong intermolecular interactions including hydrogen bonding, electrostatics, and hydrophobic forces. Upon antigen recognition, the insulating nature of the biomolecular complexes restricts electron transfer at the interface, leading to measurable changes in electrochemical signals—thus enabling transduction of biorecognition events into electrical outputs.

To evaluate the impact of each surface modification step, CV was conducted. As shown in Figure 4.9a, the dAu-modified electrode exhibits a significantly larger voltammetric area compared to the bare Ag electrode, reflecting enhanced electrochemical activity due to its high surface area and abundant electroactive sites. However, after PBASE and antibody immobilization, a marked decrease in peak current was observed, consistent with the introduction of insulating biomolecules that hinder interfacial charge transfer.

EIS further confirmed the interfacial modifications. Nyquist plots (Figure 4.9b) revealed a nearly vanished semicircle component after functionalization, indicating reduced electron transfer resistance and a dominant ion diffusion behavior, suitable for biosensing applications in complex matrices. To gain deeper insight into the interfacial electron transfer kinetics, CV measurements were performed at varying scan rates between 0.06 and 0.30 V/s (Figure 4.9c). Both anodic (I_{pa}) and cathodic (I_{pc}) peak currents increased with scan rate, showing quasi-reversible, Nernstian behavior. The linear correlation between peak current and the square root of the scan rate (Figure 4.9d) suggests a diffusion-controlled redox process, essential for consistent signal generation under dynamic conditions[206].

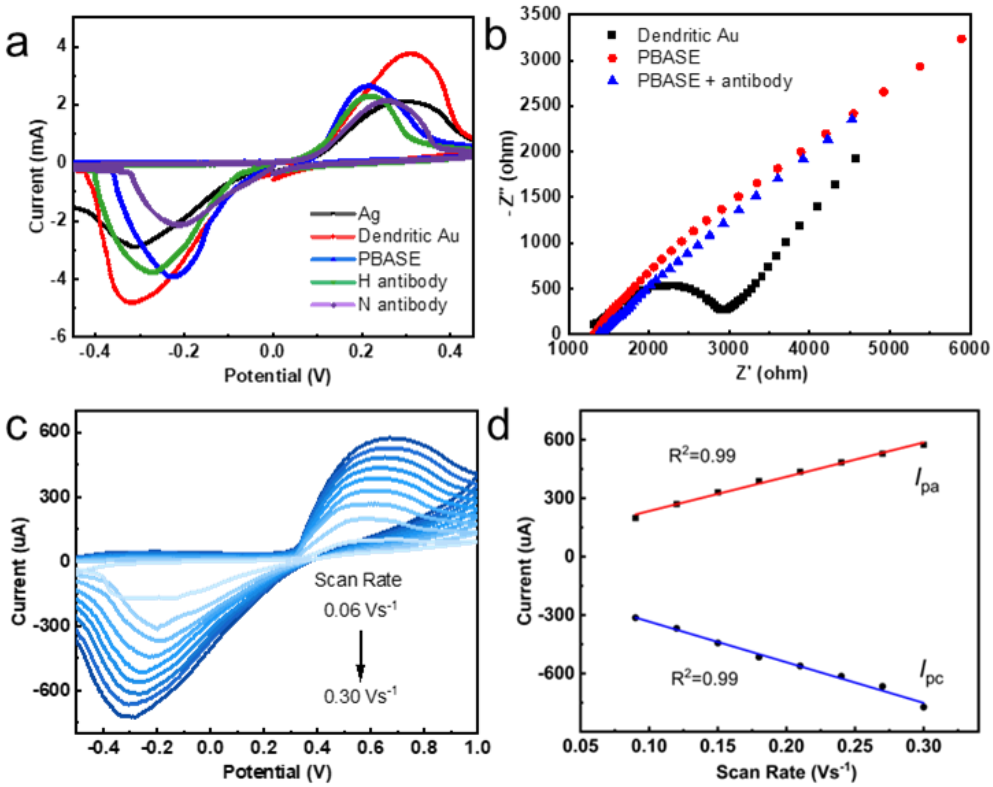

Figure 4.9 Characterization of Au/PBASE/antibody biosensor. (a) CV curves of biosensor with different structures. (b) EIS curves of Au, Au/PBASE and Au/PBASE/antibody. (c) CV curves recorded at biosensor with N antibody in 50 fg/mL N antigen solution at scan rates ranging from 0.06 to 0.30 Vs^{-1} (0.03 Vs^{-1} interval). (d) Plot showing variation of I_{pa} and I_{pc} peak currents with respect to the square root of scan rate values.

In summary, the biosensing interface constructed on dAu electrodes leverages high surface area for electrochemical activation, specific antibody-antigen recognition, and modulated interfacial charge transfer to achieve sensitive virus detection. The integration of Raman spectroscopy, SEM/AFM imaging, CV, and EIS provides a robust foundation for understanding the mechanism of signal generation and supports the practical deployment of this sensor for real-time pathogen monitoring.

4.3.3 Sensing Performance and LOD

To comprehensively assess the sensing performance of the developed biosensor, we evaluated its ability to detect SARS-CoV-2 and H_3N_2 viral proteins in synthetic analyte systems. The biosensor employs a modular design strategy, enabling the selective detection of different viral targets by simply switching the immobilized antibodies (Figure 4.10). This modularity not only enhances application flexibility and adaptability but also reduces manufacturing complexity and cost, as a single sensing platform can be readily adapted for different pathogens without requiring virus-specific instrumentation. Such reconfigurability is especially valuable during emerging infectious disease outbreaks where rapid deployment and scalability are critical.

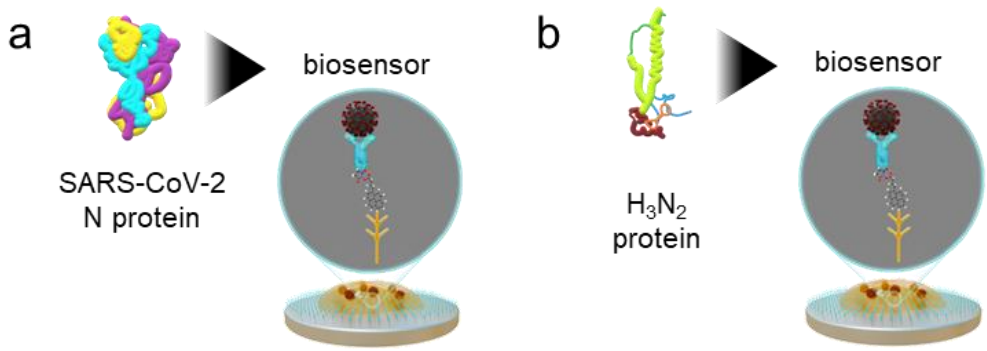

Figure 4.10 Schematic illustration of the biosensor design for detecting (a) SARS-CoV-2 protein and (b) H3N2 protein in synthetic analyte solutions.

Specifically, the working electrodes were functionalized with monoclonal antibodies selective for the nucleocapsid (N) protein of SARS-CoV-2 and the hemagglutinin (HA) protein of H3N2, enabling specific antigen recognition and signal generation[169,207,208]. These antibodies enable highly specific antigen recognition at the sensor interface[209-211]. Illustrative diagrams of the viral structures and their respective genomic organizations are provided in Figure 4.11, offering structural context for the antigen-antibody interactions. Upon target binding, the formation of antibody-antigen complexes

introduces an interfacial insulating layer, thereby modulating electron transport and altering the electrochemical signal.

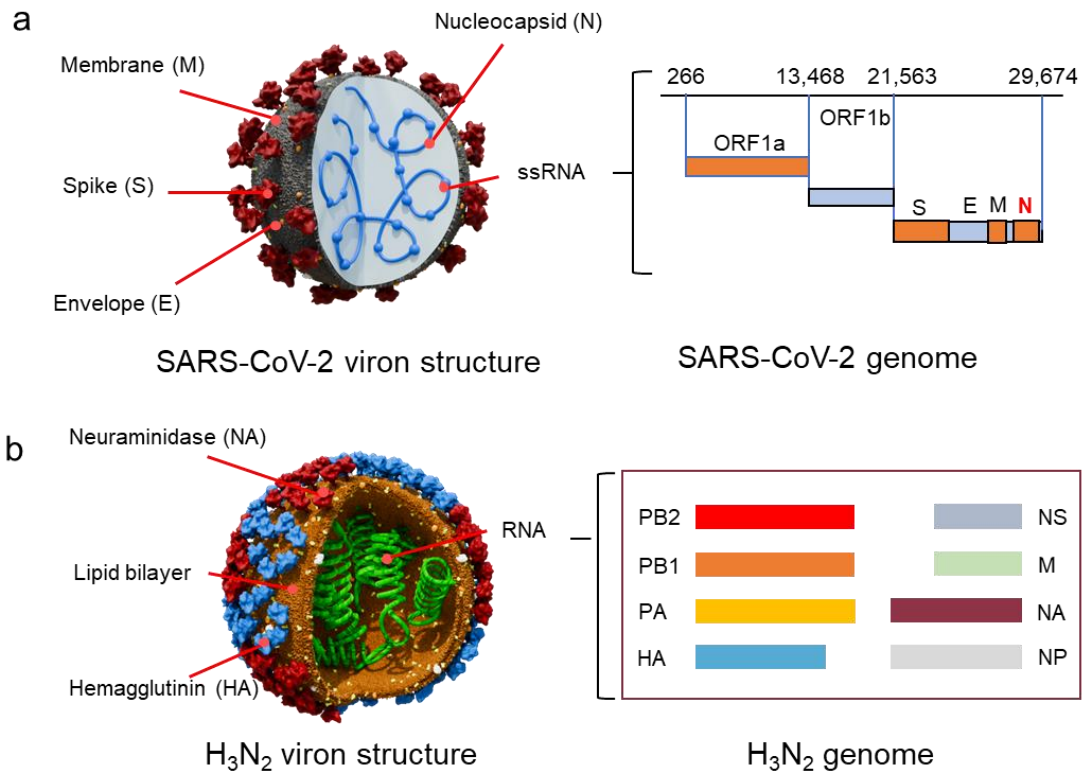

Figure 4.11 Schematic representations of (a) the SARS-CoV-2 virus particle and (b) the H3N2 virus particle, depicting their structural components along with the genomic material enclosed within the viral envelope.

The dynamic current responses of the biosensor to increasing antigen concentrations (0.1, 0.5, 1, 1,000, and 100,000 fg/mL) were recorded in real time (Figure 4.12a, b). Compared with unmodified controls, dAu -based electrodes showed significantly more stable and amplified output signals (Figure 4.12c, d), highlighting the critical role of nanostructured architectures in efficient signal transduction. Within the linear detection range of 62.5-500 fg/mL, the sensor demonstrated excellent reproducibility, with a relative standard deviation (RSD) of 4.3% (Figure 4.13). Notably, the detection limit (LOD) for both viral proteins reached 0.025 fg/mL, as derived from the calibration plots Figure 4.12e, f) [212]. This ultralow LOD was accompanied by a logarithmic current-

concentration relationship, confirming the biosensor's ability to resolve trace-level biomolecular interactions with high precision[175].

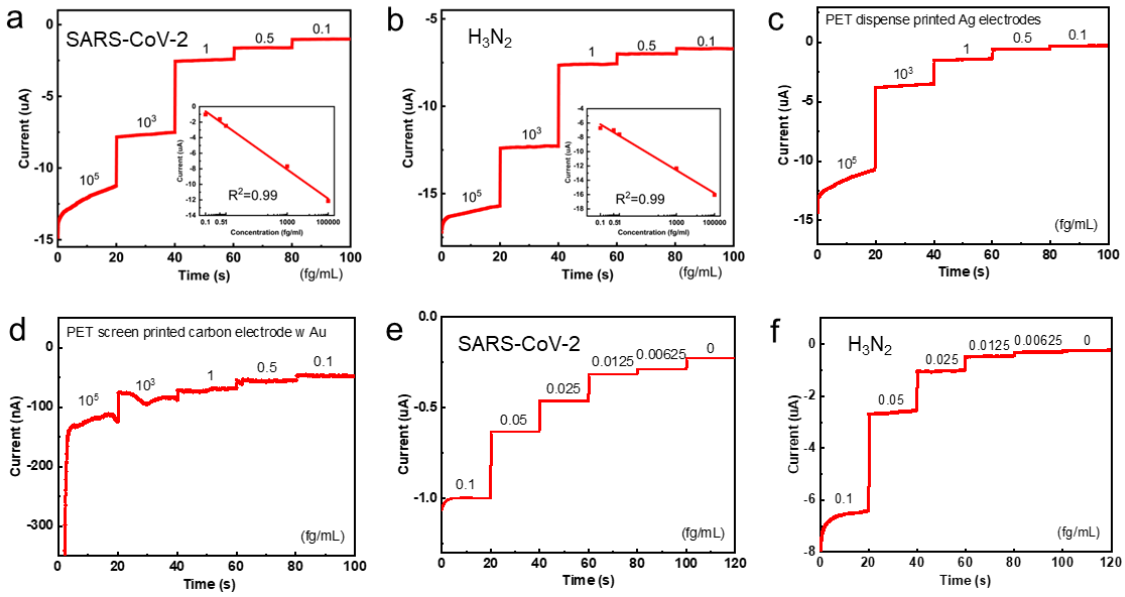

Figure 4.12 Real-time electrochemical response and performance evaluation of the virus biosensor. (a, b) Real-time current responses of the biosensor toward increasing concentrations of SARS-CoV-2 and H_3N_2 antigen proteins in PBS. (c, d) Comparative sensing performance of biosensors with and without dendritic Au modification. (e, f) Calibration curves showing the LOD of 0.025 fg/mL for both viral targets.

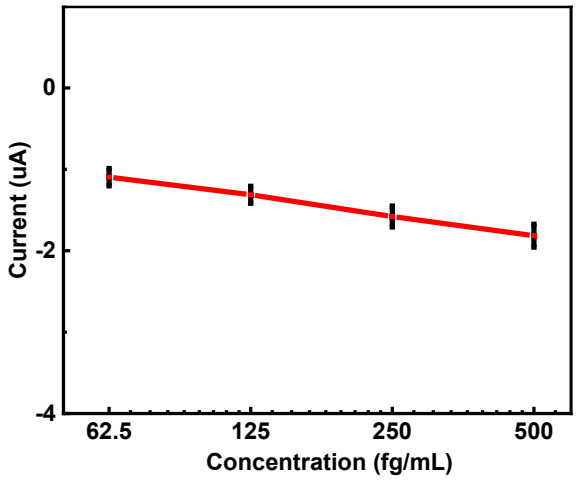

Figure 4.13 Repeatability of the dAu/PBASE/antibody biosensor. (n=3)

To further assess the sensor's specificity in realistic settings, we introduced several representative interferents typically present in wastewater, including Mg^{2+}, NH_3, NO_x, surfactants, and total suspended solids (TSS). As shown in Figure 4.14, the current signals produced by these interfering species were all below 10% of the LOD, demonstrating excellent selectivity and low cross-reactivity under complex sample conditions.

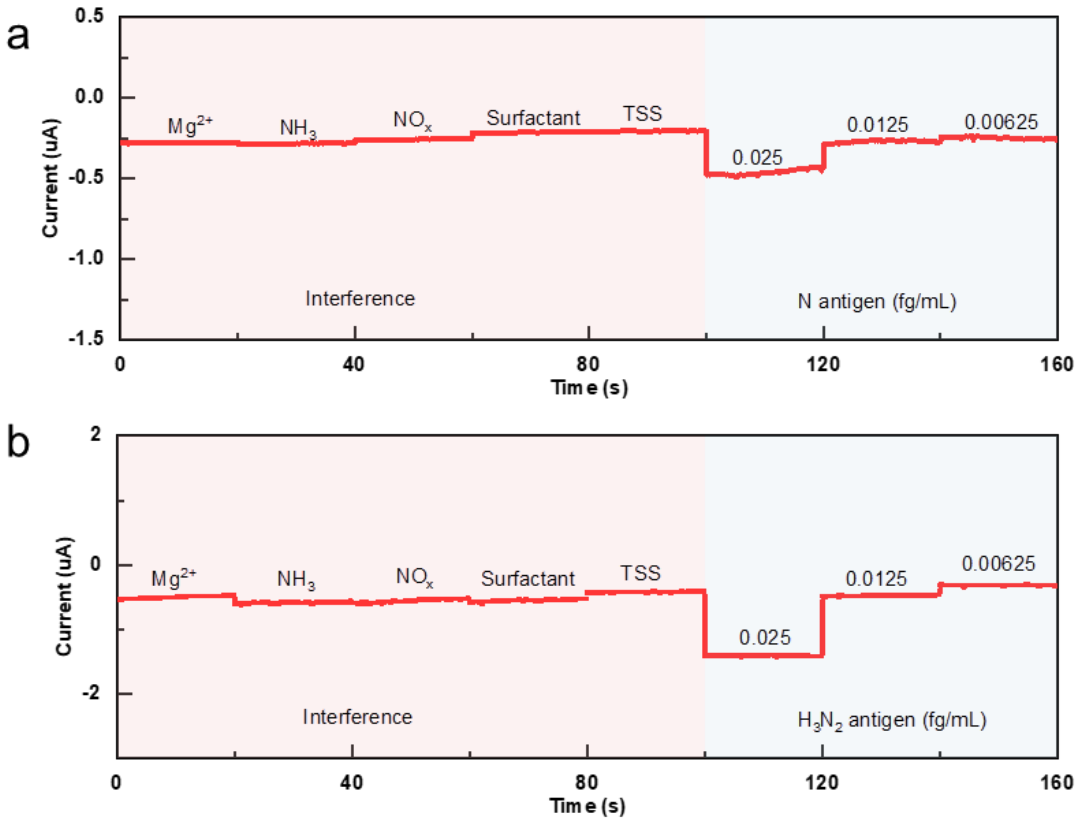

Figure 4.14 Selectivity of biosensor with (a) N antibody and (b) H_3N_2 antibody.

Mechanical stability was evaluated through cyclic bending tests (15° deflection angle) performed for 50, 100, and 150 cycles. The biosensor maintained a consistent signal output throughout these cycles (Figure 4.15a, b), indicating strong mechanical robustness and structural integrity. In addition, long-term operational stability was confirmed by continuous current monitoring, where a drift rate of only 0.023 μA/h was recorded (Figure 4.15c, d), further supporting the device's suitability for prolonged field deployment.

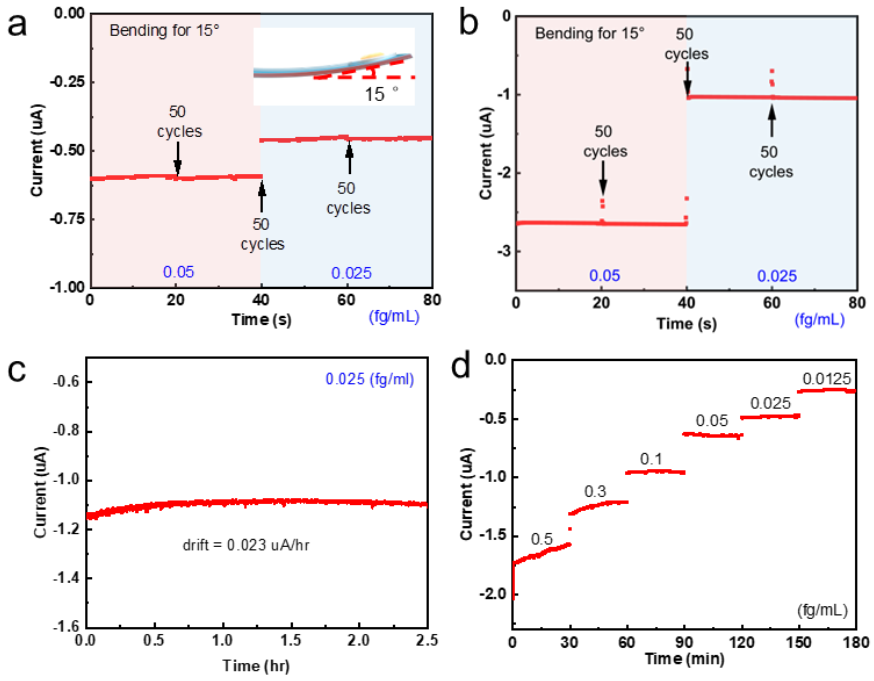

Figure 4.15 Mechanical and Long-Term Stability of virus biosensor. Real-time response of (a) SARS-CoV-2 and (b) H_3N_2 biosensor under 15 degrees bending. (c) Signal draft of virus biosensor. (d) Long-term stability.

In summary, the developed biosensor exhibits exceptional performance in terms of sensitivity, specificity, mechanical flexibility, and temporal stability. Its ability to detect multiple viral biomarkers with high fidelity, even in complex environments such as wastewater, demonstrates its strong potential for real-time epidemiological surveillance and early-stage outbreak warning systems.

4.3.4 System Integration and On-Site Validation in Sewage Samples

To enable real-time viral detection and remote data transmission, the dAu/PBASE/antibody-modified electrode was further integrated into a flexible, wearable, and portable biosensing patch. This system incorporates not only a highly selective biosensing interface but also a low-noise signal acquisition circuit, microcontroller processing unit, battery-powered supply, and Bluetooth communication

module, forming a complete sensing-processing-display feedback loop, shown in Figure 4.16.

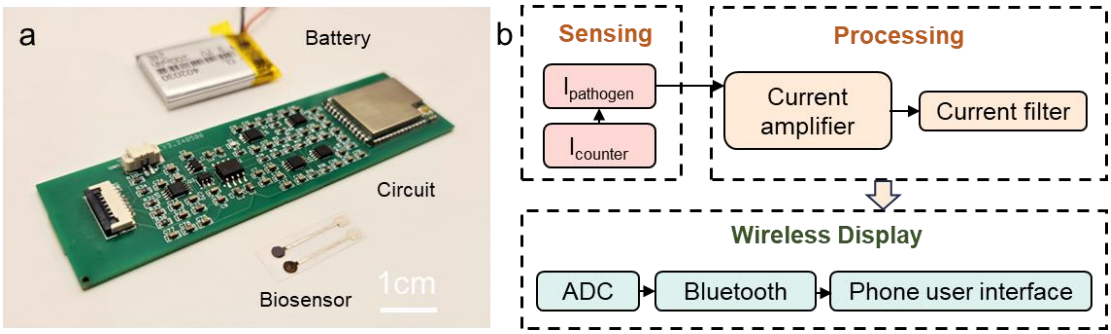

Figure 4.16 Virus biosensing system. (a) Photograph and (b) A system-level block diagram illustrating the integrated architecture of the biosensing platform.

For signal acquisition, a high-impedance potential measurement circuit was employed to accommodate the low-current nature of electrochemical signals. Amplification and filtering modules were incorporated to minimize background noise and enhance resolution. As shown in Figure 4.17, the signal acquisition pipeline includes impedance matching, analog signal conditioning, analog-to-digital conversion (ADC), and wireless transmission. The microcontroller executes real-time calibration, compensation, and data packaging, with the processed signal transmitted via Bluetooth to a mobile terminal. Each module is tightly coupled to ensure high-fidelity signal capture and rapid system response, supporting deployment in complex environmental settings. All components were mounted on a flexible printed circuit board (FPCB), which allows conformation to curved surfaces and deployment in diverse scenarios such as pipelines, floating platforms, or wearable configurations. This architecture facilitates modular operation, mobile data accessibility, and real-time visualization, which are essential for scalable environmental virus surveillance. Despite the demonstrated durability of the electrode interface, the independent long-term stability of the biological recognition elements remains a subject for further investigation. Future work will focus on evaluating the degradation kinetics of immobilized antibodies within complex environmental matrices, such as wastewater, to determine the sensor's effective operational lifespan.

Furthermore, the long-term stability of the hydrogel-based drug carriers will be systematically tested to ensure consistent release profiles and structural integrity over extended periods, which is essential for the reliability of the integrated biosensing and therapeutic platform.

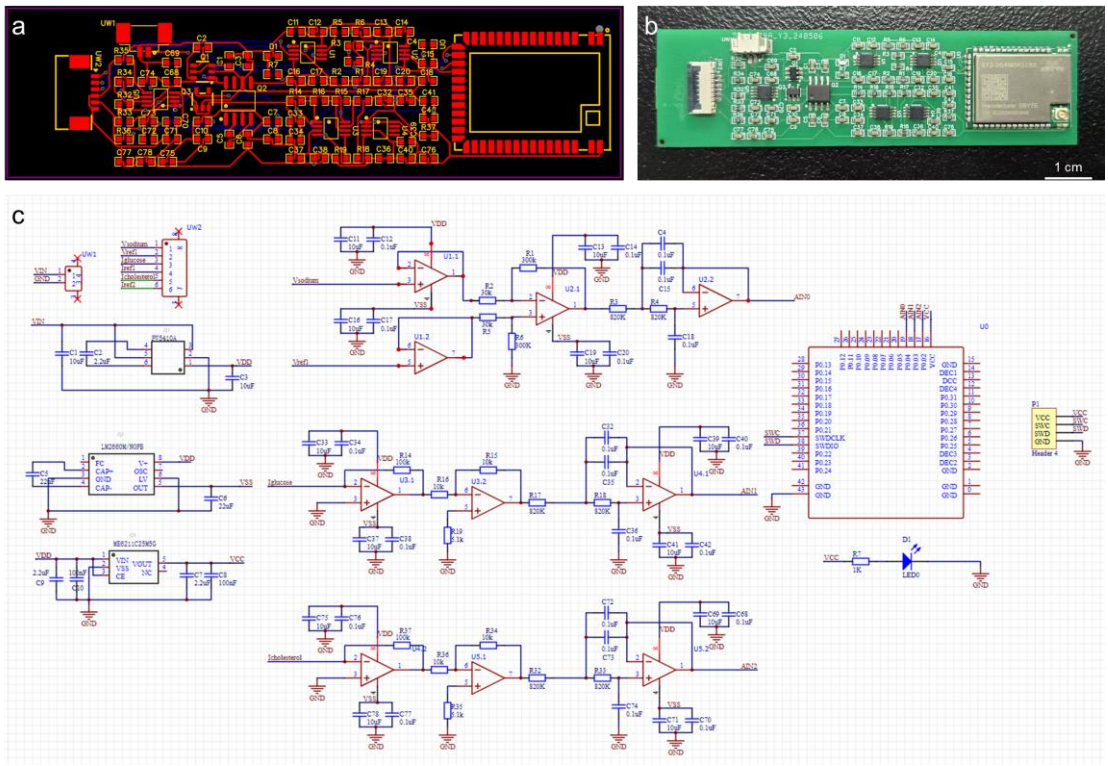

Figure 4.17 Circuit integration of the portable biosensing system. (a, b) Photograph and schematic diagram of the flexible circuit board used in the sensing patch. (c) Block diagram of the high-impedance electrochemical sensing and transmission circuit.

To assess practical performance, real municipal sewage samples collected in Hong Kong between April 11 and 15, 2024, were tested. During this timeframe, SARS-CoV-2 remained within a detectable range, while H_3N_2 levels declined due to seasonal warming, and no qualified samples were available for H_3N_2 analysis. As a reference standard, quantitative reverse transcription qRT-PCR was performed to obtain cycle threshold (Ct) values for each sewage sample (Figure 4.18). Notably, while qRT-PCR requires thermal pretreatment (60 °C for 10 minutes), the biosensor enabled direct detection of viral targets in raw, unprocessed sewage samples. The sensing results were

wirelessly transmitted to a smartphone interface, allowing real-time mobile visualization and interpretation.

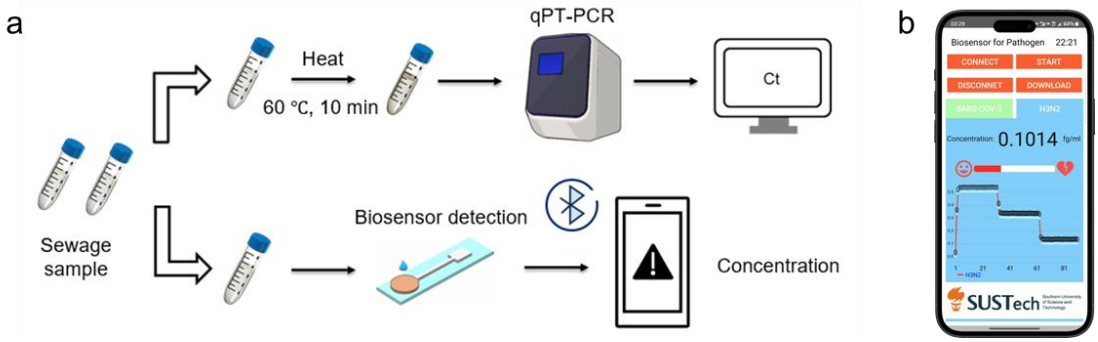

Figure 4.18 Comparison of detection workflows for virus in sewage. (a) Diagram illustrating the qRT-PCR and biosensor-based workflows. (b) Custom-developed mobile app interface for real-time signal display.

As shown in Figure 4.19, the biosensor yielded clear electrochemical responses for samples with Ct values of 31.03, 31.70, 32.66, and 38.71. Higher viral concentrations (Ct < 35) resulted in stronger current signals, whereas Ct values > 35 produced negligible output, indicating concentrations below the sensor's detection limit. Correlation analysis confirmed a strong inverse relationship between the sensor's output current and qRT-PCR Ct values, demonstrating the sensor's capability to semi-quantitatively estimate viral load.

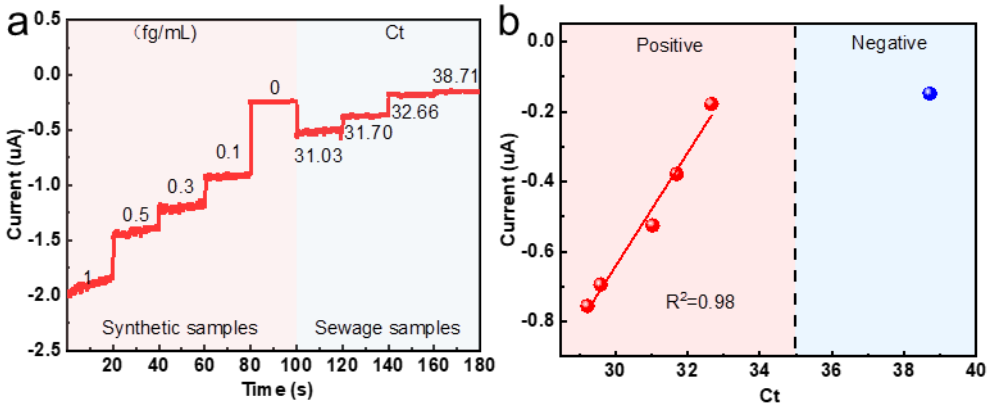

Figure 4.19 Real-time performance of the biosensor in sewage detection. (a) Real-time electrochemical responses of the biosensor to sewage samples with varying Ct values. (b) Correlation between biosensor output current and Ct values from qRT-PCR.

Additionally, Figure 4.20 presents a performance benchmark comparing this system's detection limit and response time against previously reported SARS-CoV-2 detection platforms[213-217]. The proposed system achieves an ultra-low detection limit of < 0.5 fg/mL and rapid response, outperforming many state-of-the-art biosensing strategies. This highlights the strong potential of the dAu/PBASE/antibody-functionalized biosensor for sensitive and rapid pathogen detection in complex matrices.

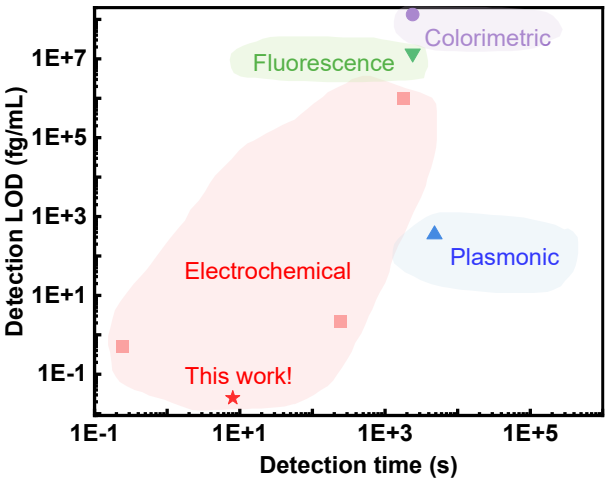

Figure 4.20 Performance comparison of various SARS-CoV-2 wastewater detection methods, highlighting detection limit and response time advantages of this work.

In conclusion, the fully integrated biosensing system successfully enables real-time and wireless monitoring of SARS-CoV-2 and H_3N_2 in untreated sewage. Its strong correlation with qRT-PCR, combined with advantages in modularity, miniaturization, cost-effectiveness, and adaptability, provides a powerful platform for urban public health surveillance and WBE.

4.3.5 Conclusion

This section systematically examined the virus recognition mechanism, surface functionalization, electrochemical behavior, and real-world integration of the electrochemical biosensor based on dAu electrodes. The functionalization process was validated using Raman spectroscopy, CV, and EIS, confirming the successful immobilization of antibodies on the dAu surface and the resulting modulation of interfacial electron transport. The dendritic architecture with high surface area significantly enhanced the electroactive interface, enabling efficient signal amplification.

The biosensor demonstrated outstanding analytical performance in detecting SARS-CoV-2 and H_3N_2 viral proteins, with an ultra-low LOD of 0.025 fg/mL and excellent reproducibility. Standard curve calibration and real-time response measurements revealed a clear, logarithmic current-concentration relationship, even in the presence of typical sewage interferents. These findings validate the biosensor's excellent specificity and operational robustness when applied to complex sample matrices. Moreover, the device exhibited strong mechanical durability and signal stability under repeated bending and continuous operation, validating its long-term reliability for field deployment.

The biosensor was further integrated into a flexible and wearable circuit system comprising signal amplification, a microcontroller unit, Bluetooth communication, and smartphone-based visualization. This platform successfully enabled real-time and wireless detection of SARS-CoV-2 in untreated municipal sewage without requiring sample preprocessing. In field tests, the biosensor's output currents showed strong correlation with qRT-PCR-derived cycle threshold (Ct) values, supporting its potential for semi-quantitative viral load estimation.

In conclusion, the developed dAu-based biosensor achieves synergistic advantages in sensitivity, selectivity, operational stability, and system integration. Its demonstrated

capability for direct, real-time virus monitoring in complex wastewater environments highlights its promising applicability for public health surveillance and early epidemic warning systems.

CHAPTER 5 WASHABLE TEXTILE BIOSENSORS ENABLED BY NANOSTRUCTURED OXIDES WITH FAST ION DIFFUSION

Textile-based biosensors have garnered growing interest for wearable health monitoring applications owing to their superior breathability, close skin conformity, and outstanding mechanical flexibility. However, achieving both high sensing performance and reliable washing durability remains a substantial challenge in the development of textile-based biosensors. Traditional approaches relying on bulky encapsulation can improve device robustness but inevitably compromise ion accessibility and comfort, which is especially problematic for ion-selective sensors that require direct contact with sweat. In this chapter, we propose a rational interface engineering strategy utilizing structurally tailored β-Bi_2O_3nanoflakes, which are electrochemically deposited onto ISMs to impart outstanding water resistance, fast ion transport, and enhanced membrane adhesion. The constructed sensing system integrates a multilayer architecture on Cu-coated PET textile, comprising a dendritic gold conductive layer, a PEDOT:PSS transducing layer, and an ISM functionalized with β-Bi_2O_3 nanoflakes. The resulting sensors exhibit excellent electrochemical performance for detecting Na^+, K^+, and H^+ ions, with a Na^+ sensitivity of 59 mV/dec and minimal signal drift of 2.5 mV/h. Notably, the sensors retain over 90% of their initial performance after 20 washing cycles and over 70% after 50 cycles, demonstrating superior washability and operational stability compared to unmodified counterparts. In addition, a fully integrated wearable wristband system was developed, incorporating Bluetooth-enabled wireless transmission and a mobile application to enable real-time data visualization. The device offers excellent skin compatibility and comfort during prolonged use, and the monitored sweat Na^+ concentrations show strong agreement with values obtained via inductively coupled plasma mass spectrometry (ICP-MS). Collectively, this work represents the first demonstration of using fast ion-conducting β-Bi_2O_3 nanoflakes as a multifunctional interface layer to enhance both the performance and washability of textile-based ion-selective sensors. This strategy effectively addresses the conventional trade-off between sensitivity and durability, and provides a scalable, engineering-oriented pathway toward

next-generation E-textile platforms for personalized health monitoring and biomedical applications.

5.1 Introduction:

With the fast advancement of personalized healthcare technologies, wearable electronics are increasingly moving toward greater flexibility, miniaturization, and daily usability. Among them, textile-based electronics (E-textiles) have emerged as a promising platform for sweat analysis, body temperature monitoring, and electrophysiological signal acquisition, owing to their intrinsic breathability, mechanical flexibility, and skin-conformable characteristics [218-220]. Particularly in continuous and noninvasive monitoring scenarios, textile biosensors enable intimate contact with sweat glands and efficient sample acquisition, making them ideal candidates for real-time, on-body chemical sensing [220,221].

Despite these advantages, the practical implementation of textile-based sweat sensors is hindered by a critical barrier: the lack of long-term reusability and washing durability [222-224]. Most conventional devices suffer from rapid degradation of functional layers, including ISMs, conductive polymers, and transducing interfaces, when exposed to sweat, humidity, and mechanical agitation during laundering [225,226]. Existing solutions often involve full encapsulation to enhance device robustness [227,228]. However, such strategies inevitably compromise ion accessibility at the sensor interface, resulting in reduced signal transduction efficiency, delayed response times, and loss of selectivity [229-231]. Moreover, encapsulation materials often diminish the breathability and softness of textile substrates, leading to reduced wearability and even skin irritation [232].

These challenges are particularly acute for ISEs, whose sensing mechanisms rely on selective ion exchange at the membrane-electrolyte interface. To operate effectively, ISEs need to maintain direct, stable contact with sweat. Therefore, the central technical challenge lies in enhancing the washability and structural integrity of the sensor without sacrificing ionic contact or electrochemical performance.

To address this challenge, interface engineering using functional materials has emerged as a promising strategy. An ideal interfacial layer should fulfill three key requirements: high chemical stability and water resistance to withstand washing and long-term exposure to humid environments fast ion conduction to maintain high sensing sensitivity; and optimized morphology and interfacial adhesion to prevent delamination and preserve membrane integrity [233]. Among various candidate materials, β-phase bismuth oxide (β-Bi_2O_3) has attracted attention for its unique tunnel-like crystal structure composed of BiO_4 tetrahedra, which form interconnected ion pathways that facilitate efficient ion transport [234-237]. In addition, β-Bi_2O_3 exhibits intrinsic moisture stability and chemical inertness, making it a compelling candidate as a multifunctional interfacial layer in wearable electrochemical sensors [238-241].

In this chapter, we propose a β-Bi_2O_3 nanoflake-enabled interfacial engineering strategy to construct a washable textile-based ion-selective sensor system. By electrochemically depositing β-Bi_2O_3 nanoflakes onto the top surface of the ISM, we simultaneously enhance the device's water resistance, ionic conductivity, and mechanical adhesion. Unlike conventional encapsulation methods, this approach does not hinder ionic diffusion, thereby preserving the electrochemical performance of the sensor. Furthermore, we integrate the functional sensors into a wireless textile wristband capable of Bluetooth communication and mobile visualization, demonstrating real-time sodium ion tracking in sweat during physical activity. This platform exhibits excellent wearability, skin compatibility, and long-term operational stability.

This chapter provides a comprehensive overview of the material design, sensor fabrication, washing durability evaluation, and system-level integration of the β-Bi_2O_3-functionalized wearable sweat sensing platform. The findings not only validate the multifunctional role of β-Bi_2O_3 nanoflakes in improving sensor robustness and reliability but also offer an engineering-oriented pathway for the development of next-generation washable and reconfigurable electronic textiles.

5.2 Experiment

5.2.1 Fabrication Process of Textile Electrode

The textile substrates were first cleaned through a sequential ultrasonic treatment using acetone, isopropanol, and deionized water, each for 15 minutes. They were then immersed for one minute in an ethanol-based solution containing 2.0 g L^{-1} DMPA, 16.0 g L^{-1} NMBA, and 30.0 mL L^{-1} METAC. After immersion, the samples were irradiated under a UVA lamp (80.0 mW cm^{-2}) for one minute and rinsed with water for an additional minute. Subsequently, the functionalized textiles were treated with a 3.2 g L^{-1} $(NH_4)_2PdCl_4$ aqueous solution for one minute, followed by another water rinse. Electroless copper plating was carried out using a mixture of two solutions: Solution A, containing $CuSO_4 \cdot 5H_2O$ (52 g L^{-1}), NaOH (48 g L^{-1}), and $KNaC_4H_4O_6 \cdot 4H_2O$ (117 g L^{-1}); and Solution B, which consisted of formaldehyde (37%) diluted to 9.5 mL L^{-1}. The catalyzed textiles were coated by immersion in the combined plating solution for 120 minutes.

The metallic textile was first coated with a uniform layer of NR9-1500p photoresist (Futurrex, USA) via dip-coating. This was followed by a soft-bake process at 120 °C for 5 minutes to solidify the photoresist layer. The sample was then exposed to double-sided UV irradiation for 1 minute through a photomask and subsequently baked again at 120 °C for 3 minutes to promote cross-linking. The development step was carried out using RD6 developer (Futurrex, USA) to remove unexposed photoresist from non-patterned regions. Etching of the exposed metal areas was performed with a 1 M $FeCl_3$ solution. Finally, the remaining photoresist was stripped using acetone, and the patterned textiles were thoroughly rinsed with alcohol and deionized water before being dried in ambient conditions.

5.2.2 Fabrication of Ion-Selective Textile Sensors

Textile-based sodium ion sensors were fabricated by initially electrodepositing nanodendritic gold onto metallic copper electrodes from an aqueous solution containing

50 mM $HAuCl_4$ and 50 mM HCl. A periodic voltage waveform with an amplitude of −2 V, a frequency of 50 Hz, and a 50% duty cycle was applied over 9000 cycles to achieve deposition. Subsequently, 3 µL of PEDOT:PSS (PH1000) was drop-cast onto the working electrode to function as an ion-to-electron transducer. The ion-selective membrane (ISM) cocktail was formulated with the following composition: 1 wt% sodium ionophore X, 0.55 wt% Na-TFPB, 33 wt% PVC, and 65.45 wt% DOS. This mixture (100 mg) was dissolved in 660 µL of tetrahydrofuran, and 6 µL of the resulting solution was drop-cast onto the PEDOT:PSS/Au-modified working electrode. For the reference electrode, 10 µL of a polyvinyl butyral (PVB)-based solution--prepared by dissolving 79.1 mg PVB and 50 mg NaCl in 1 mL methanol--was applied onto an Ag/AgCl electrode and allowed to dry overnight.

The textile-based potassium ion sensor was constructed by first synthesizing nanodendritic gold on copper substrates via electrochemical deposition. This process utilized an electrolyte containing 50 mM $HAuCl_4$ and 50 mM HCl, under a periodic potential waveform with an amplitude of −2 V, frequency of 50 Hz, and 50% duty cycle applied for 9000 cycles. A 3 µL aliquot of PEDOT:PSS (PH1000) was then drop-cast onto the working electrode to serve as an ion-to-electron transduction layer. The ion-selective membrane was formulated with the following composition: 2 wt% valinomycin, 0.5 wt% Na-TPB, 32.7 wt% PVC, and 64.7 wt% DOS. A total of 100 mg of this mixture was dissolved in 350 µL of tetrahydrofuran, and 6 µL of the resulting solution was applied over the PEDOT:PSS/Au surface. For the reference electrode, 10 µL of a reference solution-comprising 79.1 mg PVB and 50 mg NaCl dissolved in 1 mL methanol-was cast onto an Ag/AgCl electrode and dried overnight.

The textile-based pH sensor was fabricated through electrochemical synthesis of gold dendritic nanostructures from an aqueous solution of 50 mM $HAuCl_4$ and 50 mM HCl. Deposition was carried out by applying a periodic voltage waveform with an amplitude of -2 V, a frequency of 50 Hz, and a duty cycle of 50% over 9000 cycles. Polyaniline (PANI) was subsequently electrodeposited using a waveform with an amplitude of 0.9 V, frequency of 1 Hz, and duty cycle of 10% for 1200 cycles in a freshly prepared

electrolyte containing 0.1 M distilled aniline in 1 M HCl. For the reference electrode, a solution of polyvinyl butyral (PVB) was prepared by dissolving 79.1 mg PVB and 50 mg NaCl in 1 mL methanol. A volume of 10 μL of this reference membrane cocktail was cast onto an Ag/AgCl electrode and allowed to dry overnight.

5.2.3 Functionalization of Sensors with Oxide Nanomaterials

The β-Bi_2O_3 nanoflakes were functionalized onto the sensor surface via an electrodeposition process. A bismuth plating solution was prepared immediately before use by combining 10 mL of 0.1 M acetate buffer saline (ABS) containing 50 mM NaCl with 10 mL of a bismuth standard solution (1000 μg mL^{-1} in 1.5 M HNO_3), under continuous stirring. Electrodeposition was performed at a constant potential of −0.8 V for 240 seconds, which was identified as the optimal duration based on comparative performance evaluations across varying plating times. Prior to electrochemical measurements, the modified sensor was conditioned in 40 mM NaCl for 4 hours to enhance operational stability and reduce potential drift, thereby ensuring reliability during prolonged sensing applications. A similar electrodeposition protocol was applied for magnesium oxide and manganese oxide functionalization, with adjustments to the applied voltage.

α-Bi_2O_3 planar films were deposited by direct current magnetron sputtering (JDP350 system) at room temperature within an argon-oxygen mixed atmosphere. A high-purity bismuth target (99.9%) was used as the source material. The deposition chamber was initially evacuated to a base pressure of 10^{-3} Pa. During sputtering, a gas mixture of argon and oxygen was introduced at a total flow rate of 6.1 sccm, with an O_2 to Ar ratio of 20:1, resulting in a working pressure of 0.5 Pa. The process was carried out at a constant power of 20 W, yielding a film thickness of approximately 1000 Å over a deposition time of 527 seconds, corresponding to a deposition rate of 1.9 Å/s.

Al_2O_3 planar films were deposited via radio frequency magnetron sputtering in a pure argon atmosphere using a JDP350 system at room temperature. A high-purity alumina

target (99.9%) served as the source material. Prior to deposition, the chamber was evacuated to a base pressure of 10^{-3} Pa. During the process, argon was introduced at a flow rate of 6.1 sccm, maintaining a deposition pressure of 0.5 Pa. Sputtering was conducted at a power of 80 W and a frequency of 5.26 MHz. The resulting film thickness was approximately 1000 Å, achieved over a deposition time of 10,000 seconds, corresponding to a deposition rate of 0.1 Å/s.

MnO_2 nanoflakes were functionalized onto the sensor surface through anodic electrodeposition from a specially formulated electrolyte. The deposition solution was prepared by dissolving 0.01 M manganese acetate ($MnAc_2$) and 0.02 M ammonium acetate (NH_4Ac) in a solvent system comprising 90% deionized water and 10% dimethyl sulfoxide (DMSO). Electrodeposition was carried out at a constant current density of 0.5 mA cm^{-2} for a duration of 10 minutes.

MgO was functionalized on the sensor surface via an electrodeposition approach. The plating bath consisted of a 0.1 M $MgSO_4$ aqueous solution. A constant potential of -1.5 V was applied for 300 seconds to facilitate the deposition process.

5.2.4 Characterization

The morphological characteristics of the samples were examined using scanning electron microscopy (SEM; Hitachi TM3000 and ZEISS Gemini 300), polarizing optical microscopy (Nikon), and transmission electron microscopy (TEM; Thermo Scientific Talos F200X G2). Crystalline structures were analyzed by X-ray diffraction (XRD; Rigaku SmartLab) and surface chemical states were probed via XPS (ULVAC-PHI 5000 Versaprobe Ⅲ). All electrochemical deposition and sensor performance tests were conducted using either a CHI 760e or an Ivium Soft 4 electrochemical workstation. Concentrations of biomarkers in sweat samples were further validated by inductively coupled plasma mass spectrometry (ICP-MS; Thermo Scientific Q Exactive). Moisture permeability was evaluated according to the standard test method E96/E96M-13 using the cup method, wherein the moisture transmission rate ($g \cdot m^{-2} \cdot day^{-1}$) was calculated

based on water vapor loss through the specimen-sealed cup over a 20-day period. Both air permeability and moisture transfer tests were conducted under controlled conditions of 22 °C and 63% relative humidity. Mechanical properties of the sensor and copper-patterned textiles were assessed with an Instron 5599 universal testing system. Electrical performance under strain was monitored using a Keithley 2400 Sourcemeter integrated with a computer-controlled linear actuator. washing durability was evaluated using a magnetic stirring setup, wherein the sensor was partially immersed in deionized water and subjected to agitation at 1500 rpm for 30 seconds per cycle.

Calculation on the baseline drift: Baseline drift describes the gradual deviation of a measurement signal from its original reference level over time. To evaluate this phenomenon, it is quantified using the following equation.

$$\Delta V/S = \frac{V_{after\ washing} - V_{before\ washing}}{S} \quad topology \tag{5.1}$$

Here, S denotes the initial sensitivity of the sensor. This equation allows for the precise quantification of baseline drift within the established methodological framework.

Textile water vapor permeability *test*: The water vapor permeability of the fabricated textile was evaluated using the cup method following the ASTM E96 (Procedure B) standard (ASTM E96-00, 2000). Each sample was securely mounted over a cup containing distilled water, and evaporative mass loss was measured over a period of 20 days. An empty cup served as the reference for normalization. The initial mass of each assembly was recorded using an analytical balance with a resolution of 0.01 g, and repeated measurements were performed to quantify the cumulative vapor transmission through the textile. Water vapor permeability (WVP) can be calculated using Eq. (5.2):

$$WVP = \frac{(24 \times M)}{A \times T} \frac{g}{m^2 h} \tag{5.2}$$

M corresponds to the mass loss (in grams), T indicates the time interval (in hours), and *A* represents the internal area of the cup (in square meters). The value of *A* was calculated using Equation (5.3), where *d* denotes the internal diameter of the cup in millimeters.

$$A = \frac{(\pi d^2)10^{-6}}{4} \tag{5.3}$$

On-body sweat monitoring: All experiments were performed in accordance with institutional ethical regulations (Ethics Guidelines for Research Involving Human Subjects or Human Tissue, Southern University of Science and Technology, SUSTech Institutional Review Board, Approval No. 20200037). On-body sweat analysis was conducted with a cohort of 5 healthy volunteers (3 males and 2 females, aged 24-26 years). Participants were selected based on stable physical conditions, with no history of metabolic, cardiovascular, or dermatological diseases. These variations in gender and physical state were explicitly recorded to monitor their potential influence on sweat composition, ensuring the sensor's robustness across different individuals. Real-time monitoring was achieved using a wearable wristband interfaced wirelessly via Bluetooth with a smartphone application. Participants wore sensor-equipped wristband during a 20-minute warm-up cycling exercise followed by 20 minutes of stationary cycling. Throughout the activity, the application automatically initiated data acquisition, with decoded sweat analysis results displayed in real time on the phone interface. Simultaneously, sweat was sampled at 5-minute intervals for subsequent validation using inductively coupled plasma mass spectrometry (ICP-MS).

5.3 Results and Discussion

5.3.1 Structural Characteristics and Fast Ion Conducting Mechanism of β-Bi_2O_3 Nanoflakes

To ensure stable performance of wearable textile-based ion sensors under dynamic conditions such as sweat exposure and repeated washing, the interfacial materials need to simultaneously possess high electrochemical responsiveness, strong mechanical adhesion, and excellent water resistance. Conventional polymer-based interfaces are prone to swelling, delamination, or degradation of electrochemical activity during washing cycles. Therefore, it is critical to introduce inorganic nanomaterials with both structural robustness and fast ion-conducting properties to enhance the interface. In this

context, β-Bi_2O_3 has garnered considerable interest as a functional interfacial material due to its distinctive crystal structure and outstanding ionic conductivity.

In this work, nanostructured β-Bi_2O_3 was directly electrodeposited onto the ISM layer on textile substrates, and the crystal phase of the resulting material was effectively tuned by controlling the deposition potential [242-244]. It was found that a deposition potential of +1.2 V (vs. Ag/AgCl) yielded phase-pure, well-crystallized β-Bi_2O_{33} nanoflakes with uniform surface coverage, whereas lower potentials such as −0.4 V predominantly led to the formation of α-Bi_2O_3 or mixed-phase products including meta-Bi [245-247]. This phase transition behavior is attributed to the potential-dependent redox kinetics of Bi^{3+} ions, where high positive potentials facilitate complete oxidation and promote the formation of the thermodynamically stable β phase, while lower potentials lead to incomplete oxidation or metastable intermediate phases that deviate from the desired crystal structure [248-250].

SEM was used to observe the morphology of the deposited β-Bi_2O_{33} nanoflakes. The SEM images (Figure 5.1) show that the β-Bi_2O_3 nanoflakes are evenly distributed on the ISM, exhibiting excellent morphological stability. The diameter of the nanoflakes is approximately 4.14 μm, and their even distribution provides a high surface area for ion contact, which enhances ion diffusion within the membrane. The good dispersion of the nanoflakes also ensures strong adhesion to the electrode surface, maintaining sensor stability and the integrity of the membrane during washing cycles.

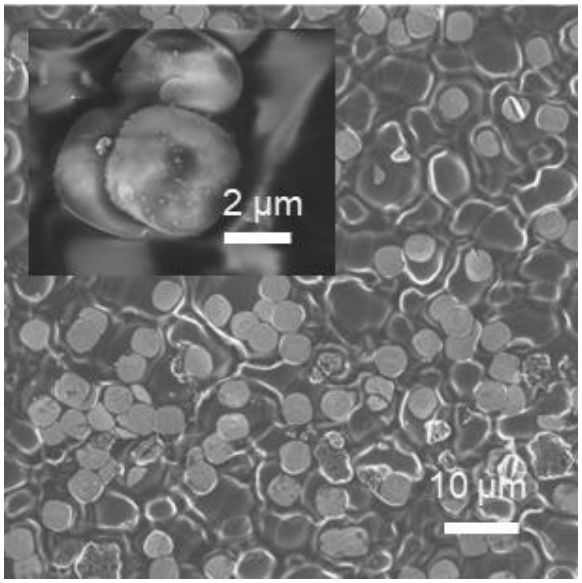

Figure 5.1 SEM images reveal the surface morphology of β-Bi_2O_3 nanoflakes, exhibiting a flake-like structure with an average diameter of approximately 4.14 μm.

XRD analysis was initially performed to verify the crystal structure of the as-deposited materials. As shown in Figure 5.2a, the sample obtained under +1.2 V displayed sharp and distinct diffraction peaks at 27.9°, 32.8°, and 46.5°, corresponding to the (201), (222), and (400) planes of tetragonal β-Bi_2O_3, in good agreement with the standard PDF#78-1793. This confirmed the successful formation of the desired β phase. XPS further verified the chemical composition and oxidation state. As illustrated in Figure 5.2b, the Bi 4f spectra exhibited two characteristic peaks at 159.3 eV and 164.6 eV, assigned to Bi $4f_{7/2}$ and Bi $4f_{5/2}$, respectively. No signals corresponding to metallic Bi or lower oxidation states were observed, indicating that the Bi element remained in the +3 oxidation state throughout the deposition process. The combined XRD and XPS results confirmed the high crystallinity and chemical stability of the synthesized β-Bi_2O_3 nanoflakes.

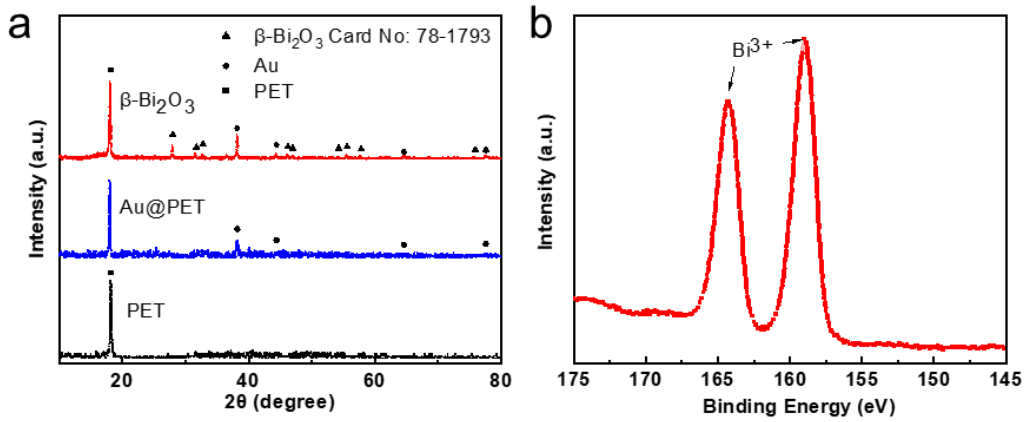

Figure 5.2 Crystallographic and surface chemical characterization of β-Bi_2O_3 deposited on Au@PET substrate. (a) XRD spectrum of the β-Bi_2O_3 deposited on Au@PET. (b)Bi 4f XPS spectra of Bi_2O_3, with discernible peaks at 159.30 and 164.62 eV corresponding to Bi^{3+} within the Bi_2O_3 component.

To further elucidate the microstructural features, transmission electron microscopy (TEM) and high-resolution TEM (HRTEM) analyses were performed. As shown in Figure 5.3a, the β-Bi_2O_3 nanoflakes exhibited a uniform sheet-like morphology with well-defined edges and appropriate thickness, forming a conformal coating on the substrate. The HRTEM image in Figure 5.3f reveals distinct lattice fringes with an interplanar spacing of 0.32 nm, corresponding to the (201) plane of β-Bi_2O_3, in agreement with the XRD data [251-254]. Selected area electron diffraction (SAED) patterns showed clear concentric rings, indicative of a polycrystalline structure with high orientation uniformity.

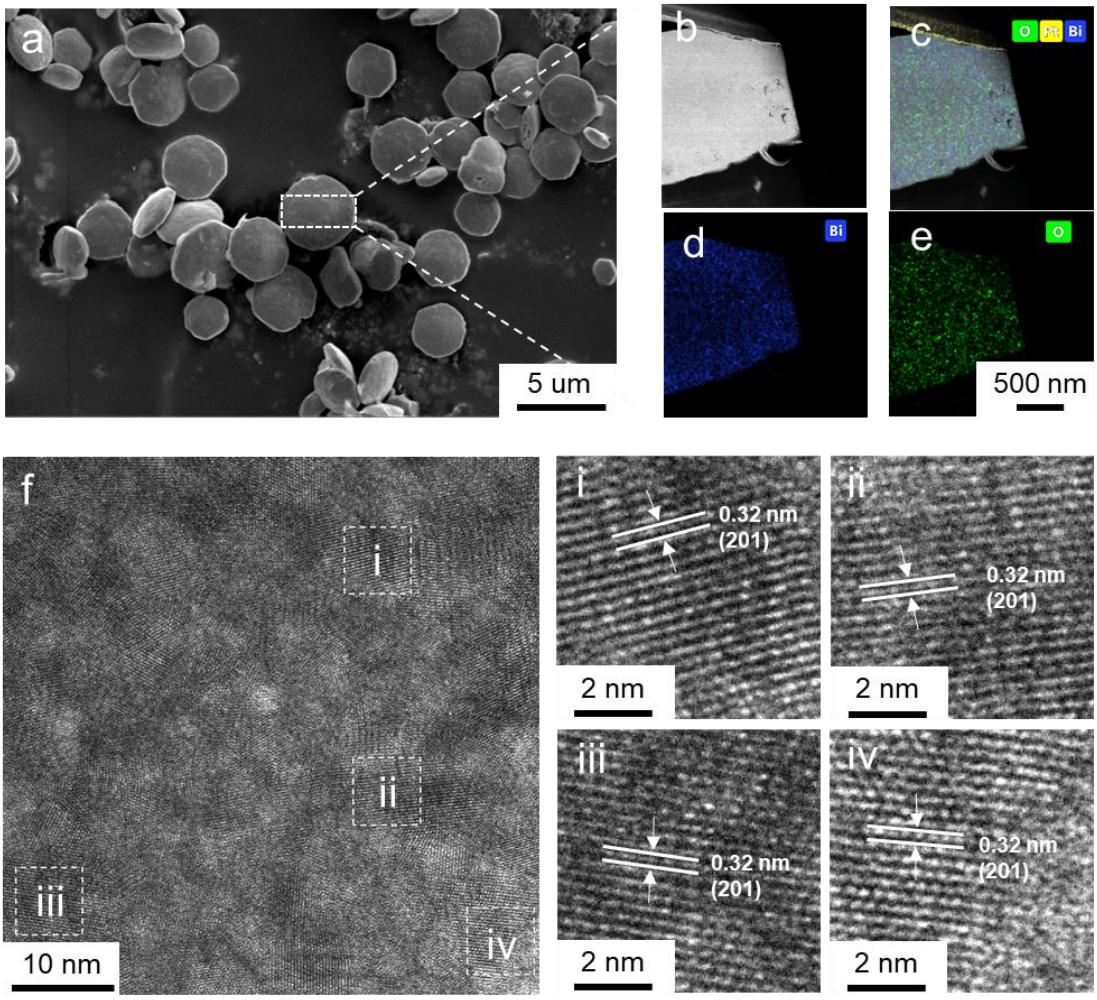

Figure 5.3 TEM characterization of structure and chemistry of β-Bi_2O_3. (a) The TEM image of β-Bi_2O_3 and selective area for focus ion beam (FIB) TEM preparation. (b-e) FIB-TEM image and Energy-dispersive X-ray spectroscopy (EDS) element mappings of O, Pt and Bi taken from a β-Bi_2O_3 nanoflake. (f) High-resolution TEM image showing the atomic structure and the existence of the β-Bi_2O_3 phase.

To further confirm the effect of deposition potential on phase formation, control samples deposited at −0.4 V were also characterized. As shown in the TEM image of the α/meta-Bi_2O_3 sample (Figure 5.4), the structure exhibited irregular morphology and a lack of long-range crystalline order, consistent with a mixed-phase composition of α-Bi_2O_3 and meta-Bi. This contrast further supports the phase-pure nature of the β-Bi_2O_{33} nanoflakes obtained at +1.2 V. These observations collectively demonstrate the

excellent structural integrity and crystallographic order of the β-Bi_2O_3 nanoflakes, which are essential for ensuring stable ion transport and interfacial performance in electrochemical sensing applications.

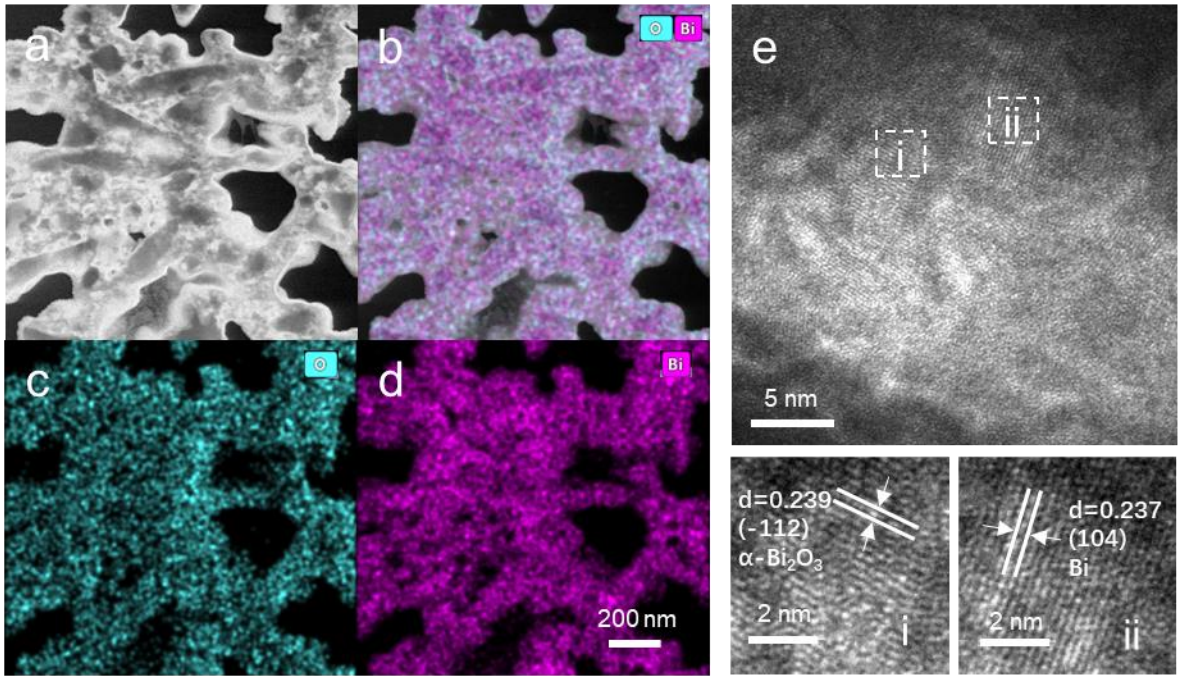

Figure 5.4 TEM characterization of structure and chemistry of Bi_2O_3. (a-d) TEM image and EDS element mappings of O Bi taken from Bi_2O_3. (e) High-resolution TEM image showing the atomic structure and the coexistence of metal-Bi and α-Bi_2O_3 phase.

From a crystallographic perspective, β-Bi_2O_3 crystallizes in a tetragonal system with a tunnel-type lattice framework composed of corner-sharing BiO_4 tetrahedra. This unique structure forms continuous three-dimensional ionic pathways, enabling efficient transport of small cations such as Na^+, K^+, and H^+. The open channels and low migration barriers make β-Bi_2O_3 a typical solid-state fast ion conductor, as shown in Figure 5.5. In contrast, α-Bi_2O_3 adopts a monoclinic structure with denser and more tortuous ionic migration paths, while meta-Bi is an amorphous or metastable phase characterized by disordered lattices and defect states, which can increase interfacial polarization and reduce conductivity.

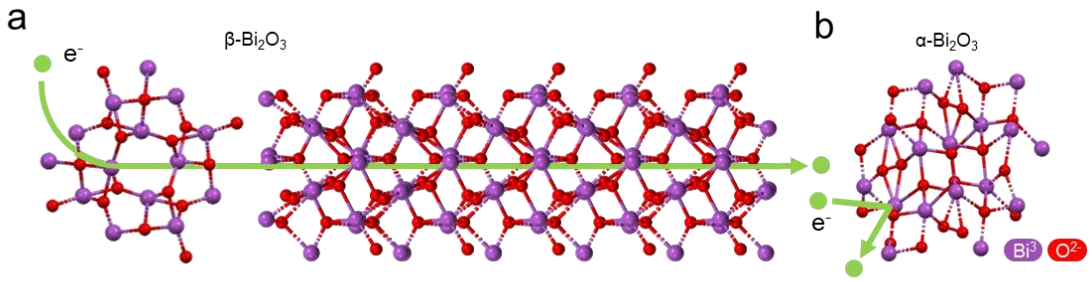

Figure 5.5 Comparison of ion transport-related molecular structures in bismuth oxide polymorphs. (a) Molecular structure of β-Bi_2O_3, highlighting its tetragonal unit cell with open ion diffusion channels. (b) Molecular structure of α-Bi_2O_3, illustrating its monoclinic crystal framework with limited ion mobility.

EIS was employed to assess the interfacial charge transfer properties of the sensing electrodes with and without β-Bi_2O_3 modification (Figure 5.6a). The Nyquist plots revealed a significantly reduced semicircular diameter for the β-Bi_2O_3-modified electrode, indicating a markedly lower charge transfer resistance (R_{ct}). This observed reduction indicates that the nanoflake-modified interface promotes more efficient electron and ion transport across the membrane-substrate junction, thereby improving signal transduction and reducing energy losses during the sensing process. In parallel, open-circuit voltage responses of Na^+ sensors with and without β-Bi_2O_3 modification were compared under different Na^+ concentrations (Figure 5.6b). Although both sensors displayed comparable sensitivity, reflected by similar slope values of the voltage-concentration calibration curves, the β-Bi_2O_3-modified sensor exhibited notably higher output voltages at equivalent Na^+ concentrations. This enhancement in signal amplitude, despite identical ISM characteristics, further corroborates the impedance findings-demonstrating that reduced interfacial resistance enables a stronger potential difference to develop across the sensor under the same ion flux.

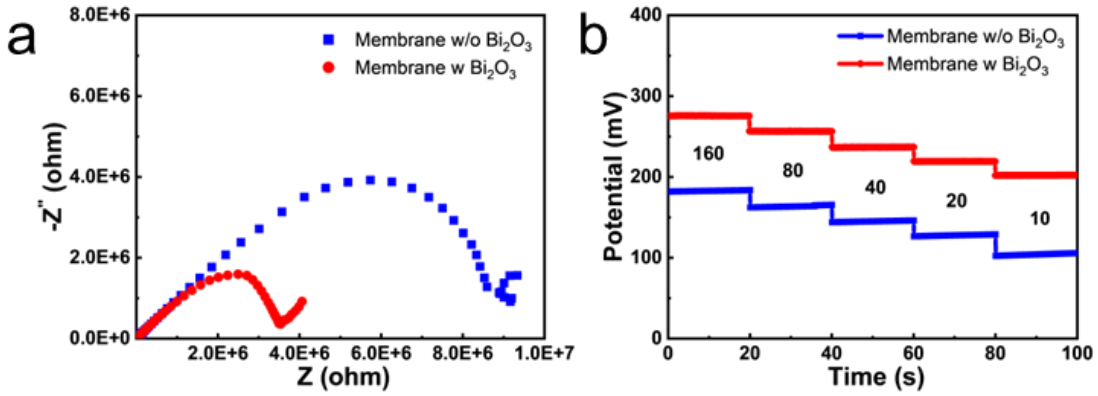

Figure 5.6 Electrochemical performance comparison of ion-selective sensors with and without β-Bi_2O_3 modification. (a) EIS of membrane with and without β-Bi_2O_3. (b) Comparison of Na^+ sensor output voltage at different concentrations, demonstrating enhanced signal amplitude with β-Bi_2O_3 nanoflakes.

Furthermore, the unique structure of β-Bi_2O_3 provides it with excellent stability in humid and high-temperature environments. This structure enables β-Bi_2O_3 to resist water-induced degradation, thus maintaining the long-term stability of the sensors. Conventional protective materials, such as metal films or polymers, often sacrifice certain properties like permeability and flexibility, but the fast ion conductivity of β-Bi_2O_3 does not significantly increase electrode impedance, allowing for enhanced sensor stability without compromising performance.

Another key factor in selecting β-Bi_2O_3 is its chemical stability. Many materials tend to undergo chemical reactions or degradation during washing, leading to performance degradation of the sensors. However, β-Bi_2O_3 not only exhibits high chemical stability but also resists oxidation in moist environments, preventing the failure of sensors due to material degradation. Thus, β-Bi_2O_3 provides a protective layer for sensors while ensuring long-term stability during use.

In summary, β-Bi_2O_3 nanoflakes synthesized via controlled electrodeposition exhibit a well-defined tunnel crystal structure, high crystallinity, and stable surface chemistry.

Their morphology ensures uniform and adhesive coverage on flexible substrates, while their intrinsic fast ion conductivity facilitates efficient signal transduction. These characteristics make β-Bi_2O_3 an ideal interfacial layer for constructing high-performance, washable, and wearable ion-selective sensors, providing a robust material foundation for the integrated textile biosensing platform developed in this work.

5.3.2 Comparative Studies on Material Structures and Validation of the Unique Role of β-Bi_2O_3

To systematically elucidate the material-specific and structure-dependent functions of β-Bi_2O_3 nanoflakes in enhancing sensor reliability, a series of comparative experiments were conducted with various metal oxide materials of distinct morphologies and device configurations (Figure 5.7a). These oxides, including MnO_2, MgO, α-Bi_2O_3, and Al_2O_3, were deposited onto the ISM through either electrochemical or physical vapor deposition processes. Their structural characteristics and influence on sensor performance were comprehensively analyzed in relation to β-Bi_2O_3 nanoflakes.

As shown in Figure 5.7b, the SEM images revealed that only β-Bi_2O_3 forms vertically oriented nanoflake arrays with porous and hierarchical structures, offering a favorable ion transport interface and robust surface anchoring. In contrast, MnO_2 presents as aggregated particulate blocks, while MgO, α-Bi_2O_3, and Al_2O_3 are deposited as flat, smooth thin films lacking vertical structuring. These morphologies indicate that the latter three oxides fail to form continuous, moisture-resistant, or ion-conducting networks, which are essential for maintaining sensor stability and performance.

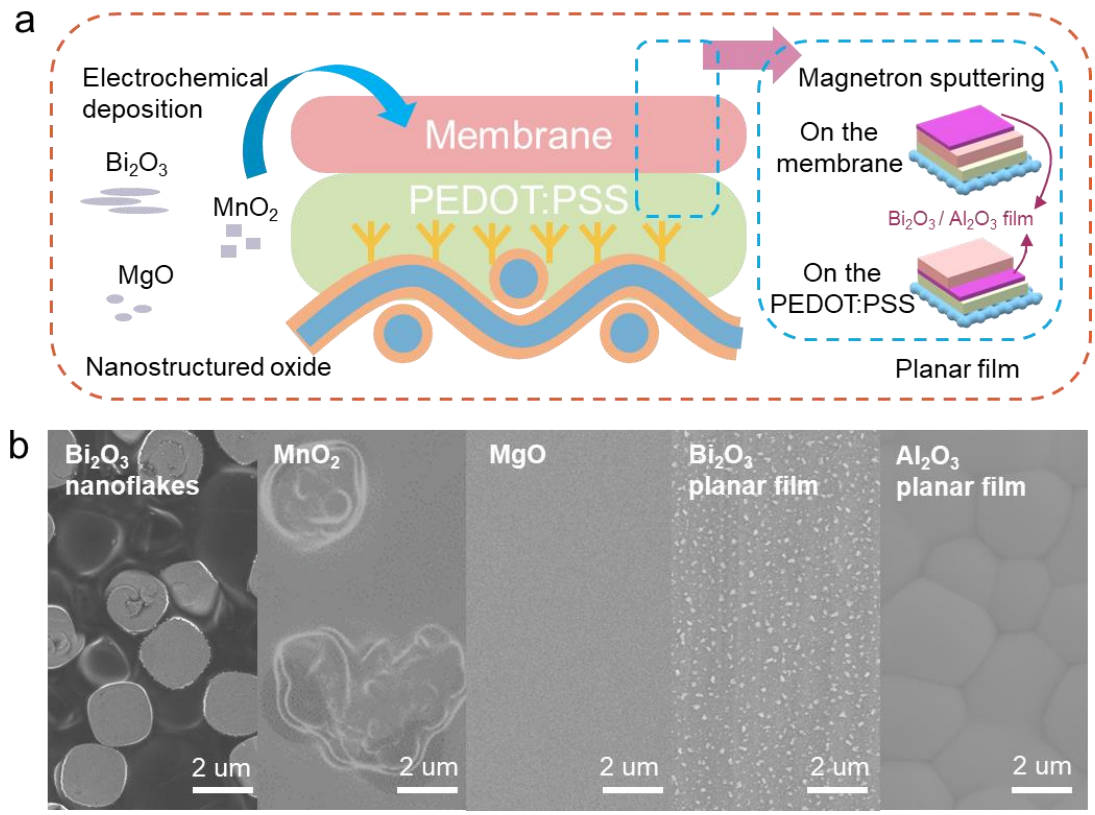

Figure 5.7 Optimization and schematic representation of the protective layer applied to the ISM. (a) A schematic illustrates various metal oxide protective layers with distinct morphologies and device configurations. (b) SEM images display the surface morphologies of different protective materials deposited on the ISM.

The corresponding sensing results (Figure 5.8c, d) further verify these conclusions. Sensors coated with β-Bi_2O_3 nanoflakes exhibited a high and stable potential response across Na^+ concentrations ranging from 10 mM to 160 mM. In contrast, the MnO_2-modified sensor suffered from large impedance and signal attenuation. The MgO-based sensor showed non-linear and inconsistent responses, indicating unstable ion pathways. Furthermore, sensors using Bi_2O_3 or Al_2O_3 planar films experienced signal failure or high potential drift, likely due to their blocking effect on ion diffusion and poor interfacial interaction. Besides, among this group of samples, the β-Bi_2O_3 nanoflake-functionalized ISM required the highest applied force to delaminate. This enhanced adhesion strength can be attributed to the unique structural properties of the β-Bi_2O_3 nanoflakes, which form a robust interface between the ISM and the electrode. The

vertically aligned nanostructure of β-Bi_2O_3 not only improves the mechanical stability by preventing delamination under mechanical stress but also facilitates better interaction between the functional layers, ensuring long-term durability and maintaining the integrity of the sensor during washing cycles. In comparison, the other oxide layers, with their smoother, more compact films, exhibited weaker interfacial bonding, resulting in lower adhesion strength and a higher tendency to delaminate under similar conditions.

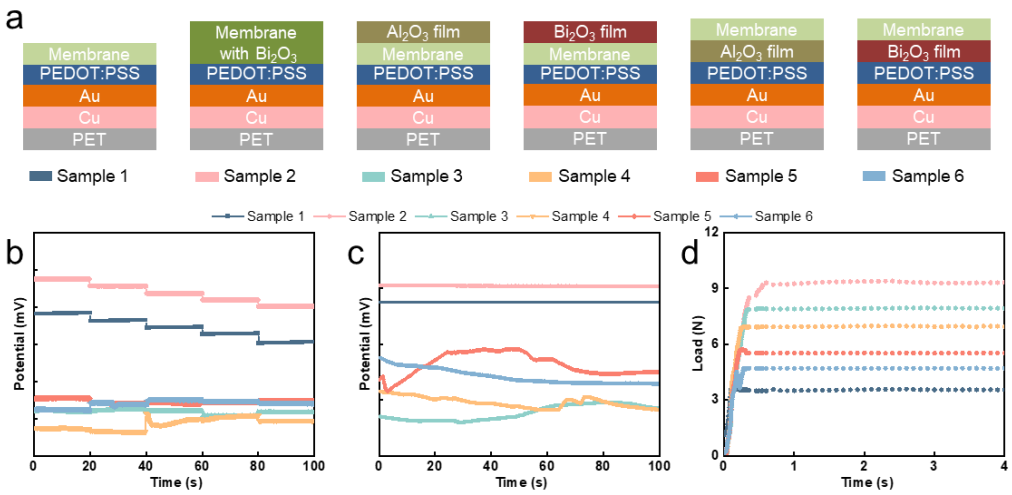

Figure 5.8 Systematic study on the oxides layers. (a) The schematic of the sensor with different structures. The (b) performance, (c) drift and (d) adhesion strength of this group of sensors.

To further verify the structural advantages of β-Bi_2O_3, performance and delamination tests were conducted (Figure 5.9a) on devices with different Bi_2O_3 configurations. These included: (i) unmodified ISM, (ii) ISM decorated with β-Bi_2O_3 nanoflakes, (iii) a planar Bi_2O_3 layer coated on top of the ISM, and (iv) a planar Bi_2O_3 layer beneath the ISM. The β-Bi_2O_3 nanoflake-functionalized ISM required the highest applied force to delaminate, underscoring its superior adhesion strength at the electrode-membrane interface. In contrast to β-Bi_2O_3 nanoflakes, planar Bi_2O_3 films-regardless of whether they are positioned above or beneath the selective membrane-severely compromise the

sensor's functionality (Figure 5.9b). This detrimental effect is likely due to their compact, non-porous morphology, which hinders ion transport and blocks the active sensing interface, thereby disrupting both signal transduction and membrane adhesion. These results highlight that not only the material itself, but also its spatial distribution and vertical orientation, critically influence the interfacial integrity and mechanical stability of the sensor.

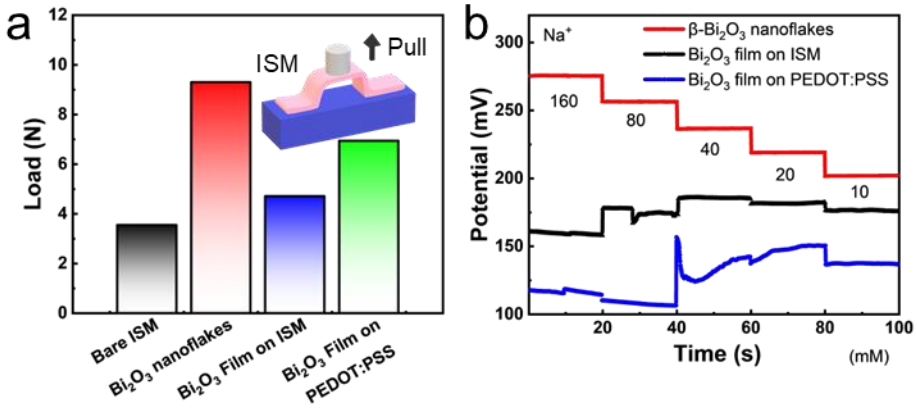

Figure 5.9 Systematic study on the Bi_2O_3 layers. (a) Quantitative evaluation of the adhesion strength. (b) Performance assessment of Na^+ biosensors incorporating Bi_2O_3 with varying morphologies and spatial configurations.

In conclusion, the comparative investigations strongly validate the dual-functional role of β-Bi_2O_3 nanoflakes: they act as both efficient ion conductors and mechanical reinforcement layers. Their unique vertically aligned nanostructure enables stable signal transduction, moisture resilience, and superior adhesion, collectively contributing to the construction of washable, high-performance textile-based biosensors.

5.3.3 Construction and Fundamental Performance Evaluation of Wearable Na^+ Sensor

This section presents a comprehensive overview of the fabrication process and baseline performance of the wearable Na^+ ion-selective sensor incorporating β-Bi_2O_3 nanoflakes. The sensor adopts a multilayer architecture designed for both electrochemical

functionality and mechanical flexibility. First, copper is chemically deposited onto a PET textile substrate to form the conductive Cu@PET layer, serving as the platform for subsequent sensor integration. A highly conductive PEDOT:PSS film is then spin-coated onto the Cu@PET surface to improve interfacial charge transport and act as an adhesion layer for the ISM. Following this, a flexible ISM layer is assembled via electrostatic self-assembly to construct the core ion recognition component. Finally, β-Bi_2O_3 nanoflakes are uniformly deposited on top of the ISM layer, forming a stable and compact functional coating with fast ion conduction and mechanical protection properties. This multilayered configuration ensures clear layer separation, strong interfacial adhesion, and optimal performance for wearable applications (Figure 5.10). The fabrication steps and the morphology of each layer are shown in the corresponding figure.

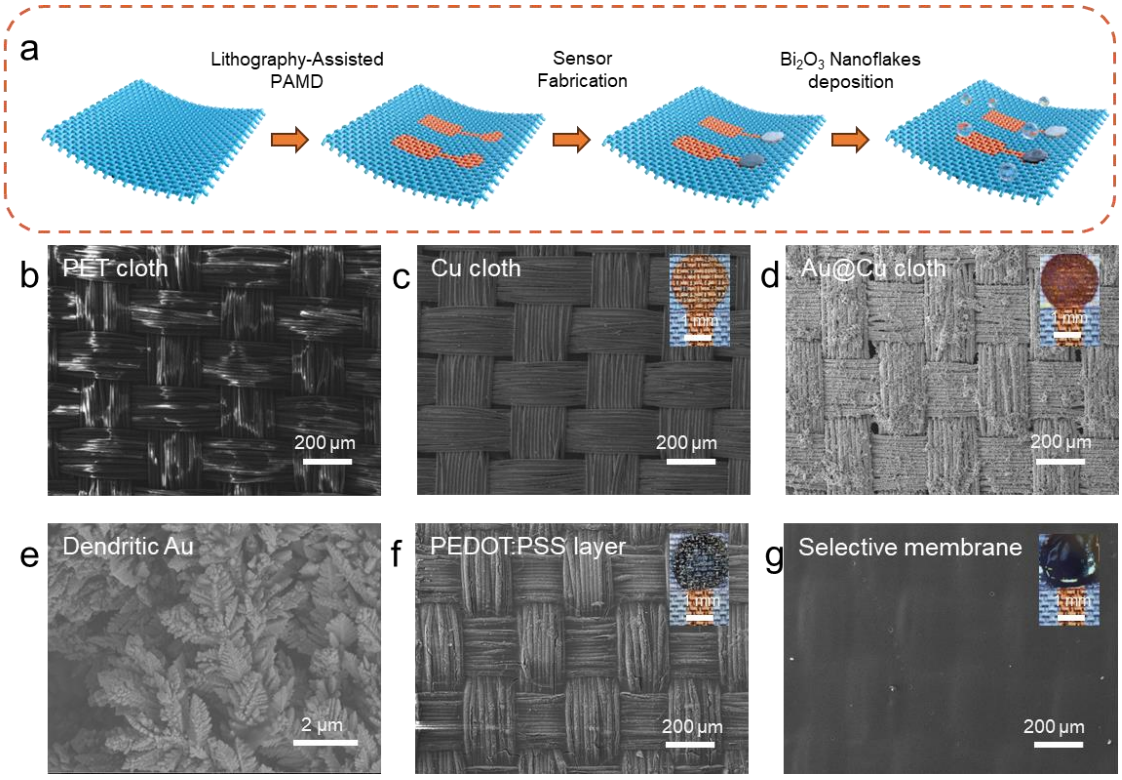

Figure 5.10 Structural construction and morphological features of the textile-based ion sensor platform. (a) Schematic illustration of the fabrication process. (b-f) SEM images of each functional layer: (b) pristine PET textile substrate; (c) Cu-deposited textile

(Cu@PET); (d) dendritic gold nanostructures electrodeposited on Cu; (e) high-resolution view of the dendritic Au architecture; (f) spin-coated PEDOT:PSS conductive layer; and (g) top view of the ISM layer.

The photos and schematic structure of the ion-selective sensor were shown in Figure 5.11. In terms of sensing performance, the sensor demonstrates a well-defined linear response in Na^+ standard solutions ranging from 10 mM to 160 mM, with a high sensitivity of 59 mV/dec, approaching the Nernst theoretical limit—indicating excellent ion-selectivity. Under a continuous 60-minute operation, a minimal potential drift of only 2.5 mV/h is observed, confirming the long-term signal stability. Batch-to-batch reproducibility was evaluated from five independently fabricated devices, yielding a RSD of 1.4%, suggesting good fabrication consistency.

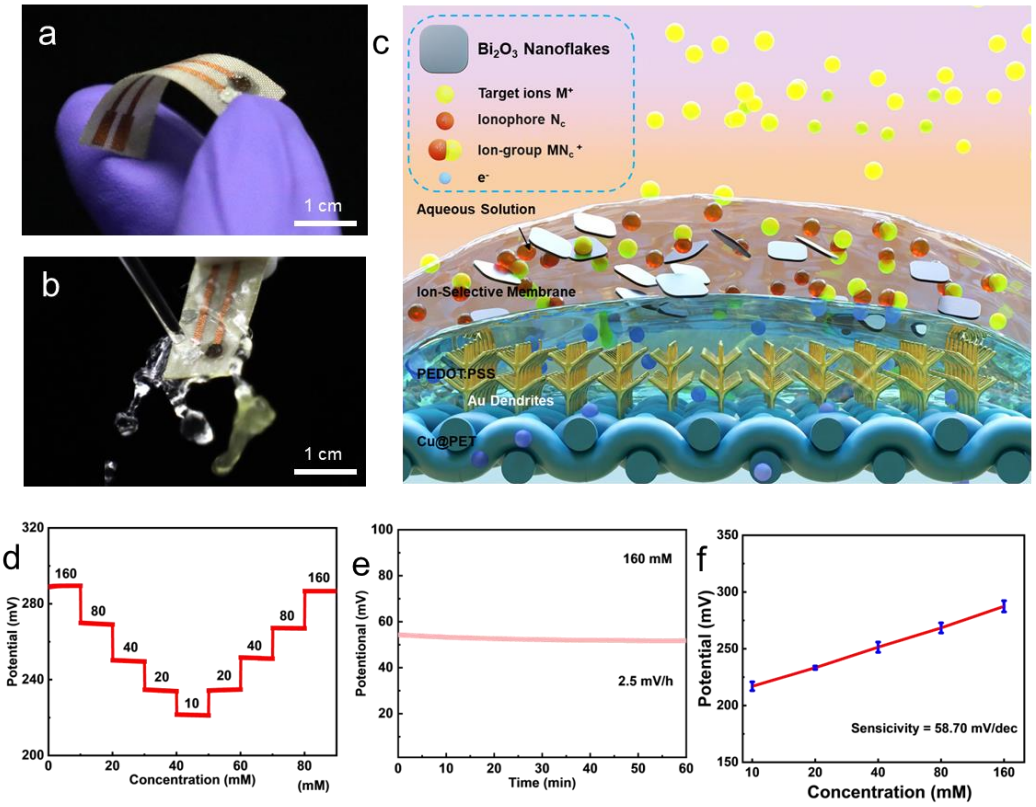

Figure 5.11 Performance and sensing mechanism of the textile-based ion-selective sensor: (a) Photo of the sensor with integrated working and reference electrodes; (b)

Washability test under running water; (c) Schematic of sensing mechanism based on β-Bi_2O_3 nanoflake-functionalized ISM. (d) Reproducibility of sensor performance across different samples functionalized with β-Bi_2O_3 nanoflakes. (e) Signal drift analysis of the sensor with dendritic gold electrode when immersed in 160 mM NaCl solution. (f) Repeatability of open-circuit potential (OCP) responses from the Na^+-selective sensor over multiple measurements.

In Figure 5.12, to assess long-term storage stability, the sensor was sealed and stored under ambient dry conditions for 20 days. Subsequent testing revealed no noticeable performance degradation, with signal variation less than 0.1%, indicating excellent shelf-life. Additionally, mechanical durability was evaluated by subjecting the sensor to repeated bending cycles (50, 100, 150, and 200). The output voltage exhibited negligible change across all cycles, highlighting its strong mechanical resilience for wearable use.

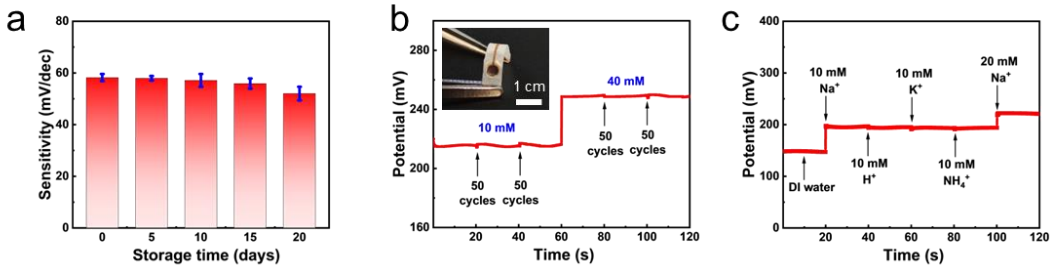

Figure 5.12 Stability and selectivity assessment of the textile-based Na^+ ion sensor. (a) Long-term storage stability of the sensor over 20 days. Error bars indicate the relative standard deviation (RSD) of the evaluated sensitivity from three independent samples. (b) Mechanical stability under repeated bending cycles (50-200 cycles), demonstrating negligible variation in response. (c) Selectivity analysis of the Na^+ ion-selective sensor in the presence of common interfering ions.

To further evaluate the practical applicability of the Na^+-selective sensor in complex physiological environments such as sweat, selectivity tests were conducted against common interfering ions including H^+, K^+, and NH_4^+. As shown in Figure 5.12c, the sensor exhibited a distinct and stable potential response to Na^+ with minimal interference from these coexisting ions, confirming its high ion selectivity. This favorable performance can be attributed to the specificity of the ISM composition and the robust interface formed with the β-Bi_2O_3 nanoflakes, ensuring accurate Na^+ detection even in the presence of physiologically relevant competing species. Altogether, the fabricated Na^+ sensor exhibits excellent performance in sensitivity, stability, reproducibility, and mechanical robustness, establishing a reliable foundation for system-level integration and real-time sweat analysis.

5.3.4 Enhancement of Sensor Washability by Fast Ion-Conducting β-Bi_2O_3 Nanoflakes

In real-world wearable applications, sweat sensors are often exposed to repeated use and washing. However, wearable electrochemical sensors commonly face structural damage and performance degradation during such cleaning processes. To systematically evaluate the role of β-Bi_2O_3 nanoflakes in improving washability, a series of standardized washing tests, morphological assessments, electrochemical performance analyses, and cross-platform validations were conducted.

To simulate practical contamination, sensors were artificially stained and rinsed with deionized (DI) water. As shown in Figure 5.13a, the textile-based sensors could be visibly cleaned via simple rinsing, indicating basic resistance to surface fouling. For a more standardized and controlled test, we established a washing protocol by immersing the sensors in DI water and stirring at 1800 rpm for 30 seconds using a magnetic rotor, effectively mimicking machine-washing conditions (Figure 5.13b). After 20 washing cycles, the surface morphologies of sensors with and without β-Bi_2O_3 nanoflakes were examined by SEM. The β-Bi_2O_3-functionalized ISM retained its structural integrity, showing no delamination or cracking (Figure 5.13c). In contrast, the unmodified ISM

exhibited severe peeling, exposing the underlying PEDOT:PSS layer (Figure 5.13d), thus confirming its poor mechanical stability under washing.

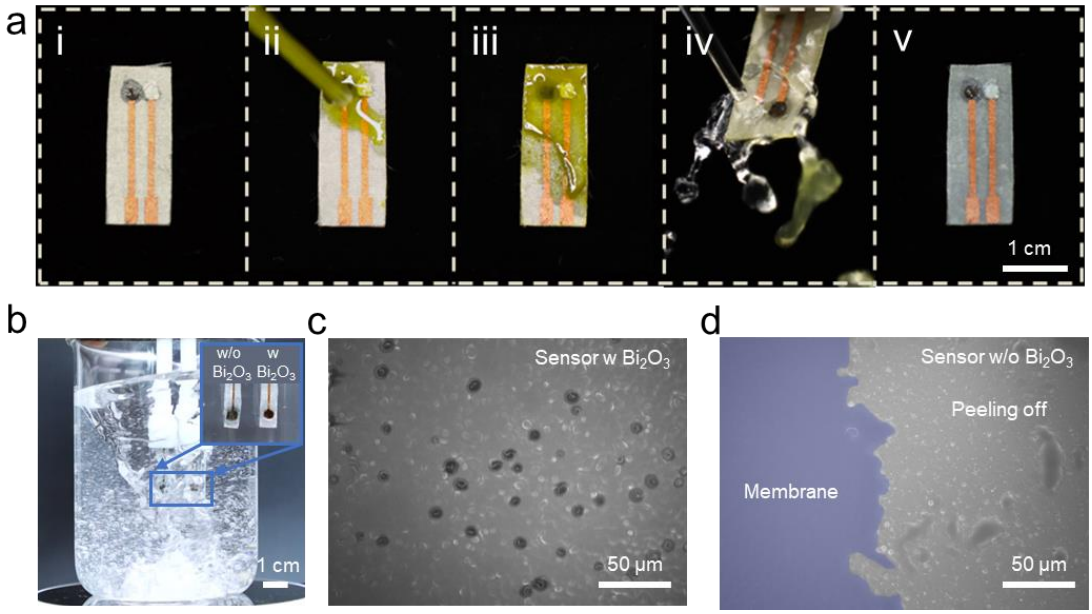

Figure 5.13 Washing protocol and morphological comparison of ion sensors with and without β-Bi_2O_3 nanoflakes. (a) Sequential images demonstrating sensor contamination and cleaning: i) Pristine sensor surface; ii) Application of artificial stains; iii) Sensor with stains adhered to the surface; iv) Rinsing under water; v) Sensor restored to a clean state. (b) Photograph of the standardized washing simulation setup using magnetic stirring at 1800 rpm. (c-d) SEM images of the sensor surfaces after 300 seconds of washing: (c) Sensor functionalized with β-Bi_2O_3 nanoflakes, maintaining structural integrity; (d) Control sensor without β-Bi_2O_3, showing severe delamination and exposure of the underlying PEDOT:PSS layer.

Electrochemical performance was monitored after every two washing cycles (Figure 5.14a). The β-Bi_2O_3-decorated Na^+ sensor maintained excellent sensitivity throughout the 20-cycle washing test, with sensitivity retention above 90% (Figure 5.14b). In contrast, the unmodified sensor showed severe degradation after only six cycles. Even after 50 washing cycles, the β-Bi_2O_3-integrated sensor retained over 70% sensitivity

(Figure 5.14d-f). Moreover, the signal drift was as low as 3.85 mV/h, and baseline drift remained under 10% (Figure 5.14c). Conversely, the control sensor exhibited signal drift nearly 10 times higher and baseline drift up to 650%, severely compromising performance stability.

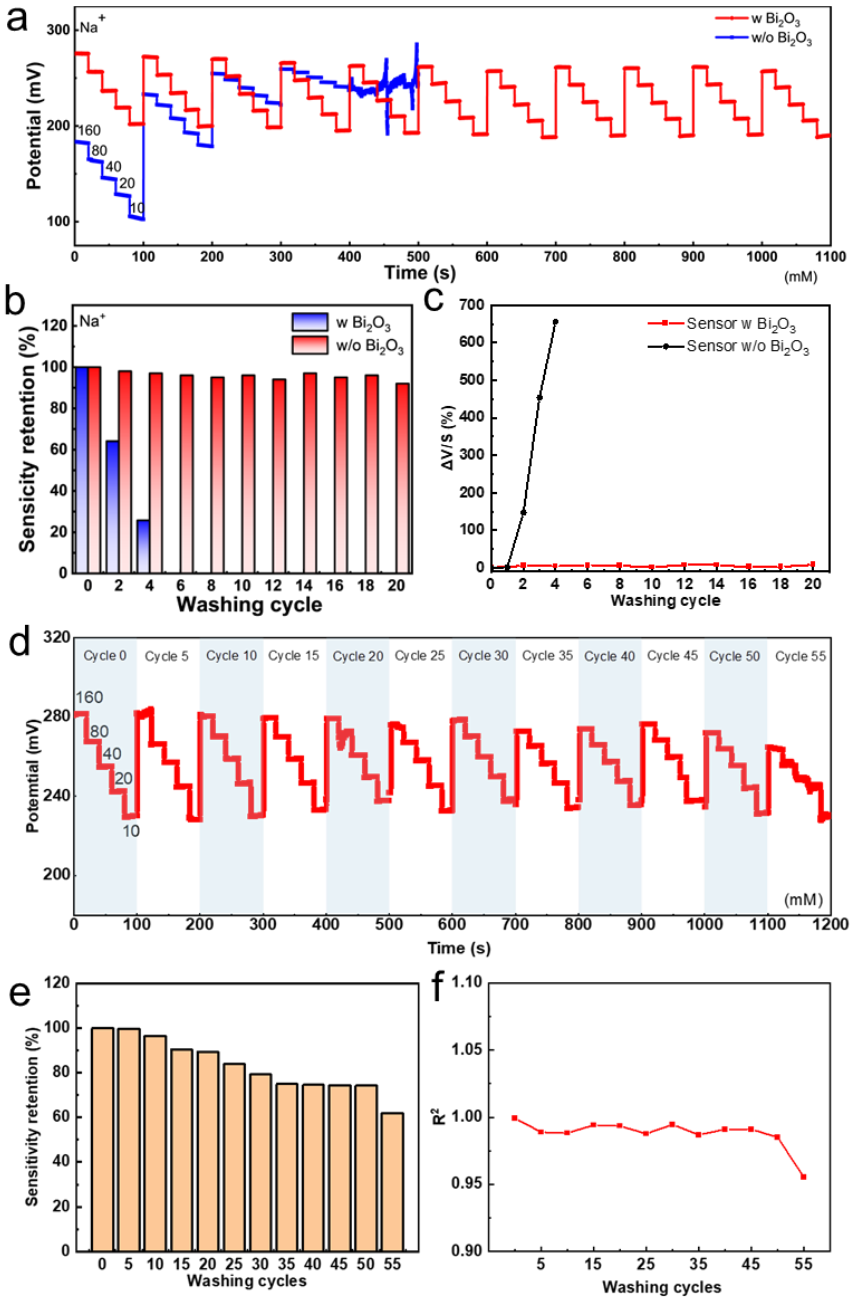

Figure 5.14 Washing durability and performance retention of β-Bi_2O_3 nanoflake-functionalized sensors. (a) Comparison of Na^+ sensor responses with and without β-

Bi_2O_3 nanoflakes after washing. (b) Sensitivity retention over successive washing cycles. (c) Baseline drift during the first 20 cycles. (d) Stepwise sensing performance after every five washing cycles. (e) Retained sensitivity and (f) correlation coefficient over 50 cycles.

To demonstrate the generality of this strategy, we extended the β-Bi_2O_3 nanoflake functionalization to highly selective K^+ and pH sensors. After five washing cycles, both sensors maintained stable output, confirming broad compatibility and durability (Figure 5.15).

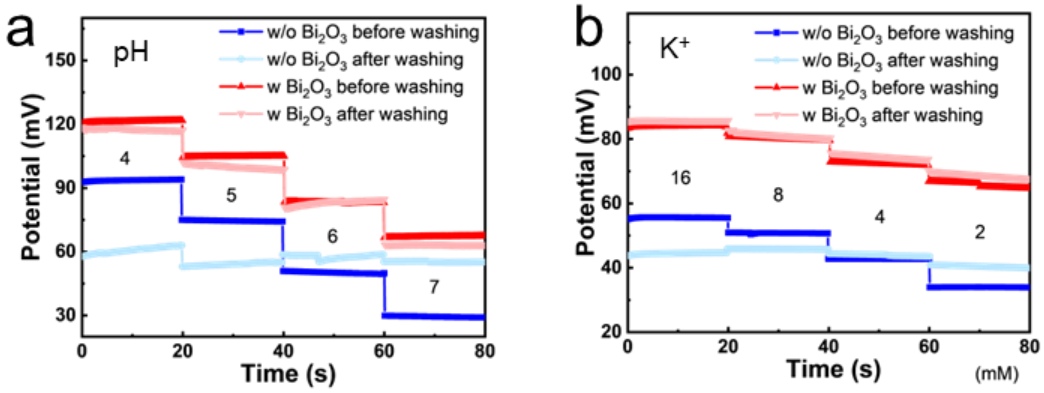

Figure 5.15 Washability enhanced by β-Bi_2O_3 nanoflakes on (a) K^+ and (b) pH sensors. Additional tests were conducted in various cleaning solutions such as laundry detergent and soapy water to simulate harsh chemical exposure. The β-Bi_2O_3-modified sensors not only preserved function but also showed improved resistance to these chemical environments (Figure 5.16).

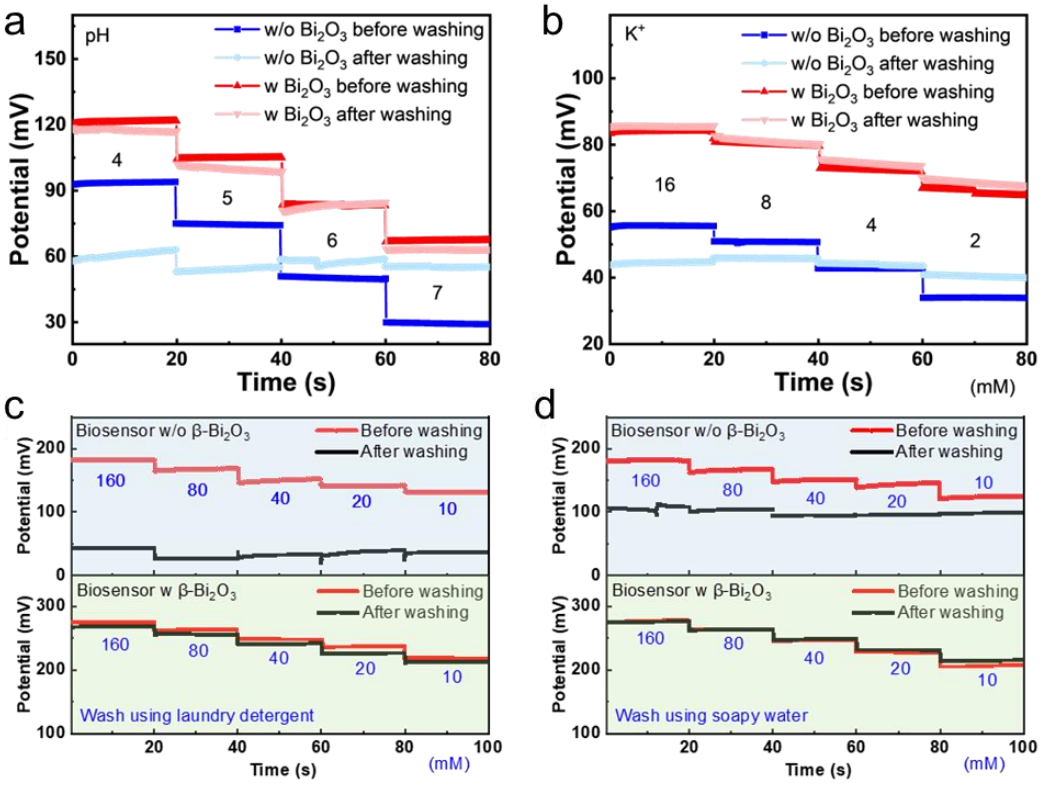

Figure 5.16 Versatile washability enhancement of β-Bi_2O_3 nanoflake-functionalized biosensors. (a-b) Improved washability of K^+ and pH sensors functionalized with β-Bi_2O_3 nanoflakes, evaluated before and after five washing cycles. (c-d) Washing durability of β-Bi_2O_3-based biosensors under exposure to laundry detergent and soapy water, assessed before and after five cycles.

A standardized washing machine test was also performed based on the AATCC LP1-2021 protocol. Textile substrates integrated with unmodified and β-Bi_2O_3-functionalized sensors were washed at 40 °C for 21 minutes with a 1.6 kg fabric load. As shown in Figure 5.17, the unmodified ISM detached completely after washing, while the β-Bi_2O_3-modified membrane remained intact with sensitivity retention above 80%. This test, captured in Video S1, confirms the robustness of the system under practical laundering conditions.

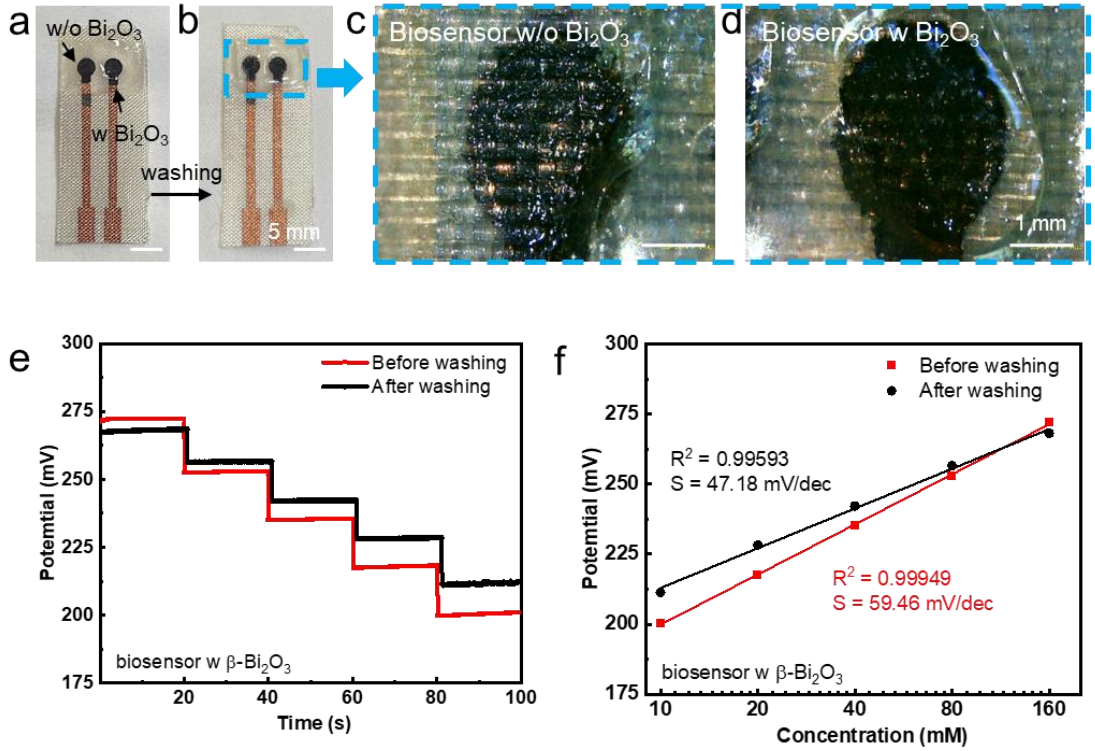

Figure 5.17 Validation of washability enhancement by β-Bi_2O_3 nanoflakes under standardized laundry conditions. (a-b) Photographs of biosensors before and after washing based on AATCC Standard LP1-2021 (Home Laundering Protocol). (c-d) Optical microscopy images of biosensors without (c) and with (d) β-Bi_2O_3 nanoflakes after standard washing. (e-f) Comparison of OCP response (e) and sensitivity (f) of biosensors functionalized with β-Bi_2O_3 before and after washing.

Based on these comprehensive experiments, the enhancement mechanisms provided by β-Bi_2O_3 nanoflakes can be summarized as follows:

- Physical Barrier and Structural Reinforcement: The nanoflakes form a dense yet porous protective layer with the ISM, which effectively shields against mechanical shear and turbulence, thus preventing delamination.

- Hydrophobicity and Chemical Stability: β-Bi_2O_3 exhibits excellent chemical stability and water-repellent properties that reduce water-induced degradation. Contact angle (CA) measurements confirmed that β-Bi_2O_{33}-modified sensors

retained a CA of ~93° after five washes (from 105°), whereas unmodified sensors dropped from 87° to 57°, indicating loss of hydrophobicity (Figure 5.18).

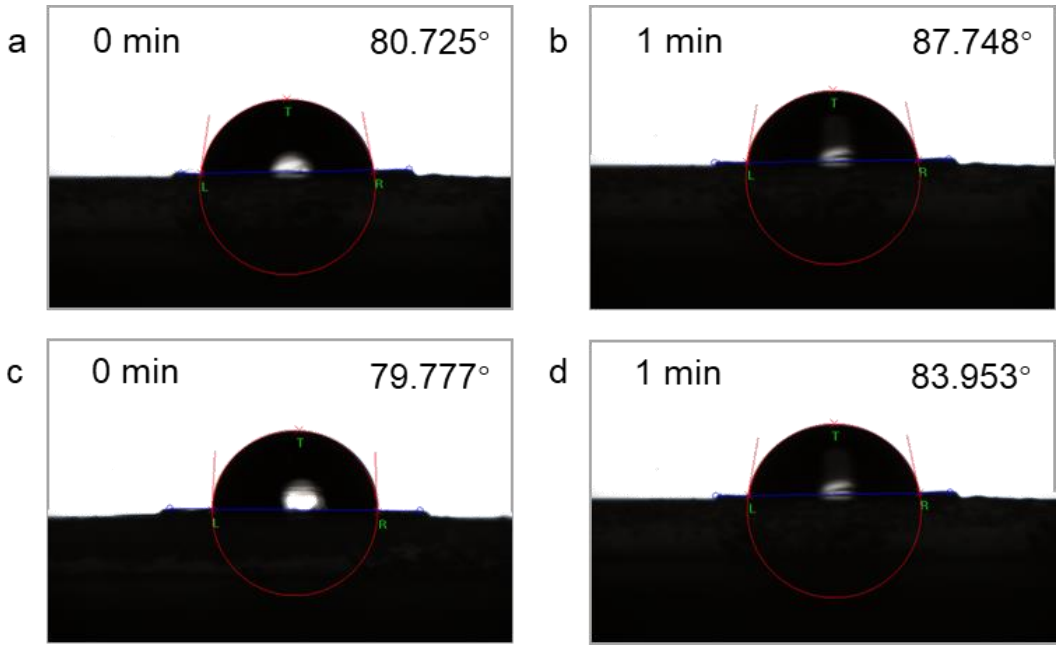

Figure 5.18 Comparison of contact angles. The contact angle of bare ISM (a) at the beginning and (b) after 1 min. The contact angle of ISM with β-Bi_2O_3 nanoflakes (c)at the beginning and (d) is after 1 min.

- Low Impedance and Enhanced Ion Transport: Although Bi_2O_3 generally has poor conductivity, engineering it into the β phase provides fast ion conduction. The nanoflake morphology further reduces impedance while maintaining membrane adhesion and integrity, enabling stable electrochemical response during washing cycles.

In summary, the functionalized of β-Bi_2O_3 nanoflakes significantly improves the washability of textile-based ion-selective sensors through a combination of physical protection, enhanced hydrophobicity, and efficient ion transport. This strategy provides a practical and scalable solution for developing reusable and washable wearable biosensing platforms with high durability and performance retention.

5.3.5 Design of Wearable Textile Structure and Evaluation of Wearing Comfort

To enable long-term and high-frequency monitoring of sodium ions in sweat, we developed an integrated wearable textile sensing platform featuring excellent structural flexibility, breathability, and skin compatibility. As illustrated in Figure 5.19a, the platform is constructed on a PET textile substrate, sequentially layered with Cu@PET conductors, PEDOT:PSS conductive film, ISM, and a functional β-Bi_2O_3 nanoflake layer. A low-power Bluetooth (BLE) module and micro-battery are further integrated to achieve seamless wireless transmission and signal acquisition. The overall system is thin, soft, and bendable, allowing for conformal contact with the human skin without requiring additional adhesives or rigid enclosures. Figure 5.19b presents the practical assembly of the system in a wristband form, validating its engineering feasibility for daily wearable scenarios.

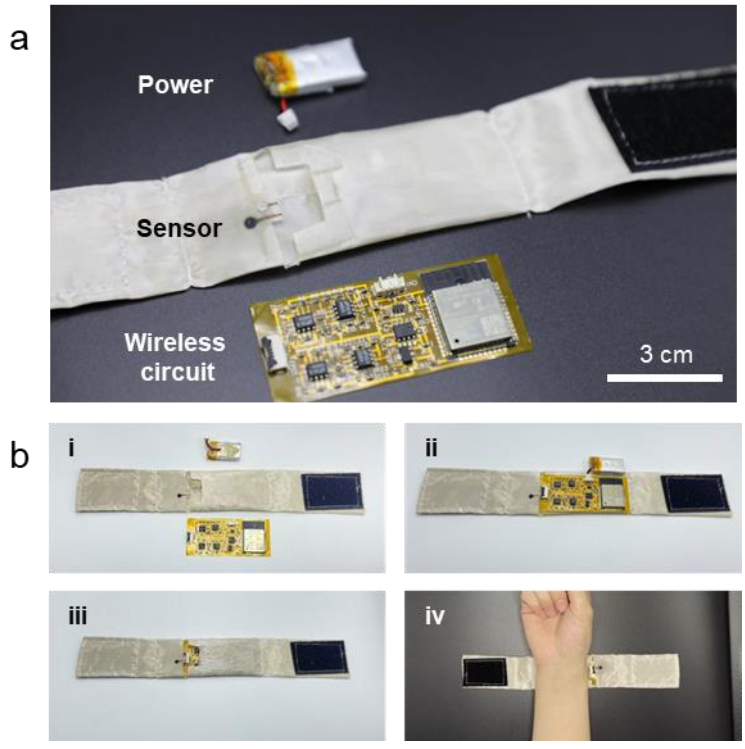

Figure 5.19 Integration and deployment of the wearable sensing wristband. (a) Photograph of the assembled wristband system, showcasing the integrated textile-based ion-selective sensor, detachable circuit module, and micro-battery unit. (b) Stepwise

illustration of the wristband assembly and wearing process: (i) Display of key components, including the battery, textile band with embedded sensor, and flexible circuit; (ii) Connection and assembly of all functional modules; (iii) Insertion of the assembled system into the wristband pocket; (iv) Final wearing of the complete device on the wrist.

To investigate the effect of the β-Bi_2O_3 nanoflake layer on wearing comfort, we systematically evaluated its influence on water vapor permeability. According to the ASTM E96 standard protocol, we measured the WVTR of sensor textiles with and without β-Bi_2O_3 modification. As shown in Figures 5.10a, b, the samples incorporating β-Bi_2O_3 retained a comparable WVTR to unmodified textiles, indicating that the nanoflake layer did not hinder the moisture diffusion pathways. This open microstructure is critical for preventing local moisture buildup and maintaining skin comfort during prolonged wear. Furthermore, a custom-built water vapor permeation setup was employed to verify gas exchange performance. As shown in Figure 5.20c, continuous condensation of water droplets at the top of the device chamber confirms that the sensor structure possesses favorable vapor permeability, enabling skin breathing and minimizing heat accumulation or moisture irritation during extended use.

Figure 5.20 Evaluation of breathability and moisture permeability of the wearable sensor system. (a) Quantitative measurement of moisture permeability for different sensor-integrated textiles using the ASTM E96 standard method. (b) Visual comparison of residual water content in bottles sealed with various samples, highlighting differences

in moisture barrier properties. (c) Demonstration of water vapor permeability for the wristband integrated with the washable ion-selective sensor, indicating its ability to maintain skin breathability during wear.

To comprehensively assess the real-world wearability of the system, we conducted a comparative skin compatibility study with conventional wearing modalities, including medical-grade adhesive tape and commercial smartwatches. As shown in Figure 5.21, the skin conditions were evaluated after 8 hours of continuous wear under identical conditions. Compared to adhesive tape (which caused redness and pressure marks) and rigid smartwatch enclosures (which induced local compression), the textile-based platform demonstrated superior comfort. No visible erythema, indentation, or irritation was observed on the skin, suggesting excellent biocompatibility and a soft conformal interface ideal for prolonged use.

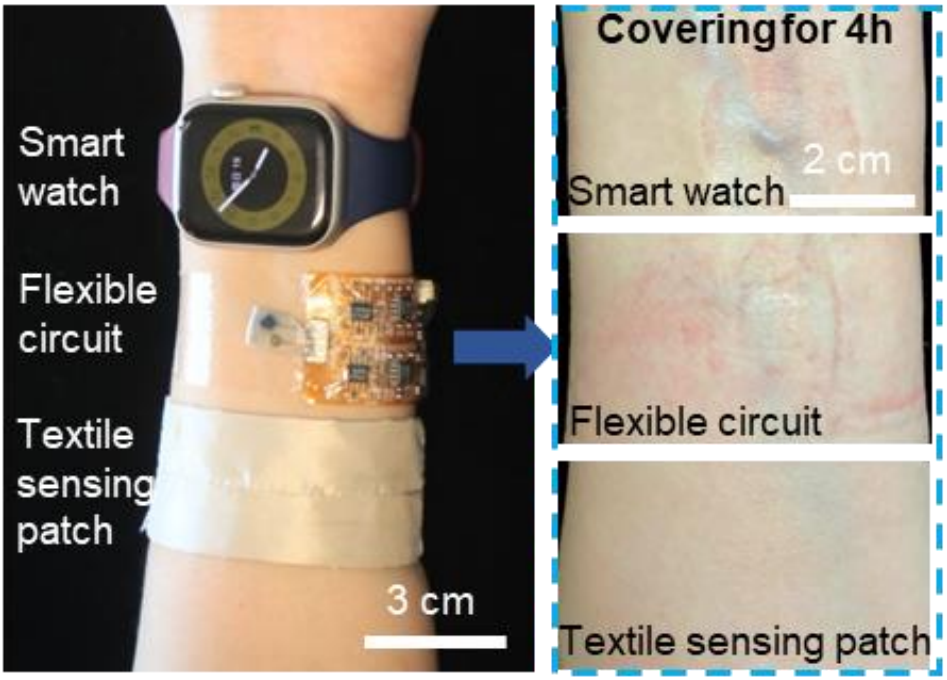

Figure 5.21 Photographs of skin irritation tests conducted by wearing a commercial smartwatch, a flexible circuit, and the fabricated textile wristband on the forearm.

In summary, the textile-based ion sensing platform developed in this study exhibits a well-balanced combination of mechanical flexibility, water vapor permeability, and skin adaptability. Its wearable construction and demonstrated comfort make it highly suitable for long-term sweat ion monitoring in dynamic and real-life conditions, offering significant potential for practical deployment in personalized health tracking.

5.3.6 BLE Wireless Module and Human-Machine Interaction System

To enable real-time, continuous monitoring of sweat Na^+ concentrations and achieve remote wireless communication, a fully integrated system was developed by embedding a low-power Bluetooth Low Energy (BLE) module, a signal processing circuit (comprising high-input impedance buffering, amplification/filtering, and a microcontroller unit, MCU), and a mobile application (App) into the wearable sensing platform. This construction established a complete closed-loop framework of "sensing-processing-transmission-interaction."

The system consists of three core modules: (1) the ISEs integrated onto the textile substrate; (2) a signal acquisition and conditioning circuit, including buffering, amplification, and analog-to-digital conversion (ADC); and (3) the BLE wireless communication and battery power supply module. The signal flow begins with the detection of weak open-circuit potential (OCP) signals from the ISEs, which are read by a high-input-impedance operational amplifier. The signal is then filtered via a low-pass filter to suppress noise, calibrated and digitized by the MCU, and finally transmitted wirelessly by the BLE module to a smart terminal for real-time visualization. To enhance user interaction, a dedicated BLE App was developed, featuring (1) real-time display of the sensor signal profile and (2) automatic Na^+ concentration conversion with standardized units. As shown in Figure 5.22, the App successfully records and displays the dynamic Na^+ concentration variations in sweat during practical use.

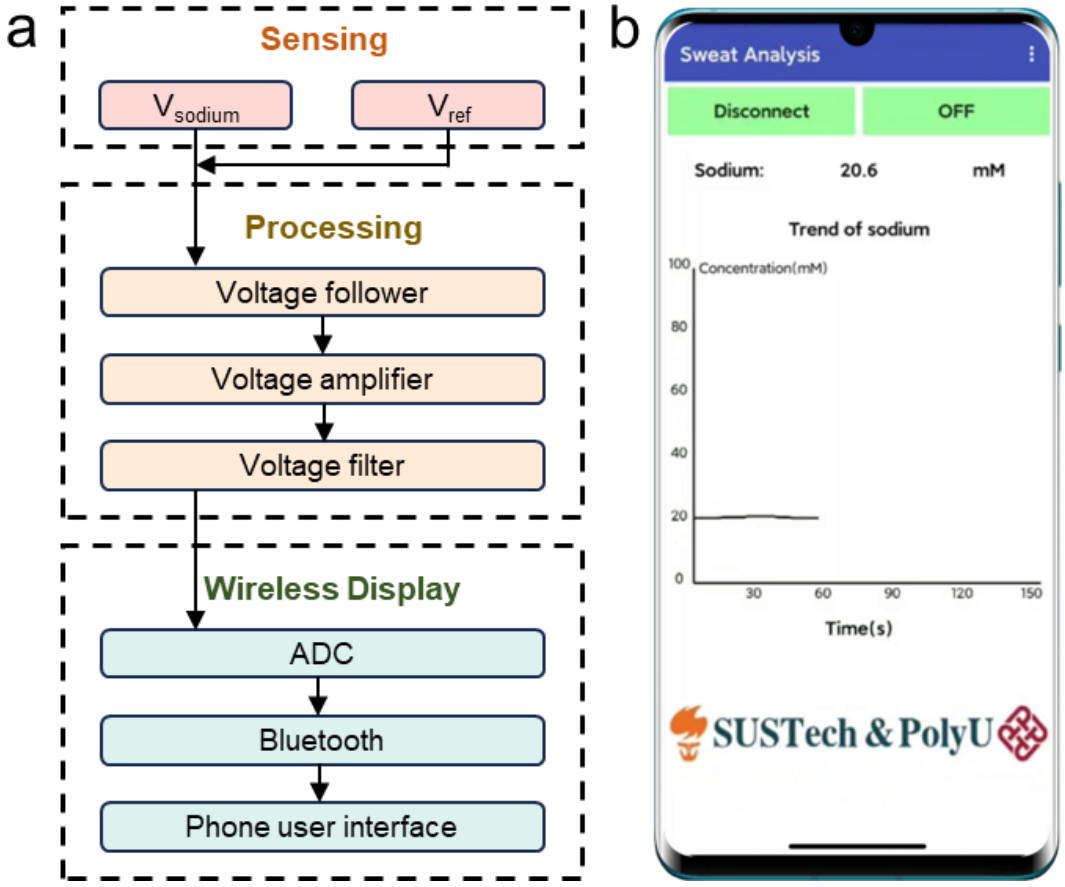

Figure 5.22 Real-time wireless sensing framework and interface design. (a) Schematic illustration of the system workflow for continuous and wireless monitoring of Na^+ levels in sweat. (b) Screenshot of the custom-developed APP designed for real-time visualization and remote tracking of Na^+ concentration.

The layout and circuit logic of the signal processing module are illustrated in Figure 5.23, which shows the flexible PCB packaging of all electronic components. These modules are connected to the textile sensors via conductive interconnects, preserving the overall flexibility and skin-conformability of the device. The entire system features a compact and lightweight design, enabling seamless integration into a soft wristband for long-term, stable monitoring when worn on the forearm or wrist.

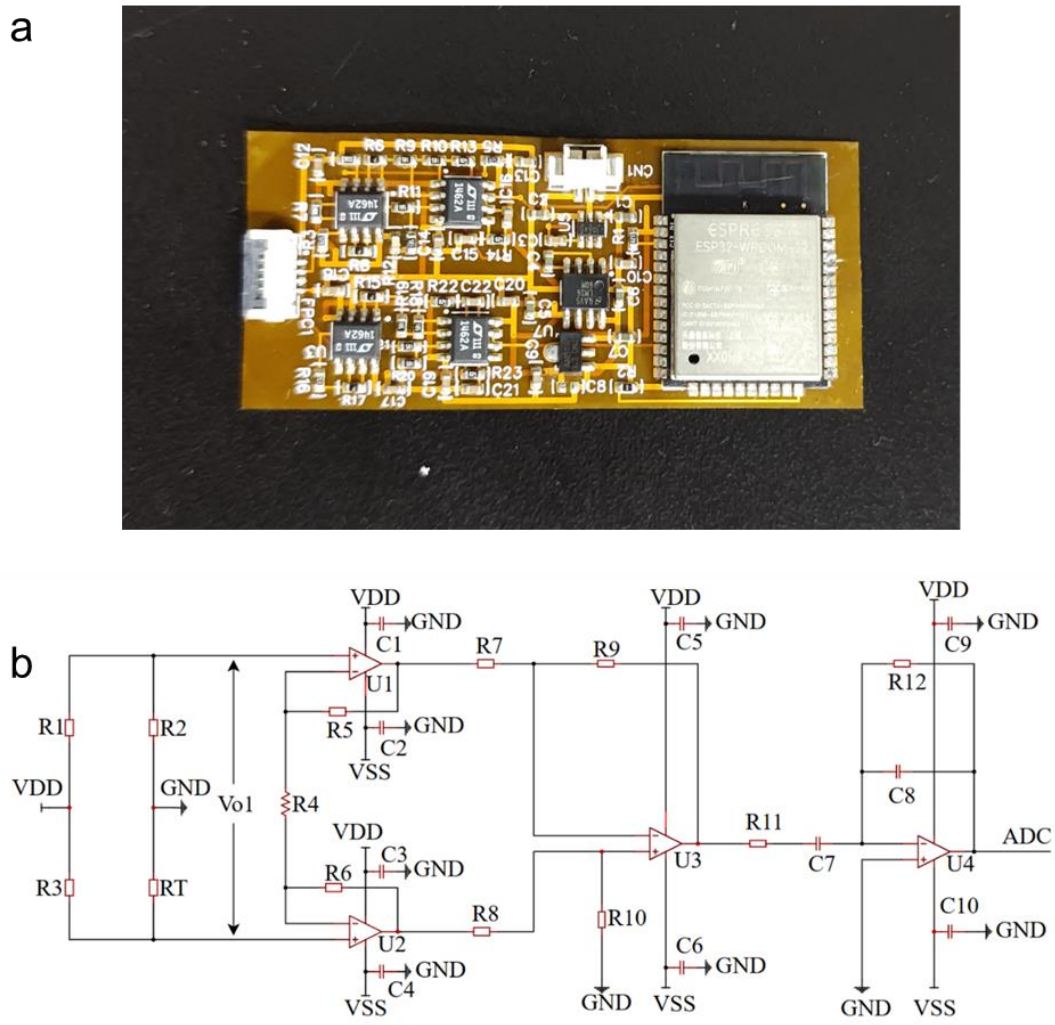

Figure 5.23 (a) Photograph and (b) schematic of the removal circuit.

To validate the system's real-time performance and detection accuracy under dynamic exercise conditions, an on-body test was conducted during an 8 km/h cycling session. The volunteer wore the integrated wristband system on the forearm, and the Na^+ concentration in sweat was continuously monitored. The acquired data were wirelessly transmitted to a smartphone via BLE and displayed in real time through the accompanying application. At the same time, sweat samples were collected for inductively coupled plasma mass spectrometry (ICP-MS) analysis to provide reference measurements. As shown in Figure 5.24a, the Na^+ profiles recorded by the sensor matched closely with the ICP-MS results, demonstrating strong agreement in concentration trends. In addition, as shown in Figure 5.24b, the system was tested across

different exercise intensities on the same individual, further confirming the sensor's sensitivity and accuracy in dynamically changing sweat environments. The BLE system also maintained excellent wireless communication and low-power operation throughout prolonged use. The signal transmission delay was consistently below 0.5 seconds, with a refresh rate exceeding two data points per second, fully meeting the requirements of continuous dynamic monitoring. No signal dropout or noticeable drift was observed during 30 minutes of continuous wear, indicating high system stability and reliability.

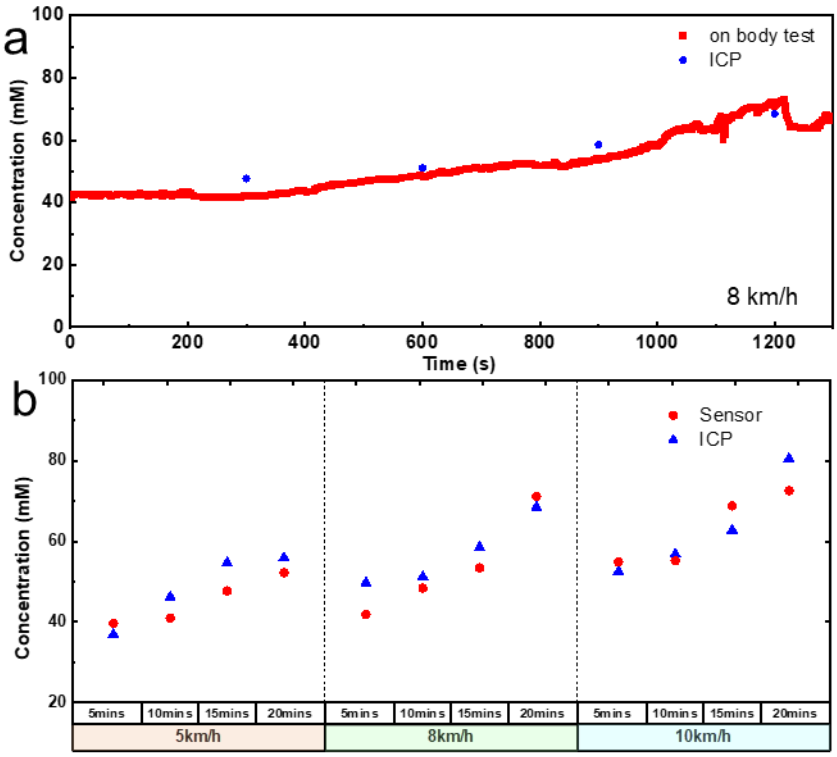

Figure 5.24 Validation of on-body sweat Na^+ monitoring during exercise. (a) Real-time monitoring of sweat Na^+ concentrations during cycling at 8 km/h using the wearable wristband, with results validated by ICP analysis. (b) Comparative analysis of sweat Na^+ concentrations measured by the wristband and corresponding ICP values at cycling speeds of 5, 8, and 10 km/h, recorded at 5-minute intervals.

In summary, the BLE-integrated wearable sweat sensing system developed in this study, featuring micro-signal amplification and calibration, low-power BLE communication,

flexible packaging, and real-time interactive App display, successfully enables dynamic and remote monitoring of sweat Na^+ concentrations. This system demonstrates significant potential for practical applications in personalized health assessment, sports performance tracking, and chronic disease telemonitoring.

5.4 Conclusion

In this chapter, we systematically developed and evaluated a wearable textile-based sodium ion sensor system enhanced by β-Bi_2O_3 nanoflakes. The investigation encompassed structural design, electrochemical performance, washing durability, wearing comfort, and wireless interaction capabilities. The sensor was fabricated by sequentially depositing a Cu conductive layer, PEDOT:PSS film, ISM, and β-Bi_2O_3 nanoflakes onto a PET textile substrate. This multilayer architecture with tight interfacial integration demonstrated excellent electrochemical response and mechanical flexibility. In standard Na^+ solutions ranging from 10 to 160 mM, the sensor exhibited a near-Nernstian sensitivity of 59 mV/decade, low potential drift (<2.5 mV/h), and high reproducibility (RSD: 1.4%), laying a stable and reliable foundation for subsequent system-level integration.

In terms of washing durability, the β-Bi_2O_3 nanoflakes served as a dense protective interfacial layer that significantly enhanced the membrane's structural integrity and interfacial adhesion. During simulated laundering cycles (1800 rpm stirring), the sensor retained more than 90% of its initial sensitivity even after 20 washes, with signal drift maintained below 3.85 mV/h—significantly outperforming control devices without β-Bi_2O_3. Additionally, under AATCC-standard household washing conditions, the functional layers remained firmly adhered, validating the system’s robustness under practical wear-and-wash scenarios.

For wearing comfort, the textile-integrated sensor exhibited excellent flexibility and water vapor permeability. Moisture transmission tests following ASTM standards and customized ventilation assessments confirmed that the sensor system allowed skin

breathing and did not significantly obstruct epidermal transpiration. Moreover, wearability trials demonstrated superior skin compatibility and comfort compared to traditional medical tapes or commercial smart watch casings, enabling prolonged usage.

Regarding system integration, the sensor was combined with a high-impedance signal acquisition and amplification circuit, a low-power BLE wireless module, and a smartphone-based application, forming a complete sensing-processing-transmission-interaction closed-loop system. Real-time monitoring of sweat Na^+ concentrations was achieved with visual output on mobile devices. The sensing results showed high consistency with ICP-MS benchmarks, and BLE transmission was stable and low-latency, supporting continuous monitoring during physical activity.

In conclusion, the β-Bi_2O_3 nanoflake-enhanced wearable textile sodium ion sensor developed in this chapter demonstrates outstanding performance across key metrics including sensitivity, stability, washability, comfort, and system integration. This work provides a practical and reusable platform for wireless sweat biomarker sensing and establishes a materials and engineering foundation for future development of multi-ion monitoring systems aimed at personalized health management.

CHAPTER 6 DESIGN AND INTEGRATION OF AN INTELLIGENT RESPONSIVE SYSTEM FOR ORGAN TRANSPORTATION UNDER COLD CONDITIONS

Organ preservation during cold transportation remains a major challenge in transplantation medicine, as conventional static cold storage fails to provide real-time monitoring or active intervention. This often leads to irreversible tissue damage caused by factors such as acidification and oxidative stress. To address these limitations, this chapter presents the development of an integrated responsive system that enables real-time sensing, autonomous energy supply, and therapeutic release triggered by pH levels along with active pH regulation mediated by a palladium electrode. The proposed platform aims to improve organ viability and transplantation outcomes by combining flexible sensors, hydrogel batteries, and PAM/CS smart drug delivery modules into a single functional system.

6.1 Introduction

Organ transplantation remains the most effective treatment for patients with end stage organ failure. However, the clinical success of transplantation heavily depends on the ability to preserve donor organs during extracorporeal cold transportation. Static cold storage (SCS), the current gold standard, involves immersing organs in hypothermic solutions (typically at 4 ℃) to suppress metabolic activity. Despite its widespread use, SCS is inherently passive and unable to respond to dynamic changes during transport, such as temperature fluctuations, mechanical vibration, and biochemical deterioration. These external stressors can induce ischemia, acidosis, oxidative stress, and irreversible tissue damage, ultimately compromising organ viability. Statistical reports indicate that a significant number of organs are discarded globally each year due to transportation-related deterioration, leading to missed transplantation opportunities and resource waste.

Moreover, current preservation strategies lack intelligent feedback mechanisms and rely heavily on centralized evaluation techniques. While emerging methods such as normothermic machine perfusion (NMP) offer better assessment of organ viability,

their complexity, size, and cost severely limit their practical use in routine transport. Most cold storage devices focus solely on passive temperature control and fail to monitor key physiological indicators such as local pH changes. Furthermore, the supporting electronic systems often depend on conventional batteries that suffer from voltage instability and performance degradation under low temperatures. Even when early signs of organ deterioration are detected, there remains a lack of timely therapeutic response. Additionally, existing strategies lack the capability for active chemical regulation to reverse acidification once it is detected. Antioxidants like N-acetylcysteine (NAC) are typically premixed into storage solutions, which results in non-specific release and ineffective protection during critical deterioration phases.

To overcome these limitations, this chapter presents the design and validation of a nanomaterial-enabled intelligent responsive system tailored for cold organ transportation. The proposed system integrates three synergistic modules: (i) a flexible pH sensor based on a polydimethylsiloxane (PDMS) substrate for real-time monitoring of acidification on the organ surface; (ii) a polyacrylamide (PMA) hydrogel battery array constructed in series-parallel configuration to provide stable energy output under subzero conditions; and (iii) an active-responsive therapeutic unit comprising a PAM/CS pH-responsive hydrogel and a palladium electrode for electrochemical pH modulation and on-demand drug release. Together, these components construct a closed-loop "sense-power-respond" platform that enables intelligent monitoring, autonomous energy supply, and active pH-triggered therapeutic intervention. This work demonstrates a materials- and systems-level strategy for improving organ preservation outcomes and advancing the development of smart logistics in transplantation medicine.

This chapter presents the design rationale, experimental validation, and application demonstration of this integrated platform. By establishing a materials- and systems-level strategy, this work offers a promising approach to intelligent organ preservation and sets the foundation for future development of smart bio-interactive logistics in transplantation medicine.

6.2 Experiment

6.2.1 Preparation of the pH-Responsive Hydrogel

The pH-responsive hydrogel in this study was developed based on a semi-interpenetrating polymer network (semi-IPN) formed by polyacrylamide (PAM) and chitosan (CS), with covalent crosslinking introduced via N,N'-methylenebisacrylamide (MBAA). The inclusion of CS imparts pH sensitivity to the material, allowing for structural transitions and controlled drug release by exploiting the protonation behavior of the amino groups under different pH conditions. This hydrogel system was prepared through a three-step process including the synthesis of the PAM/CS prepolymer solution, free radical polymerization to form the network, and post-loading of the model therapeutic agent N-acetylcysteine (NAC).

In the first step, 50 mg of CS was dissolved in 1 mL of 0.8% acetic acid solution and mixed with 2 mL of MES buffer. Subsequently, 1.0 g of acrylamide monomer and MBAA crosslinker were added to the mixture. To initiate the reaction, 7 mg of ammonium persulfate APS and 1.5 mL of TEMED were added as the initiator and catalyst respectively. The mixture was stirred and deoxygenated by nitrogen bubbling for 15 minutes and then poured into a mold. The polymerization was allowed to proceed to form a transparent semi-IPN hydrogel with a well-defined three-dimensional network.

After polymerization, the hydrogel was removed from the mold and immersed in deionized water for purification. The water was changed three times daily over the course of 5-7 days to remove any residual monomers, initiators, and low-molecular-weight impurities. Once purified, the hydrogel was used for drug post-loading. The drug-loading procedure involved immersing the hydrogel in 10 milliliters of a 5 mg/mL NAC aqueous solution, followed by equilibration at room temperature for 12 hours. During this process, NAC molecules diffused into the hydrogel network and were physically trapped within the porous structure, primarily through hydrogen bonding, electrostatic interactions, and van der Waals forces.

The pH responsive behavior of the PAM/CS hydrogel is based on the protonation of the amino groups in the CS chains. Under physiological conditions at pH 7.4, the amino groups remain largely deprotonated and the hydrogel structure stays stable with limited drug diffusion. In acidic conditions, the degree of protonation increases, leading to a greater number of positively charged amino groups and an increase in electrostatic repulsion between the CS chains and the PAM network. This internal repulsion drives the hydrogel to expand, leading to the enlargement of the pores and accelerated drug releas. The system is designed to mimic pathological conditions where local acidosis is present, allowing the hydrogel to respond to the decrease in pH by releasing the therapeutic agent on-demand, providing a timely biochemical protection during organ transportation.

6.2.2 Preparation of the Palladium Electrode for Active pH Regulation

The palladium (Pd) electrode was developed as the functional unit for active electrochemical pH modulation within the integrated preservation system. To ensure high catalytic efficiency and operational stability, a nanostructured palladium layer was synthesized through a controlled electrodeposition process on a planar gold-plated silver (Au/Ag) electrode. The fabrication procedure began with the preparation of the silver substrate which was first electroplated with a thin and uniform layer of planar gold to provide a stable conductive interface. This gold-plated silver substrate was then thoroughly cleaned using ethanol and deionized water to create a pristine surface for metal nucleation. The electrochemical synthesis of palladium was performed in an aqueous electrolyte containing 5 mM palladium chloride ($PdCl_2$) and 0.1 M hydrochloric acid (HCl). A standard three-electrode configuration was employed with the gold-plated silver electrode serving as the working electrode, a platinum wire as the counter electrode, and a saturated calomel electrode (SCE) as the reference electrode. By applying a constant reductive potential for a specific duration, a uniform and dense palladium nanostructure was successfully anchored onto the gold surface. This engineered interface provides the necessary electrochemical sites for the efficient generation or consumption of protons. Following the synthesis, the Pd electrode was

rinsed extensively and dried under a nitrogen stream to prepare for its subsequent assembly with the PAM/CS drug delivery module.

6.2.3 Fabrication of PMA Hydrogel-Based Batteries

In this study, a polyacrylamide (PAM)-based hydrogel electrolyte was synthesized via thermally initiated polymerization to construct a flexible and stretchable Zn-I_2 hydrogel battery. This energy system consists of three essential components: the gel electrolyte, flexible electrodes, and encapsulation structure.

Three types of electrolyte solutions were prepared. First, 1 mol/kg of $ZnSO_4$ (designated as ZS) was obtained by dissolving $ZnSO_4 \cdot 7H_2O$ in ultrapure water. Second, to prepare the $ZnSO_4$-MPII electrolyte (ZS-MI), 1 mol/kg of 1-methyl-3-propylimidazolium iodide (MPII) was added to the ZS solution. Third, a high-concentration $ZnCl_2$-MPII electrolyte (ZC-MI) was prepared by dissolving anhydrous $ZnCl_2$ in ultrapure water at a concentration of 8 mol/kg, followed by the addition of 1 mol/kg MPII.

The PAM hydrogel was synthesized through free-radical polymerization in aqueous solution. Specifically, 6 g of acrylamide monomer (AAm), 20 mg of ammonium persulfate (APS, initiator), 3 mg of N,N′-methylenebisacrylamide (BIS, crosslinker), and 15 μL of tetramethylethylenediamine (TEMED, accelerator) were dissolved in 20 mL of deionized water and stirred thoroughly. The resulting precursor solution was transferred into a glass petri dish, sealed to prevent evaporation, and polymerized at 50 ℃ for 12 hours to yield a transparent PAM hydrogel membrane. The hydrogel was then dried at 80 ℃ to obtain the corresponding xerogel.

The dried PAM film was immersed in the three different electrolyte solutions (ZS, ZS-MI, and ZC-MI) for 72 hours to enable full ionic diffusion and loading, forming the hydrogel electrolytes denoted as ZS-PAM, ZS-MI-PAM, and ZC-MI-PAM, respectively.

For battery assembly, flexible, freestanding carbon nanotube (CNT) paper, with a thickness of approximately 20 μm, was cut into the desired dimensions and adhered onto a polydimethylsiloxane (PDMS) substrate. A laser engraving technique was employed to create precise micropatterned electrode geometries. The prepared hydrogel electrolyte was then evenly applied onto the microelectrodes, followed by encapsulation using a PDMS layer, completing the fabrication of a single flexible Zn-I_2 hydrogel battery.

To meet the system-level energy demand, multiple battery units were configured into an integrated array through conductive interconnections. The array was designed to operate in both series and parallel modes to increase output voltage and current, respectively, thereby providing stable power for the sensing and actuation modules.

6.3 Results and Discussion

6.3.1 System Architecture and Operating Mechanism

This work targets hypothermic organ transportation and establishes a closed-loop sense-power-respond-feedback system. The platform comprises three synergistic modules including a flexible pH sensor, an electronics unit integrated with a PAM hydrogel battery array, and an active-responsive therapeutic unit consisting of a PAM/CS hydrogel and a palladium electrode. Through structural and signal coupling, these modules realize dual-track linkage of the information flow and the power flow. The integrated all-in-one patch is illustrated in Figure 6.1.

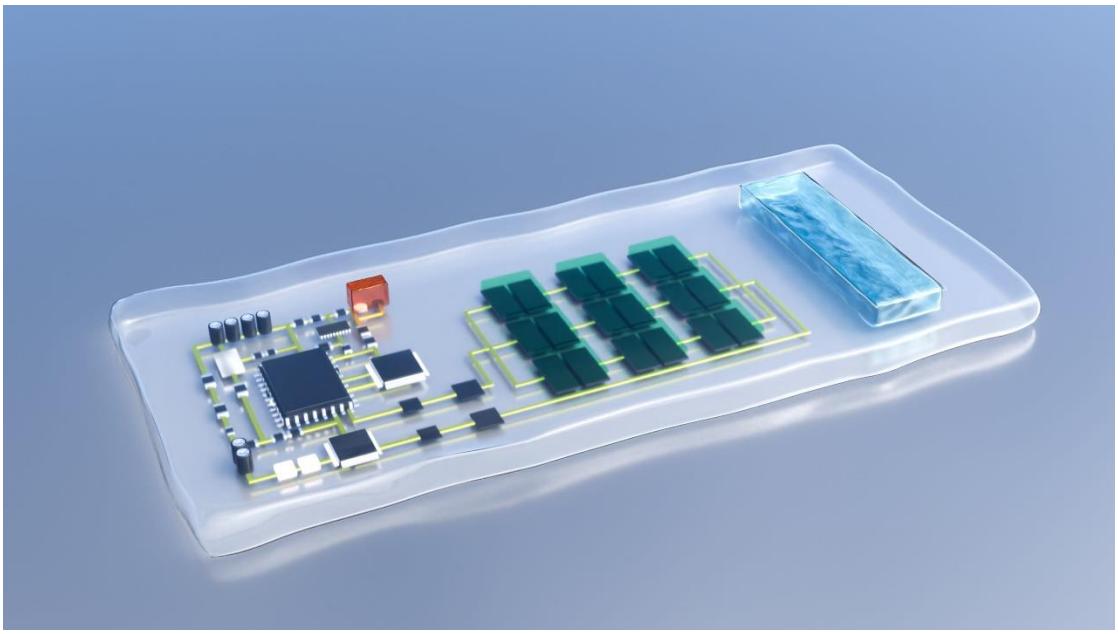

Figure 6.1 Schematic of the all-in-one hydrogel patch for hypothermic organ transport, including circuit and Bluetooth part, battery part and pH-response drug hydrogel part.

Module roles and division of function

1) Flexible pH sensor. Continuously acquires local acid-base information in the preservation medium on the organ surface. Its multilayer interfacial design provides a near-Nernstian response, anti-interference capability, and low-temperature stability, enabling early detection of acidification trends.

2) Electronics and wireless. Perform steady-state readout of high-impedance electrochemical signals, denoising/low-pass filtering, thresholding, and Bluetooth reporting for real-time display and logging on a smartphone. The circuit block diagram is shown in Figure 6.2.

3) PMA hydrogel battery array. Delivers continuous and stable power output under cold conditions; series-parallel configuration matches the required voltage and current and, after regulation, supplies the analog front end and the microcontroller.

4) Active-responsive therapeutic unit. This unit combines the passive pH-triggered release of the PAM/CS hydrogel with the active electrochemical pH modulation of the palladium electrode. Under acidification, the PAM/CS hydrogel undergoes structural expansion due to amino group protonation to accelerate NAC diffusion. Simultaneously, the electronics unit actuates the palladium electrode to actively regulate the local pH level through electrochemical proton consumption, providing a dual-mode intervention against worsening acidosis.

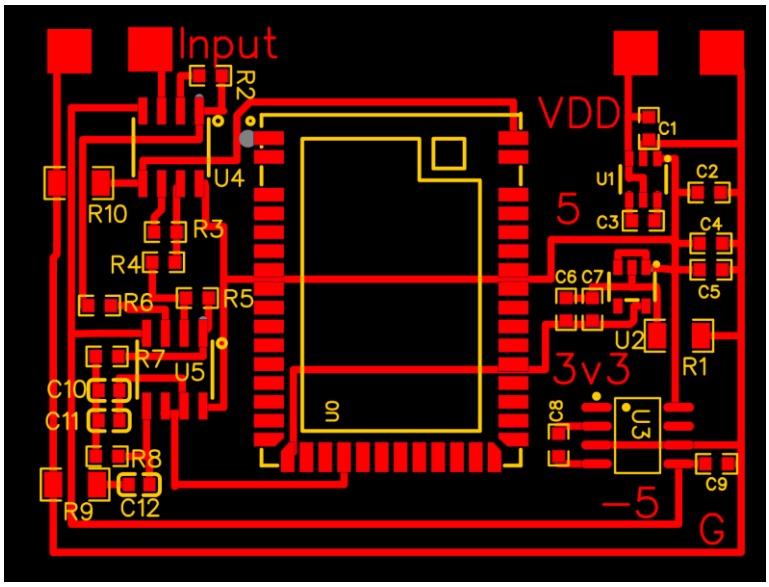

Figure 6.2 Functional circuit block diagram.

Coupling of information and power flows

The power flow originates from the battery array and, through a regulation network, supplies the analog front end and the microcontroller. The information flow starts at the pH sensor, passes through a high-input-impedance buffer and low-pass filter, then into A/D conversion and algorithmic processing, and is finally transmitted wirelessly to the mobile terminal for visualization and alerting. The drug hydrogel responds physico-chemically to environmental pH, releasing NAC and altering the local microenvironment, which in turn modulates the sensor readout-thus closing the feedback loop. Dual criteria based on absolute thresholds and temporal trends suppress sporadic noise and transient disturbances, ensuring timely and reliable interventions.

Trigger logic and closed-loop strategy

The system adopts two alert tiers plus trend detection. A primary alert flags early acidification risk, e.g., pH persistently below 6.8 for 5 min with a downward trend. A secondary alert indicates pronounced acidification, e.g., pH below 6.5 or a decline rate exceeding a preset limit. Once triggered, the smartphone issues a notification and the electronics unit activates the palladium electrode for active regulation while the PAM/CS hydrogel enters an accelerated-release regime. As NAC release remodels the microenvironment, if pH rebounds and stabilizes within the safety band, the system automatically clears the alert and archives the closed-loop event.

Low-temperature reliability and protective design

Considering temperature fluctuations and mechanical disturbances during transport, temperature adaptability of the battery array is ensured jointly by material and structural design, while the series-parallel configuration and regulation network provide supply redundancy. On the sensing side, a hydrogel protective layer suppresses interfacial dehydration and UV-induced performance degradation, preserving a repeatable electrochemical response at low temperature.

6.3.2 Flexible pH Sensor Module

During cold organ preservation, residual metabolic activities continuously generate acidic by-products such as lactic acid and CO_2, leading to gradual acidification of the surrounding microenvironment. A decrease in local pH has been widely recognized as a critical early indicator of organ dysfunction and irreversible injury. Therefore, developing a conformable pH sensor that can operate under cold and complex fluid conditions, while maintaining high sensitivity and long-term stability, is essential for real-time monitoring and early warning of organ deterioration.

Based on the electrochemical interface engineering strategies discussed in previous chapters, a flexible pH sensor was fabricated in this work for real-time surface

monitoring of preserved organs. As shown in Figure 6.3a, the sensor was constructed on a polydimethylsiloxane (PDMS) substrate and consists of a multilayer architecture: silver (Ag) base electrode, gold (Au) conduction layer, PEDOT:PSS buffer layer, polyaniline (PANI) sensing layer, a protective 5% PEDOT coating, and an outermost hydrogel encapsulation. Each layer serves a distinct function to synergistically enhance electrical conductivity, mechanical compliance, and environmental stability. Specifically, PANI functions as the pH-responsive component, where protonation and deprotonation processes modulate the electrode potential reversibly. PEDOT:PSS balances ionic-electronic coupling and improves interfacial stability, while the hydrogel/PEDOT composite encapsulation layer enhances tolerance to biofouling and chemical interference under prolonged exposure to physiological solutions such as UW preservation solutions.

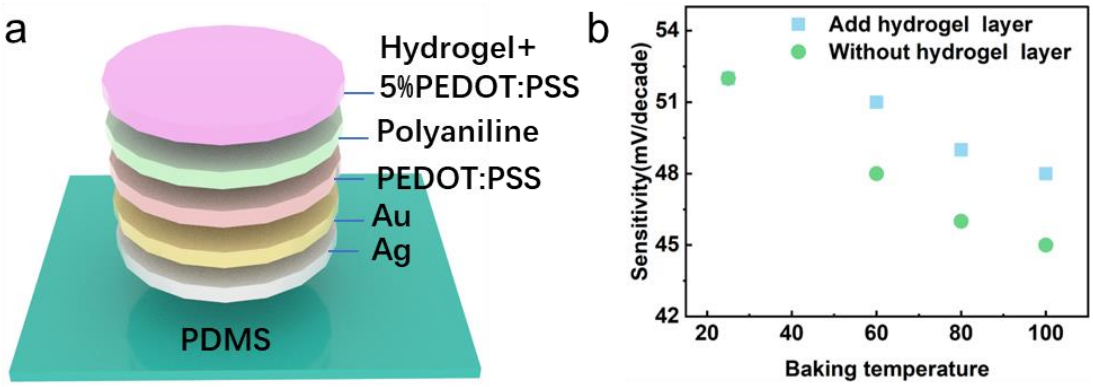

Figure 6.3 Schematic showing the structure of flexible pH sensor. Role of Hydrogel Protective Layer in Enhancing Structural. (a) Schematic showing the structure of flexible pH sensor. (b) Comparison of sensitivity of pH sensor with and without a hydrogel protective layer at various baking temperatures.

To verify the protective effect of the hydrogel layer during thermal processing, we evaluated the sensitivity of pH sensors with and without the hydrogel layer after baking at different temperatures, showing in Figure 6.3b. As illustrated in the figure, pH sensors equipped with a hydrogel protective layer consistently exhibit higher sensitivity across a range of baking temperatures compared to those without the hydrogel layer. This

difference becomes more pronounced at elevated temperatures such as 80 ℃ and 100 ℃. Specifically, the sensitivity of the unprotected sensors declines steadily from approximately 52 mV per decade to around 44 mV per decade with increasing baking temperature. In contrast, sensors incorporating a hydrogel layer maintain higher and more stable sensitivity, with values not falling below approximately 48 mV per decade. These results indicate that the hydrogel layer plays a crucial role in mitigating thermal degradation of the active sensing components, such as PEDOT:PSS and polyaniline, during the baking process. The hydrogel may help preserve the structural and interfacial integrity of the sensing layer by retaining local moisture, minimizing molecular rearrangements, stabilizing interfacial charge distribution, and enhancing durability in biological environments.

To evaluate the fundamental electrochemical performance, the sensor was tested in buffer solutions with pH ranging from 4 to 8 at 25 ℃. As illustrated in Figure 6.4a, the sensor exhibited a near-Nernstian response with a sensitivity of 52 mV per decade, despite being constructed on a soft PDMS substrate. This high sensitivity is attributed to the efficient proton transport across the hydrated PANI layer and the optimized interfacial architecture enabling rapid charge redistribution. Sensor selectivity was also evaluated by introducing common interfering species in organ transport environments, including 50 mM Na^+, 100 mM K^+, and 5 mM glucose. As shown in Figure 6.4b, the potential response remained stable with negligible drift upon sequential addition of these analytes, confirming the high ion selectivity of the sensor. This robustness is largely attributed to the specific interaction of PANI with protons, as well as the protective role of the PEDOT:PSS layer in suppressing non-specific ionic perturbations.

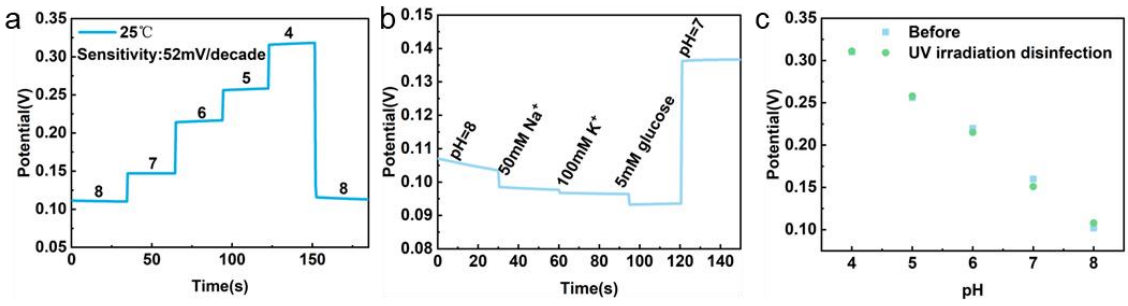

Figure 6.4 Fundamental performance evaluation of the flexible pH sensor. (a) Potentiometric response of the sensor to standard buffer solutions ranging from pH 4 to 8 at 25 ℃. (b) Selectivity assessment of the sensor under the interference of 50 mM Na^+, 100 mM K^+, and 5 mM glucose at pH 8 and pH 7. (c) Comparison of potentiometric response before and after ultraviolet (UV) irradiation.

Given that ultraviolet (UV) irradiation is commonly required for disinfection of medical devices prior to organ application, the stability of the sensor under UV exposure was also investigated. As shown in Figure 6.4c, the calibration curves before and after UV treatment remained consistent, indicating that the sensor maintained its structural and functional integrity. This UV resistance is likely due to the stable π-conjugated structures of PANI and PEDOT, and the encapsulating hydrogel layer that mitigates photodegradation and oxidation. In summary, the flexible pH sensor demonstrated high sensitivity, excellent selectivity, and robust stability against ionic interference, ultraviolet radiation, and long-term immersion in biofluid analogues. Its design ensures excellent biocompatibility, conformability to irregular organ surfaces, and stable electrochemical performance, making it a crucial component in the sensing-powering-intervention strategy of the integrated system.

To comprehensively evaluate the reliability of the developed flexible pH sensor for practical applications, a series of performance tests were conducted to assess its reproducibility, long-term operational stability, and mechanical durability. As shown in Figure 6.5a, three independently fabricated sensors exhibited nearly identical potential responses across a pH range from 4 to 8. All devices demonstrated well-defined stepwise voltage changes with a consistent sensitivity of approximately 52 mV per decade, in agreement with the theoretical Nernstian behavior. These results confirm the excellent fabrication consistency and reproducibility of the sensor.

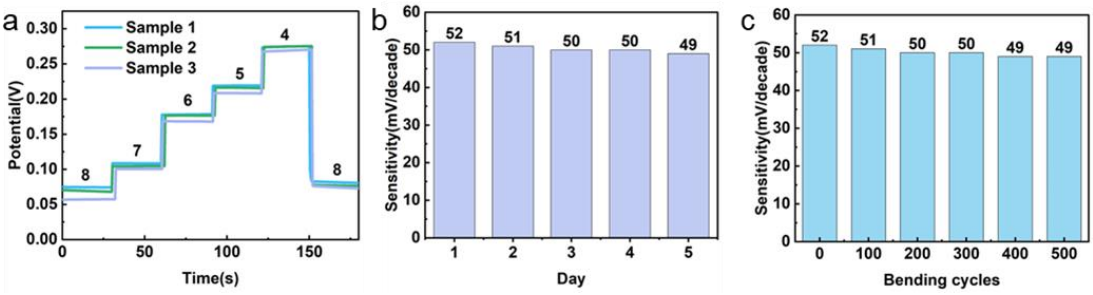

Figure 6.5 Evaluation of the Stability Performance of the Flexible pH Sensor. (a) Reproducibility of the pH sensor across three independently fabricated samples. (b) Long-term stability of the pH sensor over five consecutive days. (c) Mechanical stability of the pH sensor under 500 bending cycles.

To assess long-term stability, the sensors were tested over a continuous five-day period under ambient storage conditions. As illustrated in Figure 6.5b, the sensitivity showed only a slight decrease from 52 to 49 mV per decade, indicating strong durability during prolonged usage. Furthermore, considering the dynamic deformation environments encountered during organ transportation, the mechanical robustness of the sensor was evaluated through repeated bending tests. As shown in Figure 6.5c, the sensor maintained stable electrochemical performance after 500 bending cycles, with only minimal sensitivity degradation. Collectively, these results demonstrate that the flexible pH sensor exhibits excellent reproducibility, long-term stability, and mechanical resilience, making it well-suited for continuous monitoring in complex and dynamic biomedical scenarios.

To evaluate the feasibility of applying the proposed flexible pH sensor in cold preservation conditions, its sensitivity was systematically assessed at various temperatures relevant to organ transport, including 25 ℃, 4 ℃, 0 ℃, and -2 ℃. As shown in the figure, the sensor exhibited a sensitivity of 52 mV/decade at room temperature (25 ℃), closely approaching the theoretical Nernstian response. More importantly, the sensitivity remained relatively stable with decreasing temperature,

measuring 48 mV/decade at both 4 ℃ and 0 ℃, and only slightly decreasing to 47 mV/decade at -2 ℃. These results demonstrate that the sensor maintains reliable performance under hypothermic conditions typically employed during static cold storage using UW solution.

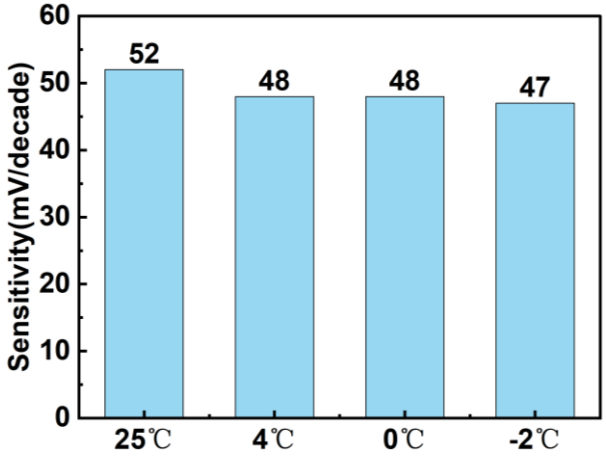

Figure 6.6 Sensitivity of the flexible pH sensor under different temperatures (25 ℃, 4 ℃, 0 ℃, and -2 ℃)

The robust low-temperature functionality can be attributed to the combination of conductive polymer interfaces and the hydrogel protective layer, which preserves ionic conductivity and maintains effective electrochemical transduction even at subzero temperatures. This temperature resilience is critical for real-time biochemical monitoring during organ transportation, where environmental conditions often fluctuate and conventional sensors may suffer from signal degradation.

To comprehensively evaluate the long-term stability of the flexible pH sensor under continuous operation, a 13-hour real-time potential monitoring test was conducted in simulated low-temperature organ preservation buffer. As shown in Figure 6.7, the sensor was initially exposed to a pH 7 buffer solution for 6 hours, during which the output potential remained highly stable with minimal fluctuation and no significant drift.

This indicates excellent electrochemical stability under near-neutral physiological conditions. Subsequently, the buffer was replaced with a pH 8 solution. The sensor responded rapidly and reached a new steady-state potential, maintaining consistent output for the remaining 7 hours of testing without noticeable signal degradation or increased noise. These results demonstrate the sensor's outstanding capability to deliver stable and reliable readings over extended periods, a critical requirement for real-time physiological monitoring during cold organ transportation.

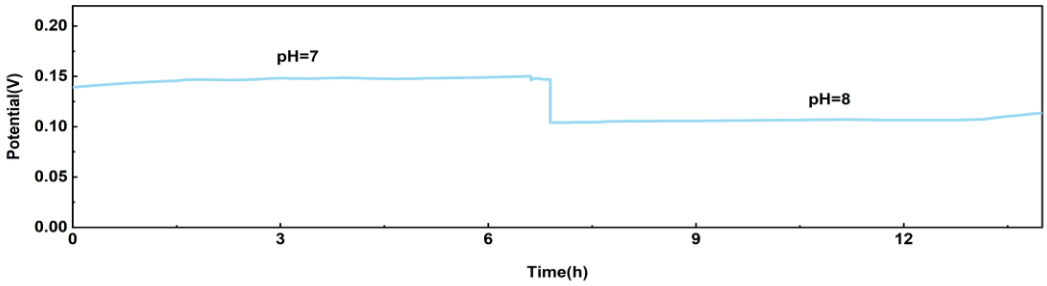

Figure 6.7 Potential response of the pH sensor continuously monitored over 13 hours under cold storage conditions.

In summary, a flexible and conformable pH sensor was successfully developed to address the critical need for real-time biochemical monitoring during cold organ preservation. Through the rational design of a multilayered sensing architecture comprising PEDOT:PSS and polyaniline interfaces protected by a hydrogel encapsulation, the sensor demonstrates near Nernstian sensitivity, excellent selectivity, and strong resistance to thermal degradation, photochemical stress, and ionic interference. Systematic evaluations confirmed the sensor’s outstanding reproducibility, long-term operational stability over five days, mechanical robustness after 500 bending cycles, and consistent electrochemical performance under hypothermic conditions as low as minus two degrees Celsius. Moreover, extended monitoring over thirteen hours revealed highly stable potential output with minimal drift, validating its reliability for

continuous use in complex physiological environments. These comprehensive results highlight the sensor's suitability as a critical component of an integrated sensing and intervention platform for intelligent organ preservation and transplant management.

6.3.3 Characterization of the Active Responsive Therapeutic Unit

The active-responsive therapeutic unit developed in this study was constructed by integrating a PAM/CS pH-responsive hydrogel with a nanostructured palladium electrode. This configuration was designed to enable both passive physicochemical responsiveness to environmental pH fluctuations and active electrochemical regulation of the local microenvironment. Within the hydrogel network, chitosan components provide the basis for structural transition. Under acidic conditions, the amino groups of chitosan are readily protonated to positively charged ions, inducing strong electrostatic repulsion between polymer chains and thereby expanding the hydrogel network. This process facilitates enhanced swelling and promotes the opening of diffusion channels for the controlled release of N-acetylcysteine NAC. Simultaneously, the integrated palladium electrode enables active pH modulation through electrochemical proton consumption, providing a synergistic intervention strategy. The combination of stimulus-triggered drug delivery and active chemical regulation endows the unit with comprehensive therapeutic functionality tailored for the organ microenvironment.

To further verify the chemical composition and the successful incorporation of chitosan into the PAM framework, X-ray photoelectron spectroscopy (XPS) was employed to analyze the surface elemental states shown in Figure 6.8. The N1s high-resolution spectra of hydrogels with varying PAM/CS ratios provide clear evidence of the hybrid network formation. For the PAM components, the N1s signal is primarily deconvoluted into two characteristic peaks including the C-N peak located around 399.5 eV and the N-H peak around 401 eV. Upon the integration of CS, a distinct peak appears at approximately 398 eV which is attributed to the amine groups within the chitosan molecular chains. Notably, as the proportion of CS in the hydrogel increases, the intensity of the peak at 398 eV exhibits a progressive enhancement. This trend

demonstrates that the chemical environment of the therapeutic unit can be precisely controlled by adjusting the monomer ratios. The quantitative correlation between the peak area and the CS content substantiates the successful construction of the semi-interpenetrating polymer network and confirms the availability of functional amino groups for pH-triggered responses.

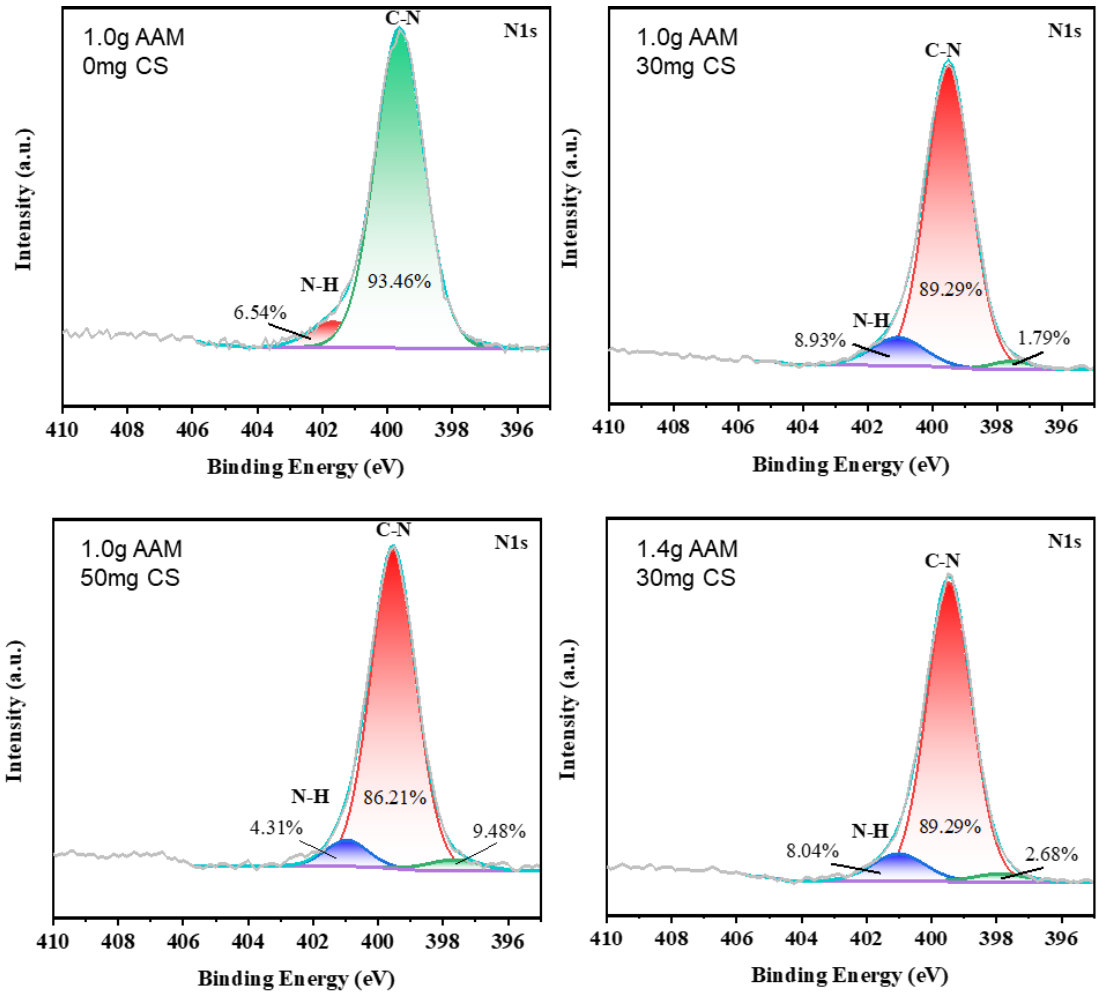

Figure 6.8 High resolution N 1s XPS spectra of PAM/CS hydrogels with varying mass ratios.

To maximize the pH sensitivity of the active-responsive therapeutic unit, the composition of the PAM/CS hydrogel was systematically optimized by evaluating its swelling performance under physiological and pathological conditions. Throughout the optimization process, the foundational components including 1 mL of 0.8% AcOH, 2 mL of MES buffer, 1.5 mL of TEMED, and 7 mg of APS remained constant. The

investigation primarily focused on the influence of CS content at 40 mg and 50 mg. This range was selected because 30 mg of CS exhibited insufficient pH responsiveness while concentrations exceeding 60 mg faced significant dissolution challenges. Alongside CS variations, the synergistic impacts of different MBAA molar percentages and AAm monomer weights were evaluated (Table 6.1).

Sample	Am (g)	MBAA (mol %)	Sample	Am (g)	MBAA (mol %)
G1	0.8	0.20	G3	1.2	0.20
	0.8	0.25		1.2	0.25
	0.8	0.30		1.2	0.30
	0.8	0.35		1.2	0.35
	0.8	0.40		1.2	0.40
	0.8	0.45		1.2	0.45
G2	1.0	0.20	G4	1.4	0.20
	1.0	0.25		1.4	0.25
	1.0	0.30		1.4	0.30
	1.0	0.35		1.4	0.35
	1.0	0.40		1.4	0.40
	1.0	0.45		1.4	0.45

Table 6.1 Composition and formulation details of PAM-CS hydrogels with varying Am and CS content.

The optimization criterion was defined as the swelling ratio difference between pH 7.5 and pH 6.8, representing the critical transition range during organ preservation. A detailed comparison revealed that the CS content plays a dominant role in determining

the magnitude of the response. Specifically, as shown in Figure 6.9 the hydrogel containing 50 mg of CS exhibited a more pronounced swelling increase than the 40 mg group. This is attributed to the higher density of primary amino groups within the network that undergo extensive protonation under acidic conditions, generating stronger electrostatic repulsion to drive the expansion of the semi-IPN framework. Furthermore, the crosslinking density determined by MBAA and AAm was found to significantly modulate network elasticity and porosity. While higher crosslinking degrees inherently restricted hydrogel expansion, an overly loose network lacked the mechanical stability required for device integration. After a comprehensive evaluation, the combination of 40 mol% MBAA, 50 mg CS, and 1.0 g AAm was identified as the optimized composition. This formulation achieves the maximum swelling contrast, ensuring the therapeutic unit provides a highly sensitive and reliable response to environmental acidification.

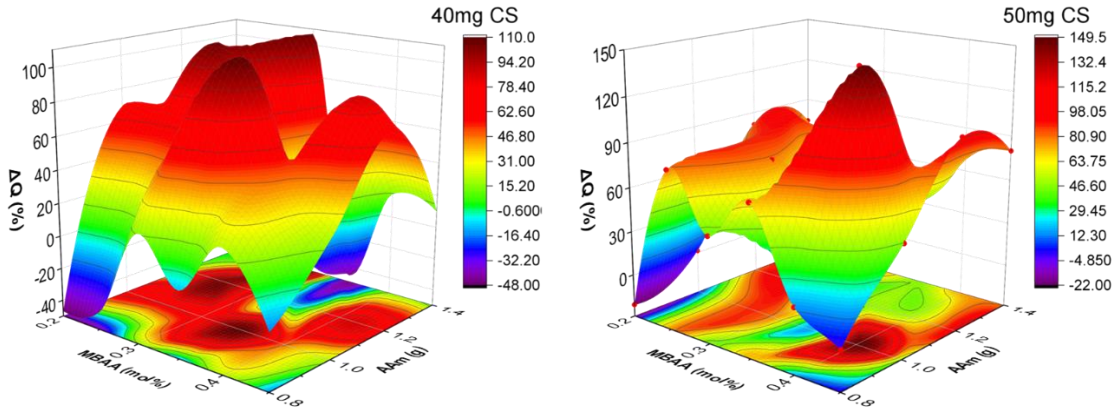

Figure 6.9 Optimization of PAM/CS hydrogel formulations based on swelling ratio differences between pH 7.5 and pH 6.8.

EIS was employed to evaluate the dynamic response of the PAM/CS hydrogel in phosphate buffered saline PBS at different pH values including 6.0, 7.4, and 8.0 as shown in Figure 6.10. The NAC loaded hydrogel was immersed in these media and monitored over a 36 hour period. Across all pH conditions, impedance values decreased

progressively and stabilized after approximately 10 hours which indicates the progression of drug release and internal ion equilibration. Specifically, the sample in the pH 6.0 solution demonstrated the lowest initial impedance and the most significant reduction over time. This trend suggests that the semi-interpenetrating polymer network semi-IPN remains more porous in acidic environments due to the protonation of chitosan amino groups and the resulting electrostatic repulsion which facilitates ion mobility and drug transport. In contrast, the pH 7.4 group exhibited the highest impedance likely because the deprotonated chitosan chains maintain a denser polymer matrix with limited fluid exchange. The pH 8.0 condition also resulted in a suppressed response with minimal impedance variation. These results collectively demonstrate that the PAM/CS hydrogel exhibits high sensitivity and structural adaptability under acidic conditions, enabling it to provide timely biochemical intervention in response to pathological acidification during organ transport.

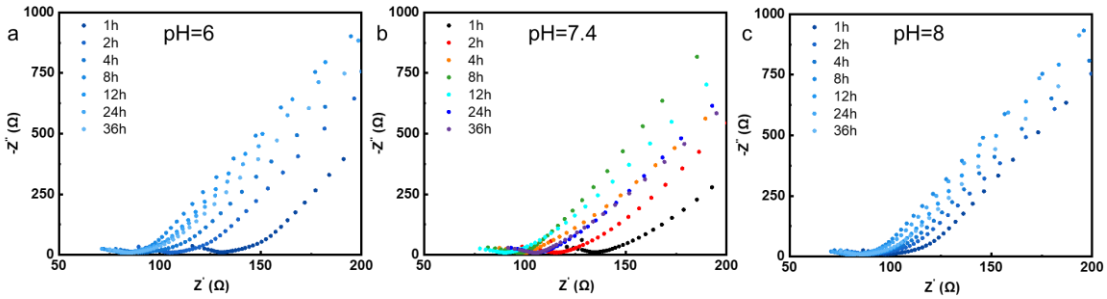

Figure 6.10 EIS spectra of NAC-loaded hydrogels in PBS at pH 6.0, 7.4, and 8.0 over 36 hours.

To systematically evaluate the impact of hydrogel state including dry and wet forms on drug adsorption efficiency, this study performed a series of experiments with the PAM/CS hydrogels engineered for the therapeutic unit as shown in Figure 6.11. The hydrogels were immersed in different concentrations such as 5 mg/mL, 10 mg/mL, and 20 mg/mL of N-acetylcysteine NAC solution to test their drug adsorption capabilities. The drug loading was quantified by UV-Vis spectroscopy where the absorbance of

standard NAC solutions was measured first to develop a standard curve. This standard curve was then used to calculate the NAC concentration sequestered within the hydrogel samples. Samples were taken at specific time intervals ranging from 1 to 15 hours and treated with Ellmans reagent DTNB derivatization for analysis using UV-Vis spectroscopy at 412 nm to determine the equilibrium loading capacity of NAC within the hydrogel.

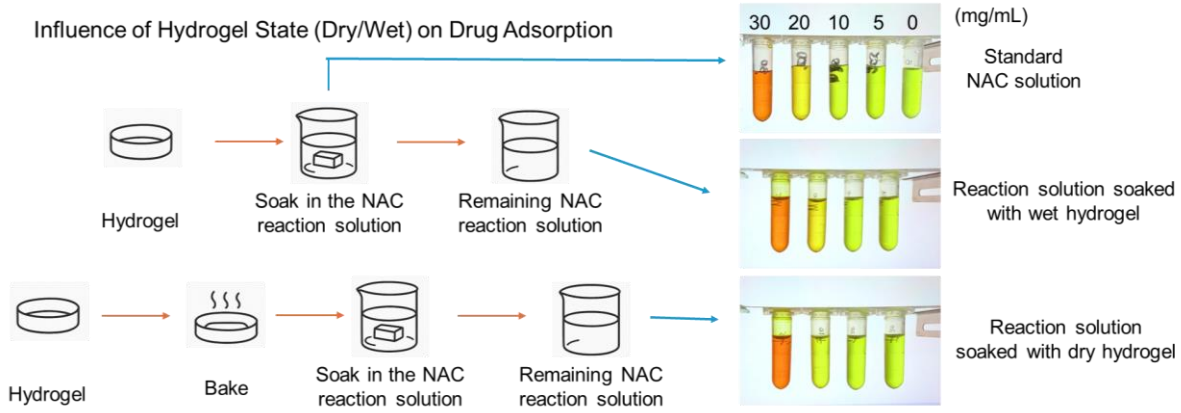

Figure 6.11 Experimental setup for studying the influence of hydrogel state (dry vs. wet) on drug adsorption.

As shown in Figure 6.12, dry hydrogels exhibited relatively low drug loading across all concentrations of NAC. At 5 mg/mL, the adsorption amount was 0.226 mg, while at 10 mg/mL and 20 mg/mL, the loading values were 1.367 mg and 0.467 mg respectively. These results indicate that dry hydrogels have limited molecular uptake, especially in higher concentration solutions where the adsorption efficiency is constrained by the compact and rigid network structure that prevents significant swelling during the loading process. In contrast, wet hydrogels demonstrated significantly higher drug loading efficiency at the same concentrations. At 5 mg/mL, the loading amount was 0.31 mg which represents a 37% increase over the dry hydrogel. At 10 mg/mL and 20 mg/mL, the amounts were 1.65 mg and 0.69 mg respectively reflecting a substantial

increase compared to the dry hydrogels. This suggests that the pre-hydrated wet hydrogel has a superior adsorption capacity owing to its expanded and accessible network structure within the semi-interpenetrating polymer network semi-IPN which allows for more effective solute diffusion and entrapment of drug molecules.

Sample	Concentration (mg/mL)	Pre-mass (g)	Pre-AA	Post-mass (g)	Post-AA	Gel-weight (mg)	Drug loading rate
Dry hydrogel	5	1.457	0.74062	1.278	0.71885	19.9	0.226
	10	1.473	0.80155	1.275	0.27154	19.4	1.367
	20	1.461	0.92615	1.211	0.71074	32.3	0.467
Wet hydrogel	5	1.451	0.71885	1.451	0.62052	15.1	0.31
	10	1.467	0.80155	1.45	0.36161	12.9	**1.65**
	20	1.464	0.92615	1.435	0.73274	14.3	0.69

Table 6.2 Drug loading rate of hydrogel under dry and wet state

In summary, the state of the hydrogel has a significant impact on drug loading capacity. Wet hydrogels not only exhibit higher adsorption efficiency but also demonstrate enhanced potential for controlled drug release. This makes wet hydrogels an ideal choice for drug delivery systems, especially in applications where sustained release or rapid release triggered by physiological conditions is needed. Based on the results of this experiment, wet hydrogels show distinct advantages in drug delivery application.

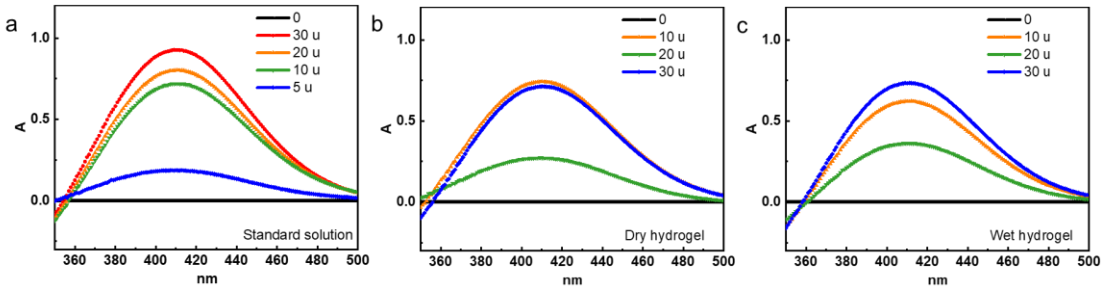

Figure 6.12 UV-Vis spectra of NAC standard solution and NAC-loaded hydrogels. (a) The UV-Vis spectrum of the standard NAC solution used for calibration. (b) UV-Vis spectrum of the NAC-loaded dry hydrogel. (c) UV-Vis spectrum of the NAC-loaded wet hydroge.

Following the evaluation of drug loading capacity, the pH responsive drug release behavior of the synthesized PAM/CS hydrogel was systematically investigated under simulated acidic conditions. N-acetylcysteine NAC was employed as a model drug for this release experiment which utilized DTNB derivatization and UV-Vis spectroscopy. The NAC loaded hydrogel was immersed in phosphate buffered saline PBS solutions with different pH values including 7.5, 7.0, 6.8, and 6.5. Aliquots were collected at predetermined time intervals ranging from 1 to 15 hours as shown in Figure 6.13. Each collected sample was subsequently treated with Ellmans reagent 5,5′-dithiobis-2-nitrobenzoic acid DTNB which reacts specifically with thiol groups in NAC to generate the yellow colored TNB^{2-} derivative. This derivative exhibits a characteristic absorbance peak near 412 nm which enables the quantitative analysis of NAC release.

The UV-Vis spectra demonstrate a clear pH dependent drug release profile. At pH 7.5, the hydrogel remained relatively stable and exhibited only a limited absorbance increase below 0.6 at 412 nm after 15 hours. This indicates minimal passive diffusion of NAC under physiological conditions. In contrast, as the environment became more acidic, a moderate enhancement in absorbance was observed at pH 7.0 with the peak reaching approximately 1.0. As the pH decreased further to 6.8 and 6.5, the absorbance intensities

increased substantially with peak values approaching 1.6 and 2.1 respectively. The sharper slope of the release curves under these acidic conditions reflects accelerated release kinetics. This pH sensitive behavior arises from the protonation of amino group.

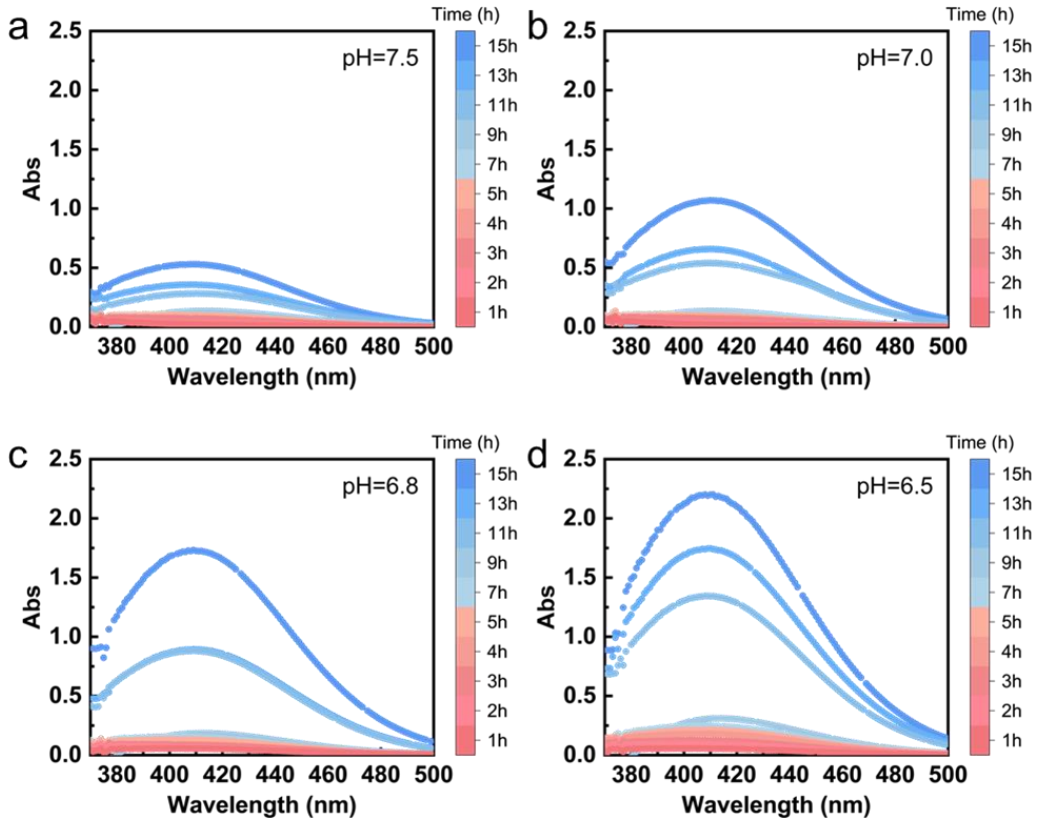

Figure 6.13 pH-dependent drug release behavior of NAC-loaded PAM-CS hydrogel. The hydrogel was immersed in PBS at different pH values, including (a) pH=7.5, (b) pH=7.0, (c) pH=6.8, and (d) pH=6.5 over a 15-hour period.

To further investigate the release characteristics of N-acetylcysteine (NAC), the drug release behavior of the hydrogel was analyzed using high-performance liquid chromatography (HPLC). Initially, the absorbance of standard NAC solutions was measured and analyzed by HPLC to establish a linear relationship between concentration and absorbance (Figure 6.14). This standard curve provided a reliable basis for the subsequent calculation of drug release.

In the drug release experiment, the hydrogel was immersed in PBS buffer at pH 6.5, and samples were taken at various time intervals for HPLC analysis. The results showed that the NAC concentration in the solution increased rapidly at the beginning and gradually decreased after 18 hours. This phenomenon can be attributed to several factors: initially, the drug molecules in the hydrogel are quickly released due to the swelling of the hydrogel network, leading to a rapid increase in NAC concentration in the solution. As the drug is gradually released, the concentration of NAC within the hydrogel decreases, and the concentration of NAC in the solution stabilizes. However, over time, the concentration of NAC in the solution begins to decrease. This decline indicates that most of the drug molecules have already been released from the hydrogel, and the release rate of the remaining drug slows down. At this stage, the drug concentration within the hydrogel reaches equilibrium, and the continued release is limited, causing the NAC concentration in the solution to gradually decrease. In summary, the hydrogel exhibits pH-responsive behavior under acidic conditions, enabling rapid initial release followed by slower release in the later stages. This characteristic provides a crucial foundation for applications that require precise control of drug release rates, especially in localized acidic pathological environments, where on-demand drug delivery is needed.

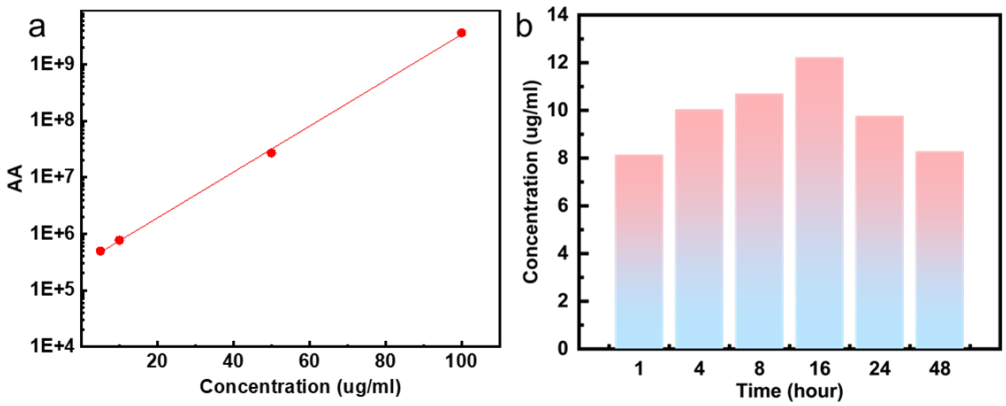

Figure 6.14 HPLC analysis of NAC drug release from hydrogel under different conditions. (a) Linear calibration curve of NAC concentration based on the absorbance

at 412 nm in the standard NAC solution, R^2=0.999. (b) Drug release profile of NAC from the hydrogel under pH=6.5.

Following the systematic optimization and chemical characterization of the PAM/CS hydrogel components, it is essential to evaluate the electrochemical properties of the integrated palladium electrode which serves as the active regulation unit. The electrochemical synthesis and growth behavior of the nanostructured palladium black interface were characterized and monitored using cyclic voltammetry CV as illustrated in Figure 6.15. This procedure was performed on the gold-plated silver substrate to ensure high surface activity and operational stability. The CV profiles recorded within a potential range from -0.3 V to 0.8 V exhibit the distinct redox fingerprints of palladium in the acidic chloride electrolyte. During the cathodic scan, a prominent reduction current is observed at potentials more negative than 0 V which represents the simultaneous deposition of palladium black, the evolution of hydrogen, and the formation of palladium hydride according to the following reactions.

$$Pd^{2+} + 2e^- \rightarrow Pd \tag{6.1}$$

$$2H^+ + 2e^- \rightarrow H_2 \tag{6.2}$$

$$Pd + xH^+ \rightarrow PdH_x \tag{6.3}$$

This electrochemical process results in a highly porous and nanostructured surface which is essential for maximizing the effective area for proton exchange. In the subsequent anodic scan, a sharp and well-defined peak appearing between 0.1 V and 0.3 V corresponds to the release of absorbed hydrogen from the palladium lattice as expressed below.

$$PdH_x \rightarrow Pd + H^+ \tag{6.4}$$

Furthermore, an additional oxidation peak is observed at higher potentials around 0.7 V which is attributed to the surface oxidation cleaning process.

$$Pd + H_2O \rightarrow PdO + 2H^+ + 2e^- \quad (6.5)$$

This step effectively removes impurity ions from the electrode surface and ensures the exposure of fresh catalytic sites. The cathodic peak observed upon reversing the scan at approximately 0.2 V represents the removal of the oxide layer through the following process.

$$PdO + 2H^+ + 2e^- \rightarrow Pd + H_2O \quad (6.6)$$

The steady overlap of these electrochemical signatures across multiple cycles confirms the stability and reproducibility of the electrodeposition process. This engineered palladium interface provides the necessary electrochemical sites for active proton flux management, serving as the functional foundation for the therapeutic intervention strategy.

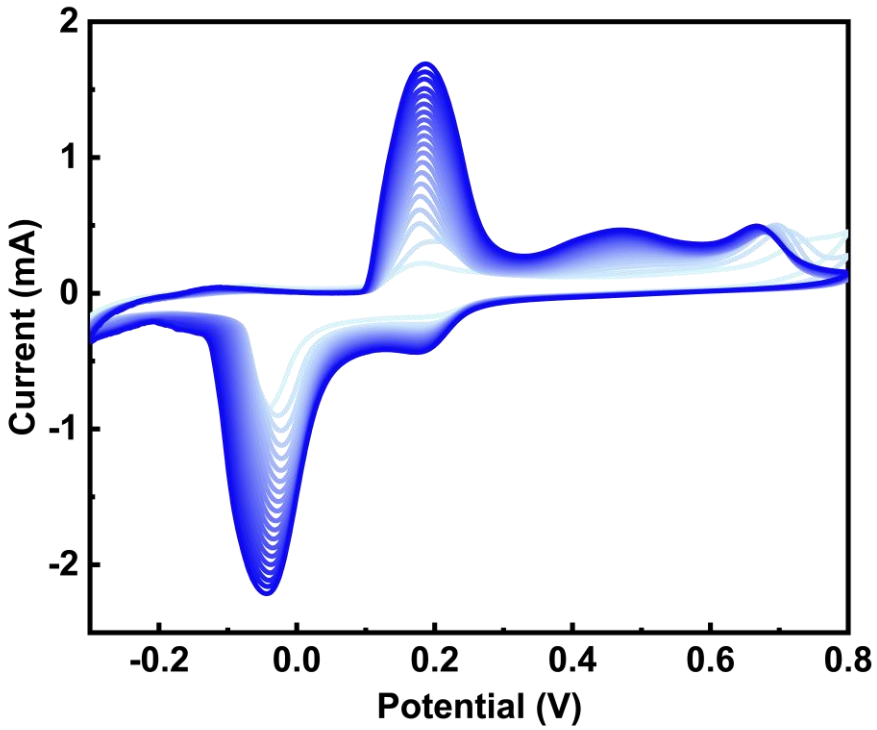

Figure 6.15 Cyclic voltammetry profiles for the electrodeposition of nanostructured palladium black on the gold-plated silver substrate for active pH regulation

Following the analysis of the redox peaks identified in the cyclic voltammetry CV fabrication process, the concentration of the palladium chloride electrolyte was systematically optimized to improve the active pH regulation capability of the therapeutic unit. The electrolyte concentration was adjusted across a range including 7, 28, 56, and 76 mM to determine the most effective deposition condition. The galvanostatic charge discharge CP method was employed as the primary evaluative tool to determine the hydrogen storage capacity and kinetic efficiency of the resulting electrodes, where a constant current of 10 μA was applied during the measurement to ensure a stable electrochemical response.. The evaluation principle of the CP method relies on the reversible electrochemical absorption and desorption of hydrogen within the palladium lattice. During the cathodic charging phase, protons are reduced and incorporated into the metal bulk to form palladium hydride.

$$Pd + xH^+ + xe^- \rightarrow PdH_x \tag{6.7}$$

In the subsequent anodic discharging phase, the absorbed hydrogen is oxidized and released back into the environment as protons.

$$PdH_x \rightarrow Pd + xH^+ + xe^- \tag{6.8}$$

The duration of the potential plateau during these processes serves as a direct measure of the effective proton flux and total storage capacity. Specifically, the discharge time represents the total amount of hydrogen available for active pH regulation, where a longer and more stable plateau signifies superior performance for sustained biochemical intervention during organ transport.

Analysis of the 7 mM and 28 mM samples showed efficient and reversible behavior, with the 28 mM concentration achieving an optimal energy efficiency of approximately

86% alongside high structural integrity (Figure 6.16). However, a significant anomaly was observed in the 56 mM and 76 mM samples where the discharge duration far exceeded the charging time. This phenomenon is identified as a dense film artifact. At these high concentrations, the electrodeposited palladium forms a non-porous and overly thick layer which hinders the internal diffusion of hydrogen atoms. The resulting sluggish mass transport kinetics cause a slow potential drift during the anodic phase which artificially extends the measured discharge time and masks the inherently low capacity of the electrode. This extended duration is a manifestation of mass transport resistance rather than an indicator of high storage capacity. Consequently, the 28 mM concentration was selected as the optimal parameter because it provides the best balance between high catalytic surface area and rapid hydrogen diffusion kinetics.

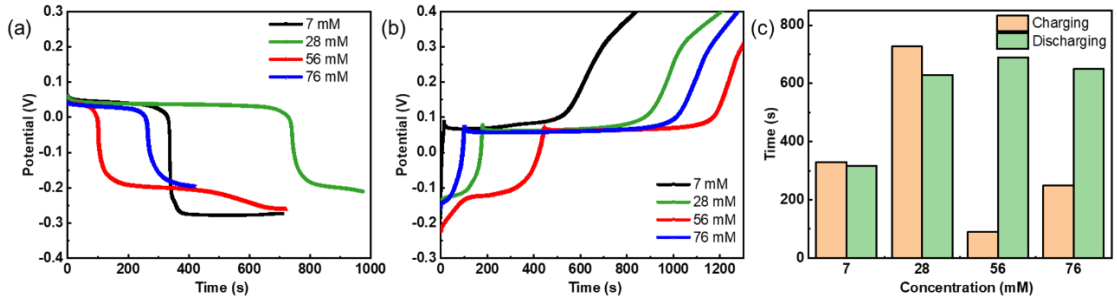

Figure 6.16 Hydrogen storage performance and morphology of palladium electrodes across varying electrolyte concentrations. (a-b) Galvanostatic charging and discharging curves at 10 microamperes. (c) Comparison of charge-discharge duration.

After establishing 28 mM as the optimal electrolyte concentration, the scan rate and cycle number of the CV process were systematically tuned to refine the morphology and stability of the palladium black interface. The study compared four specific parameter combinations including 1 mV/s with 10 cycles, 1 mV/s with 20 cycles, 5 mV/s with 30 cycles, and 5 mV/s with 50 cycles. These parameters were selected to balance the effective surface area against the mechanical robustness of the electrode. It

was observed that excessively high scan rates such as 5 mV/s hindered the formation of the characteristic cauliflower-like nanostructure which is essential for high catalytic activity. Conversely, an overabundance of deposition cycles led to a decrease in structural stability, potentially causing the active layer to peel off during operation.

To evaluate the hydrogen storage performance of these samples while maintaining time efficiency, the galvanostatic charge discharge CP method was employed at a higher current density of 100 μA. This adjustment allowed for rapid screening without compromising the relative performance trends between the different groups.

As illustrated in Figure 6.17, the electrodes prepared at a slow scan rate of 1 mV/s demonstrated superior proton flux and longer potential plateaus compared to those prepared at 5 mV/s. While both the 10-cycle and 20-cycle samples at 1 mV/s provided excellent electrochemical responses, the time cost was a critical factor for system fabrication. Specifically, the 10-cycle process required approximately 5 hours to complete, whereas the 20-cycle process extended the duration to 10 hours without providing a proportional increase in functional capacity. Therefore, the 1 mV/s with 10 cycles configuration was identified as the optimal deposition parameter. This selection ensures a highly active cauliflower-like palladium interface with optimal stability and manufacturing efficiency for the integrated therapeutic unit.

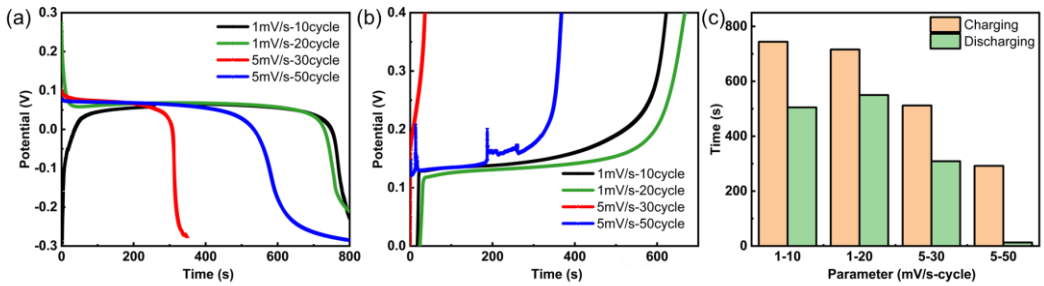

Figure 6.17 Hydrogen storage performance and morphology of palladium electrodes across varying scanning speed and cycles. (a-b) Galvanostatic charging and discharging curves at 10 microamperes. (c) Comparison of charge-discharge duration.

To gain deeper insights into the structural foundation of the superior electrochemical performance, the surface morphology of the optimized palladium electrode prepared with a 28 mM electrolyte at 1 mV/s for 10 cycles was characterized using SEM. As illustrated in Figure 6.18, the SEM micrograph reveals a highly uniform and hierarchical nanostructure across the electrode surface. The most prominent feature is the formation of dense cauliflower-like clusters which are composed of numerous interconnected palladium nanoparticles. This unique cauliflower-like morphology significantly increases the effective electroactive surface area compared to a flat film.

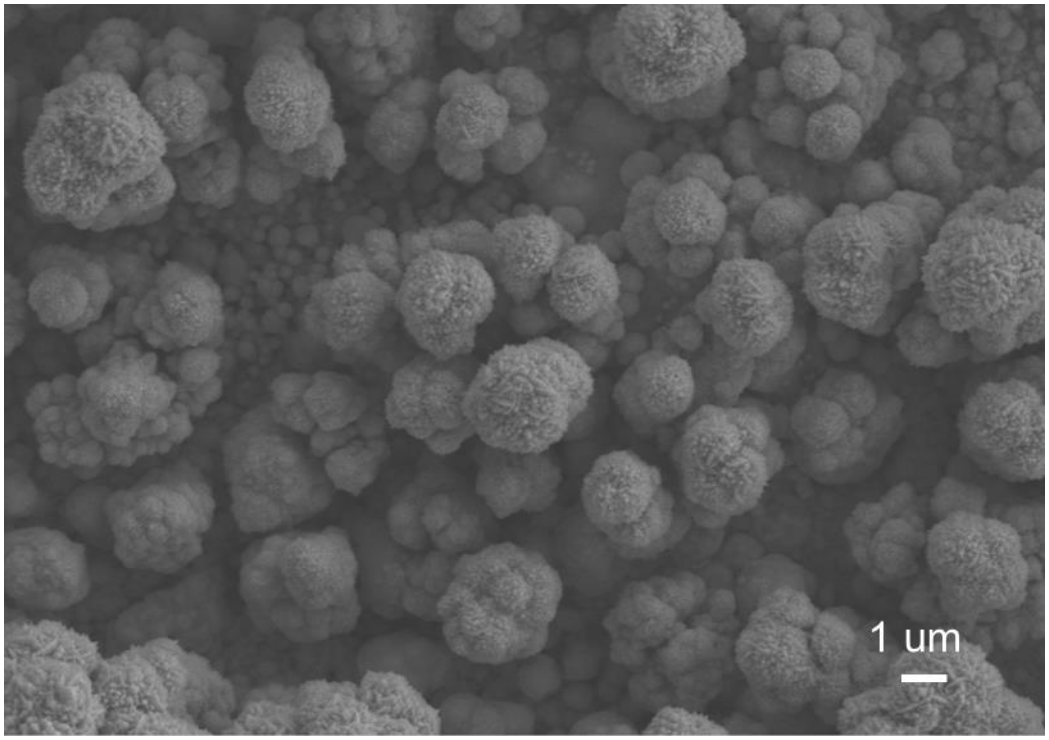

Figure 6.18 SEM image showing the morphology of pallium black surface.

To further confirm the elemental identity of the cauliflower-like nanostructures observed in the SEM micrographs, energy dispersive spectroscopy EDS analysis was performed on the optimized palladium electrode. As illustrated in Figure 6.19, the EDS

mapping results provide a clear spatial distribution of elements across the hierarchical surface. The elemental quantification reveals that palladium is the primary component of the porous clusters which confirms that the nanostructured cauliflower-like features are indeed formed by the electrodeposition of palladium black.

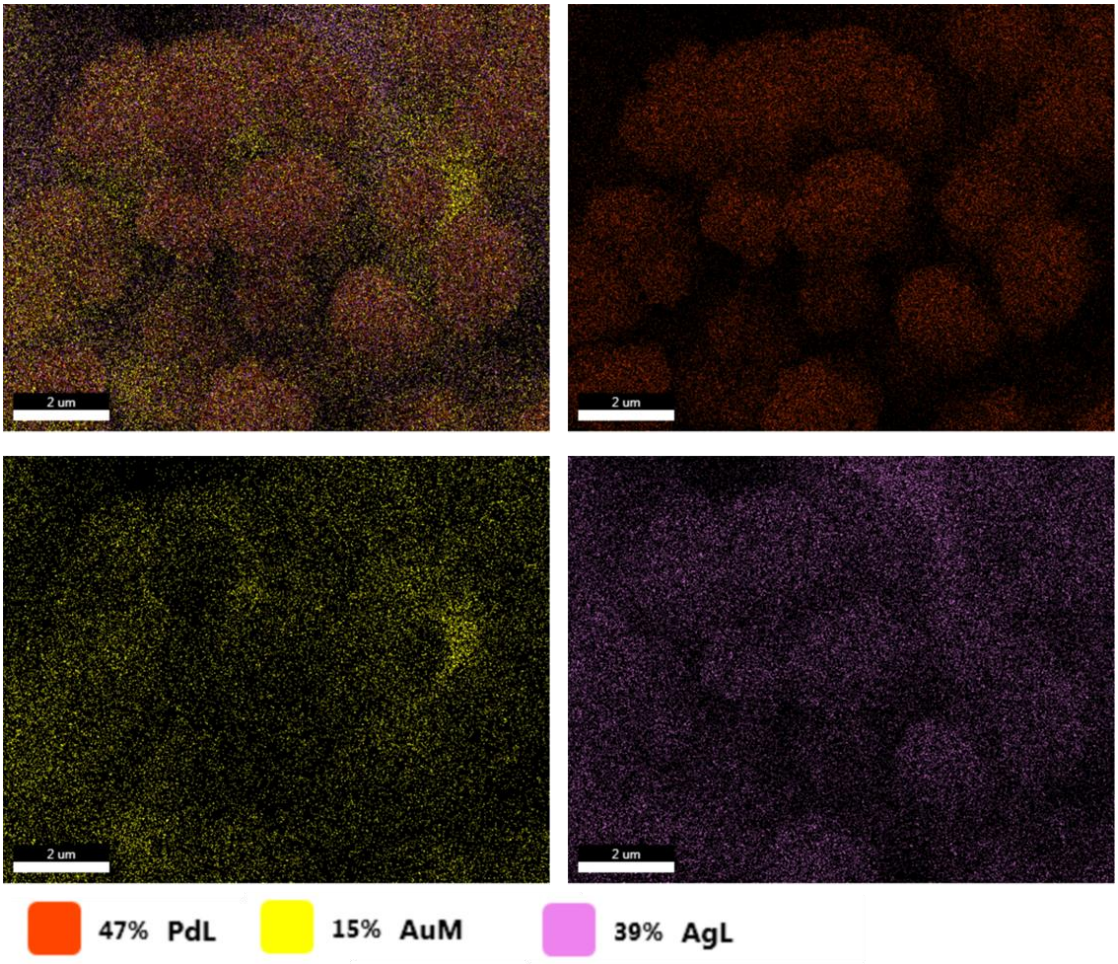

Figure 6.19 EDS elemental mapping and quantification of the optimized palladium electrode.

The presence of such a porous and three-dimensional framework is essential for the active pH regulation unit as it provides abundant catalytic sites for the reversible protonation reactions. The microscopic observations confirm that the slow scan rate of 1 mV/s allows for sufficient nucleation and controlled growth of palladium crystals, leading to a stable and non-peeling layer. This well-distributed nanostructure facilitates rapid ion transport and efficient hydrogen atom diffusion within the metal lattice,

thereby supporting the high storage capacity and rapid response times observed in the previous CP tests. The integration of this engineered interface into the therapeutic unit ensures a reliable and sensitive biochemical intervention capability during organ transport.

In summary, the engineered PAM/CS semi-interpenetrating polymer network demonstrated robust and predictable responsiveness to environmental pH fluctuations. Systematic characterization including structural configuration, swelling behavior, and electrochemical impedance characteristics confirmed the high sensitivity of the system to acidification levels typical of organ transport. Furthermore, the pH-triggered release profiles of N-acetylcysteine NAC established the capacity of the hydrogel for precise therapeutic intervention. The synergistic integration of chitosan as a responsive matrix and NAC as a protective agent significantly enhanced both the physiological sensitivity and the therapeutic potential of the device. This research on bioelectronics and biocompatible materials provides an intelligent and reliable platform for biochemical regulation during the critical window of organ preservation. The integration with a palladium electrode further enables active pH control through electrochemical proton flux management, serving as a promising strategy for intelligent intervention during organ transport.

6.3.4 PMA Hydrogel Battery

To address the urgent need for stable power supply under low-temperature conditions during organ transportation, we collaborated with Dr. Hu Linyu's group to develop a flexible and stretchable Zn-I_2 battery integrated with a polyacrylamide (PMA) hydrogel electrolyte. The battery features a spring-shaped current collector fabricated from carbon nanotube (CNT) paper through laser ablation, enabling excellent mechanical deformability. The gel electrolyte was pre-deposited in the active region of the patterned CNT paper, and the entire structure was encapsulated using PDMS to form an all-hydrogel, monolithic power unit. This design ensures mechanical robustness while

maintaining favorable ionic conductivity and electrochemical performance under deformation.

Long-term cycling stability tests were conducted at room temperature to evaluate the electrochemical reliability of the single-cell Zn-I_2 battery. As shown in Figure 6.20, the battery retained nearly 100% of its initial capacity after 500 cycles, with a coulombic efficiency as high as 99.3%. This superior stability indicates that the hydrogel electrolyte effectively suppresses the shuttle effect of iodine-based species and maintains ionic equilibrium between the electrodes. The intrinsic ionic conductivity and flexibility of the PMA hydrogel also contribute significantly to the battery's robust performance, making it a promising candidate for low-temperature biomedical applications.

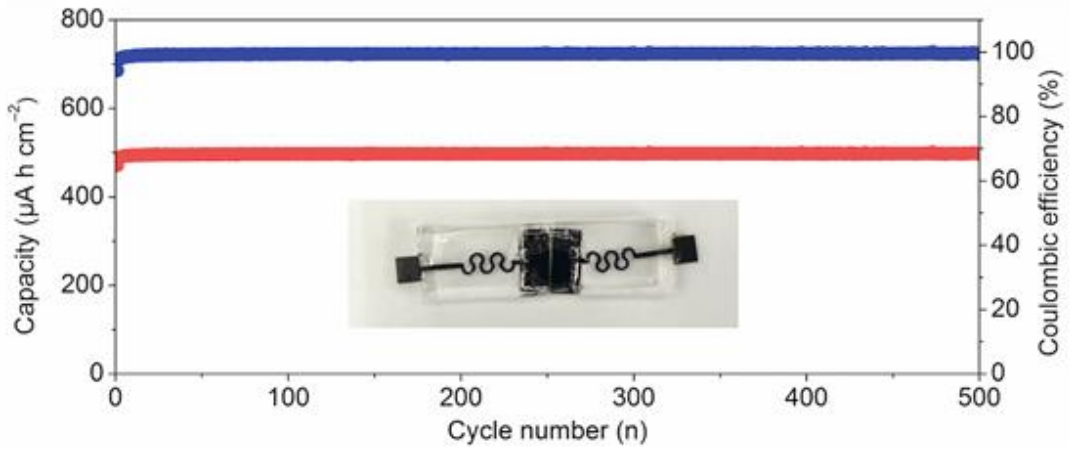

Figure 6.20 Cycling performance of the stretchable dual-plated Zn-I_2 battery.

Mechanical tests further demonstrated the battery's outstanding flexibility and stretchability (Figure 6.21 and Figure 6.22). The device maintained stable capacity and high coulombic efficiency under various bending angles (0°, 60°, 120°, 180°) and stretching strains (0%, 10%, 30%, 50%). Even at a 30% tensile strain, the battery exhibited good cycle stability, confirming that the spring-shaped CNT current collector maintained electrical continuity under deformation. These results validate the structural

integrity and electrochemical resilience of the battery under dynamic mechanical stress, which is essential for wearable integration.

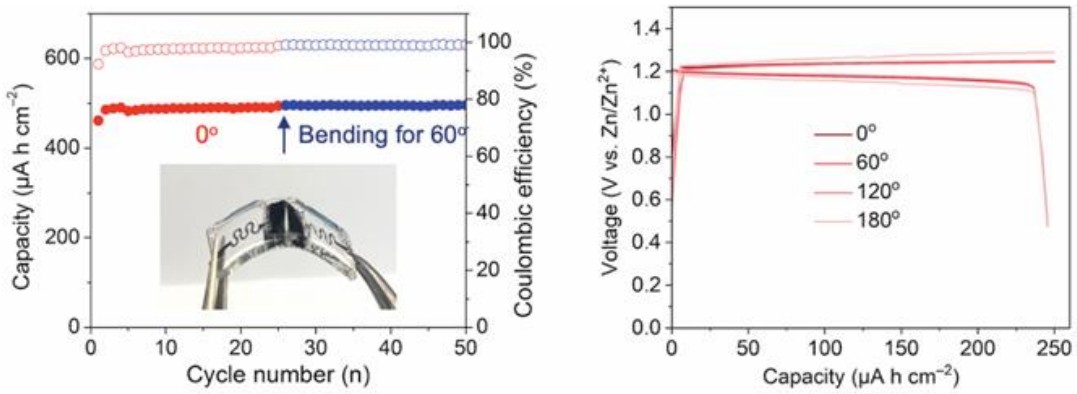

Figure 6.21 Electrochemical performance of the dual-plated Zn-I_2 battery under bending conditions.

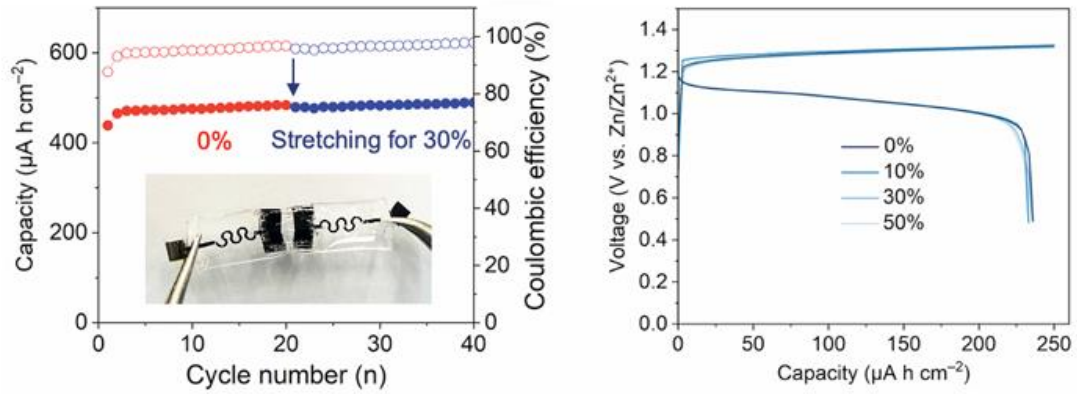

Figure 6.22 Electrochemical performance of the dual-plated Zn-I_2 battery under stretching conditions.

To further meet the diverse energy demands of wearable electronics, the team designed both parallel and series stretchable battery arrays by laser patterning of the CNT paper (Figure 6.23). In the parallel configuration, three Zn-I_2 cells were connected to significantly boost the areal capacity while maintaining high coulombic efficiency and low polarization, indicating the effectiveness of parallelization in enhancing current output for power-intensive applications. In the series configuration, three cells were

connected in series to deliver an output voltage of approximately 3.5 V, with a remarkably low polarization voltage, confirming the feasibility of voltage scaling via serial connection. Notably, both the parallel and series battery arrays maintained excellent performance under substantial bending and stretching, further highlighting their applicability in flexible electronic systems.

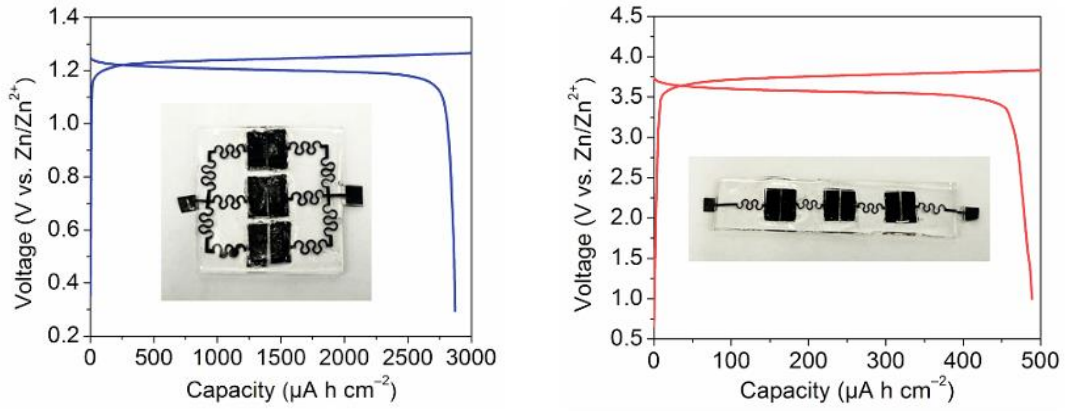

Figure 6.23 GCD curves of parallel and series-connected Zn-I_2 battery packs.

In summary, the PMA hydrogel-based Zn-I_2 battery system demonstrates high energy density, long-term cycling stability, and remarkable deformability. Through rational material and structural design, it can sustain stable output under mechanical stress and cold environments. Compared to conventional rigid batteries, this hydrogel battery offers substantial advantages in adaptability, reliability, and integration potential, making it a highly promising power solution for organ preservation, biosensor platforms, and next-generation wearable electronics.

6.4 Conclusion and Outlook

6.4.1 Conclusion

This chapter provides a comprehensive summary of the design and implementation of an integrated flexible intelligent system designed to address the environmental challenges and physiological monitoring requirements during organ transportation. The

system architecture realizes a robust closed-loop strategy by synergistically integrating real-time sensing, a stable power supply, and an active therapeutic intervention unit consisting of an optimized Pd black electrode and a responsive hydrogel. This integrated platform consists of four core functional modules including a high-performance flexible pH sensor, a polyacrylamide PMA hydrogel battery array, a nanostructured Pd black interface, and a pH-responsive drug release hydrogel. These components are engineered to maintain high functional reliability and mechanical adaptability under the demanding low-temperature conditions typical of clinical organ preservation.

The specific performance of each module is summarized below. First, the PMA hydrogel battery array demonstrates stable output performance and high capacity retention even at temperatures below 0°C, overcoming the low-temperature limitations inherent in conventional energy storage devices. Second, the flexible pH sensor exhibits a high sensitivity of 52 mV/pH alongside excellent linearity and robust mechanical resilience which facilitates continuous monitoring of the organ microenvironment during transportation. Third, the pH-responsive therapeutic unit based on the PAM/CS network provides efficient swelling and NAC release profiles to ensure timely intervention during acidotic or ischemic events. Fourth, the PAM/CS hydrogel works in tandem with the Pd electrode to provide pH-triggered drug release, ensuring timely biochemical intervention during acidotic events.

This integrated platform represents a significant advancement over traditional static cold preservation strategies. While conventional methods prolong organ viability, they lack the capacity to dynamically respond to physiological fluctuations, thereby creating a blind spot that increases the risk of irreversible damage. The proposed system addresses this limitation by enabling real-time biochemical detection and pH-triggered therapeutic release. By identifying early metabolic deviations and promptly releasing NAC to mitigate oxidative stress and metabolic imbalance, the system enhances organ stability and improves the overall success rate of transplantation.

6.4.2 Future Perspectives

Although promising results have been achieved in functionality and integration, further investigation is required to evaluate the system's translational potential. Future research will focus on several key directions. First, animal model studies will be conducted to validate the system's protective effects during organ preservation and transport. Second, long-term stability evaluations will be performed, including cyclic testing of battery performance, sensor accuracy, and sustained drug release under simulated transportation conditions. These tests will help assess the system's robustness and operational durability.

Furthermore, while the integrated organ preservation system has demonstrated effective pH-responsive drug release in controlled laboratory settings, its performance under complex dynamic conditions remains to be fully explored. In future studies, it is essential to evaluate the impacts of mechanical vibrations at different frequencies and magnitudes, as well as ambient temperature fluctuations, on the accuracy of the pH sensors and the controlled drug release rates. Such validation is critical for ensuring the system's reliability and stability during real-world organ transplantation and transportation, where external physical disturbances are inevitable. Addressing these environmental factors will bridge the gap between bench-top prototypes and clinical-grade medical devices.

In addition, further optimization of the device structure will be undertaken to enhance its mechanical conformity, reduce bulk, and improve user comfort. Emphasis will be placed on advancing an all-in-one patch concept that integrates a flexible substrate, wireless communication modules, and onboard data analysis capabilities. This approach will enable remote monitoring, early warning, and closed-loop feedback during organ shipment. By continuously refining the sensing, energy, and drug release modules, the system is expected to serve as a versatile platform not only for organ preservation but also for broader biomedical and life support applications.

CONCLUSIONS AND SUGGESTIONS FOR FUTURE RESEARCH

7.1 Conclusions

This dissertation focuses on the application of functional nanomaterials in intelligent sensing and biomedical intervention. Centered on the theme of enhancing sensing performance through rational nanomaterial engineering, it systematically investigates multiple aspects ranging from material design and device fabrication to system-level integration. The objective is to address critical challenges in environmental surveillance, personalized healthcare, thermal regulation, and organ preservation. By developing micro and nanostructured materials and incorporating them into flexible wearable or implantable platforms, the research achieves an effective synergy between high-performance sensing and intelligent responsive control, promoting the transformation of sensing systems from single-function devices to multifunctional, integrated, and intelligent solutions.

To begin with, in response to the urgent need for ultra-low LOD, this study developed an ultrasensitive electrochemical biosensor utilizing dendritic gold nanostructures and PBASE functional layers. This biosensor achieved an ultralow detection limit in the femtogram per milliliter range, enabling real-time and continuous detection of SARS-CoV-2 and H_3N_2 viruses in complex wastewater environments. Coupled with a Bluetooth-enabled wireless module, the system establishes an integrated acquisition-transmission-display platform, providing a portable, low-cost solution for wastewater-based epidemiological surveillance. The results highlight the critical role of nanostructured electrode interfaces in enhancing the sensitivity and selectivity of biosensors.

Expanding the research scope from high sensitivity, the thesis next presents a washable and ionically conductive textile biosensor based on β-Bi_2O_3 nanoflakes. The introduction of fast-ion conductors significantly improves the device's ionic

conductivity and washing stability. This textile sensor enables the continuous detection of electrolytes such as sodium and potassium ions in human sweat, and it also integrates a Bluetooth Low Energy (BLE) transmission module to facilitate real-time wireless output. Its performance in actual sweat testing demonstrates strong potential for practical, long-term wearable applications.

Finally, this research achieves the development of a closed-loop integrated system that serves as a comprehensive platform for intelligent organ preservation. The all-in-one architecture synergistically combines a high-performance flexible pH sensor for real-time monitoring, a low-temperature-stable PMA hydrogel battery array for continuous power, and an active therapeutic unit featuring an optimized palladium black interface and a pH-responsive PAM/CS hydrogel. This integrated system facilitates the continuous tracking of pH fluctuations on the organ surface during transportation and enables the autonomous, on-demand release of antioxidants including glutathione and N-acetylcysteine in direct response to local acidosis. By precisely managing the biochemical environment through these integrated bioelectronic modules, the system effectively mitigates oxidative damage and significantly enhances organ viability. This work provides a sophisticated and reliable strategy for advanced transplantation medicine by bridging the gap between real-time physiological sensing and immediate therapeutic intervention.

In summary, this dissertation presents a series of innovative and practical strategies based on the rational design of micro and nanostructured materials and their integration into multifunctional systems. The solutions proposed in the fields of environmental virus monitoring, personalized health management, dynamic thermal regulation, and organ preservation are closely interlinked and collectively contribute to the establishment of a sensing-powering-intervention platform. This work lays a solid theoretical foundation and technological basis for the development of next-generation intelligent health and environmental monitoring systems.

7.2 Suggestions for Future Research

This dissertation has explored the design and application of functional nanomaterials within intelligent sensing and biomedical intervention systems, and has successfully constructed and validated several representative subsystems under realistic or simulated conditions. Although substantial progress has been made, there remain several key directions worthy of further investigation.

First, in terms of material design, future research could explore novel nanomaterials with adaptive responsiveness, such as multi-stimuli-responsive conductive polymers and two-dimensional composite materials with self-healing or environment-adaptive properties. These materials may significantly enhance sensor performance in extreme conditions, including high or low temperatures, high humidity, and chemically complex environments. Furthermore, the integration of machine learning into material design could facilitate the establishment of structure-function correlations, enabling the intelligent and customized development of high-performance materials.

Second, regarding device fabrication, advancing the integration of sensing, power supply, and therapeutic intervention represents a crucial direction. For example, the development of flexible electrochemical sensor arrays capable of simultaneous multi-channel monitoring of physiological biomarkers such as electrolytes could be combined with micro-scale drug release modules to establish closed-loop systems for real-time sensing, feedback, and intervention. In addition, integrating energy harvesting technologies, such as photovoltaics, thermoelectric, or biofuel cells, with power supply modules could support self-powered systems for long-term operation without reliance on external energy sources, which is especially valuable for portable or implantable applications.

Third, with respect to practical applications, further efforts are needed to adapt these technologies for clinical and translational use. For instance, in the context of organ preservation, subsequent studies should investigate the performance of the integrated

system in large animal models or clinical-grade trials. These studies should focus on outcomes such as graft survival rates, reduction of oxidative stress, and mitigation of histological damage. Moreover, this platform could be extended to other pathological conditions characterized by local pH fluctuations, such as ischemic stroke or tumor microenvironments, to assess its broader applicability in precision medicine.

Finally, in terms of interdisciplinary integration, future efforts should incorporate artificial intelligence algorithms and multimodal data analytics into sensing systems to enable real-time signal interpretation, anomaly detection, and predictive diagnostics. The integration of sensors with wearable terminals and cloud-based platforms could further support remote health monitoring and personalized medical recommendations, facilitating the evolution of intelligent sensing systems from standalone devices to comprehensive healthcare services.

In summary, future research should emphasize convergence across material innovation, device engineering, system integration, clinical application, and data intelligence. These efforts are expected to advance nanomaterial-based intelligent sensing platforms toward enhanced performance, improved adaptability, and expanded applicability in the domains of smart healthcare and precision diagnostics.

REFERENCES

1 He, J. *et al.* Mode engineering in reconfigurable fractal topological circuits. *Physical Review B* **109** (2024). https://doi.org/10.1103/PhysRevB.109.235406

2 Nesbitt, N. T. *et al.* Au Dendrite Electrocatalysts for CO2 Electrolysis. *The Journal of Physical Chemistry C* **122**, 10006-10016 (2018). https://doi.org/10.1021/acs.jpcc.8b01831

3 Huang, T., Meng, F. & Qi, L. Controlled Synthesis of Dendritic Gold Nanostructures Assisted by Supramolecular Complexes of Surfactant with Cyclodextrin. *Langmuir* **26**, 7582-7589 (2009). https://doi.org/10.1021/la904393n

4 Huang, D., Bai, X. & Zheng, L. Ultrafast Preparation of Three-Dimensional Dendritic Gold Nanostructures in Aqueous Solution and Their Applications in Catalysis and SERS. *The Journal of Physical Chemistry C* **115**, 14641-14647 (2011). https://doi.org/10.1021/jp2037284

5 Fukami, K. *et al.* Gold Nanostructures for Surface-Enhanced Raman Spectroscopy, Prepared by Electrodeposition in Porous Silicon. *Materials* **4**, 791-800 (2011). https://doi.org/10.3390/ma4040791

6 Silva Junior, G. J. *et al.* Fabrication of dendritic nanoporous gold via a two-step amperometric approach: Application for electrochemical detection of methyl parathion in river water samples. *Talanta* **226** (2021). https://doi.org/10.1016/j.talanta.2021.122130

7 Li, P., Zhang, B. & Cui, T. TiO2 and shrink induced tunable nano self-assembled graphene composites for label free biosensors. *Sensors and Actuators B: Chemical* **216**, 337-342 (2015). https://doi.org/10.1016/j.snb.2015.03.111

8 Huang, T., Meng, F. & Qi, L. Controlled synthesis of dendritic gold nanostructures assisted by supramolecular complexes of surfactant with cyclodextrin. *Langmuir* **26**, 7582-7589 (2010).

9 Li, W. *et al.* Hedging Li dendrite formation by virtue of controllable tip effect. *Journal of Materials Chemistry A* **10**, 15161-15168 (2022). https://doi.org/10.1039/d2ta03336d

10 Zhou, X. *et al.* Temperature regulation growth of Au nanocrystals: from concave trisoctahedron to dendritic structures and their ultrasensitive SERS-based detection of lindane. *J. Mater. Chem. C* **5**, 10399-10405 (2017). https://doi.org/10.1039/c7tc03808a

11 Yin, X. *et al.* Engineered of Bimetallic Au@Ag Nanostars with Controllable Branching and Tunable LSPR for Rapid Ultrasensitive SERS Detection. *ACS Applied Optical Materials* **3**, 1422-1431 (2025). https://doi.org/10.1021/acsaom.5c00158

12 Guo, X., Feng, B., Gai, L. & Zhou, J. Reduced graphene oxide/polymer dots-based flexible symmetric supercapacitors delivering an output potential of 1.7 V with electrochemical charge injection. *Electrochimica Acta* **293**, 399-407 (2019). https://doi.org/10.1016/j.electacta.2018.10.057

13 Han, H., Li, Y., Wang, Y. & Pan, D. In situ monitoring of natural labile copper

during the growth process of a marine diatom. *Environmental Pollution* **382** (2025). https://doi.org/10.1016/j.envpol.2025.126662

14 Noguchi, T., Nishitani, S. & Sakata, T. Anti-Biofouling Effect of Nanoporous Gold Electrode on Nonspecific Signal Reduction for Electrochemical Biosensors. *Journal of The Electrochemical Society* **171** (2024). https://doi.org/10.1149/1945-7111/ad5d9e

15 Noguchi, T., Nishitani, S. & Sakata, T. Anti-Biofouling Effect of Nanoporous Gold Electrode on Nonspecific Signal Reduction for Electrochemical Biosensors. *Journal of The Electrochemical Society* **171**, 077507 (2024).

16 German, N., Popov, A., Ramanavicius, A. & Ramanaviciene, A. A Platform for the Glucose Biosensor Based on Dendritic Gold Nanostructures and Polyaniline-Gold Nanoparticles Nanocomposite. *Biosensors (Basel)* **15** (2025). https://doi.org/10.3390/bios15030196

17 Huang, J. *et al.* Explore how immobilization strategies affected immunosensor performance by comparing four methods for antibody immobilization on electrode surfaces. *Scientific Reports* **12** (2022). https://doi.org/10.1038/s41598-022-26768-w

18 Ramanaviciene, A., German, N., Kausaite-Minkstimiene, A. & Ramanavicius, A. Glucose Biosensor Based on Dendritic Gold Nanostructures Electrodeposited on Graphite Electrode by Different Electrochemical Methods. *Chemosensors* **9** (2021). https://doi.org/10.3390/chemosensors9080188

19 Zhu, Z., Zhao, Y., Ruan, Y., Weng, X. & Milcovich, G. Dendritic Gold Nanoparticles Loaded on 3D Graphene-like Surface and Layer-by-Layer Assembly for Enhanced Glucose Biosensing. *Biosensors (Basel)* **15** (2025). https://doi.org/10.3390/bios15040246

20 Ariasena, E. *et al.* Evaluation of electrodeposition synthesis of gold nanodendrite on screen-printed carbon electrode for nonenzymatic ascorbic acid sensor. *Sci Rep* **14**, 22854 (2024). https://doi.org/10.1038/s41598-024-69970-8

21 Khalilipour, M., Moshaii, A. & Siampour, H. Controlled electrochemical fabrication of large and stable gold nanorods with reduced cytotoxicity. *Sci Rep* **15**, 8171 (2025). https://doi.org/10.1038/s41598-025-92926-5

22 German, N., Popov, A., Ramanavicius, A. & Ramanaviciene, A. Development and Practical Application of Glucose Biosensor Based on Dendritic Gold Nanostructures Modified by Conducting Polymers. *Biosensors* **12** (2022). https://doi.org/10.3390/bios12080641

23 Lee, J. *et al.* Regenerative Strategy of Gold Electrodes for Long-Term Reuse of Electrochemical Biosensors. *ACS Omega* **8**, 1389-1400 (2023). https://doi.org/10.1021/acsomega.2c06851

24 Jamshidnejad-Tosaramandani, T., Kashanian, S., Omidfar, K. & Schioth, H. Recent advances in gold nanostructure-based biosensors in detecting diabetes biomarkers. *Front Bioeng Biotechnol* **12**, 1446355 (2024). https://doi.org/10.3389/fbioe.2024.1446355

25 Zamani, M., Klapperich, C. M. & Furst, A. L. Recent advances in gold electrode fabrication for low-resource setting biosensing. *Lab Chip* **23**, 1410-1419 (2023).

https://doi.org/10.1039/d2lc00552b
26 Singer, A. C. *et al.* A world of wastewater-based epidemiology. *Nature Water* **1**, 408-415 (2023). https://doi.org/10.1038/s44221-023-00083-8
27 Wang, Z. *et al.* Using wastewater analysis to assess the health status of two distinct populations in China. *Water Research X* **29** (2025). https://doi.org/10.1016/j.wroa.2025.100335
28 Carneiro, R. B. *et al.* A critical review of wastewater-based epidemiology as a tool to evaluate the unintentional human exposure to potentially harmful chemicals. *Analytical and Bioanalytical Chemistry* **417**, 495-511 (2024). https://doi.org/10.1007/s00216-024-05596-z
29 Azubuike, C. C. *et al.* Developing Biosensors for SARS-CoV-2 Wastewater-Based Epidemiology: A Systematic Review of Trends, Limitations and Future Perspectives. *Sustainability* **14** (2022). https://doi.org/10.3390/su142416761
30 Lorenzo, M. & Picó, Y. Wastewater-based epidemiology: current status and future prospects. *Current Opinion in Environmental Science & Health* **9**, 77-84 (2019). https://doi.org/10.1016/j.coesh.2019.05.007
31 Wampler, D. *et al.* Estimation of the prevalence of substance use by wastewater-based epidemiology study in four cities of Guangdong, China. *Plos One* **20** (2025). https://doi.org/10.1371/journal.pone.0320141
32 Ort, C. *et al.* Spatial differences and temporal changes in illicit drug use in Europe quantified by wastewater analysis. *Addiction* **109**, 1338-1352 (2014). https://doi.org/10.1111/add.12570
33 Bastardo-Méndez, M. *et al.* Detection of SARS-CoV-2 in wastewater as an earlier predictor of COVID-19 epidemic peaks in Venezuela. *Scientific Reports* **14** (2024). https://doi.org/10.1038/s41598-024-78982-3
34 Wu, F. *et al.* SARS-CoV-2 Titers in Wastewater Are Higher than Expected from Clinically Confirmed Cases. *mSystems* **5** (2020). https://doi.org/10.1128/mSystems.00614-20
35 Medema, G., Heijnen, L., Elsinga, G., Italiaander, R. & Brouwer, A. Presence of SARS-Coronavirus-2 RNA in Sewage and Correlation with Reported COVID-19 Prevalence in the Early Stage of the Epidemic in The Netherlands. *Environmental Science & Technology Letters* **7**, 511-516 (2020). https://doi.org/10.1021/acs.estlett.0c00357
36 Peccia, J. *et al.* Measurement of SARS-CoV-2 RNA in wastewater tracks community infection dynamics. *Nature Biotechnology* **38**, 1164-1167 (2020). https://doi.org/10.1038/s41587-020-0684-z
37 Hamilton, K. A., Wade, M. J., Barnes, K. G., Street, R. A. & Paterson, S. Wastewater-based epidemiology as a public health resource in low- and middle-income settings. *Environmental Pollution* **351** (2024). https://doi.org/10.1016/j.envpol.2024.124045
38 Balcázar, J. L. Wastewater-Based Epidemiology as a Complementary Tool for Antimicrobial Resistance Surveillance: Overcoming Barriers to Integration. *BioEssays* (2025). https://doi.org/10.1002/bies.70034
39 Yang, F. *et al.* Research Progress and Perspectives on Wastewater-Based

Epidemiology: A Bibliometric Analysis. *Water* **16** (2024). https://doi.org/10.3390/w16121743

40 Calabria de Araujo, J. *et al.* Detection of Multiple Human Viruses, including Mpox, Using a Wastewater Surveillance Approach in Brazil. *Pathogens* **13** (2024). https://doi.org/10.3390/pathogens13070589

41 Tisza, M. *et al.* Wastewater sequencing reveals community and variant dynamics of the collective human virome. *Nature Communications* **14** (2023). https://doi.org/10.1038/s41467-023-42064-1

42 Hernaez, B. *et al.* Monitoring monkeypox virus in saliva and air samples in Spain: a cross-sectional study. *The Lancet Microbe* **4**, e21-e28 (2023). https://doi.org/10.1016/s2666-5247(22)00291-9

43 Serpilli, M., Rizzoni, R. & Lebon, F. Hard interfaces with microstructure: the cases of strain gradient elasticity and micropolar elasticity. *Philosophical Transactions of the Royal Society A: Mathematical, Physical and Engineering Sciences* **382** (2024). https://doi.org/10.1098/rsta.2023.0308

44 Juutinen, A. *et al.* The effects of RT-qPCR standards on reproducibility and comparability in monitoring SARS-CoV-2 levels in wastewater. *Scientific Reports* **14** (2024). https://doi.org/10.1038/s41598-024-77155-6

45 Grube, A. M. *et al.* Detection of SARS-CoV-2 RNA in wastewater and comparison to COVID-19 cases in two sewersheds, North Carolina, USA. *Science of The Total Environment* **858** (2023). https://doi.org/10.1016/j.scitotenv.2022.159996

46 Luraschi, R. *et al.* The Comparative Analysis of Two RT-qPCR Kits for Detecting SARS-CoV-2 Reveals a Higher Risk of False-Negative Diagnosis in Samples with High Quantification Cycles for Viral and Internal Genes. *Canadian Journal of Infectious Diseases and Medical Microbiology* **2022**, 1-10 (2022). https://doi.org/10.1155/2022/2594564

47 Thakali, O. *et al.* Real-time evaluation of signal accuracy in wastewater surveillance of pathogens with high rates of mutation. *Scientific Reports* **14** (2024). https://doi.org/10.1038/s41598-024-54319-y

48 Martínez de Alba, Á. E. *et al.* SARS-CoV-2 RNA Detection in Wastewater and Its Effective Correlation with Clinical Data during the Outbreak of COVID-19 in Salamanca. *International Journal of Molecular Sciences* **25** (2024). https://doi.org/10.3390/ijms25158071

49 Shinde, M., Lavania, M., Rawal, J., Chavan, N. & Shinde, P. Evaluation of droplet digital qRT-PCR (dd qRT-PCR) for quantification of SARS CoV-2 RNA in stool and urine specimens of COVID-19 patients. *Frontiers in Medicine* **10**, 1148688 (2023).

50 Choi, G., Moehling, T. J. & Meagher, R. J. Advances in RT-LAMP for COVID-19 testing and diagnosis. *Expert Review of Molecular Diagnostics* **23**, 9-28 (2023). https://doi.org/10.1080/14737159.2023.2169071

51 Bhalla, N. Nanoplasmonic acceleration of nucleic acid amplification for pathogen detection. *Nature Nanotechnology* **18**, 846-847 (2023). https://doi.org/10.1038/s41565-023-01398-z

52 Tian, J. *et al.* T cell immune evasion by SARS-CoV-2 JN.1 escapees targeting two cytotoxic T cell epitope hotspots. *Nat Immunol* **26**, 265-278 (2025). https://doi.org/10.1038/s41590-024-02051-0

53 Gootenberg, J. S. *et al.* Nucleic acid detection with CRISPR-Cas13a/C2c2. *Science* **356**, 438-442 (2017). https://doi.org/doi:10.1126/science.aam9321

54 Gootenberg, J. S. *et al.* Nucleic acid detection with CRISPR-Cas13a/C2c2. *Science* **356**, 438-442 (2017).

55 Zafar, H., Channa, A., Jeoti, V. & Stojanović, G. M. Comprehensive Review on Wearable Sweat-Glucose Sensors for Continuous Glucose Monitoring. *Sensors* **22** (2022). https://doi.org/10.3390/s22020638

56 Gao, F. *et al.* Wearable and flexible electrochemical sensors for sweat analysis: a review. *Microsystems & Nanoengineering* **9** (2023). https://doi.org/10.1038/s41378-022-00443-6

57 Vo, D.-K. & Trinh, K. T. L. Advances in Wearable Biosensors for Healthcare: Current Trends, Applications, and Future Perspectives. *Biosensors* **14** (2024). https://doi.org/10.3390/bios14110560

58 Vural, B. *et al.* Fluid-based wearable sensors: a turning point in personalized healthcare. *Turkish Journal of Chemistry* **47**, 944-967 (2023). https://doi.org/10.55730/1300-0527.3588

59 Chen, M. *et al.* Universal Flexible Wearable Biosensors for Noninvasive Health Monitoring. *ACS Applied Materials & Interfaces* **17**, 20741-20755 (2025). https://doi.org/10.1021/acsami.4c22623

60 Yang, X. & Cheng, H. Recent Developments of Flexible and Stretchable Electrochemical Biosensors. *Micromachines* **11** (2020). https://doi.org/10.3390/mi11030243

61 Shinde, S. *et al.* Wearable sweat-sensing patches for non-invasive and continuous health tracking. *Sensors and Actuators Reports* **9** (2025). https://doi.org/10.1016/j.snr.2024.100265

62 Childs, A. *et al.* Diving into Sweat: Advances, Challenges, and Future Directions in Wearable Sweat Sensing. *ACS Nano* **18**, 24605-24616 (2024). https://doi.org/10.1021/acsnano.4c10344

63 Assalve, G. *et al.* Advanced Wearable Devices for Monitoring Sweat Biochemical Markers in Athletic Performance: A Comprehensive Review. *Biosensors* **14** (2024). https://doi.org/10.3390/bios14120574

64 Noor, A. M. *et al.* Wearable Device for Continuous and Real-Time Monitoring of Human Sweat Sodium. *Sensors* **25** (2025). https://doi.org/10.3390/s25113467

65 Xu, J., Fang, Y. & Chen, J. Wearable Biosensors for Non-Invasive Sweat Diagnostics. *Biosensors* **11** (2021). https://doi.org/10.3390/bios11080245

66 Gao, N., Xu, G., Chang, G. & Wu, Y. From Lab to Life: Self-Powered Sweat Sensors and Their Future in Personal Health Monitoring. *Advanced Science* **12** (2024). https://doi.org/10.1002/advs.202409178

67 Chen, Y. *et al.* A Wearable Molecularly Imprinted Electrochemical Sensor for Cortisol Stable Monitoring in Sweat. *Biosensors* **15** (2025). https://doi.org/10.3390/bios15030194

68 Xuan, X. *et al.* Fully Integrated Wearable Device for Continuous Sweat Lactate Monitoring in Sports. *ACS Sensors* **8**, 2401-2409 (2023). https://doi.org/10.1021/acssensors.3c00708

69 Pirovano, P. *et al.* A wearable sensor for the detection of sodium and potassium in human sweat during exercise. *Talanta* **219** (2020). https://doi.org/10.1016/j.talanta.2020.121145

70 Gao, W. *et al.* Fully integrated wearable sensor arrays for multiplexed in situ perspiration analysis. *Nature* **529**, 509-514 (2016). https://doi.org/10.1038/nature16521

71 Lyzwinski, L. *et al.* Opportunities and challenges for sweat-based monitoring of metabolic syndrome via wearable technologies. *Communications Engineering* **2** (2023). https://doi.org/10.1038/s44172-023-00097-w

72 Yang, G., Hong, J. & Park, S.-B. Wearable device for continuous sweat lactate monitoring in sports: a narrative review. *Frontiers in Physiology* **15** (2024). https://doi.org/10.3389/fphys.2024.1376801

73 Shajari, S., Kuruvinashetti, K., Komeili, A. & Sundararaj, U. The Emergence of AI-Based Wearable Sensors for Digital Health Technology: A Review. *Sensors* **23** (2023). https://doi.org/10.3390/s23239498

74 Barba, A. B. *et al.* in *2022 IEEE International Conference on Flexible and Printable Sensors and Systems (FLEPS)* 1-4 (2022).

75 Huang, G., Chen, X. & Liao, C. AI-Driven Wearable Bioelectronics in Digital Healthcare. *Biosensors* **15** (2025). https://doi.org/10.3390/bios15070410

76 Zahed, M. A. *et al.* Self-Powered Wireless System for Monitoring Sweat Electrolytes in Personalized Healthcare Wearables. *Advanced Functional Materials* **35** (2024). https://doi.org/10.1002/adfm.202421021

77 Yang, M. *et al.* Screen-Printed Wearable Sweat Sensor for Cost-Effective Assessment of Human Hydration Status through Potassium and Sodium Ion Detection. *Micromachines* **14** (2023). https://doi.org/10.3390/mi14081497

78 Cai, X. *et al.* Fully Integrated Multiplexed Wristwatch for Real-Time Monitoring of Electrolyte Ions in Sweat. *ACS Nano* **18**, 12808-12819 (2024). https://doi.org/10.1021/acsnano.3c13035

79 Bi, Y. *et al.* Universal Fully Integrated Wearable Sensor Arrays for the Multiple Electrolyte and Metabolite Monitoring in Raw Sweat, Saliva, or Urine. *Analytical Chemistry* **95**, 6690-6699 (2023). https://doi.org/10.1021/acs.analchem.3c00361

80 Wang, S. *et al.* Multisensing Wearables for Real-Time Monitoring of Sweat Electrolyte Biomarkers During Exercise and Analysis on Their Correlation With Core Body Temperature. *IEEE Transactions on Biomedical Circuits and Systems* **17**, 808-817 (2023). https://doi.org/10.1109/tbcas.2023.3286528

81 Jalal, N. R. *et al.* Wireless wearable potentiometric sensor for simultaneous determination of pH, sodium and potassium in human sweat. *Scientific Reports* **14** (2024). https://doi.org/10.1038/s41598-024-62236-3

82 Mansour, M., Saeed Darweesh, M. & Soltan, A. Wearable devices for glucose monitoring: A review of state-of-the-art technologies and emerging trends.

Alexandria Engineering Journal **89**, 224-243 (2024). https://doi.org/10.1016/j.aej.2024.01.021

83 Patel, V., Mardolkar, A., Shelar, A., Tiwari, R. & Srivastava, R. Wearable sweat chloride sensors: materials, fabrication and their applications. *Analytical Methods* **16**, 1439-1453 (2024). https://doi.org/10.1039/d3ay01979a

84 Ray, T. R. *et al.* Soft, skin-interfaced sweat stickers for cystic fibrosis diagnosis and management. *Science Translational Medicine* **13**, eabd8109 (2021). https://doi.org/doi:10.1126/scitranslmed.abd8109

85 Ji, W. *et al.* Wearable Sweat Biosensors Refresh Personalized Health/Medical Diagnostics. *Research* **2021** (2021). https://doi.org/10.34133/2021/9757126

86 Maroli, G. *et al.* Wearable, battery-free, wireless multiplexed printed sensors for heat stroke prevention with mussel-inspired bio-adhesive membranes. *Biosensors and Bioelectronics* **260** (2024). https://doi.org/10.1016/j.bios.2024.116421

87 Kong, L. *et al.* Wireless Technologies in Flexible and Wearable Sensing: From Materials Design, System Integration to Applications. *Advanced Materials* **36** (2024). https://doi.org/10.1002/adma.202400333

88 Feng, J. *et al.* An Energy-Efficient Flexible Multi-Modal Wireless Sweat Sensing System Based on Laser Induced Graphene. *Sensors* **23** (2023). https://doi.org/10.3390/s23104818

89 Yang, P., Wei, G., Liu, A., Huo, F. & Zhang, Z. A review of sampling, energy supply and intelligent monitoring for long-term sweat sensors. *npj Flexible Electronics* **6** (2022). https://doi.org/10.1038/s41528-022-00165-9

90 Xing, Z., Hui, J., Lin, B., Wu, Z. & Mao, H. Recent Advances in Wearable Sensors for the Monitoring of Sweat: A Comprehensive Tendency Summary. *Chemosensors* **11** (2023). https://doi.org/10.3390/chemosensors11090470

91 Liu, H. *et al.* Printed circuit board integrated wearable ion-selective electrode with potential treatment for highly repeatable sweat monitoring. *Sensors and Actuators B: Chemical* **355** (2022). https://doi.org/10.1016/j.snb.2021.131102

92 Wang, Z. *et al.* Engineering Materials for Electrochemical Sweat Sensing. *Advanced Functional Materials* **31** (2020). https://doi.org/10.1002/adfm.202008130

93 Clua Estivill, M., Ait Yazza, A., Blondeau, P. & Andrade, F. J. Ion-selective organic electrochemical transistors for the determination of potassium in clinical samples. *Sensors and Actuators B: Chemical* **401** (2024). https://doi.org/10.1016/j.snb.2023.135027

94 Pan, Y. *et al.* A laser-Engraved Wearable Electrochemical Sensing Patch for Heat Stress Precise Individual Management of Horse. *Advanced Science* **11** (2024). https://doi.org/10.1002/advs.202310069

95 Ates, H. C. *et al.* End-to-end design of wearable sensors. *Nature Reviews Materials* **7**, 887-907 (2022). https://doi.org/10.1038/s41578-022-00460-x

96 Ferreira, R. G., Silva, A. P. & Nunes-Pereira, J. Current On-Skin Flexible Sensors, Materials, Manufacturing Approaches, and Study Trends for Health Monitoring: A Review. *ACS Sensors* **9**, 1104-1133 (2024).

https://doi.org/10.1021/acssensors.3c02555
97 Wang, S. *et al.* Trends in Flexible Sensing Technology in Smart Wearable Mechanisms–Materials–Applications. *Nanomaterials* **15** (2025). https://doi.org/10.3390/nano15040298
98 Fu, W. *et al.* Intelligent fibers and textiles for wearable biosensors. *Responsive Materials* **2** (2024). https://doi.org/10.1002/rpm.20240018
99 Akter, A., Apu, M. M. H., Veeranki, Y. R., Baroud, T. N. & Posada-Quintero, H. F. Recent Studies on Smart Textile-Based Wearable Sweat Sensors for Medical Monitoring: A Systematic Review. *Journal of Sensor and Actuator Networks* **13** (2024). https://doi.org/10.3390/jsan13040040
100 Yin, J. *et al.* Flexible Textile-Based Sweat Sensors for Wearable Applications. *Biosensors* **13** (2023). https://doi.org/10.3390/bios13010127
101 Zhang, S., Tan, R., Xu, X., Iqbal, S. & Hu, J. Fibers/Textiles-Based Flexible Sweat Sensors: A Review. *ACS Materials Letters* **5**, 1420-1440 (2023). https://doi.org/10.1021/acsmaterialslett.2c01207
102 Shi, Y., Zhang, Z., Huang, Q., Lin, Y. & Zheng, Z. Wearable sweat biosensors on textiles for health monitoring. *Journal of Semiconductors* **44** (2023). https://doi.org/10.1088/1674-4926/44/2/021601
103 Alhashmi Alamer, F. *et al.* Review on PEDOT:PSS-Based Conductive Fabric. *ACS Omega* **7**, 35371-35386 (2022). https://doi.org/10.1021/acsomega.2c01834
104 Smith, R. E. *et al.* pH-responsive and antibacterial PANI-PEDOT:PSS fibres for wearable applications. *Materials Advances* **5**, 2306-2315 (2024). https://doi.org/10.1039/d3ma00711a
105 Park, J., Hanif, A., Kim, D. S. & Jeong, U. Fibrillar Strings for Wearable Sensor Applications. *Korean Journal of Chemical Engineering* (2025). https://doi.org/10.1007/s11814-025-00422-3
106 Shak Sadi, M. & Kumpikaitė, E. Advances in the Robustness of Wearable Electronic Textiles: Strategies, Stability, Washability and Perspective. *Nanomaterials* **12** (2022). https://doi.org/10.3390/nano12122039
107 Zhou, B., Zhao, X. & Liu, Y. Simple preparation of multifunctional PEDOT-based composites for wearable smart textiles. *Materials Today Nano* **27** (2024). https://doi.org/10.1016/j.mtnano.2024.100502
108 Fan, W. *et al.* Sweat permeable and ultrahigh strength 3D PVDF piezoelectric nanoyarn fabric strain sensor. *Nature Communications* **15** (2024). https://doi.org/10.1038/s41467-024-47810-7
109 Liu, M. *et al.* Perspiration permeable, textile embeddable microfluidic sweat sensor. *Biosensors and Bioelectronics* **237** (2023). https://doi.org/10.1016/j.bios.2023.115504
110 Wang, R. *et al.* Sweat Pore-Inspired Functional Nanofiber Fabrics for Sweat Management and Simultaneous Detection. *Small* **20** (2024). https://doi.org/10.1002/smll.202408465
111 Bilbao, E. *et al.* Electrochemical Sweat Sensors. *Chemosensors* **11** (2023). https://doi.org/10.3390/chemosensors11040244
112 Guan, M. *et al.* Durable, breathable, sweat-resistant, and degradable flexible

sensors for human motion detection. *Chemical Engineering Journal* **462** (2023). https://doi.org/10.1016/j.cej.2023.142151

113 Rovira, M. *et al.* Assessing the performance of a robust multiparametric wearable patch integrating silicon-based sensors for real-time continuous monitoring of sweat biomarkers. *Biosensors and Bioelectronics* **262** (2024). https://doi.org/10.1016/j.bios.2024.116560

114 Yin, L. & Sun, X. Textile-based sensors for human motion sensing: recent developments and future perspectives. *Nanocomposites* **11**, 79-98 (2025). https://doi.org/10.1080/20550324.2025.2477392

115 Shi, Y. *et al.* Washable textile biosensors enabled by nanostructured oxides with fast ion diffusion. *Device* **2** (2024). https://doi.org/10.1016/j.device.2024.100503

116 Sankauskaite, A., Pauliukaite, R., Baltusnikaite-Guzaitiene, J. & Abraitiene, A. Smart textile with integrated wearable electrochemical sensors. *Current Opinion in Electrochemistry* **42** (2023). https://doi.org/10.1016/j.coelec.2023.101410

117 Yan, B. *et al.* Breathable and washable MXene@gallic acid cross-linked textile assisted by borax for personal multi-protection wearables. *Chemical Engineering Journal* **487** (2024). https://doi.org/10.1016/j.cej.2024.150570

118 Guo, R. *et al.* Matrix-Assisted Catalytic Printing for the Fabrication of Multiscale, Flexible, Foldable, and Stretchable Metal Conductors. *Advanced Materials* **25**, 3343-3350 %* Copyright © 2013 WILEY-VCH Verlag GmbH & Co. KGaA, Weinheim %U https://onlinelibrary.wiley.com/doi/abs/3310.1002/adma.201301184 (2013).

119 Zhang, Y. *et al.* Destructive-Treatment-Free Rapid Polymer-Assisted Metal Deposition for Versatile Electronic Textiles. *ACS Applied Materials & Interfaces* **14**, 56193-56202 %U https://doi.org/56110.51021/acsami.56192c19278 (2022).

120 Li, P., Zhang, Y. & Zheng, Z. Polymer-Assisted Metal Deposition (PAMD) for Flexible and Wearable Electronics: Principle, Materials, Printing, and Devices. *Advanced Materials* **31**, 1902987 %* © 1902019 WILEY-VCH Verlag GmbH & Co. KGaA, Weinheim %U https://onlinelibrary.wiley.com/doi/abs/1902910.1901002/adma.201902987 (2019).

121 Yu, Y., Yan, C. & Zheng, Z. Polymer-Assisted Metal Deposition (PAMD): A Full-Solution Strategy for Flexible, Stretchable, Compressible, and Wearable Metal Conductors. *Advanced Materials* **26**, 5508-5516 %* © 2014 WILEY-VCH Verlag GmbH & Co. KGaA, Weinheim %U https://onlinelibrary.wiley.com/doi/abs/5510.1002/adma.201305558 (2014).

122 Hisadome, Y. *et al.* Hypothermic machine perfusion prevents hyperacute graft loss in pig-to-primate kidney xenotransplantation after 5-hours of cold Ischemia. *Commun Med (Lond)* **5**, 117 (2025). https://doi.org/10.1038/s43856-025-00842-6

123 Mico-Carnero, M. *et al.* A Potential Route to Reduce Ischemia/Reperfusion Injury in Organ Preservation. *Cells* **11** (2022).

https://doi.org/10.3390/cells11172763
124 Knijff, L. W. D., van Kooten, C. & Ploeg, R. J. The Effect of Hypothermic Machine Perfusion to Ameliorate Ischemia-Reperfusion Injury in Donor Organs. *Front Immunol* **13**, 848352 (2022). https://doi.org/10.3389/fimmu.2022.848352
125 Yemaneberhan, K. H. *et al.* Beyond the icebox: modern strategies in organ preservation for transplantation. *Clin Transplant Res* **38**, 377-403 (2024). https://doi.org/10.4285/ctr.24.0039
126 Rossignol, G. *et al.* HOPE Mitigates Ischemia-Reperfusion Injury in Ex-Situ Split Grafts: A Comparative Study With Living Donation in Pediatric Liver Transplantation. *Transpl Int* **37**, 12686 (2024). https://doi.org/10.3389/ti.2024.12686
127 Ghosh, S., Kumar, N. & Chattopadhyay, S. Electrically conductive "SMART" hydrogels for on-demand drug delivery. *Asian J Pharm Sci* **20**, 101007 (2025). https://doi.org/10.1016/j.ajps.2024.101007
128 Regato-Herbella, M. *et al.* ROS-Responsive 4D Printable Acrylic Thioether-Based Hydrogels for Smart Drug Release. *Chem Mater* **36**, 1262-1272 (2024). https://doi.org/10.1021/acs.chemmater.3c02264
129 Li, S. *et al.* The application of nanotechnology in kidney transplantation. *Nanomedicine (Lond)* **19**, 413-429 (2024). https://doi.org/10.2217/nnm-2023-0286
130 Naaz, A., Turnquist, H. R., Gorantla, V. S. & Little, S. R. Drug delivery strategies for local immunomodulation in transplantation: Bridging the translational gap. *Adv Drug Deliv Rev* **213**, 115429 (2024). https://doi.org/10.1016/j.addr.2024.115429
131 Gao, K. & Xu, K. Advancements and Prospects of pH-Responsive Hydrogels in Biomedicine. *Gels* **11** (2025). https://doi.org/10.3390/gels11040293
132 Patroklou, G. *et al.* pH-Responsive Hydrogels: Recent Advances in Pharmaceutical Applications. *Polymers (Basel)* **17** (2025). https://doi.org/10.3390/polym17111451
133 Vegad, U. *et al.* pH stimuli-responsive hydrogels from non-cellulosic biopolymers for drug delivery. *Front Bioeng Biotechnol* **11**, 1270364 (2023). https://doi.org/10.3389/fbioe.2023.1270364
134 Hosgood, S. A. *et al.* Normothermic machine perfusion versus static cold storage in donation after circulatory death kidney transplantation: a randomized controlled trial. *Nat Med* **29**, 1511-1519 (2023). https://doi.org/10.1038/s41591-023-02376-7
135 Peng, P. *et al.* Hypothermic Machine Perfusion Versus Static Cold Storage in Deceased Donor Kidney Transplantation: A Systematic Review and Meta-Analysis of Randomized Controlled Trials. *Artif Organs* **43**, 478-489 (2019). https://doi.org/10.1111/aor.13364
136 Ran, Q. *et al.* Organ preservation: current limitations and optimization approaches. *Front Med (Lausanne)* **12**, 1566080 (2025). https://doi.org/10.3389/fmed.2025.1566080
137 Viana, P. *et al.* Normothermic Machine Perfusion vs. Static Cold Storage in

Liver Transplantation: A Systematic Review and Meta-Analysis. *Artif Organs* **49**, 945-954 (2025). https://doi.org/10.1111/aor.14960

138 Jing, L., Yao, L., Zhao, M., Peng, L. P. & Liu, M. Organ preservation: from the past to the future. *Acta Pharmacol Sin* **39**, 845-857 (2018). https://doi.org/10.1038/aps.2017.182

139 Mohr, A., Brockmann, J. G. & Becker, F. HTK-N: Modified Histidine-Tryptophan-Ketoglutarate Solution-A Promising New Tool in Solid Organ Preservation. *Int J Mol Sci* **21** (2020). https://doi.org/10.3390/ijms21186468

140 Zhao, Y., Main, K., Aujla, T., Keshavjee, S. & Liu, M. Necroptosis in Organ Transplantation: Mechanisms and Potential Therapeutic Targets. *Cells* **12** (2023). https://doi.org/10.3390/cells12182296

141 Bardallo, R. G. *et al.* Mitigating Cold Ischemic Injury: HTK, UW and IGL-2 Solution's Role in Enhancing Antioxidant Defence and Reducing Inflammation in Steatotic Livers. *Int J Mol Sci* **25** (2024). https://doi.org/10.3390/ijms25179318

142 Bejaoui, M. *et al.* Emerging concepts in liver graft preservation. *World J Gastroenterol* **21**, 396-407 (2015). https://doi.org/10.3748/wjg.v21.i2.396

143 Alghannam, F. *et al.* Recent Progress in PDMS-Based Microfluidics Toward Integrated Organ-on-a-Chip Biosensors and Personalized Medicine. *Biosensors (Basel)* **15** (2025). https://doi.org/10.3390/bios15020076

144 Izadifar, Z. *et al.* Organ chips with integrated multifunctional sensors enable continuous metabolic monitoring at controlled oxygen levels. *Biosens Bioelectron* **265**, 116683 (2024). https://doi.org/10.1016/j.bios.2024.116683

145 Singh, G. *et al.* Advancement of organ-on-chip towards next generation medical technology. *Biosensors and Bioelectronics: X* **18** (2024). https://doi.org/10.1016/j.biosx.2024.100480

146 Zang, X., Zhou, J., Zhang, X., Han, Y. & Chen, X. Ischemia Reperfusion Injury: Opportunities for Nanoparticles. *ACS Biomater Sci Eng* **6**, 6528-6539 (2020). https://doi.org/10.1021/acsbiomaterials.0c01197

147 Tara, A. *et al.* Mitochondrial Targeting Therapy Role in Liver Transplant Preservation Lines: Mechanism and Therapeutic Strategies. *Cureus* **13**, e16599 (2021). https://doi.org/10.7759/cureus.16599

148 Wang, L. *et al.* Mitochondrial quality control in hepatic ischemia-reperfusion injury. *Heliyon* **9**, e17702 (2023). https://doi.org/10.1016/j.heliyon.2023.e17702

149 Mealer, C., Konsek, H., Travis, Z., Suk, R. N. & Rajab, T. K. Mechanisms of Cold Preservation and Reperfusion Injury for Solid Organ Transplantation: Implications for Partial Heart Transplantations. *Transplantology* **4**, 124-138 (2023). https://doi.org/10.3390/transplantology4030013

150 Hofmann, J. *et al.* Novel, Innovative Models to Study Ischemia/Reperfusion-Related Redox Damage in Organ Transplantation. *Antioxidants (Basel)* **12** (2022). https://doi.org/10.3390/antiox12010031

151 Dery, K. J., Yao, S., Cheng, B. & Kupiec-Weglinski, J. W. New therapeutic concepts against ischemia-reperfusion injury in organ transplantation. *Expert Rev Clin Immunol* **19**, 1205-1224 (2023).

https://doi.org/10.1080/1744666X.2023.2240516
152 Ostrozka-Cieslik, A. Modification of Preservative Fluids with Antioxidants in Terms of Their Efficacy in Liver Protection before Transplantation. *Int J Mol Sci* **25** (2024). https://doi.org/10.3390/ijms25031850
153 Kosieradzki, M. & Rowinski, W. Ischemia/reperfusion injury in kidney transplantation: mechanisms and prevention. *Transplant Proc* **40**, 3279-3288 (2008). https://doi.org/10.1016/j.transproceed.2008.10.004
154 Pühringer, M., Messner, F. & Schneeberger, S. Normothermic Machine Perfusion of Kidney Grafts: Devices, Endpoints, and Clinical Implementation. *European Surgery* **57**, 88-99 (2025). https://doi.org/10.1007/s10353-025-00856-3
155 Lin, Y. *et al.* Mitochondria-Inspired Nanoparticles with Microenvironment-Adapting Capacities for On-Demand Drug Delivery after Ischemic Injury. *ACS Nano* **14**, 11846-11859 (2020). https://doi.org/10.1021/acsnano.0c04727
156 Mughal, S. *et al.* Organs-on-Chips: Trends and Challenges in Advanced Systems Integration. *Advanced Materials Interfaces* **9** (2022). https://doi.org/10.1002/admi.202201618
157 Protsak, I. S. & Morozov, Y. M. Fundamentals and Advances in Stimuli-Responsive Hydrogels and Their Applications: A Review. *Gels* **11** (2025). https://doi.org/10.3390/gels11010030
158 Luo, Q. *et al.* Multi-stage cooperative ROS-responsive hydrogel platform for drug delivery in myocardial ischemia-reperfusion injury repair. *Mater Today Bio* **32**, 101854 (2025). https://doi.org/10.1016/j.mtbio.2025.101854
159 He, Z. *et al.* Reactive oxygen species (ROS): utilizing injectable antioxidative hydrogels and ROS-producing therapies to manage the double-edged sword. *J Mater Chem B* **9**, 6326-6346 (2021). https://doi.org/10.1039/d1tb00728a
160 Liu, D. *et al.* Low-temperature resistant self-healing hydrogel electrolyte for dendrite-free flexible zinc-ion hybrid supercapacitors. *Journal of Power Sources* **621** (2024). https://doi.org/10.1016/j.jpowsour.2024.235265
161 Li, B. *et al.* A wearable zinc-air battery based on an Agar hydrogel electrolyte for stable operation at −30 °C. *Chemical Physics Letters* **832** (2023). https://doi.org/10.1016/j.cplett.2023.140883
162 Liu, W. *et al.* Low-temperature suitability of flexible photo-rechargeable devices integrated with hydrogel-based lithium-ion batteries and perovskite solar cells. *Journal of Materials Chemistry A* **12**, 18214-18223 (2024). https://doi.org/10.1039/d4ta03076a
163 Khadka, B., Lee, B. & Kim, K.-T. Drug Delivery Systems for Personal Healthcare by Smart Wearable Patch System. *Biomolecules* **13** (2023). https://doi.org/10.3390/biom13060929
164 Khodaparast, M., Sharley, D., Marshall, S. & Beddoe, T. Advances in point-of-care and molecular techniques to detect waterborne pathogens. *npj Clean Water* **7** (2024). https://doi.org/10.1038/s41545-024-00368-9
165 Ando, H., Iwamoto, R., Kobayashi, H., Okabe, S. & Kitajima, M. The Efficient and Practical virus Identification System with ENhanced Sensitivity for Solids

(EPISENS-S): A rapid and cost-effective SARS-CoV-2 RNA detection method for routine wastewater surveillance. *Science of The Total Environment* **843**, 157101 (2022). https://doi.org/https://doi.org/10.1016/j.scitotenv.2022.157101

166 Zhou, B. *et al.* SARS-CoV-2 hijacks neutralizing dimeric IgA for nasal infection and injury in Syrian hamsters

1. *Emerging Microbes & Infections* **12** (2023). https://doi.org/10.1080/22221751.2023.2245921

167 Kadadou, D. *et al.* Detection of SARS-CoV-2 in clinical and environmental samples using highly sensitive reduced graphene oxide (rGO)-based biosensor. *Chemical Engineering Journal* **453** (2023). https://doi.org/10.1016/j.cej.2022.139750

168 Chaibun, T. *et al.* Rapid electrochemical detection of coronavirus SARS-CoV-2. *Nature Communications* **12** (2021). https://doi.org/10.1038/s41467-021-21121-7

169 Tao, S. *et al.* SARS-Cov-2 Spike-S1 Antigen Test Strip with High Sensitivity Endowed by High-Affinity Antibodies and Brightly Fluorescent QDs/Silica Nanospheres. *ACS Applied Materials & Interfaces* **15**, 27612-27623 (2023). https://doi.org/10.1021/acsami.3c03434

170 Cesewski, E. & Johnson, B. N. Electrochemical biosensors for pathogen detection. *Biosensors and Bioelectronics* **159** (2020). https://doi.org/10.1016/j.bios.2020.112214

171 Akarapipad, P. *et al.* Smartphone-based sensitive detection of SARS-CoV-2 from saline gargle samples via flow profile analysis on a paper microfluidic chip. *Biosensors and Bioelectronics* **207**, 114192 (2022). https://doi.org/https://doi.org/10.1016/j.bios.2022.114192

172 Silva, P. B. d. *et al.* Detection of SARS-CoV-2 virus via dynamic light scattering using antibody-gold nanoparticle bioconjugates against viral spike protein. *Talanta* **243** (2022). https://doi.org/10.1016/j.talanta.2022.123355

173 Somvanshi, S. B. *et al.* Microfluidic paper-based aptasensor devices for multiplexed detection of pathogenic bacteria. *Biosensors and Bioelectronics* **207**, 114214 (2022). https://doi.org/https://doi.org/10.1016/j.bios.2022.114214

174 Unione, L. *et al.* Probing altered receptor specificities of antigenically drifting human H3N2 viruses by chemoenzymatic synthesis, NMR, and modeling. *Nature Communications* **15**, 2979 (2024). https://doi.org/10.1038/s41467-024-47344-y

175 Yu, H. *et al.* Recent Advances in Field-Effect Transistor-Based Biosensors for Label-Free Detection of SARS-CoV-2. *Small Science* **4** (2023). https://doi.org/10.1002/smsc.202300058

176 Lee, S.-K. *et al.* Method for the Rapid Detection of SARS-CoV-2-Neutralizing Antibodies Using a Nanogel-Based Surface Plasmon Resonance Biosensor. *ACS Applied Polymer Materials* **5**, 2195-2202 (2023). https://doi.org/10.1021/acsapm.2c02187

177 Iravani, S. Nano- and biosensors for the detection of SARS-CoV-2: challenges and opportunities. *Materials Advances* **1**, 3092-3103 (2020).

https://doi.org/10.1039/d0ma00702a
178 Tepeli Büyüksünetçi, Y. & Anik, Ü. Graphene-Based Nanomaterial Electrochemical Biosensors for the Determination of the H3N2 Virus. *Analytical Letters* **57**, 2544-2559 (2023). https://doi.org/10.1080/00032719.2023.2297407
179 Kadadou, D. *et al.* Recent advances in the biosensors application for the detection of bacteria and viruses in wastewater. *Journal of Environmental Chemical Engineering* **10** (2022). https://doi.org/10.1016/j.jece.2021.107070
180 Jiménez-Rodríguez, M. G. *et al.* Biosensors for the detection of disease outbreaks through wastewater-based epidemiology. *TrAC Trends in Analytical Chemistry* **155** (2022). https://doi.org/10.1016/j.trac.2022.116585
181 Eftekhari, A. *et al.* A Comprehensive Review of Detection Methods for SARS-CoV-2. *Microorganisms* **9** (2021). https://doi.org/10.3390/microorganisms9020232
182 Liu, Y. *et al.* Antibody screening-assisted multichannel nanoplasmonic sensing chip based on SERS for viral screening and variants identification. *Biosensors and Bioelectronics* **271**, 117015 (2025). https://doi.org/https://doi.org/10.1016/j.bios.2024.117015
183 Butler, D. & Ebrahimi, A. Rapid and sensitive detection of viral particles by coupling redox cycling and electrophoretic enrichment. *Biosensors and Bioelectronics* **208**, 114198 (2022). https://doi.org/https://doi.org/10.1016/j.bios.2022.114198
184 del Caño, R. *et al.* Amplification-free detection of SARS-CoV-2 using gold nanotriangles functionalized with oligonucleotides. *Microchimica Acta* **189** (2022). https://doi.org/10.1007/s00604-022-05272-y
185 Büyüksünetçi, Y. T. & Anık, Ü. Electro-Nano Diagnostic Platform Based on Antibody–Antigen Interaction: An Electrochemical Immunosensor for Influenza A Virus Detection. *Biosensors* **13** (2023). https://doi.org/10.3390/bios13020176
186 Polli, F. *et al.* Nanoparticles in Electrochemical Immunosensors – A Concept and Perspective. *ChemElectroChem* **11** (2023). https://doi.org/10.1002/celc.202300408
187 Orzari, L. O. *et al.* in *Covid-19 Metabolomics and Diagnosis* Ch. Chapter 4, 61-70 (2023).
188 Zamzami, M. A. *et al.* Carbon nanotube field-effect transistor (CNT-FET)-based biosensor for rapid detection of SARS-CoV-2 (COVID-19) surface spike protein S1. *Bioelectrochemistry* **143** (2022). https://doi.org/10.1016/j.bioelechem.2021.107982
189 Wang, L. *et al.* Ultrasensitive and on-site eDNA detection for the monitoring of crown-of-thorns starfish densities at the pre-outbreak stage using an electrochemical biosensor. *Biosensors and Bioelectronics* **230** (2023). https://doi.org/10.1016/j.bios.2023.115265
190 Sun, X. *et al.* A novel oriented antibody immobilization based voltammetric immunosensor for allergenic activity detection of lectin in kidney bean by using

AuNPs-PEI-MWCNTs modified electrode. *Biosensors and Bioelectronics* **143** (2019). https://doi.org/10.1016/j.bios.2019.111607

191 Lee, J. Carbon Nanotube-Based Biosensors Using Fusion Technologies with Biologicals & Chemicals for Food Assessment. *Biosensors* **13** (2023). https://doi.org/10.3390/bios13020183

192 Goscianska, J., Freund, R. & Wuttke, S. Nanoscience versus Viruses: The SARS-CoV-2 Case. *Advanced Functional Materials* **32** (2021). https://doi.org/10.1002/adfm.202107826

193 Patel, M., Agrawal, M. & Srivastava, A. Signal amplification strategies in electrochemical biosensors via antibody immobilization and nanomaterial-based transducers. *Materials Advances* **3**, 8864-8885 (2022). https://doi.org/10.1039/d2ma00427e

194 Kim, D. *et al.* Detection of Alpha-Fetoprotein in Hepatocellular Carcinoma Patient Plasma with Graphene Field-Effect Transistor. *Sensors* **18** (2018). https://doi.org/10.3390/s18114032

195 Ghafary, Z., Salimi, A. & Hallaj, R. Exploring the Role of 2D-Graphdiyne as a Charge Carrier Layer in Field-Effect Transistors for Non-Covalent Biological Immobilization against Human Diseases. *ACS Biomaterials Science & Engineering* **8**, 3986-4001 (2022). https://doi.org/10.1021/acsbiomaterials.2c00607

196 Seo, G. *et al.* Rapid Detection of COVID-19 Causative Virus (SARS-CoV-2) in Human Nasopharyngeal Swab Specimens Using Field-Effect Transistor-Based Biosensor. *ACS Nano* **14**, 5135-5142 (2020). https://doi.org/10.1021/acsnano.0c02823

197 Wang, L. *et al.* Rapid and ultrasensitive electromechanical detection of ions, biomolecules and SARS-CoV-2 RNA in unamplified samples. *Nature Biomedical Engineering* **6**, 276-285 (2022). https://doi.org/10.1038/s41551-021-00833-7

198 Zhao, Y. *et al.* All-solid-state SARS-CoV-2 protein biosensor employing colloidal quantum dots-modified electrode. *Biosens Bioelectron* **202**, 113974 (2022). https://doi.org/10.1016/j.bios.2022.113974

199 Ramos-Mandujano, G. *et al.* An open-source, automated, and cost-effective platform for COVID-19 diagnosis and rapid portable genomic surveillance using nanopore sequencing. *Scientific Reports* **13**, 20349 (2023). https://doi.org/10.1038/s41598-023-47190-w

200 Lin, Y. *et al.* Porous Enzymatic Membrane for Nanotextured Glucose Sweat Sensors with High Stability toward Reliable Noninvasive Health Monitoring. *Advanced Functional Materials* **29** (2019). https://doi.org/10.1002/adfm.201902521

201 Lai, S. *et al.* Ultrasensitive detection of SARS-CoV-2 antigen using surface-enhanced Raman spectroscopy-based lateral flow immunosensor. *Journal of Biophotonics* **16** (2023). https://doi.org/10.1002/jbio.202300004

202 Huang, J. *et al.* On-Site Detection of SARS-CoV-2 Antigen by Deep Learning-Based Surface-Enhanced Raman Spectroscopy and Its Biochemical

Foundations. *Analytical Chemistry* **93**, 9174-9182 (2021). https://doi.org/10.1021/acs.analchem.1c01061

203 Wang, X. *et al.* Robust nCuO modulated by defect engineering enhanced photoelectrochemical biosensor for the detection of miRNA-21. *Biosensors and Bioelectronics* **271**, 117014 (2025). https://doi.org/https://doi.org/10.1016/j.bios.2024.117014

204 Lee, H. *et al.* Plug-and-play protein biosensors using aptamer-regulated in vitro transcription. *Nature Communications* **15**, 7973 (2024). https://doi.org/10.1038/s41467-024-51907-4

205 Yeh, Y.-J. *et al.* Plasmonic nanostructure-enhanced Raman scattering for detection of SARS-CoV-2 nucleocapsid protein and spike protein variants. *Analytica Chimica Acta* **1239** (2023). https://doi.org/10.1016/j.aca.2022.340651

206 Verma, S. *et al.* ZnO-rGO nanocomposite based bioelectrode for sensitive and ultrafast detection of dopamine in human serum. *Biosensors and Bioelectronics* **165** (2020). https://doi.org/10.1016/j.bios.2020.112347

207 Hodge, C. D. *et al.* Rigid monoclonal antibodies improve detection of SARS-CoV-2 nucleocapsid protein. *mAbs* **13** (2021). https://doi.org/10.1080/19420862.2021.1905978

208 Zhu, Y. *et al.* A post-pandemic perspective: Evolution of SARS-CoV-2 early detection. *TrAC Trends in Analytical Chemistry* **170** (2024). https://doi.org/10.1016/j.trac.2023.117458

209 Sadique, M. A. *et al.* Highly Sensitive Electrochemical Immunosensor Platforms for Dual Detection of SARS-CoV-2 Antigen and Antibody based on Gold Nanoparticle Functionalized Graphene Oxide Nanocomposites. *ACS Applied Bio Materials* **5**, 2421-2430 (2022). https://doi.org/10.1021/acsabm.2c00301

210 Krejcova, L., Hynek, D., Adam, V., Hubalek, J. & Kizek, R. Electrochemical Sensors and Biosensors for Influenza Detection. *International Journal of Electrochemical Science* **7**, 10779-10801 (2012). https://doi.org/10.1016/s1452-3981(23)16902-1

211 Zeng, Z. *et al.* Molecular epidemiology and phylogenetic analysis of influenza viruses A (H3N2) and B/Victoria during the COVID-19 pandemic in Guangdong, China. *Infectious Diseases of Poverty* **13**, 56 (2024). https://doi.org/10.1186/s40249-024-01218-z

212 Tang, W. *et al.* Touch-Based Stressless Cortisol Sensing. *Advanced Materials* **33** (2021). https://doi.org/10.1002/adma.202008465

213 Drobysh, M. *et al.* Electrochemical biosensing based comparative study of monoclonal antibodies against SARS-CoV-2 nucleocapsid protein. *Science of The Total Environment* **908** (2024). https://doi.org/10.1016/j.scitotenv.2023.168154

214 de Araujo, W. R., Lukas, H., Torres, M. D. T., Gao, W. & de la Fuente-Nunez, C. Low-Cost Biosensor Technologies for Rapid Detection of COVID-19 and Future Pandemics. *ACS Nano* **18**, 1757-1777 (2024). https://doi.org/10.1021/acsnano.3c01629

215 Torres, M. D. T., de Araujo, W. R., de Lima, L. F., Ferreira, A. L. & de la Fuente-Nunez, C. Low-cost biosensor for rapid detection of SARS-CoV-2 at the point of care. *Matter* **4**, 2403-2416 (2021). https://doi.org/10.1016/j.matt.2021.05.003

216 Wei, H., Zhang, C., Du, X. & Zhang, Z. Research progress of biosensors for detection of SARS-CoV-2 variants based on ACE2. *Talanta* **251** (2023). https://doi.org/10.1016/j.talanta.2022.123813

217 Nascimento, E. D. *et al.* COVID-19 diagnosis by SARS-CoV-2 Spike protein detection in saliva using an ultrasensitive magneto-assay based on disposable electrochemical sensor. *Sensors and Actuators B: Chemical* **353** (2022). https://doi.org/10.1016/j.snb.2021.131128

218 Mei, J., Liao, T., Ayoko, G. A. & Sun, Z. Two-Dimensional Bismuth Oxide Heterostructured Nanosheets for Lithium- and Sodium-Ion Storages. *ACS Applied Materials & Interfaces* **11**, 28205-28212 (2019). https://doi.org/10.1021/acsami.9b09882

219 Cheng, H. *et al.* Synergistic effect of crystal and electronic structures on the visible-light-driven photocatalytic performances of Bi2O3 polymorphs. *Physical Chemistry Chemical Physics* **12** (2010). https://doi.org/10.1039/c0cp01189d

220 Younis, A. A., El-Sabbah, M. M. B. & Holze, R. The effect of chloride concentration and pH on pitting corrosion of AA7075 aluminum alloy coated with phenyltrimethoxysilane. *Journal of Solid State Electrochemistry* **16**, 1033-1040 (2011). https://doi.org/10.1007/s10008-011-1476-7

221 Zhang, J. *et al.* Doping indium in β-Bi2O3to tune the electronic structure and improve the photocatalytic activities: first-principles calculations and experimental investigation. *Phys. Chem. Chem. Phys.* **16**, 23476-23482 (2014). https://doi.org/10.1039/c4cp02656j

222 Ankhili, A. *et al.* Ambulatory Evaluation of ECG Signals Obtained Using Washable Textile-Based Electrodes Made with Chemically Modified PEDOT:PSS. *Sensors* **19**, 416 %* http://creativecommons.org/licenses/by/413.410/ %U https://www.mdpi.com/1424-8220/1419/1422/1416 (2019).

223 Gao, W. *et al.* Wearable Microsensor Array for Multiplexed Heavy Metal Monitoring of Body Fluids. *ACS Sensors* **1**, 866-874 %U https://doi.org/810.1021/acssensors.1026b00287 (2016).

224 Jiang, Y. *et al.* Real-Time Monitoring of Heavy Metals in Healthcare via Twistable and Washable Smartsensors. *Analytical Chemistry* **92**, 14536-14541 %U https://doi.org/14510.11021/acs.analchem.14530c02723 (2020).

225 Jose, M. *et al.* Monitoring Body Fluids in Textiles: Combining Impedance and Thermal Principles in a Printed, Wearable, and Washable Sensor %W world %* © 2021 American Chemical Society %U https://pubs.acs.org/doi/full/10.1021/acssensors.0c02037. *ACS Sensors* (2021).

226 Sadeqi, A. *et al.* Washable Smart Threads for Strain Sensing Fabrics. *IEEE Sensors Journal* **18**, 9137-9144 (2018).

227 Sala de Medeiros, M., Goswami, D., Chanci, D., Moreno, C. & Martinez, R. V.

Washable, breathable, and stretchable e-textiles wirelessly powered by omniphobic silk-based coils. *Nano Energy* **87**, 106155 %U https://www.sciencedirect.com/science/article/pii/S2211285521004110 (2021).

228 Shathi, M. A., Chen, M., Khoso, N. A., Rahman, M. T. & Bhattacharjee, B. Graphene coated textile based highly flexible and washable sports bra for human health monitoring. *Materials & Design* **193**, 108792 %U https://www.sciencedirect.com/science/article/pii/S0264127520303269 (2020).

229 Yao, D. *et al.* Gas-permeable and highly sensitive, washable and wearable strain sensors based on graphene/carbon nanotubes hybrids e-textile. *Composites Part A: Applied Science and Manufacturing* **149**, 106556 %U https://www.sciencedirect.com/science/article/pii/S1359835X21002785 (2021).

230 Yang, S. *et al.* Permeable and washable electronics based on polyamide fibrous membrane for wearable applications. *Composites Science and Technology* **207**, 108729 %U https://www.sciencedirect.com/science/article/pii/S0266353821000853 (2021).

231 Xuan, X., Hui, X., Yoon, H., Yoon, S. & Park, J. Y. A rime ice-inspired bismuth-based flexible sensor for zinc ion detection in human perspiration. *Microchimica Acta* **188**, 97 %U https://doi.org/10.1007/s00604-00021-04752-x (2021).

232 Zhang, H. *et al.* A fully integrated wearable electronic device with breathable and washable properties for long-term health monitoring. *Sensors and Actuators A: Physical* **322**, 112611 %U https://www.sciencedirect.com/science/article/pii/S0924424721000728 (2021).

233 Mei, J., Liao, T., Ayoko, G. A. & Sun, Z. Two-Dimensional Bismuth Oxide Heterostructured Nanosheets for Lithium- and Sodium-Ion Storages. *ACS Applied Materials & Interfaces* **11**, 28205-28212 %U https://doi.org/28210.21021/acsami.28209b09882 (2019).

234 A. R, R., Ragula, U., Kothurkar, N. & Rangarajan, M. Nano- and Micro-Hexagons of Bismuth on Polycrystalline Copper: Electrodeposition and Heavy Metal Sensing. *CrystEngComm* **16**, 2032-2038 (2013).

235 Hatfield, K. O. *et al.* Electrodeposition and analysis of thick bismuth films. *Scientific Reports* **13**, 1202 %* 2023 The Author(s) %U https://www.nature.com/articles/s41598-41023-28042-z (2023).

236 Jiang, S., Huang, Y.-H., Luo, F., Du, N. & Yan, C.-H. Synthesis of bismuth with various morphologies by electrodeposition. *Inorganic Chemistry Communications* **6**, 781-785 %U https://www.sciencedirect.com/science/article/pii/S1387700303001047 (2003).

237 Economou, A. Bismuth-film electrodes: recent developments and potentialities for electroanalysis. *TrAC Trends in Analytical Chemistry* **24**, 334-340 %U https://www.sciencedirect.com/science/article/pii/S0165993604030912 (2005).

238 Mehring, M. From molecules to bismuth oxide-based materials: Potential homo- and heterometallic precursors and model compounds. *Coordination Chemistry Reviews* **251**, 974-1006 %U https://www.sciencedirect.com/science/article/pii/S0010854506001810 (2007).

239 Yao, L. *et al.* Bismuth oxychloride-based materials for the removal of organic

pollutants in wastewater. *Chemosphere* **273**, 128576 %U https://www.sciencedirect.com/science/article/pii/S0045653520327715 (2021).

240 Sandnes, E., Williams, M. E., Bertocci, U., Vaudin, M. D. & Stafford, G. R. Electrodeposition of bismuth from nitric acid electrolyte. *Electrochimica Acta* **52**, 6221-6228 %U https://linkinghub.elsevier.com/retrieve/pii/S001346860700463X (2007).

241 Li, Z. *et al.* Three-dimensionally Ordered Macroporous β-Bi2O3 with Enhanced Electrochemical Performance in a Li-ion Battery. *Electrochimica Acta* **214**, 103-109 %U https://www.sciencedirect.com/science/article/pii/S0013468616317261 (2016).

242 Helfen, A. *et al.* Structure and stability studies of electrodeposited δ-Bi2O3. *Solid State Ionics* **176**, 629-633 %U https://www.sciencedirect.com/science/article/pii/S0167273804005326 (2005).

243 Hao, C. *et al.* A glassy carbon electrode modified with bismuth oxide nanoparticles and chitosan as a sensor for Pb(II) and Cd(II). *Microchimica Acta* **183**, 1823-1830 %U https://doi.org/1810.1007/s00604-00016-01816-00605 (2016).

244 Bobade, R. G. *et al.* Nanoarchitectonics of Bi2CuO4 electrodes for asymmetric Bi2CuO4//AC solid-state device in supercapacitor application. *Inorganic Chemistry Communications* **154**, 110998 %U https://www.sciencedirect.com/science/article/pii/S138770032300610X (2023).

245 Laurent, K., Wang, G. Y., Tusseau-Nenez, S. & Leprince-Wang, Y. Structure and conductivity studies of electrodeposited δ-Bi2O3. *Solid State Ionics* **178**, 1735-1739 %U https://www.sciencedirect.com/science/article/pii/S0167273807003542 (2008).

246 Koza, J. A., Bohannan, E. W. & Switzer, J. A. Superconducting Filaments Formed During Nonvolatile Resistance Switching in Electrodeposited δ-Bi2O3. *ACS Nano* **7**, 9940-9946 %U https://doi.org/9910.1021/nn4038207 (2013).

247 Huang, C.-C., Wen, T.-Y. & Fung, K.-Z. Orientation-controlled phase transformation of Bi2O3 during oxidation of electrodeposited Bi film. *Materials Research Bulletin* **41**, 110-118 %U https://www.sciencedirect.com/science/article/pii/S0025540805002837 (2006).

248 Zhao, K., Ge, L. & Lisak, G. Facile synthesis of electrocatalytically active bismuth oxide nanosheets for detection of palladium traces in pharmaceutical wastewater. *Environmental Pollution* **307**, 119524 %U https://www.sciencedirect.com/science/article/pii/S0269749122007382 (2022).

249 Wang, Y., Long, Y. & Zhang, D. Facile in situ growth of photoactive β-Bi2O3 films. *Journal of the Taiwan Institute of Chemical Engineers* **75**, 183-188 %U https://www.sciencedirect.com/science/article/pii/S1876107017301505 (2017).

250 Liu, X. *et al.* 2D Metal–Organic Frameworks Derived Nanocarbon Arrays for Substrate Enhancement in Flexible Supercapacitors. *Small* **14**, 1702641 %* © 1702017 WILEY-VCH Verlag GmbH & Co. KGaA, Weinheim %U https://onlinelibrary.wiley.com/doi/abs/1702610.1701002/smll.201702641 (2018).

251 Wu, D., Huo, G., Chen, W., Fu, X.-Z. & Luo, J.-L. Boosting formate production at high current density from CO2 electroreduction on defect-rich hierarchical mesoporous Bi/Bi2O3 junction nanosheets. *Applied Catalysis B: Environmental* **271**, 118957 %U https://www.sciencedirect.com/science/article/pii/S0926337320303726 (2020).

252 Xu, M. *et al.* High-capacity Bi2O3 anode for 2.4 V neutral aqueous sodium-ion battery-supercapacitor hybrid device through phase conversion mechanism. *Journal of Energy Chemistry* **65**, 605-615 %U https://www.sciencedirect.com/science/article/pii/S209549562100382X (2022).

253 Qiu, Y. *et al.* Phase-transitions of α- and β-Bi2O3 nanowires. *Materials Letters* **65**, 780-782 %U https://www.sciencedirect.com/science/article/pii/S0167577X10010153 (2011).

254 Kim, H. W. Synthesis and characterization of crystalline β-Bi2O3 nanobelts. *Thin Solid Films* **516**, 3665-3668 %U https://www.sciencedirect.com/science/article/pii/S0040609007014605 (2008).